OPTICAL ACTIVITY AND APPLICATIONS OF
PLANAR CHIRAL METAMATERIALS

Wen Zhang

PhD Thesis, September 2006

UNIVERSITY OF SOUTHAMPTON

OPTICAL ACTIVITY AND APPLICATIONS OF PLANAR CHIRAL METAMATERIALS

by

Wen Zhang

A thesis submitted for the degree of
Doctor of Philosophy

FACULTY OF ENGINEERING AND APPLIED SCIENCES
SCHOOL OF ELECTRONICS AND COMPUTER SCIENCE

September 2006

UNIVERSITY OF SOUTHAMPTON

ABSTRACT

FACULTY OF ENGINEERING AND APPLIED SCIENCES
SCHOOL OF ELECTRONICS AND COMPUTER SCIENCE

Doctor of Philosophy

OPTICAL ACTIVITY AND APPLICATIONS OF PLANAR CHIRAL METAMATERIALS

by Wen Zhang

The polarization and intensity behaviours of optical planar chiral metamaterials have been investigated in order to further understand the fundamental mechanisms that produce optical activity in these materials, and to seek applications for the unique properties that they offer.

A range of planar chiral metamaterials were fabricated using electron beam lithography, reactive ion etching and lift-off techniques to produce high densities of complex planar chiral patterns distributed over large areas on silicon and silica substrates. A range of materials have been used to form the active layer of the planar chiral metamaterials.

Planar chiral metamaterials produced using all metallic and dielectric layers are found to induce large changes in the polarization state of first-order reflected and transmitted beams. The anisotropic optical activity in higher-order diffracted beams is sensitive to both the two-dimensional chirality and the thickness of the patterned layer. These results provide further evidence of the role of planar chirality in determining the direction and magnitude of the polarization changes observed in planar chiral metamaterials. Meanwhile, the dependence of the polarization response of the first-order diffracted beams on the thickness of the active layers and the lack of activity of samples where chiral patterns were simply etched into a substrate, suggest that thin film interference has a significant role in the mechanisms that determine the optical activity of all planar chiral metamaterials.

Analysis of the intensities of diffracted beams shows that the planar chiral structures induce significant intensity modulations that are dependent on the polarization state of the incident light. Silicon photodiodes with integrated planar chiral metamaterials are designed and fabricated. The magnitude of the photoresponse of these devices shows strong dependence on the polarization of the incident beam and responses for enantiomeric structures are significantly different. Intensity responses observed for both stand-alone and integrated planar chiral materials indicate potential for polarization sensitive detectors, polarimeter and polarization modulators.

The principles of optical reciprocity are considered along with the implications of non-reciprocity. In a number of particular configurations, certain diffraction processes with planar chiral metamaterials are experimentally shown to be non-reciprocal and non-reversible, although practical applications of these effects would be limited unless non-diffractive device configurations can be found. One such device is proposed that would also allow studies of the fundamental symmetries of planar chiral structures by combining two planar chiral gratings and blocking the zero-order beam using a Bragg reflector.

Contents

List of Figures

List of Tables

List of Symbols

ε	-	permittivity
μ	-	permeability
ϵ_0	-	permittivity of free space
μ_0	-	permeability of free space
K	-	chirality index
$\triangle$	-	triangle's area
$\mathbf{r}$	-	coordinate vectors
$\rho_{\mathbf{r}}$	-	point density function
$\Gamma_{\mathbf{r}}$	-	dimensionless chirality index
$\mathbf{E}$	-	electric field
$\mathbf{H}$	-	magnetic field
$\mathbf{D}$	-	electric displacement field
$\mathbf{B}$	-	magnetic flux density
k	-	wave number
ω	-	angular frequency
ϕ	-	phase constant
c	-	velocity of light
ν	-	wave velocity
λ	-	wavelength
λ_0	-	wavelength in the vacuum
n	-	refractive index
ρ	-	free electric charge density
$\mathbf{J}$	-	free electric current density
S_0, S_1, S_2, S_3	-	Stokes parameters
Φ	-	polarization azimuth angle
η	-	ellipticity
R	-	degree of polarization
$\mathbf{I}$	-	irradiance
Δ	-	optical path length
θ	-	diffraction angle
β	-	angle of incidence
d	-	grating period
m	-	diffraction order
Λ	-	gammadion pitch size
ξ	-	gammadion arm length
α	-	gammadion bending angle
ϕ_0	-	input polarization azimuth

ϕ	-	output polarization azimuth
$\Delta\phi$	-	polarization azimuth rotation angle
σ	-	filling factor
w	-	line width
i,j	-	diffraction order
$\mathbf{J}(\phi,\eta)$	-	Jones vector
r_i	-	amplitude of polarization state
δ_i	-	phase of the polarization state
$\mathcal{A}$	-	transfer matrix for forward process
$\mathcal{B}$	-	transfer matrix for reverse process
μ_a	-	scaling function for forward process
μ_b	-	scaling function for reverse process
$\mu_{\sigma\sigma}$	-	eigenvalue of output polarization state
$\mathbf{J}\ (\phi,\eta)$	-	polarization eigenstates
$\Delta\Theta$	-	non-orthogonality angle
R_I	-	relative intensity
I_I	-	intensity of the incident beam
$\mathrm{I}_{i,j}$	-	intensity of the diffracted beam
$\mathbb{C}$	-	relative intensity contrast
$\mathbb{A}$	-	relative intensity amplification
$\mathbf{P}$	-	parity operation
$\mathbf{T}$	-	time operation
$\mathbf{C}$	-	charge operation
r	-	reflection coefficient
t	-	transmission coefficient
R	-	normalized reflection coefficient
T	-	normalized transmission coefficient
$\mathbf{M}$	-	characteristic matrix

Acknowledgment

First, I would like to thank my Ph.D. supervisor, Dr. Darren Bagnall, for providing me this opportunity to be his student and work on this optical metamaterials project. Thanks for his guidance, support and understanding throughout my PhD project. He provided me with a good opportunity to start my professional career in the fields of microelectronics, optics and nano-technology, as well as a very pleasant working environment within the Nanoscale System Integration group during the past four years. Thanks for standing by my side not only as a professional supervisor, but also as a great friend.

Many thanks goes to Dr. Adrian Potts for his professional advice, theories and lots of interesting discussions. Thanks for the "physics to dummies" lectures and I will definitely keep the notes with thousands of equations.

I would like to thank Aris Papakostas for his technical discussions about this project and his professional advice on my experimental setup and measurements. He provided valuable data to this project.

Also, I would especially thank Dr. Brian Davidson for the brilliant work and great support to the samples fabrication. Thanks for all the patient explanations, generous help and all the professional suggestions and advice. Additionally, i would like to thank all the staff from Innos Ltd. for their technical support in the clean room. Thanks for all the professional training and practical suggestions on my device fabrication.

A very special thanks to Dr Graham Ensell for his great advice throughout my PhD project. I greatly appreciate appreciate his proofreading of this thesis with all the valuable suggestions. Thanks for his kind help, caring and all the lovely walks while taking me to explore the new forest.

I would also like to thank my fellow PhD student: Dr. Harald Sehr, thanks for the friendship and all the support in the past four years; Dr. Ruth houlihan, thanks for the lovely chats at our regular Friday staff club "meetings"; Dr. Claudia Cerrina, thanks for all the support and encouragement; Dr. Dominik Kunz, thanks for all the great advices on my thesis writing and for your continuous support; Enrico Gill, thank you so much for getting me into rock climbing and it is great to have you as a friend; Tristan Temple and Stuart Boden, thanks for all the help and support while I was writing my thesis, I really enjoyed our lunch breaks and chats after work.

Also to my group of friends: Dr. Angelique Faver, Kathrin Feller, Dr. HuaBing Yin, WenJun Niu, Katerina Gargaroni, Colleen Butler, Judith Joseph, Charlotte

Tupman, Sophie Monje-Dumas, and Jos Akhtman. Thanks for standing by my side and continuously supporting me throughout my PhD.

A very special thanks for my boy friend, Cormac Long. Thank you for your great support of my work, thanks for your looking after me and keeping me strong. Last, a very important thanks goes to my parents and my sister for their gracious understanding, support and encouragement. Without you, I will not be standing here as who I am today!

Chapter 1

Introduction

1.1 Introduction

Optical structures artificially engineered on a mezoscopic level such as photonic bandgap crystals [1], periodically altered dielectric materials [2] and microsculptured films [3] are attracting tremendous attention because of their potential importance in optoelectronic technologies. These artificial structures with unique electromagnetic properties are known as *metamaterials*. These metamaterials, which can in principle be synthesized by embedding or including various constituents of novel geometrical shapes and forms in some host media, possess exciting features and interesting electromagnetic properties. They are not easily available in nature but are physically realizable, and they have new potential applications in the design of optical devices and components.

In this work, a particular type of optical metamaterial: planar chiral metamaterial, is studied. A planar object is said to be chiral in two dimensions if it can not be brought into congruence with its mirror image unless it is lifted from the plane. The measure of this inability is the chirality content of the structure [4]. Planar chirality is a special case of chirality for two-dimensional (2D) structures. Planar chiral structures consist of chiral elements that posses no line of symmetry in the plane of structure. In recent years the concept of 2D chirality has been recognized as an important one. The optical properties of planar chiral media have been attracting increasing attention from the scientific community. A material which rotates the plane of incident linearly polarized light is said to be optically active [5]. Optical activity can be explained by considering that in optically active crystals the velocity of propagation of circularly polarized light is different for different directions of rotation, that is the crystal has refractive indices n_r and n_l for right and left circularly polarized light [6]. The ability of left- and right-handed asymmetrical

chiral three-dimensional (3D) helical molecules to rotate the polarization state of light is an important phenomenon in modern optics as well as having important consequences in both chemical and biological systems. As a result, whether planar chiral media can affect the polarization state of light in a manner similar to 3D chiral media is under investigation. If this were shown to be the case then it could lead to new generations of optical devices and components with potential applications in optoelectronic devices and communications. In recent years, the properties of electromagnetic radiation scattered by, and propagating through, planar chiral structures of various sizes and geometries have been the subject of theoretical studies by a number of researchers [7, 8], who predicted strong optical rotatory power and polarization state modulation inherent to 2D chiral microstructures.

Based on the theoretical predictions, the first experimental work on the optical properties of planar chiral metamaterials was carried out by Papakostas *et al* [9–11]. Their experimental results demonstrated that planar chiral structures could affect the polarization state of light in a manner similar to 3D chiral media. In their work, a range of planar chiral structures were successfully fabricated in a Ti/Au/Ti multilayer structure on a silicon substrate. Each of these artificial media consisted of an array of microscopic gammadion-shaped holes distributed regularly in a plane, with a density of several million elements per square centimeter. Initial results showed that these planar chiral gammadions etched in the Ti/Au/Ti multilayer with characteristic sizes about 2 μm were capable of manipulating the polarization state of light in both the visible and the infra-red regions of the spectrum. In particular, it was demonstrated that linearly polarized light experienced both polarization azimuth rotation and elliptization when diffracted by arrays of these nanoscale gammadion-shaped structures. The direction and the degree of the polarization rotation were shown to correlate to the chirality of the gammadion-shaped elements. However, the mechanism behind the optical activities of these planar chiral metamaterials was not completely understood, although electric current induction as well surface plasmon response were considered as part of the explanations.

1.2 Aims of this work

The broad objectives of this work have been to carry out investigations into the nature of the optical activity of planar chiral metamaterials. At the beginning of this project there remained a number of uncertainties with regard to the underlying science and the prospects for future applications of this new class of optical structures. Thus, the first objectives were to explore simple planar chiral structures in order to understand and explain their optical properties, later work was to become more

applications based, and more complex structures and devices were to be considered.

As this project commenced, planar chiral metamaterials had been shown to exhibit a number of interesting properties. In some of the earliest work it had been shown that linearly polarized light experienced strong polarization azimuth rotation and elliptization when diffracted from arrays of gammadion-shaped holes etched in a Ti/Au/Ti multilayer structure. It had been demonstrated that the direction and the degree of the polarization rotation were dependent on the chirality and the geometry of the gammadion structures [10, 11]. A new theoretical model had created a *chirality index* showing that the magnitude of polarization state rotation and elliptization of reflected beams from metallic planar chiral structures were dependent on the asymmetry of the nanostructures [12] .

The mechanism behind the polarization activity of planar chirality was understood as being due to the creation of electric currents by the electromagnetic field within metallic features of the chiral structures. It was felt that polarization response from metallic planar chiral metamaterials was likely to be due in part to surface plasmon responses [10, 13, 14].

Although strong polarization effects had been observed for higher-order diffracted beams, no polarization changes had been observed in the zero-order beam from planar chiral metamaterials and only diffractive structures had been explored. It was felt that the key to develope device applications for planar chiral metamaterials would be progress to non-diffractive, loss-less and zero-order systems.

At the beginning it was not known if polarization behaviour of the Ti/Au/Ti planar chiral metamaterials could only be observed for Ti/Au/Ti structure, other materials had not been tested. This project aimed to fabricate and test alternative metal and even dielectric planar chiral metamaterials. If similar polarization responses could be observed from a range of metallic and dielectric planar chiral metamaterials, new mechanisms to explain the optical activity of planar chiral metamaterials could be proposed.

Previous work had concentrated on polarization measurements, a second key objective of this work was to study intensity variations of light beams reflected and transmitted by planar chiral materials. It was felt that if planar chiral structures could exhibit strong intensity anisotropy, devices could be designed to selectively reflect and transmit different polarization states and have applications in polarization sensitive detectors and modulators. This project aimed to explore these possibilities.

Additionally, important questions regarding the possibility of optical non-reciprocity in planar chiral structures remained. If non-reciprocal planar chiral effects could be demonstrated experimentally and be realized with loss-less and non-diffractive de-

vices, this would be an exciting scientific discovery with very interesting commercial potential.

1.3 Structure of this thesis

Chapter 2 provides a literature review on optical metamaterials with brief introduction of planar chiral metamaterials and their optical activities. The reported optical activities of planar chiral metamaterials, including both theoretical predictions and experimental studies, are introduced.

In Chapter 3, the principles of light-matter interactions with planar chiral metamaterials, including basic laws of electromagnetic theory, polarization of light, optical activity, and light interference and diffraction, are described in the context of this work.

Chapter 4 describes design and fabrication process for all of the planar chiral samples investigated in this work. A process of patterning high density of nanoscale planar chiral structures using electron beam lithography is developed and optimized.

Chapter 5 investigates the polarization response of planar chiral metamaterials fabricated in a thin aluminium layer. How the polarization state of the first-order diffracted beams by these planar chiral structures is influenced by the chirality and geometry of the diffracting elements is discussed. These results are compared with those obtained for the Ti/Au/Ti chiral sample.

Inspired by the metallic chiral metamaterials, loss-less dielectric planar chiral structures are fabricated and characterized in chapter 6. Their polarization response in the transmission regime is investigated and is compared with those for the metallic chiral samples. The dependence of the polarization response on the geometry, type of resist, and the thickness of the film are investigated. A transfer matrix is established to predict the polarization response of planar chiral metamaterials for all possible input polarization states. An underlying mechanism behind the polarization response of these planar chiral structures is proposed and discussed.

In Chapter 7, the intensity response of planar chiral metamaterials is investigated. The intensity of the first-order diffracted beams by the aluminium sample, the polymeric sample and the silicon nitride samples is measured. The dependence of the intensity response on the chirality, geometry and the film thickness is investigated. Additionally, a new device design composed of a thin Ti layer patterned with planar chiral structures integrating onto silicon photodiodes is proposed and characterized.

In Chapter 8, the reciprocity and reversibility of planar chiral structures are tested experimentally. Several experiments are designed and conducted on both aluminium and the silicon nitride chiral samples.

Based on the discussions carried out in Chapter 8, a new device, comprised of a highly reflective dielectric multilayer in the middle of two dielectric planar chiral gratings, is proposed in Chapter 9. The design and fabrication details and insight of the device is introduced.

At the end of the thesis, a conclusion is given followed by some suggestions on future work.

Chapter 2

Optical metamaterials and 2D chirality - A review

2.1 Metamaterials

As briefly introduced in the previous chapter, metamaterials refer to any artificial structured composites that exhibit unique electromagnetic properties that are not inherent in the individual constituent components. They have potential to fill critical voids in the electromagnetic spectrum, where material response is limited, and enable the construction of novel devices [15]. The concept of metamaterials has been the subject of research interest for many investigators worldwide. New concepts in synthesis and novel fabrication techniques may allow construction of new classes of composite materials with interesting electromagnetic properties.

One of the principal claims of metamaterial research is negative refractive material, in which permittivity, ε, and/or permeability, μ, are negative. These materials are commonly referred to as left-handed materials (LHMs). This class of metamaterials have received substantial attention in the scientific and engineering communities [16–19]. The theory of the propagation of electromagnetic waves in such medium was developed more than three decades ago by Veselago [20]. Veselago's paper was ignored until recently, when negative refraction attracted much more interest and offered a rich ground for both theoretical and experimental research. The essential ideas of negative refraction, which led to the fabrication of the first LHMs, were proposed by Pendry *et al.* [16]. Meanwhile, a network of thin metallic wires, which behaved as a metal with a negative permittivity ε_{eff} at microwave frequencies, was reported [21, 22]. By combining these two structures, Smith *et al.* [23] hit on the idea of simply combining two artificial materials in the same space, one producing negative permittivity, ε, and another one producing negative permeability, μ, at a

frequency region in the microwave regime. Based on these theoretical predictions, several experiments have been demonstrated by different research groups and negative refraction was confirmed [17, 24–30]. Additionally, three-dimensional photonic crystals, which is a type of material lying on the transition between metamaterial and ordinary structured dielectric, has also been used to attain negative refraction recently [31–33].

The properties of electromagnetic wave propagation in these LHMs have been studied theoretically [34, 35], and their transmission properties have been broadly investigated experimentally [23, 36]. Researches on the spectral dependences of optical extraordinary transmission of isotropic [37] and anisotropic [38] arrays of holes have attracted a lot of attention. In summary, the unique properties of LHMs have allowed novel applications, concepts, and devices to be developed. Microfabrication of composite materials for electromagnetic applications is pursued with the aim of tailoring the electromagnetic properties of such materials by suitably designing the micropatterns.

2.2 Planar chiral metamaterials

Almost one century ago, chirality was defined by Lord Kelvin in the following terms: "I call any geometrical figure, or group of points, chiral, and say it has chirality, if its image in a plane mirror, ideally realized, cannot be brought to coincide with itself." It is equivalently said that a system is achiral when its symmetry group contains at least one indirect isometry, otherwise the system is chiral [39]. The two mirror image objects are known as *enantiomers*. In 1846 Faraday made the plane of polarization of linearly polarized light beam rotate by applying a magnetic field parallel to the beam [6]. This discovery demonstrated the intimate connection between electromagnetism and light, but it also raised the question of whether there is a distinction between Faraday's magnetic optical rotation and the natural optical rotation in certain crystals and fluids. Such natural optical activity is due to the handedness within the microstructure of the crystals and fluids [40].

Chirality in two dimensions arises when two distinct enantiomers, confined to a plane or surface, are inter-converted by parity but not by any rotation within the plane about an axis perpendicular to the plane [41]. In two dimensions, however, the parity operation is no longer equivalent to an inversion through the coordinate origin as in three dimensions because this will not change the handedness of the two coordinate axes. Instead, an inversion of just one of the two axes is required [42]. In recent years the concept of 2D chirality has been attracting a lot of attention. Sev-

eral experiments have revealed that 2D chiral order can be formed spontaneously in thin films and monolayers composed of non-chiral molecules. For example, 2D chiral textures in freely suspended smectic films have been described by Selinger *et al.*, who proposed a general theory of chiral symmetry-breaking on a small length scale [43]. Later on, chiral molecules on an isotropic surface were observed by Hicks *et al.* [44]. They also demonstrated that these chiral molecules generated huge circular intensity differences in pre-resonance second harmonic scattering via pure electric dipole interactions. Additionally, 2D chiral textures have also been observed in liquid crystal films [45, 46], Langmuir monolayers [47, 48], and self-assembled monolayers of organic discotic molecules on a graphite surface [49]. These nanostructured chiral surfaces can also exhibit strong enantiomer-specific behaviour that will be of considerable interest in many areas of chemistry [50, 51].

In order for the chiral properties of these various artificial planar materials to be designed more efficiently, a quantifiable measure of 2D chirality (K) is required. Over the last fifteen years there were significant progresses in this area, but most of these work were driven by the needs of stereochemists. As a consequence, the resulting chiral measures tended to be more applicable to microscopic systems of discrete points [52, 53] where the points themselves were usually taken to represent the spatial positions of atomic nuclei, whether in molecules or on planar surfaces. Unfortunately, most of these discrete chirality measures were not easily extendable to a continuous system. Therefore, an algebraic formulation of 2D chirality theory, which can be applied to any 2D mass distribution (discrete or continuous) is desired. One of the first and most promising algebraic models to incorporate continuous mass distributions was developed by Osipov *et al.* [54]. They pointed out that the simplest chiral object in two dimensions is a scalene triangle. Consequently, if one can construct a chirality measure for this simple set of three points, it then becomes a trivial exercise to extend the measure to any larger distribution of points merely by summing over all possible triangular permutations. By employing this approach they derived an expression for the chirality of a single triangle of points:

$$K = \frac{1}{(a_1 a_2 a_3)^2} \Delta [(\frac{a_1^2}{a_3^2} - \frac{a_1^2}{a_2^2}) \cos(\theta_1) + (\frac{a_2^2}{a_1^2} - \frac{a_2^2}{a_3^2}) \cos(\theta_2) + (\frac{a_3^2}{a_1^2} - \frac{a_3^2}{a_2^2}) \cos(\theta_3)] \quad (2.1)$$

Here, a_1, a_2 and a_3 are the lengths of the three sides of the triangle while θ_1, θ_2 and θ_3 are the angles opposite the sides, a_1, a_2 and a_3, respectively. The term Δ represents the triangle's area. By convention, all vertices, sides and angles of the triangle are numbered in a clockwise direction as shown in Fig. 2.1.

However, this expression for the chirality of a set of three points clearly diverges as the length of any side of the triangle tends to be zero and, consequently, it is not

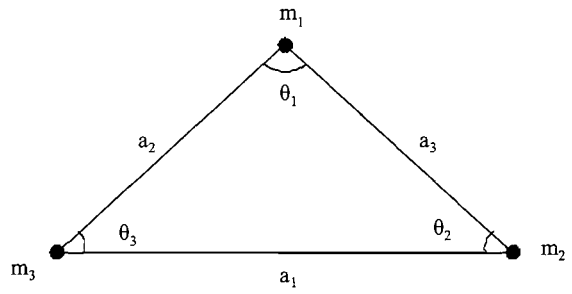

Figure 2.1: The labeling conventions of the sides, vertices and angles of a triangle [12].

integrable unless a cut-off parameter is introduced. Recently, a new measure of 2D chirality based on purely geometric considerations, that is scalable and integrable and is capable of being applied to any generalized continuous distribution for any 2D surface, was developed by Potts *et al.* [12]. The chirality index, K, is regarded as a quantifiable measure of 2D chirality. A chirality measure for a triangular set of points based on asymmetry in the area of that triangle is defined first, then this measure can be extended to any structure with any degree of complexity. If a particular triangle has sides of length a_1, a_2 and a_3, the chirality measure for that triangle can be defined in terms of the minimum distance separating points in the chiral triangle from its closest achiral form [12]. It can be calculated by summing the chirality indices of all possible permutations of triangles by bisecting each of the angles in turn. Therefore, the chirality index, K, can be calculated [12]:

$$K = \frac{1}{6}\int\int\int \rho(\mathbf{r}_1)\rho(\mathbf{r}_2)\rho(\mathbf{r}_3)\Delta(\mathbf{r}_1,\mathbf{r}_2,\mathbf{r}_3)\times\Gamma(\mathbf{r}_1,\mathbf{r}_2,\mathbf{r}_3)d^2\mathbf{r}_1 d^2\mathbf{r}_2 d^2\mathbf{r}_3 \tag{2.2}$$

where $\Delta(\mathbf{r}_1,\mathbf{r}_2,\mathbf{r}_3)$ is the area of an individual triangle defined by coordinate vectors $\mathbf{r}_1$, $\mathbf{r}_2$, and $\mathbf{r}_3$. $\rho(\mathbf{r})$ is the point density function, which represents the local density of point masses and is, in effect, a 2D mass density function for that surface. $\Gamma(\mathbf{r}_1,\mathbf{r}_2,\mathbf{r}_3)$ is the dimensionless chirality index and is defined as:

$$\Gamma(\mathbf{r}_1,\mathbf{r}_2,\mathbf{r}_3) = \frac{a_1 - a_2}{a_1 + a_2} + \frac{a_2 - a_3}{a_2 + a_3} + \frac{a_3 - a_1}{a_3 + a_1} \tag{2.3}$$

Considering the two mathematical models of 2D chirality index (Eqn. 2.1 and Eqn. 2.2), the sign of chirality index determines the handedness of the chiral object. The chirality index changes sign with reflection in respect to a line in 2D space. Correspondingly, both the chirality index and the optical rotatory power have opposite signs for 2D enantiomeric pairs.

2.3 Optical activity of planar chiral metamaterials

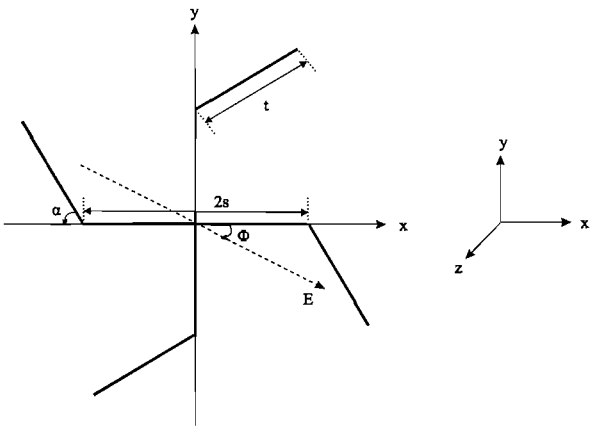

Figure 2.2: Schematic diagram of a single four-leg gammadion and its characteristic parameters [8].

As introduced in Chapter 1, 3D chiral helical molecules are able to rotate the polarization state of light. However, whether does this optical activity exhibit in 2D chirality is still under investigation. First, Hecht and Barron predicted incoherent circular differential Rayleigh and Raman light scattering from an ensemble of planar chiral molecules [55]. They showed that genuine strong chiral scattering phenomena could appear through pure electric dipole interactions. Then, Arnaut and Davis calculated the scattered fields from a simple metallic wire gammadions (as shown schematically in Fig. 2.2) in the microwave regime [8, 56]. In Fig. 2.2, s and t represent a stem length and a tail length of each leg respectively; α is the bending angle; and ϕ defines the angle between the orientation of the incident beam and that of the xy-plane. Considering a linearly polarized wave propagating along oz-direction (perpendicular to the xy plane) is incident onto the structure. The dispersion characteristics of the changes in the wave polarization state for the far forward scattered field for this single gammadion was computed for various α, $\frac{s}{t}$ and ϕ. A rotation of the polarization azimuth of the scattered field was found indicating that these chiral structures may exhibit distinct polarization sensitive properties and photonic bandgap anomalies when arranged randomly in a plane and illuminated at normal incidence.

Following Arnaut's work, a new group of layered planar and quasi-planar metamaterials emerged with promising unique electromagnetic properties [13]. Svirko and Zheludev *et al.* analyzed a layered metallic microstructure which consisted of a pair of space separated highly conductive strips. Each conductive stripe had length d and width Δ, where $d>\Delta$. The strips were spaced by a flat layer of homogeneous

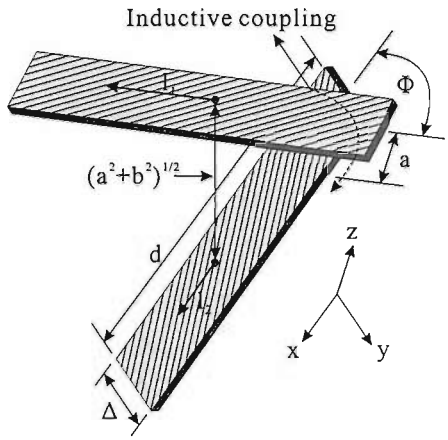

Figure 2.3: An element of a bi-layered planar chiral metallic microstructure with inductive cross-layer coupling [13].

dielectric as schematically shown in Fig. 2.3, in which a is the spacing between the layers of the trips and b is the mutual displacement of the centers of the strips in the plane of the layer. When observed in the direction perpendicular to the flat layer, the strips appear to be partially overlapping, and are oriented at angle ϕ to one another. They explained that if an electromagnetic wave was incident on such a layered structure, it induced oscillating electric currents in the strips. These induced currents were due to the electromagnetic inductive coupling between the different layers, which caused the strong optical rotatory power in these layered chiral metallic micro-structures.

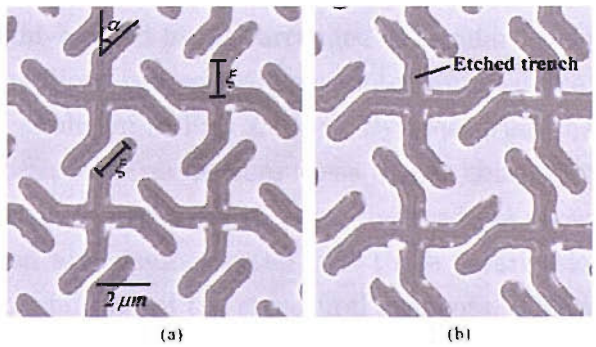

Figure 2.4: SEM image of an array of (a) right-handed and (b) lefthanded chiral gammadion structures etched in a Ti/Au/Ti layer deposited on a double polished silicon substrate [58].

In spite all of these theoretical calculations, however, there were very few reports of experimental observations of any optical activity of planar chirality. An observation of a random chiral component in a highly localized near-field polarization effect in metallic fractal aggregates was reported by Drachev *et al.* [57]. Later on, inspired by Arnaut's theoretical calculation of the scattered fields from the planar chiral

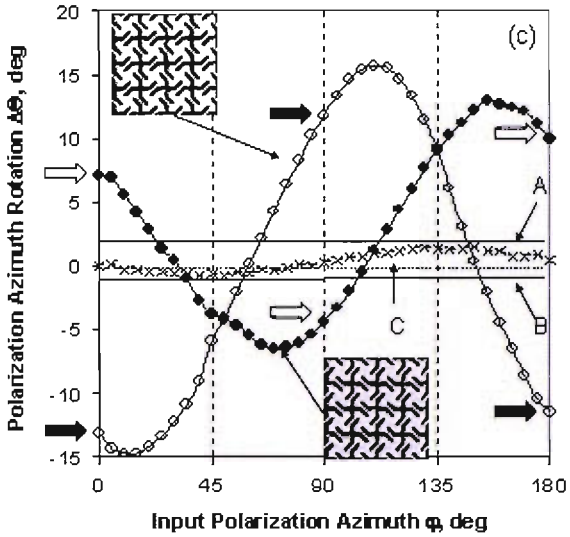

Figure 2.5: Polarization azimuth rotation of first-order diffracted beam from left-handed and right-handed gammadion arrays and reflected from an unstructured Ti/Au/Ti multilayer surface plotted as a function of input polarization azimuth [10].

structure (four-arm gammadion) and his discovery of polarization azimuth rotation of the scattered field, and Svirko's prediction of the strong optical rotatory power shown in a bi-layered metallic microstructures, Papakostas *et al.* reported experimental results that planar chiral structures affected the polarization state of light in a manner similar to 3D chiral media [10, 11, 58]. In their work, arrays of gammadions (in left- and right-handed forms) arranged in regular 2D square gratings with a density of several millions per square centimeter were fabricated in a Ti/Au/Ti multilayer structure, as shown in Fig. 2.4 [58]. By measuring the polarization state of the higher order diffracted beams from these planar chiral gratings, a rotation of the polarization azimuth in excess of 15° was observed (as shown in Fig. 2.5 [10]). Furthermore, they had also demonstrated that these polarization effects were correlate to the degree of chirality of the structural elements. This suggested potential device applications for planar chiral metamaterials. Additionally, more recent work on asymmetric L-shaped metallic nano-particles demonstrated significantly larger rotations together with evidence of second harmonic generation (SHG) [59].

However, there was no dominant evidence of any chirality-induced polarization change in the zero-order diffracted beam from planar chiral metamaterials either in the reflection or the transmission regimes. The zero-order beam transmitted by arrays of gammadions etched in the Ti/Au/Ti multilayer structure failed to show any polarization changes [58]. Meanwhile, Ebbesen *et al.* reported particularly attractive optical transmission experiments on periodical arrays of subwavelength cylindrical

holes etched in a thin metallic layer deposited on glass [60]. They showed that the zero-order transmission pattern did not depend on the polarization of the incident light at normal incidence. Later on, Vallius *et al.* studied similar subwavelength structures and detected very small rotations ($\sim 2°$) of the plane of polarization of the transmitted beam [61]. The authors ascribed this effect to non-uniformities in the sample itself (such as in-plane birefringence or a small degree of non-orthogonality between the axes of the lattice structure) rather than being the result of 2D chirality in the structures. These experimental results were supported by theoretical calculations perpormed by Bedeaux *et al.* They predicted that the polarization change at normal incidence should vanish if the interface structure was isotropic and was invariant under rotations about the normal to the surface [62].

On the microscopic level, the mechanism behind the optical activities of 2D chirality is not yet completely understood. A numerical model was originally developed for microwave application by Prosvirnin [63]. This model treated the metallic chiral gammadions as thin narrow strips of ideal conductors which would interact with the electric field of the incident wave, therefore changing the polarization state of the incident wave. This layered metallic microstructure was subsequently fabricated by Svirko *et al.* and was found to exhibit pronounced polarization-sensitive properties [13]. They explained that this structure consisted of a number of small, 3D 'fully-metallic molecules', which consisted of a pair of spatially separated highly conductive (metallic) strips. If an electromagnetic wave is incident on such a layered structure, it induces oscillating electric currents in the strips, which explains the strong optical rotatory power observed in these layered chiral metallic microstructure. In Papakostas *et al.*'s later work, they extended the mechanism behind the polarization response of planar chirality further. They believed that this property could be understood if one considered an electromagnetic field polarizing a gammadion [10]. They explained that if a conductive gammadion interacted with the electric field of the incident wave directed along one of the gammadion legs, for instance, the positive and the negative carriers were driven into opposite legs. As the conductive strip was bent in a chiral implementation, charges would be shifted not only along the direction of the field, but also into the bent ends of the legs, thereby inducing a polarization perpendicular to the driving electric field with a sign that depended on the direction of the bend and, therefore on the chirality of the gammadion. When fields were re-emitted by the chiral currents, a rotation of the polarization state of the scattered field was observed. Alternatively, these gammadion structures were fabricated by etching holes into a gold film by Sobnack *et al.* [64]. They explained the polarization response observed in planar chiral metamaterials was likely to be formed by excitation of surface plasmons in grooves of the structure. However, neither of these mechanisms were sufficient to explain the

optical activities shown in the planar chiral structures.

2.4 Reciprocity of planar chiral metamaterials

In contrast to the case of 3D chirality, planar chiral metamaterials exhibit an opposite handedness when viewed from opposite directions. Therefore planar chiral metamaterials should induce opposite polarization changes for light transmitted through these structures in opposite directions. Such effects have been predicted theoretically for a number of idealized physical structures subject to various preliminary assumptions and approximations [8, 13]. The origin of this form of non-reciprocity has been theoretically analyzed [14]. Very recently Prosvirnin and Zheludev conducted a theoretical analysis of the polarization eigenstates for partial waves diffracted from arrays of planar chiral gammadions [65]. They showed that the polarization eigenstates of the array are bi-orthogonal for light diffracted in opposite directions or from opposite enantiomers. Consequently the polarization eigenstates for opposite directions of propagation were not necessarily the same and light propagation along the path of individual diffracted beams may be non-reciprocal. However, Kuwata-Gonokami *et al.* demonstrated that the polarization changes exhibited by planar chiral layers were due to the presence of residual 3D chirality rather than 2D chirality [66]. They studied the polarization altering properties of gold gammadion arrays in transmission within the sub-wavelength regime and claimed to have observed small changes to the polarization state of the transmitted beam which were partially reversed for opposing enantiomeric designs. However, when measured from the reverse direction each of these enantiomeric structures exhibited the same polarization change as it did in the forward direction, thus suggesting that the polarization change was reciprocal and due to 3D chirality. They attributed this chirality to the asymmetry in the structure along the direction of light propagation due to an asymmetry in the layer structure of the material and its material interfaces (air-metal-slica-air). As a result, the material boundaries at either side of the chirally patterned metal layer were different. However, none of these works has reported a comparison of enantiomeric structures in order to fully test the reciprocity of planar chiral metamaterials or the influence of chirality.

Chapter 3

Theories of light-matter interactions with planar chiral metamaterials

3.1 Wave nature of light and basic laws of electromagnetic theory

Light can be regarded as an electromagnetic wave of wavelength λ. It is characterized by a combination of time-varying electric field ($\mathbf{E}$) and magnetic field ($\mathbf{H}$) propagating through space. The electric and magnetic fields vibrate perpendicularly to one another and perpendicularly to the direction of propagation. The simplest waves are sinusoidal waves, which can be expressed mathematically by the equation:

$$\mathbf{E}(x,t) = E_0 \cos(\omega t - kx + \phi) \tag{3.1}$$

where $\mathbf{E}$ is the value of the electric field at the point x at time t, E_0 is the amplitude of the wave, ω is the angular frequency, k is the wave number and ϕ is the phase constant. This equation describes a perfectly monochromatic plane wave of infinite extent propagating in the positive x direction.

Maxwell showed that both electric and magnetic fields satisfy the same partial differential equation [67]:

$$\nabla^2(\mathbf{E},t) = \frac{1}{c^2}\frac{\partial^2(\mathbf{E})}{\partial t^2} \tag{3.2}$$

$$\nabla^2(\mathbf{H},t) = \frac{1}{c^2}\frac{\partial^2(\mathbf{H})}{\partial t^2} \tag{3.3}$$

These are called the *wave equations*, which implies that changes in the electric and

magnetic fields propagate through space with a speed of c, the speed of light. The frequency of oscillation of the fields, ν, and their wavelength in vacuum, λ_0, are related by:

$$c = \nu\lambda_0 \tag{3.4}$$

In any other medium the speed of propagation is given by:

$$v = \frac{c}{n} = \nu\lambda = \frac{\nu\lambda_0}{n} \tag{3.5}$$

where n is the refractive index of the medium and λ is the wavelength in that medium. The refractive index, n, is given by:

$$n = \sqrt{\mu_r \varepsilon_r} \tag{3.6}$$

where μ_r and ε_r are the relative permeability and relative permittivity of the medium respectively.

Name	**Equation**
Gauss's law	$\nabla \cdot \mathbf{D} = \rho$
Gauss's law for magnetism	$\nabla \cdot \mathbf{B} = 0$
Faraday's law of induction	$\nabla \times \mathbf{E} = -\frac{\partial \mathbf{B}}{\partial t}$
Ampère's law	$\nabla \times \mathbf{H} = \mathbf{J} + \frac{\partial \mathbf{B}}{\partial t}$

Table 3.1: Maxwell equations.

Symbol	**Meaning**
$\mathbf{E}$	electric field
$\mathbf{H}$	magnetic field
$\mathbf{D}$	electric displacement field
$\mathbf{B}$	magnetic flux density
ρ	free electric charge density
$\mathbf{J}$	free electric current density
$\nabla \cdot$	the divergence operator
$\nabla \times$	the curl operator

Table 3.2: Representations of symbols in Maxwell equations.

In electromagnetics, the best way to describe the behaviour of both the electric and magnetic fields, as well as their interactions with matter is *Maxwell equations*, which are listed in Table 3.1. The meaning of each symbol in the these equations

is provided in Table 3.2. The Maxwell equations connect the five basic quantities (**E**, **H**, **B**, **D**, and **J**). A remarkable symmetry between the electric field, **E**, and magnetic field, **B**, is exhibited in the equations, which represent one of the most elegant and concise ways to state the fundamentals of electricity and magnetism.

3.2 Polarization of light

Light, as mentioned previously, can be regarded as a wave with electric and magnetic components lying at right angles to one another. If the electric field vector of an electromagnetic wave propagating in free space vibrates in a specific plane, the wave is said to be plane polarized [6]. There are two commonly used approaches to describe the polarization states of light. Firstly, an algebraic approach in which polarization states are represented by wave equations; secondly, a geometric approach in which polarization states are mapped on a 2D surface of a sphere and the transformations are represented by appropriate circular arcs on the sphere.

3.2.1 The algebraic description of polarized light

Light can be polarized in a number of different ways. Considering two orthogonal electric field components, $\mathbf{E}_x$ and $\mathbf{E}_y$, of a propagating wave with the same frequency but different phase:

$$\overrightarrow{\mathbf{E}_x}(z,t) = \hat{\mathbf{i}}E_{0x}\cos(kz - \omega t) \tag{3.7}$$

$$\overrightarrow{\mathbf{E}_y}(z,t) = \hat{\mathbf{j}}E_{0y}\cos(kz - \omega t + \phi) \tag{3.8}$$

where ϕ is the relative phase difference between the waves, both of which are travelling in the z-direction. The resultant optical disturbance is the vector sum of these two perpendicular waves:

$$\overrightarrow{\mathbf{E}}(z,t) = \overrightarrow{\mathbf{E}_x}(z,t) + \overrightarrow{\mathbf{E}_y}(z,t) \tag{3.9}$$

If ϕ is zero or an integral multiple of $\pm 2\pi$, the resultant wave becomes:

$$\overrightarrow{\mathbf{E}} = (\hat{\mathbf{i}}E_{0x} + \hat{\mathbf{j}}E_{0y})\cos(kz - \omega t) \tag{3.10}$$

in this case, the wave is linearly polarized as illustrated in Fig. 3.1.

Another type of polarized light occurs when both constituent waves have equal amplitudes, $\mathrm{E}_{0x} = \mathrm{E}_{0x} = \mathrm{E}_0$, and in addition, their relative phase difference, $\phi =$

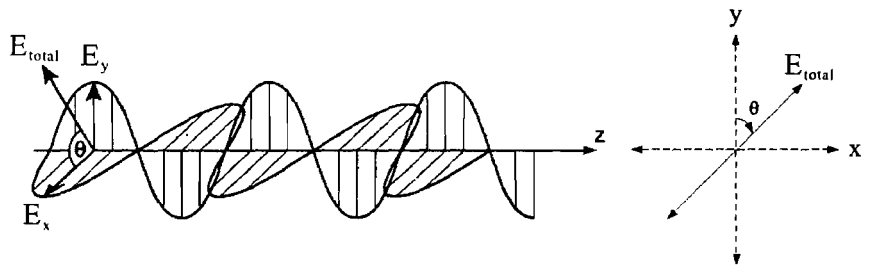

Figure 3.1: Schematic diagram of linearly polarized light.

$2m\pi \pm \frac{-\pi}{2}$, where m=0,±1,±2,... This consequent wave becomes:

$$\overrightarrow{\mathbf{E}} = E_0[\hat{\mathbf{i}}\cos(kz - \omega t) + \hat{\mathbf{j}}\sin(kz - \omega t)] \tag{3.11}$$

and it is circularly polarized as shown in Fig. 3.2. When this resultant electric field vector, $\overrightarrow{\mathbf{E}}$, is rotating clockwise, as seen by an observer toward whom the wave is moving, such wave is right-circularly polarized; and when $\overrightarrow{\mathbf{E}}$ rotates anticlockwise, the wave is left-circularly polarized.

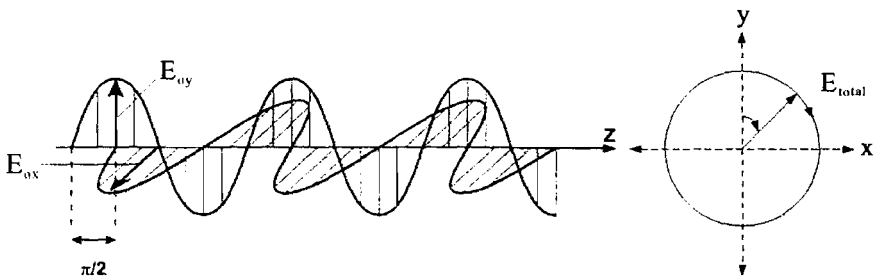

Figure 3.2: Schematic diagram of right-circularly polarized light.

In general, both linearly and circularly polarized light may be considered to be special cases of elliptically polarized light, which means that the resultant electric field vector $\overrightarrow{\mathbf{E}}$ will rotate, and its magnitude changes at the same time as well. In this case, the focus of $\overrightarrow{\mathbf{E}}$ will be an ellipse as illustrated in Fig. 3.3. The figure illustrates elliptically polarized light (with an ellipticity, η,) without rotation (a) and with a polarization azimuth angle, Φ, (b) respectively. The ellipticity, η, is defined as the length ratio of the minor-to-major axes of the polarization ellipse. The azimuth angle, Φ, is defined as the angle between the major axis of the ellipse and the x-axis. The polarization state of any electromagnetic wave can be uniquely determined, therefore, by knowing the ellipticity, η, and the polarization azimuth angle, Φ. In addition, any plane polarized wave can be resolved into two circularly polarized waves with opposite directions of rotation. If they travel through the crystal at different speeds, a phase difference will be introduced between them at

different distances through the crystal. This corresponds to a rotation of the plane of the plane polarized wave which results from the recombination of the two circularly polarized waves.

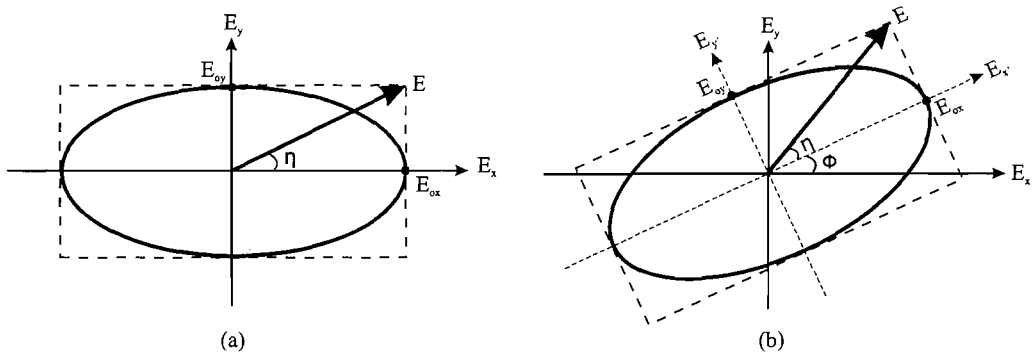

Figure 3.3: Schematic diagram of elliptically polarized light. (a) without rotation (b) with a polarization azimuth angle Φ.

3.2.2 The Stokes parameters

Although, the definition of polarization azimuth angle and ellipticity is very simple, these two parameters are applicable only for totally polarized light but can not be used for partially polarized light. In 1852, Sir G. G. Stokes discovered that the polarization behaviour could be represented in terms of observables. He found that any state of polarized light could be completely described by four measurable quantities now known as *the Stokes polarization parameters*, S_0, S_1, S_2, and S_3 [68]. S_0 expresses the total intensity of the optical field; S_1 describes the amount of linear horizontal or vertical polarization; S_2 describes the amount of linear +45° or -45° polarization; and S_3 describes the amount of right or left circular polarization contained within the beam [69]. For an electromagnetic wave described by Eqn. 3.7 and Eqn. 3.7, the Stokes parameters can be defined as:

$$S_0 = {E^2}_{0x} + {E^2}_{0y} \tag{3.12}$$

$$S_1 = {E^2}_{0x} - {E^2}_{0y} \tag{3.13}$$

$$S_2 = 2E_{0x}E_{0y}\cos\phi \tag{3.14}$$

$$S_3 = 2E_{0x}E_{0y}\sin\phi \tag{3.15}$$

where $\phi = \phi_x - \phi_y$, the phase difference between the x and y components.

Light is totally polarized if the Stokes parameters satisfy the following equation:

$$S_0 = \sqrt{S^2{}_1 + S^2{}_2 + S^2{}_3} \tag{3.16}$$

If the Stokes parameters are known, the polarization azimuth angle and ellipticity can be defined as:

$$\tan 2\Phi = \frac{S_2}{S_1} \tag{3.17}$$

$$\sin 2\eta = \frac{S_3}{S_0} \tag{3.18}$$

Alternatively, by knowing polarization azimuth angle and ellipticity, the Stokes parameters can be calculated according to the equations:

$$S_1 = RS_0 \cos(2\eta)\cos(2\Phi) \tag{3.19}$$

$$S_2 = RS_0 \cos(2\eta)\sin(2\Phi) \tag{3.20}$$

$$S_3 = RS_0 \sin(2\eta) \tag{3.21}$$

where R represents the degree of polarization of partially polarized light, which is defined as:

$$R = \frac{\sqrt{S^2{}_1 + S^2{}_2 + S^2{}_3}}{S_0} \tag{3.22}$$

Therefore, various polarization states of light can be represented using Stokes parameters as shown in Tab. 3.3:

Polarization state	**Stokes parameters**
Linearly polarized light along X axis	S=S_0(1;1;0;0)
Linearly polarized light along Y axis	S=S_0(1;-1;0;0)
Linearly polarized light at +45 degree to X axis	S=S_0(1;0;1;0)
Linearly polarized light at -45 degree to X axis	S=S_0(1;0;-1;0)
Right-handed circularly polarized light	S=S_0(1;0;0;1)
Left-handed circularly polarized light	S=S_0(1;0;0;-1)

Table 3.3: Representations of different polarization states of light using Stokes parameters.

3.2.3 The geometric description of polarized light

A 3D coordinate system relating to the Stokes parameters and used to represent a particular polarization state was introduced by Henri Poincaré. This is known as

the *Poincaré sphere* [70]. Every polarization state of the system can be represented by a unique point on the surface of the sphere as shown in Fig. 3.4. The radius of the sphere is $\sqrt{S^2{}_1 + S^2{}_2 + S^2{}_3}$. The north and south poles of the sphere represent right- and left-hand circularly polarized light respectively. All of the points on the equator of the sphere represent linearly polarized light. Therefore, the Poincaré sphere is a very clear and convenient geometric representation of the polarization state of a light wave.

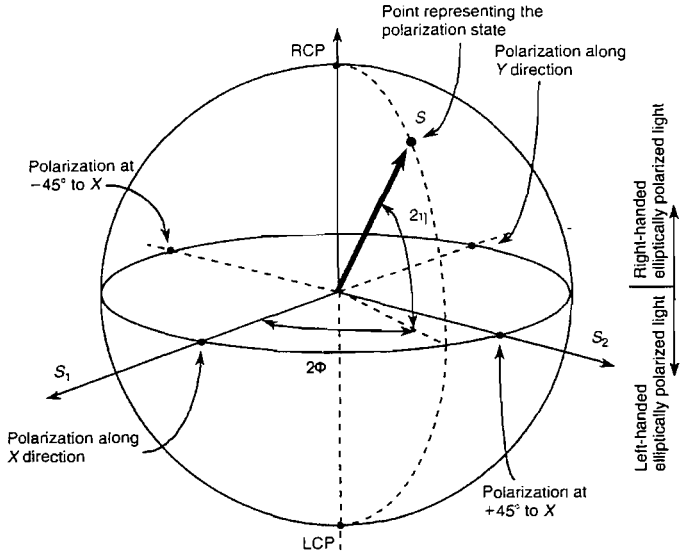

Figure 3.4: Representations of the polarization state of light on the Poincaré sphere.

3.3 Optical activity

A system is called 'optical active' if it has the power to rotate the plane of polarization of a linearly polarized light beam. Substances that are optically active in the absence of external influences are said to exhibit 'natural' optical activity. Otherwise, all substances in magnetic fields are optically active, and electric fields can sometimes induce optical activity in special situations [41]. The rotation of the optical field occurs because optical activity is a manifestation of an unsymmetric isotropic medium; that is, the molecules lack not only a center of symmetry but a plane of symmetry as well [68]. Optical rotation is just one of a number of optical activity phenomena which can all be reduced to the common origin of a different response to right- and left-circularly polarized light. The polarization changes in

a light beam passing through a transparent medium are usually accounted for in terms of circular and linear birefringence which refer to different refractive indices for right- and left-circularly polarized light and light linearly polarized in two perpendicular directions respectively. Birefringence is an intrinsic material property and isotropic materials, such as glass, do not exhibit birefringence unless the material is subjected to stress. The two refractive indices are usually designated as n_x and n_y, and a measure of the birefringence can be expressed as:

$$\Delta n = n_y - n_x \tag{3.23}$$

If light propagates through a transparent medium or is reflected from a metallic medium, the electrons of the media, driven by the incident electric field, $\overrightarrow{E}$, acquire

recombining, and the resultant refracted or reflected wave continues its propagation. Thus, the refractive index and the speed of the wave propagation can be determined by the difference between the frequency of the incident electric field, $\overrightarrow{E}$, and the natural frequency of the atoms. For many crystalline substances, whose atoms are not completely symmetrically arranged, the binding forces on the valence electrons are anisotropic. Therefore, their optical properties are not the same in all directions. Any anisotropy in the binding forces within the material will result in anisotropy in the refractive index and therefore birefringence.

Furthermore, a birefringent material that absorbs one or its orthogonal polarization state, is called *dichroic* [5]. As introduced previously, linearly polarized light can be regarded as a superposition of coherent left- and right-circularly polarized light beams of equal amplitude, and the orientation of the plane of polarization is a function of the relative phases of the two components. Therefore, the optical rotation can be attributed to a difference in the velocity of propagation of the left- and right-circularly polarized components of the linearly polarized beam in the medium. By the same principle, since elliptically polarized light can be decomposed into coherent left- and right-circularly polarized components of different amplitude, the generation of an ellipticity can therefor be ascribed to a difference in the absorption of the two circular components in an absorbing optically active medium. This differential absorption of left- and right-circularly polarized light is referred as *circular dichroism* [41].

3.4 Interference of light

Optical interference corresponds to the interaction of two or more lightwaves yielding a resultant irradiance that deviates from the sum of the component irradiance. In accordance with the principle of superposition, the electric field intensity $\overrightarrow{\mathbf{E}_I}$, at a point in space, arises from the separate fields $\overrightarrow{\mathbf{E}_{I1}}$, $\overrightarrow{\mathbf{E}_{I2}}$,..., of various contributing sources and is given by:

$$\overrightarrow{\mathbf{E}_I} = \overrightarrow{\mathbf{E}_{I1}} + \overrightarrow{\mathbf{E}_{I2}} + \cdots \tag{3.24}$$

3.4.1 The Stokes treatment

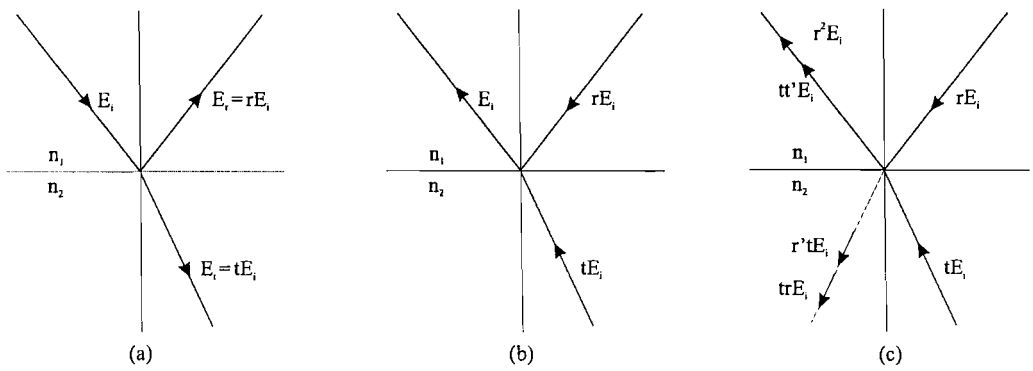

Figure 3.5: An illustration of the Stokes treatment of light reflection and refraction.

There is another way to look at reflection and transmission at a boundary. As shown in Fig. 3.5, E_i represents the amplitude of the incident beam, E_r represents the amplitude of the reflected beam from the boundary between n_1 and n_2, and E_t represents the amplitude of the transmitted beam in n_2. The reflection and transmission coefficients are defined as:

$$\begin{aligned} r &= \frac{E_r}{E_i} \\ t &= \frac{E_t}{E_i} \end{aligned} \tag{3.25}$$

so that at the interface, E_i is divided into a reflected part, $E_r = rE_i$, and a transmitted part, $E_t = tE_i$, as shown in Fig. 3.5 (a). According to the principle of time-reversal invariance (which describes that if a process occurs, the reverse process can also occur [5]) the configuration in Fig. 3.5 (b) is also physically realizable. Therefore, if there are two rays incident at the interface, each ray results in a reflected and transmitted beam with appropriate amplitude as seen in Fig. 3.5 (c).

The configuration in Fig. 3.5 (b) and Fig. 3.5 (c) are physically equivalent, so that:

$$E_i = (r^2 + tt')E_i \tag{3.26}$$

and

$$0 = (r't + tr)E_i \tag{3.27}$$

therefore,

$$tt' = 1 - r^2 \tag{3.28}$$

$$r = -r' \tag{3.29}$$

Eqn. 3.29 indicates that there is a 180° phase difference between the waves internally and externally reflected but with same amplitude.

3.4.2 Two beam interference

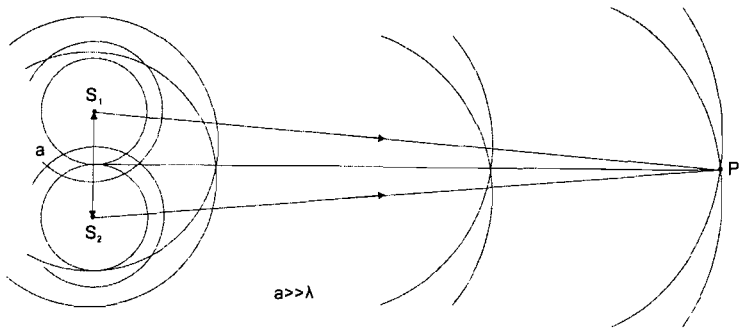

Figure 3.6: Schematic diagram of waves from two point sources interfere in space.

As a very simple example of interference, consider two point sources S_1 and S_2 emitting monochromatic waves of the same frequency in a homogeneous medium as shown in Fig. 3.6. The distance between S_1 and S_2, a, is much greater than the wavelength λ. The point of observation P is far enough away from the sources so that at P the wavefronts can be considered as planes. Considering only linearly polarized waves of the form:

$$\overrightarrow{\mathbf{E}_1}(\overrightarrow{\mathbf{r}}, t) = \overrightarrow{\mathbf{E}_{01}} \cos(\overrightarrow{\mathbf{k}_1} \cdot \overrightarrow{\mathbf{r}} - \omega t + \phi_1) \tag{3.30}$$

$$\overrightarrow{\mathbf{E}_2}(\overrightarrow{\mathbf{r}}, t) = \overrightarrow{\mathbf{E}_{02}} \cos(\overrightarrow{\mathbf{k}_2} \cdot \overrightarrow{\mathbf{r}} - \omega t + \phi_2) \tag{3.31}$$

The irradiance at P is expressed as:

$$I = I_1 + I_2 + I_{12} = \langle \overrightarrow{\mathbf{E}_1^2} \rangle_T + \langle \overrightarrow{\mathbf{E}_2^2} \rangle_T + 2\langle \overrightarrow{\mathbf{E}_1} \cdot \overrightarrow{\mathbf{E}_2} \rangle_T \tag{3.32}$$

in which the last term is known as the *interference term*, and $\langle\overrightarrow{\mathbf{E}^2}\rangle_T$ means the time average of the magnitude of the electric field intensity squared. From Eqn. 3.30 and Eqn. 3.31, the interference term can be formed:

$$I_{12} = 2\langle\overrightarrow{\mathbf{E}_1}\cdot\overrightarrow{\mathbf{E}_2}\rangle_T = \overrightarrow{\mathbf{E}_{01}}\cdot\overrightarrow{\mathbf{E}_{02}}\cos\delta \tag{3.33}$$

in which, $\delta = \overrightarrow{k_1}\cdot\overrightarrow{r} - \overrightarrow{k_2}\cdot\overrightarrow{r} + \phi_1 - \phi_2$, and it is the phase difference arising from a combined path length and initial phase angle difference. If $\overrightarrow{\mathbf{E}_{01}}$ and $\overrightarrow{\mathbf{E}_{02}}$ are perpendicular, $I_{12} = 0$ and $I = I_1 + I_2$. When $\overrightarrow{\mathbf{E}_{01}}$ and $\overrightarrow{\mathbf{E}_{02}}$ are parallel, the interference term becomes:

$$I_{12} = E_{01}E_{02}\cos\delta \tag{3.34}$$

Considering the time average of a function *f(t)*, taken over an interval T, is:

$$\langle f(t)\rangle_T = \frac{1}{T}\int_t^{t+T} f(t')dt' \tag{3.35}$$

therefore, the irradiance at S_1 and S_2 can be rewritten:

$$I_1 = \langle\overrightarrow{\mathbf{E}_1^2}\rangle_T = \frac{nE_{01}^2}{2Z} \tag{3.36}$$

and

$$I_2 = \langle\overrightarrow{\mathbf{E}_2^2}\rangle_T = \frac{nE_{02}^2}{2Z} \tag{3.37}$$

Then the interference term becomes:

$$I_{12} = 2\sqrt{I_1 I_2}\cos\delta \tag{3.38}$$

so the total irradiance at P is:

$$I = I_1 + I_2 + 2\sqrt{I_1 I_2}\cos\delta \tag{3.39}$$

When $\delta = 0, \pm 2\pi, \pm 4\pi, \ldots$ a maximum irradiance is obtained:

$$I_{max} = I_1 + I_2 + 2\sqrt{I_1 I_2} \tag{3.40}$$

In this case, the disturbances are in phase and result in a total constructive interference. For any case, where $0 < \cos\delta < 1$, the waves are out-of-phase, $I_1 + I_2 < I < I_{max}$, and the result is constructive interference. In the same way, when $\delta = \pm\pi, \pm 3\pi, \ldots$ a minimum irradiance is obtained:

$$I_{min} = I_1 + I_2 - 2\sqrt{I_1 I_2} \tag{3.41}$$

For -1 < $\cos\delta$ < 0, a destructive interference is obtained.

3.4.3 Multiple beam interference in a parallel plate

In addition to the situations in which two coherent beams are combined to produce interference patterns, there are other circumstances under which a large number of mutually coherent waves interfere. Consider E_0 be the amplitude of the electric vector of the incident wave, which is assumed to be linearly polarized with the electric vector perpendicular (TE) to the plane of incidence. The incident angle is θ_i, as shown in Fig. 3.7. The refractive index of the thin film is n_f, and the refractive index of the air is $n = 1$, d is the thickness of the film. The reflection and transmission amplitude coefficients are r and t at an external reflection, and r' and t' at an internal reflection as defined by the *Stokes treatment*. The scalar amplitudes of the external reflected waves $\overrightarrow{E}_{1r}$, $\overrightarrow{E}_{2r}$, $\overrightarrow{E}_{3r}$,..., are rE_0, $tt'rE_0$, $tt'r'^3E_0$,... respectively, where E_0 represents the amplitude of the initial incoming wave. The scalar amplitudes of the external transmitted waves $\overrightarrow{E}_{1t}$, $\overrightarrow{E}_{2t}$, $\overrightarrow{E}_{3t}$,..., have amplitudes $tt'E_0$, $tt'r'^2E_0$, $tt'r'^4E_0$,... In a same manner, all the internal reflected waves have amplitudes $tr'E_0$, tr'^2E_0, tr'^3E_0,...Multiple parallel beams emerge from the top and from the bottom of the plate. Multiple-beam interference takes place when either set is focused to a point P by a converging lens, as shown for the transmitted beam.

Consider the set of parallel reflected rays, each ray bears a fixed phase relationship to the other reflected rays. The phase difference, δ, arises from a combination of optical path length (OPL) differences and phase shifts occurring at the various reflections. From Fig. 3.7, the OPL difference, Δ, for the first two reflected beams is given by:

$$\Delta = n_f[(\overline{AB}) + (\overline{BC})] - \overline{AD} = 2n_f d\cos\theta_t \tag{3.42}$$

Therefore, the phase difference between two adjacent rays is given by:

$$\delta = k\Delta = 2kn_f d\cos\theta_t \tag{3.43}$$

If the incident beam is $E_0e^{i\omega t}$, the superposition of all the successive reflected beams

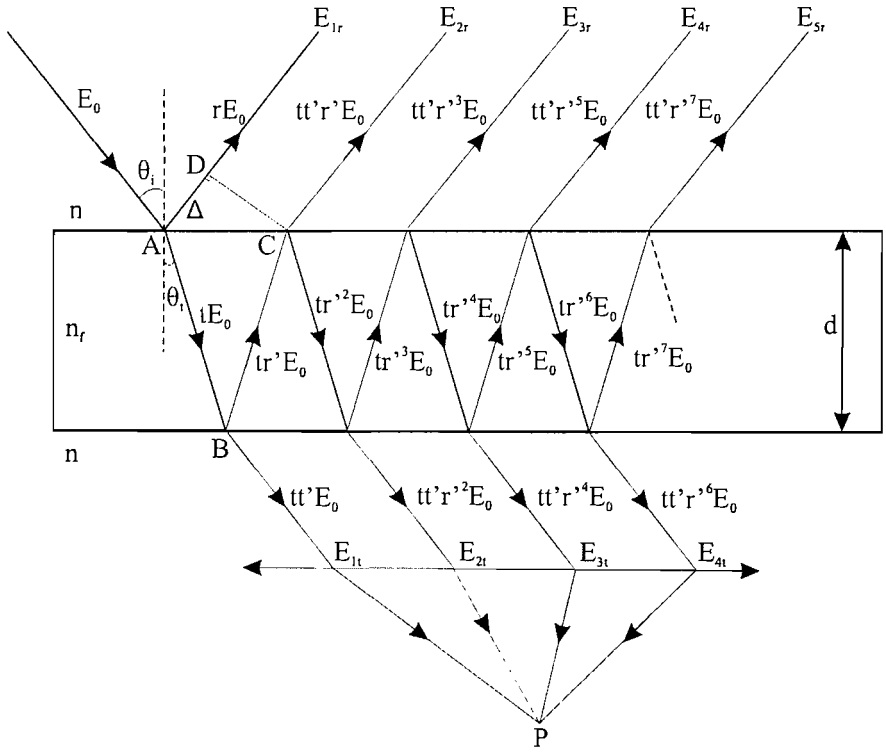

Figure 3.7: Schematic diagram of multiple reflected and transmitted beams in a parallel film.

are:

$$\begin{aligned} E_R &= \sum_{N=1}^{\infty} E_N = rE_0e^{i\omega t} + \sum_{N=2}^{\infty} tt'r'^{(2N-3)}E_0e^{i\omega t-(N-1)\delta} \\ &= E_0e^{i\omega t}[r + tt'r'e^{-i\delta}\sum_{N=2}^{\infty} r'^{(2N-4)}e^{-i(N-2)\delta}] \\ &= E_0e^{i\omega t}(r + \frac{tt'r'e^{-i\delta}}{1-r'^2e^{-i\delta}}) \end{aligned} \tag{3.44}$$

According to Stokes relations as expressed in Eqn. 3.28 and Eqn. 3.29:

$$\begin{aligned} E_R &= E_0e^{i\omega t}[r - \frac{(1-r^2)re^{-i\delta}}{1-r^2e^{-i\delta}}] \\ &= E_0e^{i\omega t}[\frac{r(1-e^{-i\delta})}{1-r^2e^{-i\delta}}] \end{aligned} \tag{3.45}$$

Therefore, the irradiance, I_R, of the resultant beam is proportional to the square of the amplitude, E_R, as expressed:

$$I_R = [\frac{2r^2(1-\cos\delta)}{1+r^4-2r^2\cos\delta}]I_i \tag{3.46}$$

In a same manner, the irradiance of the resultant transmitted beams is:

$$I_T = [\frac{(1-r^2)^2}{1+r^4-2r^2\cos\delta}]I_i \tag{3.47}$$

Eqn. 3.46 shows that when $\cos\delta = 1$ ($\Delta = m\lambda$), there is no light is reflected and all the incoming energy is transmitted. In this case, the second reflected beam and all subsequent beams are in phase with one another but exactly out of phase with the first reflected beam. Similarly, reflection is maximum when $\cos\delta$ = -1 (Δ = (m + 1/2)λ), in which case the first and second rays are in-phase, and all other adjacent waves are $\lambda/2$ out-of-phase. Therefore, Eqn. 3.46 and Eqn. 3.47 become:

$$I_R = [\frac{4r^2}{(1+r^2)^2}]I_i \tag{3.48}$$

$$I_T = [\frac{(1-r^2)^2}{(1+r^2)^2}]^2 I_i \tag{3.49}$$

As a consequence, the refractive index of the material, the thickness of the film, and the angle of incident will all affect the the light-interactions with the medium, in which multiple beam interference takes place. Additionally, the above mathematical treatments of light interference are applicable if the the electric vector of the linearly polarized incident is perpendicular (TE) to the plane of incidence. Regarding the other polarization state when the electric vector of the linearly polarized incident is parallel (TM) to the plane of incidence, a more comprehensive solution based on the transfer matrix method is required to explain the interference of light [71].

3.5 Diffraction

The diffraction effect is a general characteristic of wave phenomena occurring whenever a portion of a wavefront is obstructed in some way. In the course of encountering an obstacle, a region of the wavefront is altered in amplitude or phase, causing diffraction to occur. The various segments of the wavefront that propagate beyond the obstacle interfere, leading to a particular energy-density distribution referred to as the *diffraction pattern* [69]. In general there are two regimes regarding the complex diffraction process. First, diffraction very close to the object which interacts with the light, is called *Fresnel diffraction*; and second, the effects of diffraction far from the object which interacts with the light, is called *Fraunhofer diffraction*.

3.5.1 The Huygens-Fresnel principle

Huygens-Fresnel principle states that *each point on a primary wave front can be considered to be a new source of a secondary spherical wave and that a secondary wave front can be constructed as the envelope of theses secondary spherical waves* [72], as illustrated in Fig. 3.8. If the wavelength is large compare to the aperture, the waves will spread out at large angles into the region beyond the obstruction, and the smaller the aperture gets, the more nearly circular the diffracted waves become. This fundamental principle of physical optics is a method to analyze wave propagation both in far field and near field diffraction.

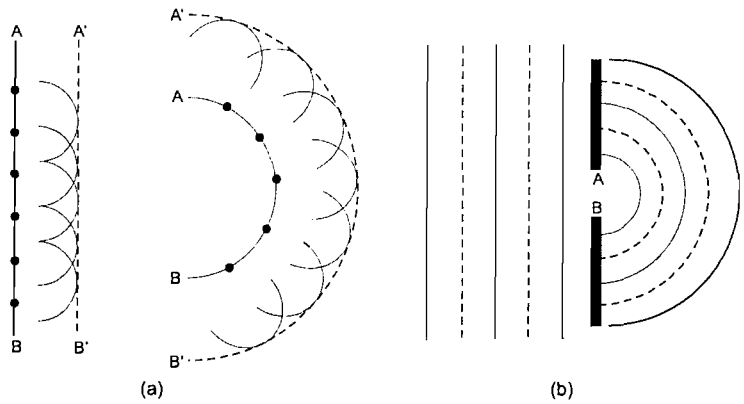

Figure 3.8: (a) An illustration of Huygen's principle for plane and spherical waves. (b) Huygen's construction for an obstructed wavefront, illustrating a wave diffraction through a small aperture $\overline{AB}$.

3.5.2 Fraunhofer diffraction

Diffraction from a single slit

Considering light waves hit a single rectangular aperture, whose length, l, is much larger than the width, b, and is placed far enough away from the screen as illustrated in Fig. 3.9. A focus lens is placed between the aperture and the screen. Therefore, light reaching any point, P, on the screen is due to parallel rays of light from different portions of the wavefront at the slit. According to the Huygens-Fresnel principle, the spherical wavelets, which reaches the plane of the slit, composes all the wavelets emanating from each point of the wavefront. Therefore, the result electric field at P can be calculated by adding all these waves together according to the principle of superposition. As shown in Fig. 3.9, the slit is divided into interval ds and each of these intervals is regarded as a wave source that contributes spherical wavelets at P

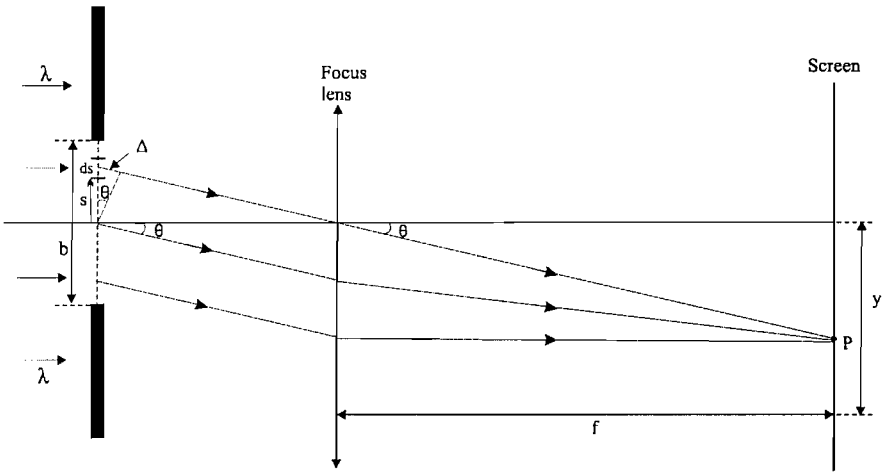

Figure 3.9: Schematic diagram of single-slit Fraunhofer diffraction.

of the form:

$$dE_p = (\frac{dE_0}{r})e^{i(kr-\omega t)} \tag{3.50}$$

in which r is the OPL from the interval ds to the point P. Then for any other wave originating at the interval s+ds, the differential field at P can be calculated by taking the phase difference into account, expressed as:

$$dE_p = (\frac{dE_0}{r_0+\Delta})e^{i[k(r_0+\Delta)-\omega t]} \tag{3.51}$$

The difference of OPL between two rays, Δ, as illustrated in Fig. 3.9, satisfies the expression:

$$\Delta = s\sin\theta \tag{3.52}$$

Because $\Delta \ll r_0$, the Δ term can be neglected in the amplitude expression but not the phase expression in Eqn. 3.51. The amplitude of the radiation from each interval clearly depends on the size of ds. Therefore, the total effect at P can be obtained by adding all the contributions together by integration.

$$dE_0 = E_L\, ds \tag{3.53}$$

where $\mathbf{E}_L$ is the amplitude per unit width of the slit at unit distance away. By substituting Eqn. 3.53 and Eqn. 3.52 into Eqn. 3.51 and integrating over the width of the slit, the electric field at point P can be expressed as:

$$E_p = (\frac{E_L}{r_0}\int_{-b/2}^{b/2} e^{iks\sin\theta}ds)e^{i(kr_0-\omega t)} \tag{3.54}$$

$$= \frac{E_L b}{r_0}\frac{\sin[(kb/2)\sin\theta]}{(kb/2)\sin\theta}\sin(kr_0-\omega t) \tag{3.55}$$

Now by letting

$$\beta = (kb/2)\sin\theta \tag{3.56}$$

so that

$$E_p = \frac{E_L b}{r_0}\frac{\sin\beta}{\beta}\sin(kr_0 - \omega t) \tag{3.57}$$

the irradiance at P can be expressed as:

$$I(\theta) = \langle E_p^2 \rangle_T = \frac{1}{2}(\frac{E_L b}{r_0})^2(\frac{\sin\beta}{\beta})^2 \tag{3.58}$$

where $\langle \sin^2(kr_0 - \omega t)\rangle_T = \frac{1}{2}$. When $\theta = 0$, $\sin\beta/\beta = 1$ and I(θ)=I(0), which corresponds to the principle maximum. Therefore, the irradiance resulting from an idealized coherent line source in the Fraunhofer approximation is given by:

$$I(\theta) = I(0)(\frac{\sin\beta}{\beta})^2 \equiv I(0)sinc^2(\beta) \tag{3.59}$$

The variation of irradiance with β for single slit Fraunhofer diffraction can be plotted from Eqn. 3.59, as illustrated in Fig. 3.10 (solid line). A sinc function is also plotted in the same figure (dotted line) for comparison.

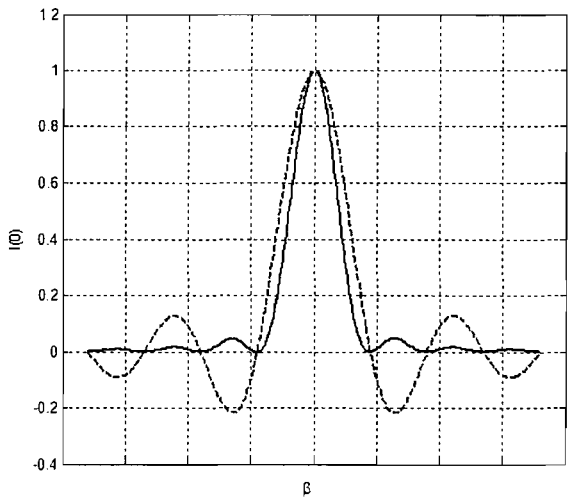

Figure 3.10: Sinc function curve (dotted line) and the irradiance function for single slit Fraunhofer diffraction (Solid line).

Diffraction from two slits

In the same manner, the diffraction pattern of a plane wavefront that is obstructed everywhere except at two narrow slits can also be calculated. In this case, the

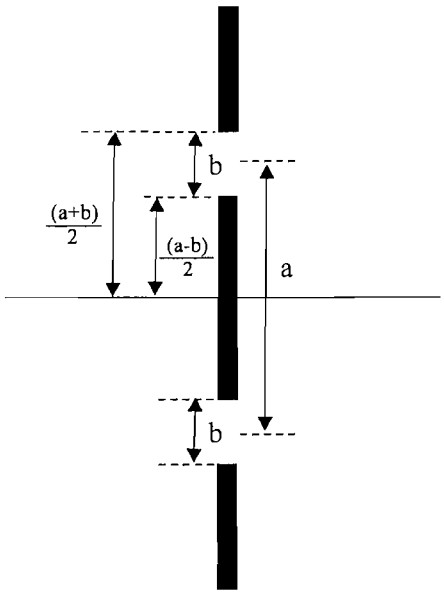

Figure 3.11: Schematic diagram of double-slit Fraunhofer diffraction.

irradiance is given by:

$$I(\theta) = 4I(0)(\frac{\sin\beta}{\beta})^2\cos^2(\alpha) \tag{3.60}$$

where $\beta = (\mathrm{kb}/2)\sin\theta$ and $\alpha = (\mathrm{ka}/2)\sin\theta$, and a and b represent the slit separation and the slit width respectively, as shown in Fig. 3.11. By extending the single slit and double slit Fraunhofer diffraction principle, an aperture of multiple slits can be derived by integrating the system over N slits. The resultant irradiance of the diffraction with multiple slits can be expressed:

$$I(\theta) = I(0)\frac{\sin\beta^2}{\beta}(\frac{\sin N\alpha}{\sin\alpha})^2 \tag{3.61}$$

in which α and β have the same definition as introduced before.

3.5.3 Diffraction grating

Based on the diffraction principles from multiple slits, array of diffracting elements, either apertures or obstacles that has the effect of producing periodic alterations in the phase, amplitude, or both of an emergent wave, is said to be a *diffraction grating* [5]. There are two types of diffraction gratings: transmission and reflection gratings (as shown in Fig. 3.12). A transmission grating has alternating clear and opaque lines and diffraction effects are observed in light which has been allowed to pass through the clear strips. A reflection grating consists of a set of grooves or blazes and diffraction effects are observed in the light reflected from the patterned

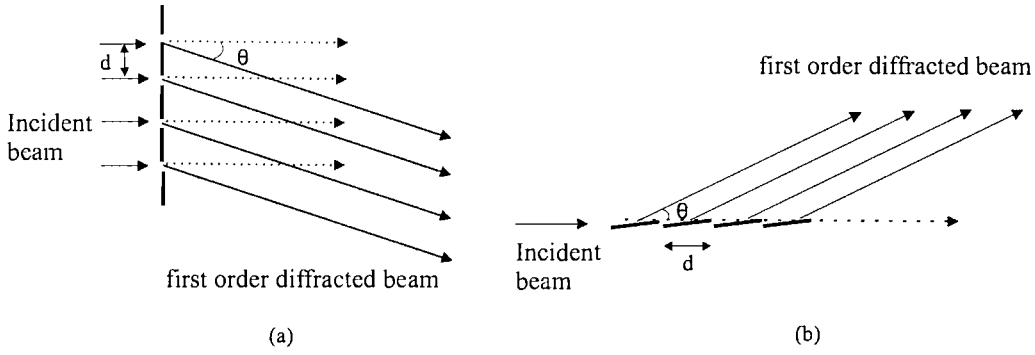

Figure 3.12: Schematic diagram of light diffraction by (a) a transmission diffraction grating, and (b) a reflection diffraction grating.

surface. In passing through such a system, a wavefront is expected to generate a diffracted beam in addition to the zero-order refracted beam. The condition for the generation of zero- and higher-order diffracted beams can be determined from the well known grating formula [73], presuming the incident medium is air or vacuum:

$$\sin\theta = \frac{m\lambda}{d} + n\sin\theta_m \tag{3.62}$$

where d represents the grating period (pitch size), λ is the free space wavelength, n represents the refractive index of the medium, θ_m is the angle of incidence to the normal from the medium side and θ is the refraction angle. Various diffraction order, m, has a value of 0, ±1, ±2... The first-order spectrum m=±1 appears on either side of θ_0 and is followed, along with alternate intervals of darkness, by the higher-order spectra, m = ±2, ±3,... This equation accounts for both refraction (second term) as well as diffraction (first term). According to Eqn. 3.62, for materials with moderate values of refractive index, when $d \ll \lambda$ no diffracted beams are possible. However, when the grating length is on the order of or greater than the free space wavelength, one or more diffracted beams can be generated.

Chapter 4

Design and fabrication of planar chiral metamaterials

A number of planar chiral samples with various nanoscale structures and dimensions have been fabricated. Different materials, including aluminium thin film, polymeric electron beam resist, and silicon nitride thin film, were used to create planar chiral patterns. A number of electron beam lithography (EBL) processes were developed to fabricate these nanoscale planar chiral structures with high density and complexity. In this chapter, the design and fabrication details of these different chiral samples are introduced and discussed.

4.1 Design of planar chiral metamaterials

All the planar chiral gratings are arranged in a regular 2D square matrix. All the nanoscale structures are defined by EBL, during which process the chiral patterns were transferred into a medium layer by either a dry etch or PMGI resist lift-off process. In general, the layout of various planar chiral samples follows a hierarchy principle. The top level of the design is composed of a certain number of 17mm by 17mm square chips; on each chip, there are thirty-six square gratings, which are also arranged in a square matrix. Each square includes a specific pattern. The area of each array is approximately 1 mm^2 and the space between different arrays is approximately 2.6 mm, so that the optical characterizations of each array can be performed without the laser beam probe impinging on the adjacent patterns. For most of the chiral samples, there are four chip designs (A,B,C,D) and each design is repeated four times on each wafer. All the patterns defined in the EBL process were first designed using a computer aided design (CAD) program, L-Edit, which illustrated the layout of the device structures and transformed the layout to

a standard exchange format. This standard design format is then transformed to GDSII format and exported to computer aided proximity correction (CAPROX). CAPROX is a professional pattern conversion software package used to generate the final design file. In summary, the hierarchical electron mask and the arrangement of individual chiral array are schematically shown in Fig. 4.1.

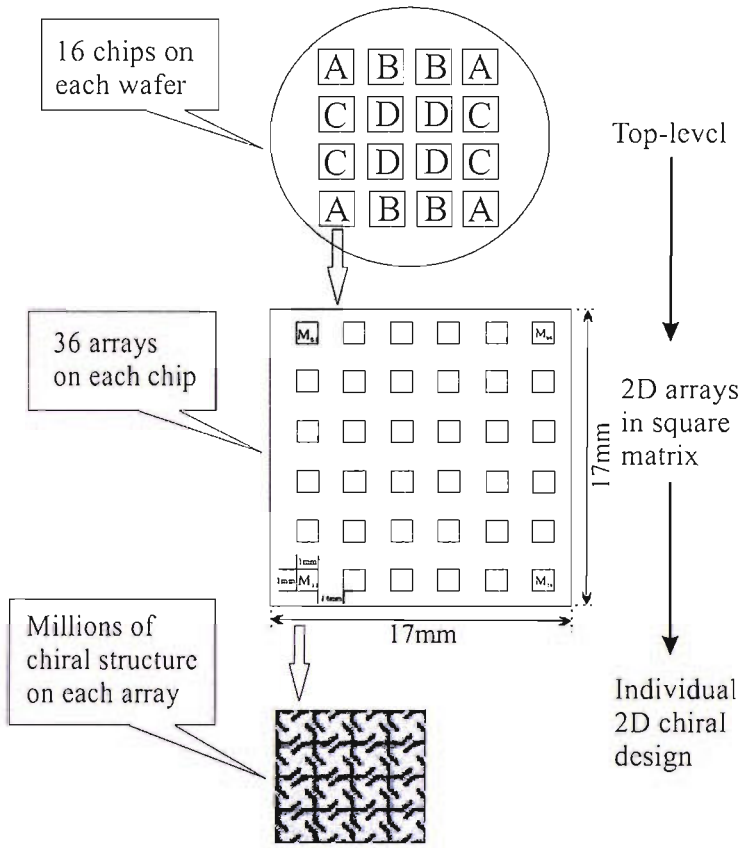

Figure 4.1: Schematic diagram of the design of planar chiral gratings distributed in a square matrix.

A series of four-fold rotational symmetrical gammadions were designed and characterized in this work. These gammadion arrays are characterized by handedness (left- or right-handed), arm length, ξ, bending angle, α, and pitch size, Λ. Fig. 4.2 shows a schematic diagram of two right-handed gammadions with an illustration of these characteristic parameters. In order to investigate the dependence of the polarization response of these planar chiral metamaterials on their characteristic parameters, six basic chiral gammadion gratings with different handedness (left- and right-handed gammadions) and different bending angles (positive values corresponding to right-handed gammadions and negative values corresponding to left-handed gammadions) were designed. The arm length, ξ, and pitch size, Λ, were also varied in different gratings for the purpose of characterization. These six basic gammadion

designs provide three pairs of enantiomeric forms of planar chiral metamaterials, as illustrated in Fig. 4.3.

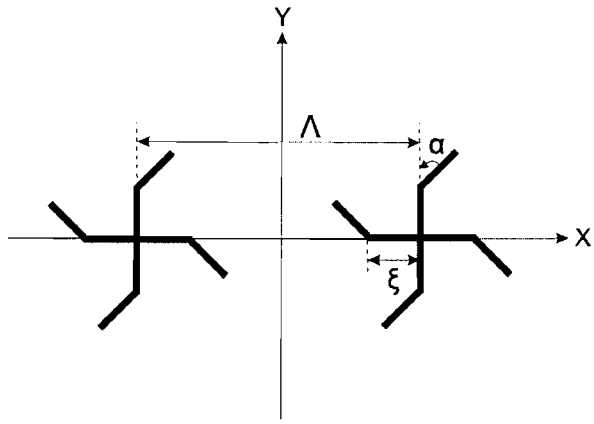

Figure 4.2: Schematic diagram of two four-fold symmetric right-handed gammadion.

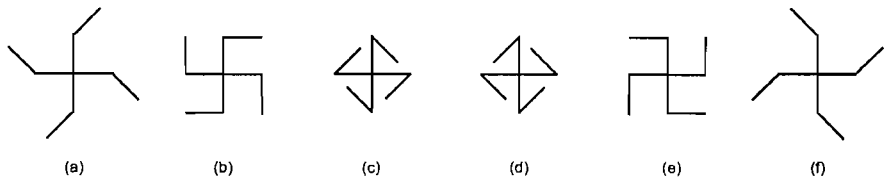

Figure 4.3: Schematic diagram of six different chiral gammadion designs with opposite handedness and different bending angles.

4.2 Fabrication of planar chiral metamaterials

The fabrication procedure for metallic and dielectric chiral samples is summarized in Table 4.1.

4.2.1 Electron beam lithography

EBL is a technique commonly used to create an image of an object by rastering with a well-focused electron beam over a predetermined area of a substrate. It has extremely high resolution capabilities, and can be used to fabricate novel optical and electronic devices with nanoscale features, for example, sub-wavelength waveguides [74], photonic-crystal enhanced lasers [75], and isolated silicon quantum dots [76].

In general, there are two types of EBL system in use: a scanning EB pattern generator, and an E-beam projection system. In a scanning EB pattern generator,

Fabrication process	Metallic chiral sample	Dielectric chiral sample
1	EBL process to define the chiral patterns	Deposition of the dielectric material in which the chiral structures are fabricated.
2	Deposition of the metallic material in which the chiral structures are fabricated.	EBL process to define the chiral patterns
3	Transfer patterns to the thin metallic film	Transfer patterns to the thin dielectric film

Table 4.1: The fabrication procedure of metallic and dielectric planar chiral metamaterials by EBL.

the electron beam is produced in an electron-optical column and is focused to a fine spot at the target [77]. Most electron guns generate currents of a few micro-amperes from a cathode with a diameter 10-100 μm. For that reason focusing lenses are used to reduce the spot size for sub-micrometer patterns with diameters of 2-200 nm. The sample is positioned on a table that has a mechanical XY translator controlled by a computer to move the beam to any point on the sample. The most common procedure to fabricate a structure using EBL can be explained in four steps. First the substrate to be patterned is coated with a thin layer of electron beam resist. Then the resist is exposed to a particular dose of electrons. Solubility of the resist changes after being exposed to electrons, thus a specific pattern or trench in the thin layer of the photoresist can be defined by dissolving the exposed (or unexposed) resist in a suitable solvent. Then the pattern is transferred to the substrate by an etch process or metal is deposited and selectively removed using a lift-off technique. The final step is removal of the resist. In addition, wafers need to be baked in an oven several times at different stages throughout the complete EBL process, including softbake before exposure, post-exposure bake and hardbake after development. Softbake has the function of reducing the solvent volume and alleviating stress; it also plays an important role in optimizing lithographic performance and feature profiles for chemically amplified resists; the post-exposure bake is used for driving the photochemical reaction and reducing standing wave interference effects. An additional bake after development removes residual solvents and, therefore, can improve stability and adhesion during etching [78].

Electron exposure of resists occurs through bond breaking (positive resist) or the formation of bonds or crosslinks between polymer chains (negative resist) [78]. The incident electrons have far greater energies than the bond energies in the resist molecules, and so all the electrons are effective. Both bond breaking and bond formation occur simultaneously. Which process predominates determines whether

the resist is positive or negative. In this project, both negative electron beam resist (UVN30) and positive electron beam resist (UVIII) were used to create either gammadion-shaped chiral mesas or gammadion-shaped holes in the matrix layer deposited on the substrate. UVN30 is a negative-tone photoresist for deep ultraviolet (DUV), X-ray, and e-beam applications, which is targeted for fast throughput device production down to 150 nm; and UVIII is a type of positive DUV photo resist and is optimized to provide a wide applications where the feature sizes are smaller than 250 nm.

Two factors are of major importance in limiting the resist resolution: swelling of the resist in the developer and electron scattering. Swelling of resists has two deleterious effects. First, two adjacent lines of resist may swell to such a degree that they touch. Second, this expansion and contraction weakens the adhesion of very small resist features to the substrate and can cause small undulations in narrow lines. Regarding electron scattering, when electrons strike a material, they penetrate the material and lose energy from atomic collisions. These collisions can cause the striking electrons to 'scatter', a phenomenon that is aptly known as 'scattering'. The scattering of electrons may be backward (or back-scattering, wherein electrons 'bounce' back), but it is often forward through small angles with respect to the original path. During EBL, scattering occurs as the electron beam interacts with the resist and substrate atoms. This electron scattering also has two major effects. First it broadens the diameter of the incident electron beam as it penetrates the resist and substrate; second it gives the resist unintended extra doses of electron exposure as back-scattered electrons from the substrate bounce back to the resist. In addition, the resolution and accuracy of the lithography process also depends strongly on the resist layer thickness and contrast of the resist. The thinner the layer and higher the contrast, the higher the resolution and accuracy. However, the thickness of the resist layer has to be sufficient to withstand the dry etching process [79].

4.2.2 Fabrication of aluminium chiral metamaterials

In order to investigate if the polarization response observed in the Ti/Au/Ti chiral sample is a unique property belong to this particular structure, a thin aluminium film patterned with the same surface microstructures was fabricated using the same electron beam mask as was used to fabricate the Ti/Au/Ti chiral samples. A standard 4-inch p-type silicon substrate with 30 Ω/cm resistivity was used as the starting material. The wafer was 525 μm thick and polished on both sides. The wafer was cleaned using a standard RCA process [78].

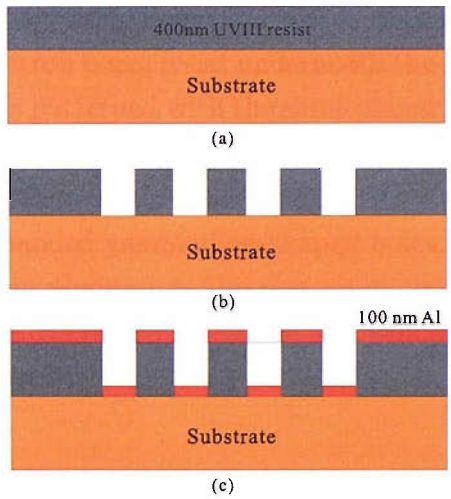

Figure 4.4: Schematic diagram of the fabrication process of aluminium planar chiral structures. (a) UVIII electron beam resist spin. (b) Resist development. (c) Al evaporation.

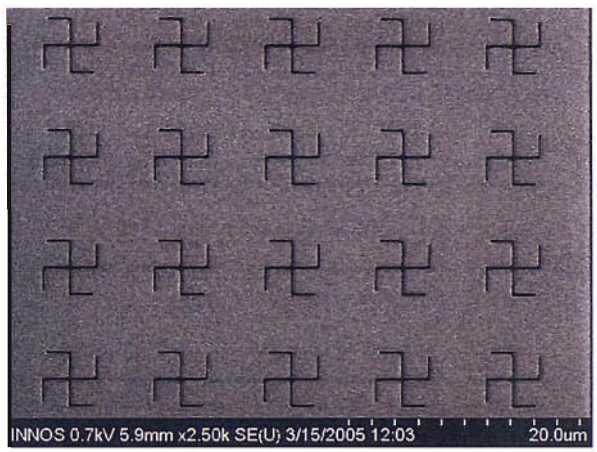

Figure 4.5: SEM image of an array of left-handed gammadions with a bending angle of -90° fabricated in a thin aluminium layer by EBL.

The wafer was then primed for 3 minutes to promote adhesion between the UVIII electron beam resist to the substrate. Next, the wafer was baked at 190°C for an hour before spinning a 400 nm thick layer of UVIII electron beam resist at 2500 rpm. The resist layer was exposed for 60 seconds to define all the planar chiral structures, followed by one minute baking at 140°C. Then the electron beam resist was developed for 2 minutes in a MF322 developer. The high density planar chiral structure images were therefore transferred to the electron beam resist. Next, a uniform 100 nm thick aluminium layer was evaporated on the surface by electron-gun evaporation. During this evaporation stage, the substrate was at room temperature. The base pressure was set at 10^{-6} mbar and the pressure rose to 10^{-5} mbar to 10^{-4} mbar during evaporation due to outgassing and the evaporating material. The

deposition rate of the aluminium layer was about 250 nm/minute. Due to the surface typology of the electron beam resist underneath the thin aluminium layer, the evaporated metal layer was patterned with the same planar chiral structures as those in the resist layer. In summary, Fig. 4.4 schematically illustrates the fabrication process of aluminium chiral metamaterials using EBL. Fig. 4.5 illustrates a SEM image of an array of left-handed gammadion-shaped holes, with a bending angle, α = -90°, fabricated in a thin aluminium film deposited on a silicon substrate. Very well defined chiral patterns can be seen from Fig. 4.5, which provides strong evidence of the successful fabrication process.

4.2.3 Fabrication of dielectric planar chiral metamaterials

Following the work on the metallic chiral metamaterials, a range of planar chiral structures were designed and fabricated in a thin dielectric silicon nitride (Si_3N_4) film deposited onto an optically transparent substrate of fused silica by plasma-enhanced chemical vapour deposition (PECVD). These dielectric chiral structures are especially attractive for device purposes because, unlike their metallic counterparts, they can be formed entirely from loss-less dielectric materials, and consequently have no free charge carriers or collective charge excitations (such as excitons or plasmons) that can attenuate the transmitted (or reflected) intensity. If such structures are fabricated on dielectric substrates such as fused silica, these devices can operate in the transmission regime in the visible region of the electromagnetic spectrum.

Unfortunately, the insulating properties of these dielectric structures coupled with their small feature sizes posed a number of difficult challenges during the EBL process. Firstly, an exposed pattern element receives exposure not only from the incident electron beam but also from scattered electrons from the adjacent element. This is called the *proximity effect* and is more pronounced as the space between pattern elements gets smaller. The proximity effects, as well as charging problems in non-conductive materials, can lead to poor pattern transfer, especially for nanoscale features. Secondly, the main-field stitching is another crucial problem in EBL, which can have serious consequences on yield. Due to the writing mode of the EBL equipment, which divides and sub-divides the chip writing into main and sub-fields, there are many possible causes for main field stitching errors such as temperature drift, contamination, mechanical vibration, etc. Therefore, a specific EBL process was developed in this work in order to fabricate dielectric planar chiral metamaterials that combine large area coverage, high resolution and a high degree of structural complexity.

Due to the nature of the optical characterization of these 2D dielectric chiral

structures, a number of high-threshold criteria need to be satisfied. First, the chiral structures need to be designed and patterned on the nanoscale, typically with resolutions of 50 nm or better. This, combined with the need for sufficient flexibility to vary design parameters between structures, requires the use of high-resolution EBL as a primary lithographic tool. Second, these chiral patterns, designed for the dielectric chiral sample, generally consist of high-density and complex structures that extend over areas of several square millimeters. This combination of high-resolution, high density and large area patterning requires not only an EBL system with excellent stitching accuracy between fields, but also a high current density to generate the required writing speed. This latter consideration also mitigates in favor of using high-speed chemically amplified resists such as UVIII and UVN30 rather than the more commonly used PMMA (polymethyl methacrylate) electron beam resist. Another important consideration that needs to be addressed is the performance of the electron beam resist during pattern transfer. For this process either reactive ion etching (RIE) or an ion beam milling process is generally required to etch deep trenches into the dielectric surface, or to sputter away non-reactive thin films of material. This again favours the use of high durability resists such as UVIII and UVN30. However, one consequence of using a high-speed writing process on wafers that are composed entirely of dielectric materials is that the pattern distortion due to charging becomes a significant process issue. This is particularly critical for the stitching of adjacent scan fields. Any significant imperfections can have serious repercussions for the optical performance of these planar chiral structures as they can break the overall periodicity or symmetry of the structures.

Considering the fabrication of planar chiral structures in a thin silicon nitride film using negative electron beam resist (UVN30), the starting material was a 4-inch optically transparent wafer of fused silica. The wafer was 0.75 mm thick and polished on both sides. Prior to processing, the wafer was cleaned, first in fuming nitric acid and then using a standard RCA process. A layer of PECVD Si_3N_4 was then deposited on one side of the wafer. The thickness of the Si_3N_4 layer was varied between 50 nm and 500 nm for the purpose of characterization. EBL and RIE were used afterwards to pattern the Si_3N_4 layer with various structures. Before resist coating, the wafer was given a dehydration bake at 140°C for an hour. Then, immediately prior to the application of the resist layer, it was exposed to a vapour of HMDS (hexamethyldisilazane) adhesion promoter for 3 minutes, which increased the adhesion of photoresist on the wafer surface. A 400 nm thick layer of UVN30 resist was then spun onto the surface at 2500 rpm and soft-baked at 110°C for 1 minute to drive out the majority of the remaining solvent (to prevent out-gassing during the EBL process) and to improve the thickness uniformity of the resist. The wafer was then loaded into the EBL system with the minimum delay and the resist was

exposed with the required patterns. A post-exposure bake at 115°C was then used to drive the photochemical reaction and reduce standing wave interference effects. After exposure, the UVN30 resist was developed in Shipley MF322 developer for 2 minutes and then hard-baked at 140°C for 20 minutes. Then a standard RIE using CHF_3 was performed at a r.f. power of 200 W to transfer the resist patterns into the underlying Si_3N_4 layer. The pressure used during RIE of Si_3N_4 was 100 mTorr and the flow rate of CHF_3 was 25 sccm. This resulted in an etch rate for Si_3N_4 of about 25nm/min.

All the chiral patterns themselves were written using a JEOL JBX9300FS EBL system operating at 100 KeV with a beam current of 2 nA and a focussed spot size of 10 nm. The higher beam voltage was used to minimize lateral scattering. The field size used was 500 μm, which is less than the area of most of the chiral designs (most of them cover areas of 1 mm^2 or more). Consequently, most chiral structures were written across multiple fields, with associated stage movements being performed between each field exposure. Due to the relatively large dimensions of each chip and the high density of the nanoscale chiral structures, the writing time of each wafer took approximately five hours.

The doses used to expose the resist varied between 8 and 10 $\mu C/cm^2$, depending on the density of the pattern. The exposed pattern element adjacent to another element receives exposure not only from the incident electron beam but also from scattered electrons from the adjacent elements. Thus, as the pattern density increases, it becomes necessary to adjust the exposure for different parts of the elements. In principle, the higher the density of the design, the lower the dose is set to compensate for proximity effects and increased backscattering; and in terms of the area, if larger areas receive a base dose of unity, then the smaller and/or isolated features receive a larger dose to compensate.

In this work, a dose modulation scheme was used to minimize the proximity effect while writing these planar chiral patterns (for which the pattern density and line width were both fairly uniform). Each individual chiral pattern was assigned a dose such that the shape appears at its correct size. The doses used in the final EBL process were modulated using the CAPROX program, which generated an optimal dose for each specific pattern. The corresponding dose distribution scheme is illustrated in Fig. 4.6. The horizontal axis represents a factor, by which the dose needs to be increased compared with the base dose. The base dose is a reference dose required to clear the electron beam resist from a large exposed area. The vertical axis is the number of shapes within a certain chiral pattern that need a particular dose modulation. The column bars represent different chiral patterns written by the developed EBL. As a result, different doses were modulated and applied during the

EBL process.

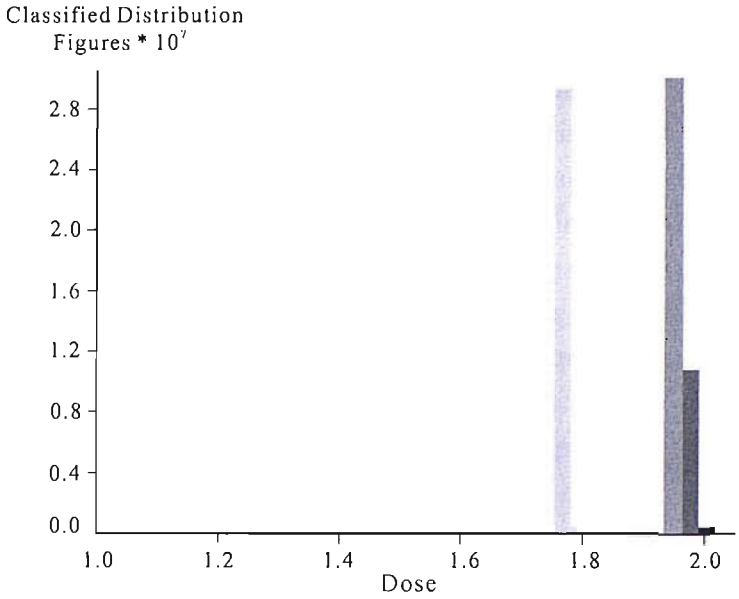

Figure 4.6: Final dose distribution chart for the fabrication of silicon nitride chiral metamaterials with different complexity and densities by EBL.

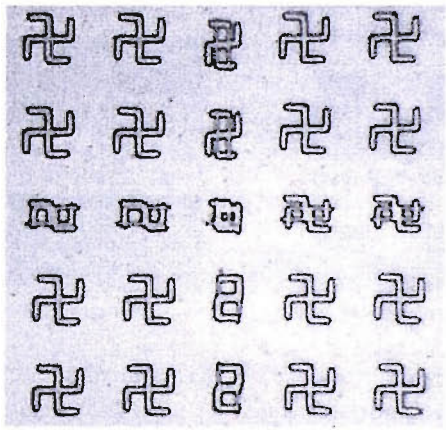

Figure 4.7: Optical micrographs of arrays of gammadion-shaped holes etched into a thin Si_3N_4 layer with an appearance of stitching errors due to the the charging issue.

Unfortunately, many of these structures were adversely limited in their size and integrity by stitching errors in adjacent fields. The origin of these errors is the build-up of charge in the structure during the exposed process. The stitching errors can lead to misalignments within the exposure pattern as large as several microns. This is comparable with the size or periodicity of the individual chiral elements themselves. As a result, these stitching errors could have significant repercussions for the optical performance of these planar chiral structures. Although the JEOL system used to

fabricate the chiral structures incorporates a laser-interference controlled stage with a positional stitching accuracy of 20 nm, charge build-up in both silicon nitride film and the dielectric silica substrate during the exposure of one field resulted in an additional deflection of the beam at the extremities of the field. As a consequence, the field size can be increased by several microns. Thus when the adjacent field is written the two fields overlap slightly at their common boundary. For example, Fig. 4.7 shows one such boundary running vertically through the micrograph and lying within one of the columns of the gammadion-shaped holes while a second boundary runs horizontally through a single row. As a result each gammadion that overlaps one of these boundaries has part of its structure in one field and the reminder in an adjacent field. Since the charging-enhanced field size is now greater than the distance that the stage moves between field exposures, these two segments of the pattern are then written partially on top of each other.

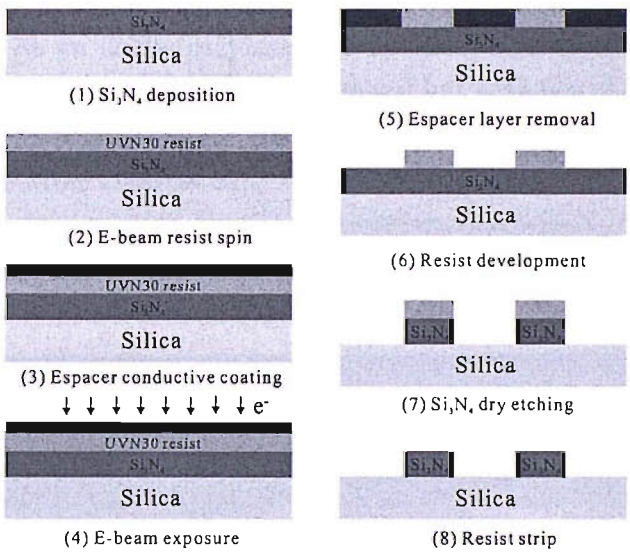

Figure 4.8: Schematic diagram of the fabrication processes of Si_3N_4 chiral mesas on a fused silica substrate. (1) Si_3N_4 deposition (2) Electron beam resist spin (3) Espacer 300 conductive layer deposition (4) E-beam exposure (5) Conductive layer removal (6) Resist development (7) Pattern transfer via dry etch (8) Resist strip.

In order to prevent this charging effect during e-beam exposure, it is necessary to employ a conductive interface layer of some form in order to allow most of the charge penetrating the resist from the electron beam to escape rapidly to earth [80 82]. One of the most common methods of achieving this is to coat the wafer prior to exposure with a thin film of metal, either on top of the resist or between the resist and the substrate. However both of these methods have significant drawbacks. A metal layer above the resist will increase the forward scattering of the electrons during the resist exposure and degrade the optimum resolution while also making alignment of the

pattern to designated features on the wafer more difficult. A metal layer beneath the resist can increase backscattering, and hence reduce contrast. It will also need to be patterned by a pattern-transfer process from the exposed resist, before the pattern can be applied to the substrate. This makes the use of subsequent processes such as lift-off difficult to implement. Additionally, both of these approaches require the removal of the metal layer at some stage. This adds additional complexity to the overall fabrication process. An alternative solution is adopted in this project to solve the charging issue. A layer of Espacer 300 conductive polymer was applied on the top of the UVN30 electron beam resist prior to exposure in the EBL system followed by a soft-bake at 95°C for 1 minute. The Espacer layer was spun at 2000 rpm for 30 seconds at room temperature, and the resulting thickness of this layer was about 40 nm. Immediately after exposure the Espacer layer was rinsed off in deionized (DI) water and the wafer was spun dry before developing the resist. Therefore, no impact on the features in the resist is expected as they are only revealed during the developing stage. As an acidic polymer, this Espacer layer protects the resist and has all the advantages of using a top layer of metal but with few of the disadvantages. The Espacer layer does not scatter the electron beam any more than the UVN30 resist and it is electron transparent. Therefore accurate alignment to the wafer surface is possible. In summary, the fabrication process of Si_3N_4 chiral gammadion-shaped mesas on a fused silica substrate incorporating the use of a charge dispersion layer is schematically illustrated in Fig. 4.8.

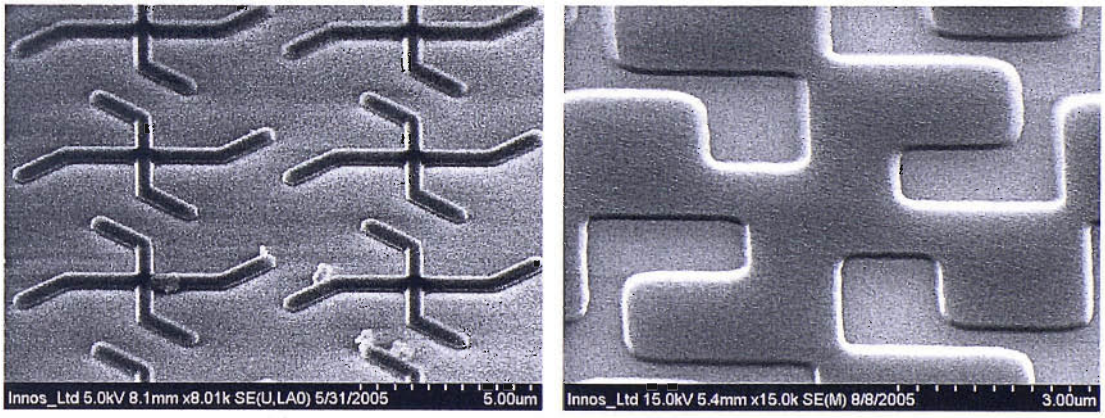

Figure 4.9: SEM images of (a) an array of gammadion-shaped Si_3N_4 mesas, and (b) an array of Si_3N_4 phase gratings on a fused silica substrate.

Due to the effective application of a charge dispersion layer and the dose modulation scheme, a large number of nanoscale dielectric planar chiral structures of much larger area that are not limited in their overall quality or integrity by stitching errors and field misalignment have been fabricated. Fig. 4.9 includes two SEM images of arrays of Si_3N_4 gammadion-shaped mesas (a), and phase-grating mesas

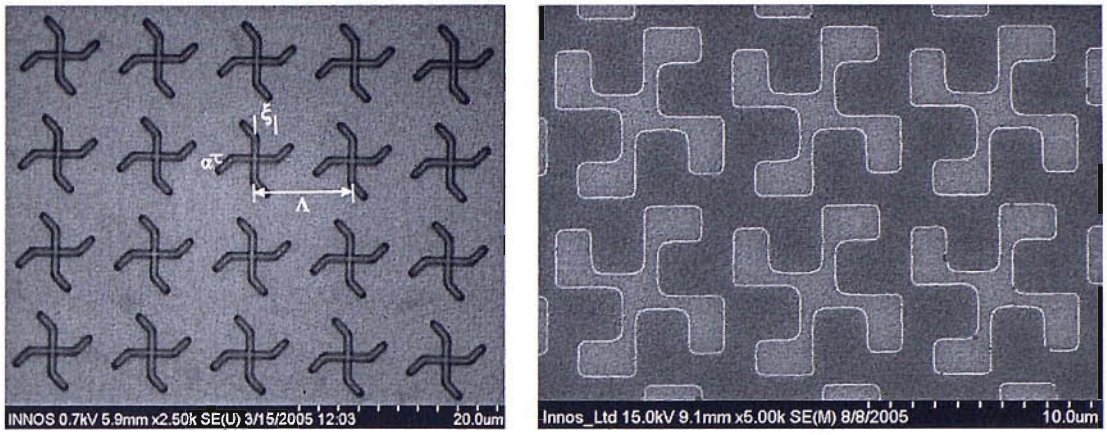

(a) (b)

Figure 4.10: SEM images of (a) an array of gammadion-shaped holes, and (b) an array of phase gratings, etched into a thin Si_3N_4 film deposited on a fused silica substrate fabricated by EBL.

(b) on a fused silica substrate at a tilt angle of approximately 30°. These structures were fabricated by the application of negative electron beam resist (UVN30). As a comparison, Fig. 4.10 illustrates two SEM images of arrays of gammadion-shaped holes (a), and phase gratings (b) etched into a thin Si_3N_4 film deposited on a fused silica substrate. Positive electron beam resist (UVIII) was used to create these structures. Additionally, more complex structures compared to gammadions and phase gratings were also fabricated. Fig. 4.11 shows a SEM image of an array of well defined Peano-Gosper fractal structures of about 80 μm dimension fabricated by EBL. Very little distortion and a uniform line width are obtained, which provides excellent evidence to the successful development of the EBL fabrication process. A much larger design composed of thousands of this Peano-Gosper fractal fundamental element structure is shown in Fig. 4.12, in which the fractals extend over distances of several millimetres and yet exhibit no appreciable discontinuities at the borders between adjacent exposure fields.

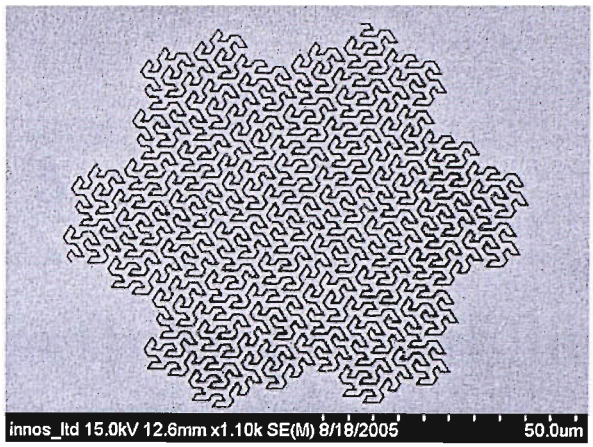

Figure 4.11: SEM image of a Peano-Gosper fractal fabricated in a thin Si_3N_4 film.

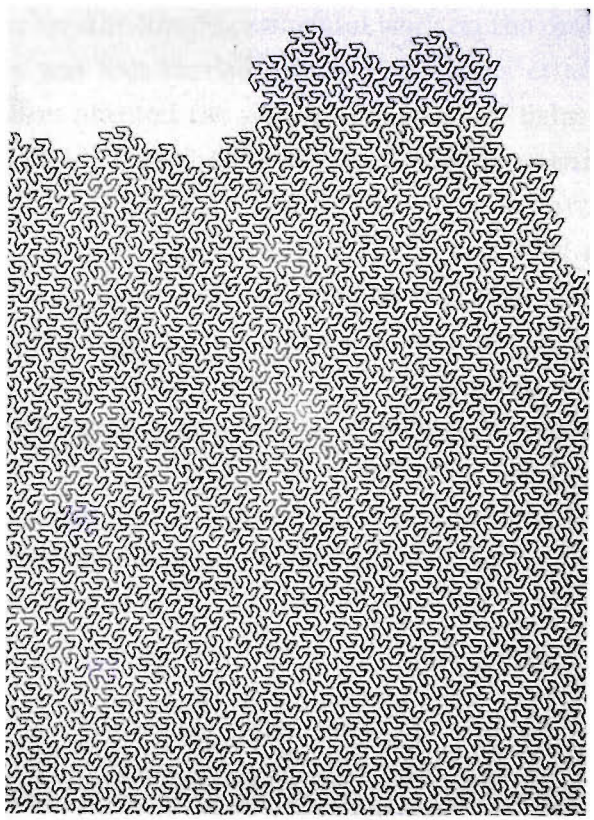

Figure 4.12: Optical micrograph of a large area high density Peano-Gosper fractals fabricated in a thin Si_3N_4 film.

Chapter 5

Optical activity of metallic planar chiral metamaterials

5.1 Introduction

As introduced earlier on, the first experimental work on the optical properties of 2D chiral metamaterials was first carried out by Papakostas *et al*, who reported that planar chiral structures affected the polarization state of light in a manner similar to 3D chiral media [9–11]. They showed that arrays of gammadion-shaped holes etched in a Ti/Au/Ti multilayer structure on a silicon substrate were capable of manipulating the polarization state of both far- and near-field diffracted light. The direction and degree of rotation and elliptization had been shown to be dependent on the chirality and geometry of planar chiral structures. In order to investigate if this optical activity could be observed in alternative metal with the same surface microstructures, aluminium was chosen to be a medium in which planar chiral structures were fabricated. The polarization response of various gammadion array with a range of dimensions and geometries are studied in this chapter. All these results are compared with the results obtained from the Ti/Au/Ti sample [10, 83].

5.2 Optical activity of aluminium chiral metamaterials

5.2.1 Sample description

The optical characterizations of the aluminium chiral sample were carried out on Chip B. As most of the other chiral samples, there are thirty-six square gratings arranged in a six by six matrix format on the chip, where each row contains six basic gammadion designs as illustrated in Fig. 5.1. These six patterns form three pairs of enantiomeric designs with opposite handedness (left-handed and right-handed) and different bending angles, $\alpha = \pm 45°$, $\pm 90°$ and $\pm 135°$ respectively. The pitch size, Λ, and characteristic arm length, ξ were varied on different chiral gratings. The characteristic parameters of individual grating are listed in Table 5.1.

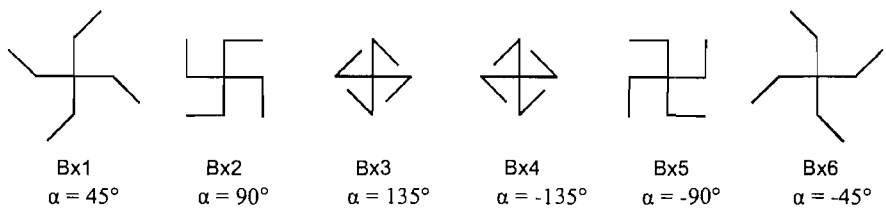

Figure 5.1: Schematic diagram of six chiral gammadion designs with opposite handedness and different bending angles fabricated in a thin aluminium film.

Grating	pitch size Λ (μm)	arm length ξ (μm)
B61-B66	4	0.8
B51-B56	4	1
B41-B46	4	1.4
B31-B36	4.4	2
B21-B26	7.2	2.8
B11-B16	9	4

Table 5.1: Characteristic parameters of aluminium chiral gammadion arrays under investigation.

5.2.2 Optical arrangement

Several optical experiments were performed in order to measure the polarization state of light diffracted from various arrays of aluminium chiral gammadions with different bending angles and handedness. The behaviour of the first-order diffracted

beams, which are in the same horizontal plane as the incident beam, was studied. The reason for choosing the first-order diffracted beam is due to the four-fold rotational symmetrical property of the planar chiral gammadions. When optical experiments are conducted at normal incidence, the zero-order reflected beam and the incident beam are coincident (but opposite in direction), thus making any measurement of the polarization state of the zero-order beam difficult. It has been shown that the zero-order beam reflected from 2D chiral gammadions with four-fold rotational symmetry does not exhibit any discernable change of polarization, whereas all the higher order beams appear to show appreciable polarization effects [10–12]. Additionally, the first-order diffracted beams are the most closely approximated to the zero-order diffracted beam and they have relatively large luminous intensities compared to most higher order diffracted beams, thus making them easier to be measured.

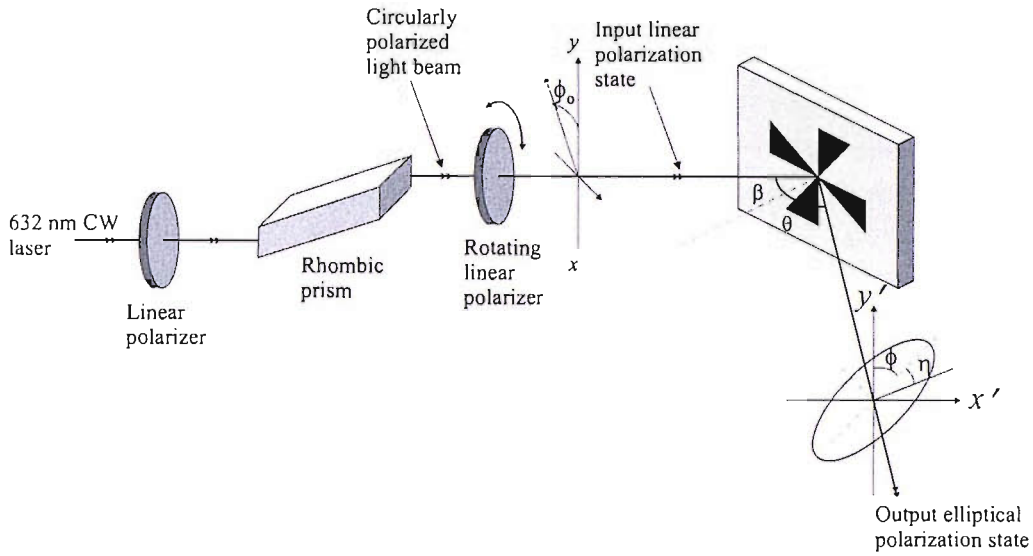

Figure 5.2: Experimental setup used to characterize the polarization state of the diffracted beams from the aluminium chiral sample in the reflection regime.

In order to measure the polarization state of the diffracted beams from these planar chiral gratings, a flexible optical measurement system was designed (schematically illustrated in Fig. 5.2). There are several important parameters (as illustrated in Fig. 5.2) that are used to characterize the optical activities of planar chiral metamaterials. Their definitions are included in Table. 5.2. The horizontal plane, which includes the incident beam, the zero-order diffracted beam and the normal to the sample, is defined as the plane of incidence. The first-order diffracted beams lie either side of the zero-order beam in this plane and are denoted as the (+1,0) and (-1,0) orders respectively. Their configurations in the reflection and the transmission regimes are schematically illustrated in Fig. 5.3 (a) and (b) respectively. According

Symbol	Parameter	Definition
η	Ellipticity	The length ratio of the minor-to-major axes of the polarization ellipse.
ϕ_0	Input polarization azimuth	The polarization azimuth angle of the incident beam.
ϕ	Output polarization azimuth	The polarization azimuth angle of the diffracted beam.
$\Delta\phi$	Polarization azimuth rotation angle	The rotated angle compared to the polarization azimuth rotation angle of the diffracted beam and that of the incident beam. In the reflection regime: $\Delta\phi = \phi + \phi_0$; In the transmission regime: $\Delta\phi = \phi - \phi_0$
β	Angle of incidence	The angle between the incident beam and the optical axis of the sample. Positive values are measured to the right of the sample normal, as looking directly at the patterned surface.
θ	Diffraction angle	The angle between the diffracted beam and the optical axis of the sample.

Table 5.2: Definitions of the parameters used to characterize the optical activities of planar chiral structures.

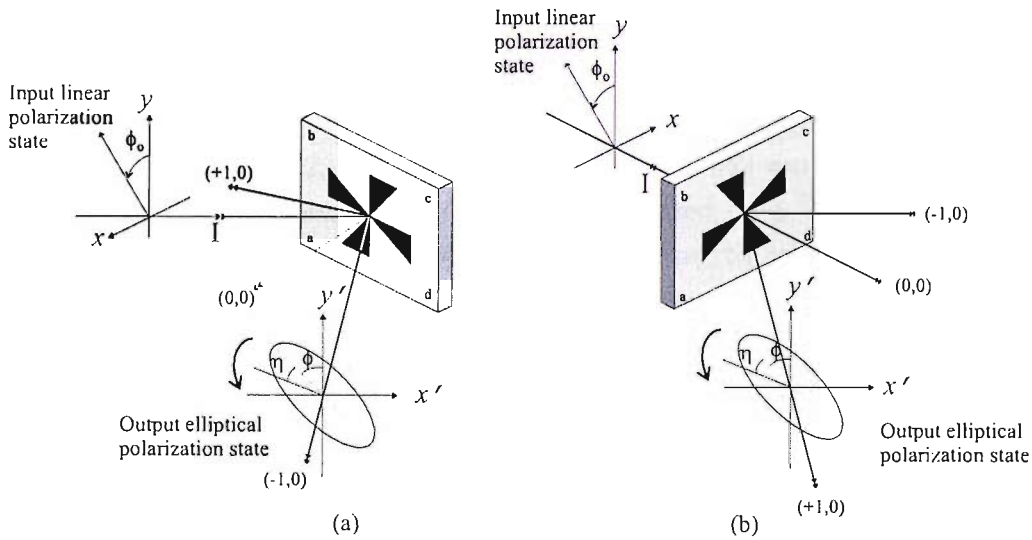

Figure 5.3: Configurations of the first-order diffracted beams from planar chiral metamaterials in (a) the reflection regime, and (b) the transmission regime.

to the grating formula introduced in Chapter 3, $\sin\theta = \frac{m\lambda}{d} + n\sin\theta_m$, the diffraction angle between the first-order diffracted beams reflected from the aluminium chiral gratings and the incident beam can be calculated directly. For example, considering the chiral gammadion gratings B41 and B46 on the aluminium sample are illuminated by visible red light at normal incidence, (d = Λ = 4 μm, λ = 632 nm, θ_m = β = 0), the diffraction angles of the (+1,0) and (-1,0) reflected beams are therefore

$\pm 9°$ respectively.

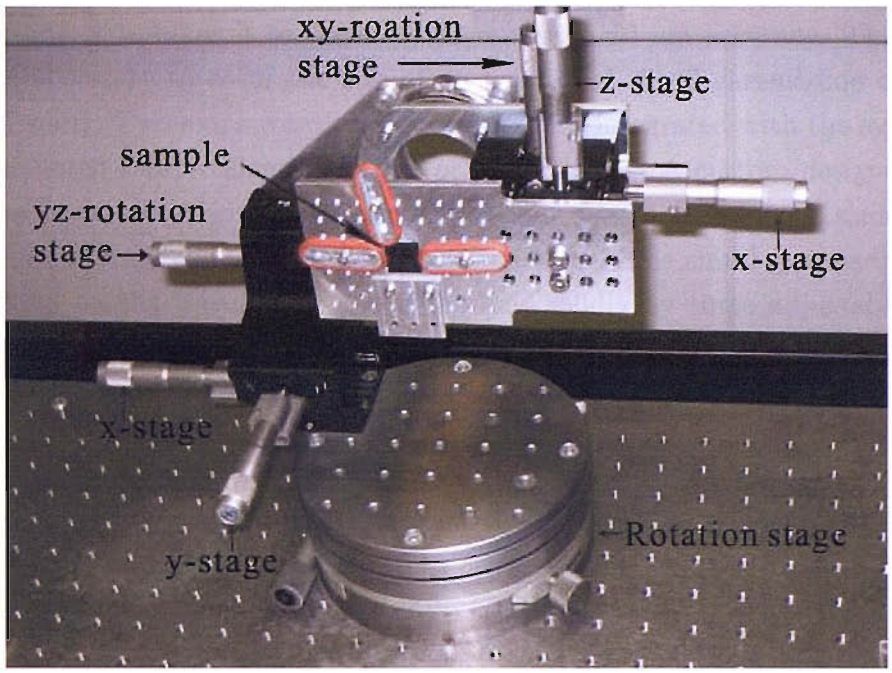

Figure 5.4: Photograph of the multi-functional custom designed sample holder.

As shown in Fig. 5.2, a HeNe laser operating at 632 nm was used as a light source. The output beam was first linearly polarized by a linear polarizer. The linearly polarized light then passed through a Fresnel rhomb prism to generate a circularly polarized beam. A second linear polarizer was then incorporated in the system after the prism to convert the circularly polarized beam back into a linearly polarized state. With this configuration, the input polarization azimuthal angle, ϕ_0, of the linearly polarized incident beam could be rotated radially about the beam direction by rotating the second polarizer. As a result, it is possible to rotate the direction of polarization of the beam incident on the sample without changing the beam's intensity. Finally, in order to ensure that the beam was focussed onto a single gammadion array without impinging on any adjacent designs, a plano-convex lens with a focal length of 20 cm was incorporated into the beam path between the second polarizer and the chiral sample. The relatively long focal length of this lens minimized any possible perturbation of the polarization state of the incident beam as it was transformed from a plane wave into a spherical wave.

A bespoke sample holder system was designed to be able to adjust the chiral sample in any x, y, z directions as well as to rotate the sample about all three orthogonal axes. A 360° precision rotation stage was mounted at the bottom of the system, with a x, y, z three-dimensional modular translation system on the top.

This 3D translation system consisted of three linear x-stages that were mounted together in a mutually orthogonal configuration. Each linear stage was controlled by a micrometer to allow it to travel by 25 mm with 10 μm accuracy. This travel range was necessary to cover the size of an individual chiral gammadion chip (17 mm by 17 mm). Two extra rotation stages were also integrated with the system to tilt the mounted sample along either xz or yz direction. A custom designed solid aluminium breadboard with a 15 mm by 15 mm square hole in the middle was fabricated and mounted to the main translation stage. The chiral gammadion chip was mounted on the breadboard above the hole solidly by three adjustable folks. Fig. 5.4 is a photograph of the sample holder with an illustration of each component.

Parameters	**Comments**
DOP	Degree of polarization
DOLP	Degree of linear polarization
DOCP	Degree of circular polarization
S1,S2,S3	Coordinates of the polarization vector located on the Poincaré Sphere
Ellipticity	Measured length ratio of the minor-to-major axes of the polarization ellipse (ω)
Orientation	Measured orientation angle of the major axis with respect to the horizontal axis (α in degrees)
Voltages	Reflect the signal after the gain stages

Table 5.3: Representations of the polarization parameters acquired from PA510-EC polarimeter system.

The polarization parameters of the first-order diffracted beams were then measured and analyzed using a commercial polarimeter system (Thorlabs model PA510-EC) with a wavelength range of 450 to 700 nm. This system included a polarimeter head (PA530) to detect the diffracted beams; a console to store and analyze all the data from the diffracted beams; and a computer to act as a data acquisition system. By connecting the computer to the console, the real time data, including the degree of polarization and ellipticity, could be acquired directly from the console for further analysis. A powerful real-time display system, which was integrated into the polarimeter system, could demonstrate the Poincaré Sphere graphically. The actual tabulated values of the Stokes parameters, and values for ellipticity and polarization azimuth rotation, were integrated into the polarimeter system as well. The polarization azimuth angle, ϕ, and the ellipticity, η, of diffracted beams were therefore calculated from the Stokes parameter as shown in Eqn. 5.1 and Eqn. 5.2. The accuracy of this polarimetry system is approximately $\pm 1°$, which reflects the accuracy of all the polarization measurements implemented in this work. The representations of

all the available parameters from the polarimeter system are included in Table. 5.3.

$$\tan 2\phi = \frac{S_2}{S_1} \tag{5.1}$$

$$\sin 2\eta = \frac{S_3}{S_0} \tag{5.2}$$

In summary, the design and implementation of the optical system illustrated in Fig. 5.2 has achieved the following targets:

- The characterization of sample diffraction in the plane of incidence (angle of incidence, β) over a nearly full 180° range of angles.
- 100 μm beam focusing and sampling capability.
- Sample positioning within $\pm$10 μm accuracy.
- Independent control of the direction, position and polarization state of the incident beam.
- Limited control of the direction of the diffracted beams.
- Capability to measure both the polarization state and the intensity of diffracted beams.

5.2.3 Optical activity of aluminium planar chiral metamaterials

Enantiomeric chiral structures

The first optical experiment on the aluminium chiral sample involved the polarization state measurement of the first-order diffracted beams reflected from an enantiomeric pair of gammadion arrays with bending angles, α = +45° (B41), and α = -45° (B46) respectively. In each case the gammadions have a characteristic arm length, ξ = 1.4 μm, and a pitch size, Λ =4 μm. The linearly polarized light at 632 nm was incident normal to each gammadion array and the output polarization states of the first-order reflected beams in the plane of incidence were measured. The polarization azimuth angle, ϕ_0, of the incident beam was varied, with ϕ_0 being measured in an anti-clockwise direction from the perpendicular to the plane of incidence as seen by an observer looking into the incident beam. The resulting polarization changes, including both ellipticity, η, and polarization azimuth rotation angle, $\Delta\phi$, as a function of input polarization azimuth, ϕ_0, of the first-order diffracted beams reflected from arrays B41 and B46 are illustrated in Fig. 5.5.

Fig. 5.5 clearly shows that the first-order diffracted beams reflected from each enantiomeric gammadion array exhibit strong changes to their polarization state,

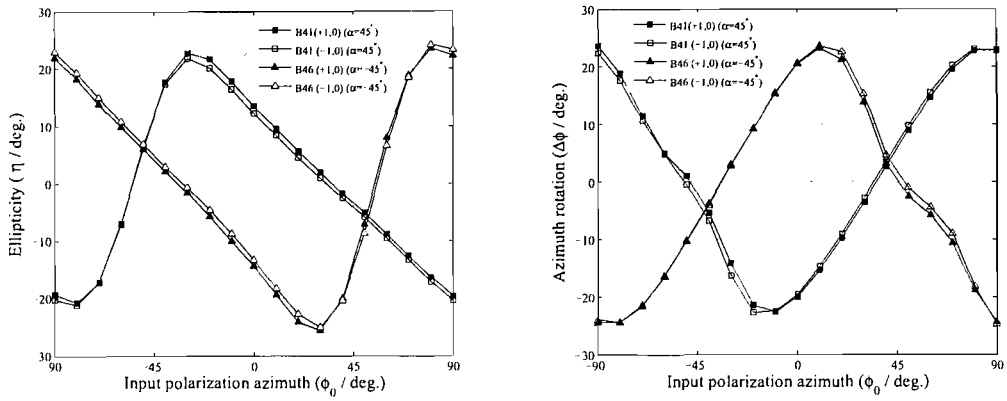

(a) (b)

Figure 5.5: The polarization changes for the first-order diffracted beams reflected from enantiomeric arrays of gammadion-shaped holes etched in a thin aluminium film when illuminated with 632 nm linearly polarized light at normal incidence. (ϕ_0, η and $\Delta\phi$ are defined in Table 5.2)

as characterized by the change in the polarization azimuth rotation, $\Delta\phi$, and the ellipticity, η (as they are defined in Table 5.2). Both $\Delta\phi$ and η vary considerably with the input polarization azimuth, ϕ_0. Comparison of the polarization changes for opposite diffraction orders (+1,0) and (-1,0) from the same gammadion array shows that they exhibit an almost the same response as a function of input polarization state. However, a comparison of the polarization changes for the same diffraction order beam but from opposite chiral enantiomers shows an opposite polarization effect. As each sample was measured with the same experimental arrangement with the only significant difference being the 2D chirality of the sample surface in each case, these results constitute clear evidence that these polarization changes arise from the chirality of the particular surface, and therefore represent a characteristic signature of the presence of 2D chirality in the structure and hence its effect on the form of the light-matter interaction.

This effect is further supported by experiments on achiral unpatterned aluminium surface. The polarization state of the zero-order reflected beam from the unpatterned aluminium surface was also measured using the same experimental arrangement as shown in Fig. 5.2. The sample was rotated clockwise 2° to prevent the zero-order reflected beam by unpatterned aluminium surface from overlapping with the incident beam, in which case the polarization state of the reflected beams could not be measured. The results are shown in Fig. 5.6 and the polarization changes of the first-order diffracted beam (+1,0) reflected from the enantiomeric pair of gammadion arrays (B41 and B46) are plotted in the same graph for comparison. The results show virtually no evidence of polarization change in the reflected beam from

the unstructured aluminium surface compared to the significant polarization modulation seen in the diffracted beams reflected from the aluminium surfaces patterned with planar chiral structures.

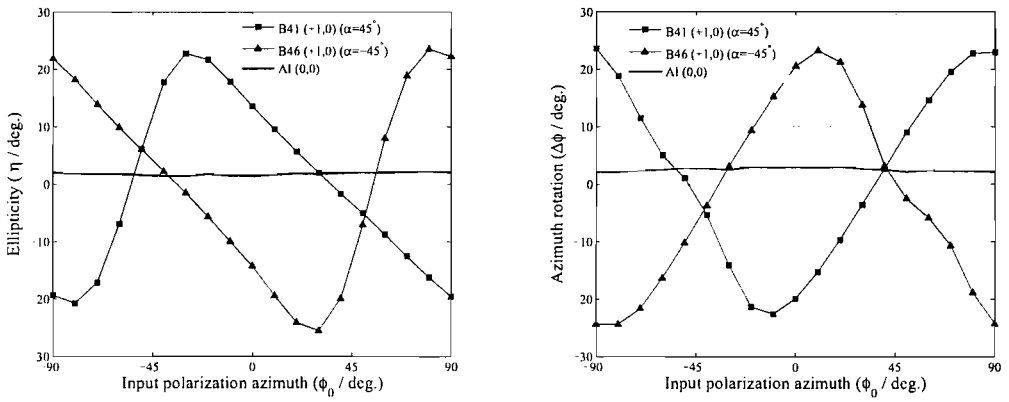

(a) (b)

Figure 5.6: Observed ellipticity and polarization azimuth rotation for the first-order diffracted beams reflected from enantiomeric chiral gammadion arrays and unpatterned aluminium surface.

In summary, results illustrated in Fig. 5.5 and Fig. 5.6 clearly show that the optical polarization response of these metallic planar chiral structures are due to the presence of planar chirality. These structures generated significant polarization changes that were not observed when the structures were lacking planar chirality. These results agree with the previous experimental investigations on the polarization response of planar chiral structures fabricated in the Ti/Au/Ti multilayer structure, as reported by Papakostas *et al.* [10, 11]. However, no polarization changes were observed for the zero-order diffracted beam from these aluminium chiral structures, which had been the case for all the previous experimental investigations [10, 11, 58]. This agrees with a recent theoretical work on the polarization properties of light reflected from structured 2D chiral surfaces [62], where Bedeaux *et al.* have derived modified surface boundary conditions and surface constitutive equations for 2D chiral interfaces and then shown how they can lead to polarization changes of the reflected light. Since the chiral gammadion structures possess a four-fold rotational symmetry, this can explain why the polarization state of the zero-order beam is unaffected by the surface chirality in the experimental arrangement as shown in Fig. 5.2.

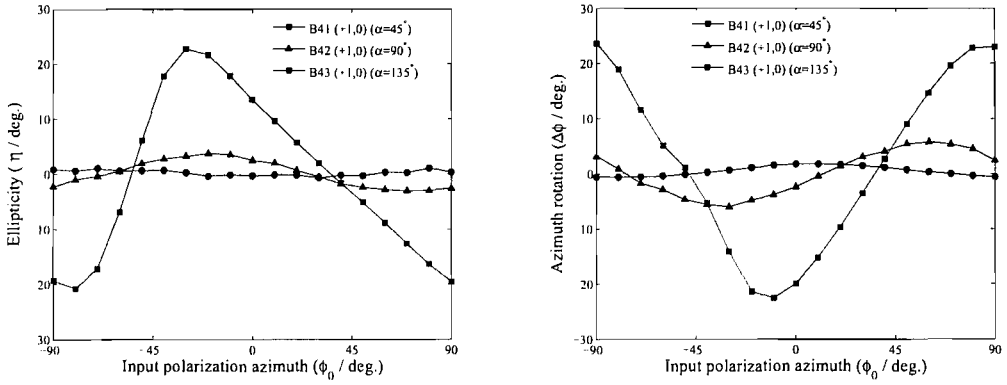

(a) (b)

Figure 5.7: The polarization changes for the first-order diffracted beams reflected from arrays of gammadion-shaped holes with different bending angles etched in a thin aluminium film when illuminated with 632 nm linearly polarized light at normal incidence.

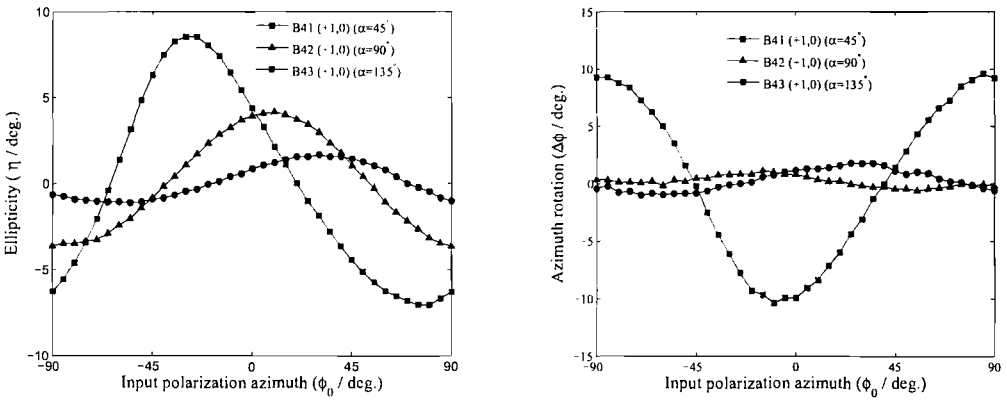

(a) (b)

Figure 5.8: The polarization changes for the first-order diffracted beams reflected from arrays of gammadion-shaped holes with different bending angles etched in a Ti/Au/Ti multilayer structure when illuminated with 632nm linearly polarized light at normal incidence [82].

Dependence on bending angle

A second experiment was designed to characterize the effect of different bending angles, α. As the gammadion bending angle is expected to be a major factor in determining the magnitude of the chirality for a given gammadion array, it is anticipated that the study of the dependence of polarization response on the gammadion bending angle will provide evidence of a degree of correlation between the chirality of the samples and the polarization state changes in the diffracted beams. The polarization states of the first-order diffracted beams from three aluminium gam-

madion gratings with different bending angles, $\alpha = 45°$, 90°, and 135° respectively (B41, B42 and B43), illuminated by linearly polarized light at normal incidence, were measured and characterized. The results are plotted in Fig. 5.7. The figure shows a dramatic difference in the polarization changes in different chiral gammadion arrays with various bending angles. The polarization response observed in the chiral gammadion array with a 45° bending angle is much more significant than the response seen from the gammadion arrays with larger bending angle, 90°. In fact, when $\alpha = 135°$, the polarization changes is negligible. A similar trend of behaviour was also observed in the Ti/Au/Ti chiral sample as shown in Fig. 5.8.

A comparison of Fig. 5.7 and Fig. 5.8 indicates that the polarization changes from all the arrays of gammadions are strongly dependent on the gammadion bending angle regardless of the material. This implies that the magnitude of the polarization changes may be correlated with the magnitude of the chirality of the 2D chiral structures. These results are supported by the theoretical model of planar chirality [12] described in Chapter 2. Applying this mathematical model to the case of a single gammadion of a bending angle α, a dependence of chirality index, K, on the gammadion bending angle can be calculated, as shown in Fig. 5.9 [12]. From the curve, it can be seen that the chirality index of a single gammadion is maximal at a bending angle of approximately 55°. Then it decreases rapidly with the increasing of α, and eventually becomes slightly negative just prior to α reaching 180°. Consequently, as the bending angle changes, the chirality index of the gammadion varies in a manner that is qualitatively similar to that of the polarization response from gammadion arrays.

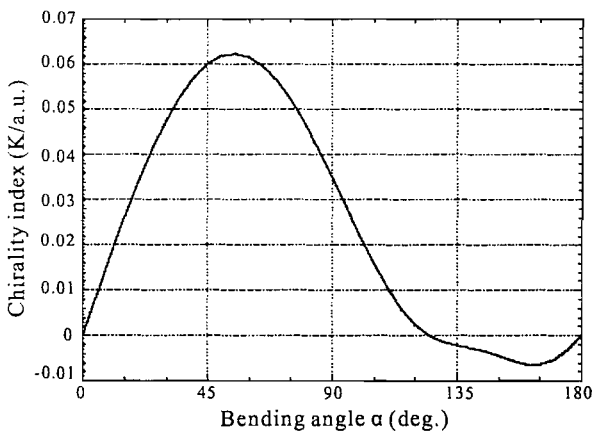

Figure 5.9: Variation of the chirality index (K) for a single gammadion as a function of the bending angle, α [12].

Size dependence and scaling behaviour

As discussed previously, the geometry of the planar chiral surfaces can be characterized by three parameters: the characteristic gammadion arm length, ξ; the pitch size of the gammadions in the square array, Λ; and the bending angle, α. The effect of varying α has been demonstrated in the previous section. In this section, the dependence of the polarization response on the gammadion arm length and the scaling behaviour of the metallic planar chiral metamaterials are investigated.

In most physical systems the strength of the light-matter interaction is usually highly dependent on the relative length-scales of the material structure (as defined by its geometry and material constants) and the irradiating electromagnetic radiation (as defined by the wavelength, λ). Thus, varying the magnitude of one relative to the other should have a profound influence on the optical behaviour of the structure. For this reason, three different aluminium gammadion gratings (B46, B56, and B66) were chosen to investigate the dependence of polarization response on the size of the planar chiral structures for a constant wavelength (λ = 632 nm). All three arrays of gammadions have the same bending angle, α = -45°, and pitch size, Λ = 4μm, but different arm lengths. The main advantage of this approach is that any size-dependent effects that are detected can be assumed to be purely due to the surface topology of the sample and its chirality rather than possible variations in metamaterial properties.

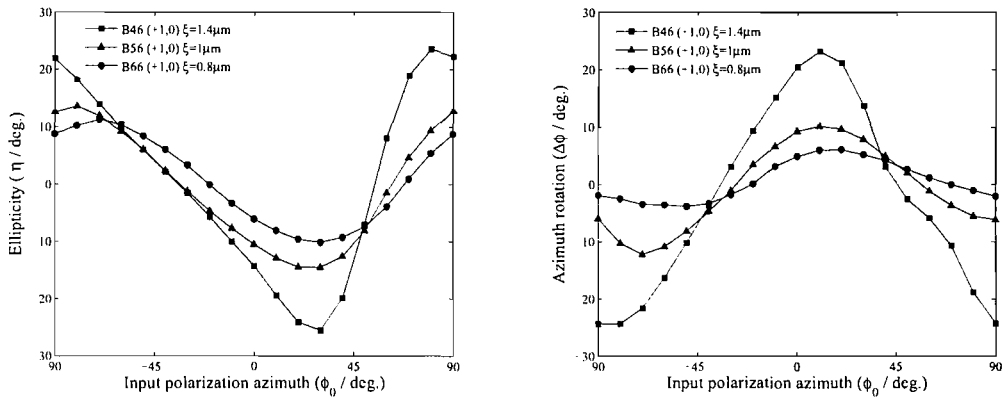

(a) (b)

Figure 5.10: The polarization changes for the (+1,0) order diffracted beam reflected from arrays of gammadion-shaped holes with different arm lengths etched in a thin aluminium film when illuminated with 632 nm linearly polarized light at normal incidence.

The changes in polarization state for the (+1,0) order diffracted beam from aluminium chiral sample B46, B56 and B66 illuminated at normal incidence are plotted

in Fig. 5.10. The results clearly demonstrate that as ξ decreases, the changes in both the polarization azimuth rotation angle and the ellipticity of the (+1,0) diffracted beam decrease. This tends to suggest that the magnitude of the polarization effect scales with gammadion size ξ, or with the ratio of ξ/λ. Since the pitch of each gammadion array studied in Fig. 5.10 is identical ($\Lambda = 4$ μm), an increase in ξ results in an increase in the proportion of the metal surface that is covered by these gammadion-shaped holes. In fact, for this set of structures a filling factor term can be defined as:

$$\sigma = 4\xi^2/\Lambda^2 \tag{5.3}$$

which represents the proportion of the unit cell of each array that is filled by the gammadion. As Λ is the same for each array, it is evident that the filling factor varies with ξ^2 for this particular set of structures. The strength of the polarization response shown in Fig. 5.10 appears to increase with ξ in a similar manner. This in turn suggests that the polarization change in these planar chiral metamaterials may be dependent on the density of gammadions, or more specifically on the filling factor, σ.

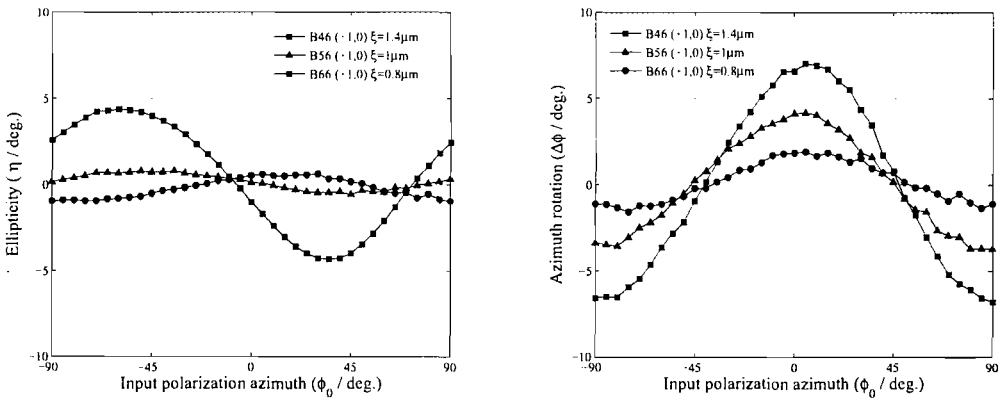

(a) (b)

Figure 5.11: The polarization changes for the (+1,0) order diffracted beam reflected from arrays of gammadion-shaped holes with different arm lengths etched in a Ti/Au/Ti multilayer structure film when illuminated with 632 nm linearly polarized light at normal incidence [82].

Although the data curves illustrated in Fig. 5.10 show different magnitudes for polarization response as a function of ξ, it is clearly seen that the data curves for each gammadion array appear to have similar functional forms. For each set of gammadions, the change in ellipticity of the (+1,0) diffracted beam is an oscillatory function of the input polarization azimuth, ϕ_0, that peaks at approximately $\phi_0 \approx 30°$ (see Fig. 5.10 (a)), and this behaviour is independent of ξ with only the amplitude of the oscillatory function changing as ξ is varied. A similar phenomenon is seen

from the changes in polarization azimuth rotation but with the maximum change now occurring at $\phi_0 \approx 10°$ (see Fig. 5.10 (b)). In comparison, the data in Fig. 5.7 indicates that changing the gammadion shape via its bending angle, α, will not only change the magnitude of the polarization response, but also affect the values of the input polarization azimuth, ϕ_0, at which the maximum and minimum polarization response will occur. This suggests that while all the three main gammadion design parameters (α, ξ and Λ) can influence the magnitude of the observed polarization response, the ϕ_0 dependence of the maximum polarization response is determined principally by the bending angle, α, and hence by the chirality of the individual diffracting elements. The results presented in Fig. 5.10 are similar to those seen previously for similar sized gammadion arrays on the Ti/Au/Ti sample, as shown in Fig. 5.11. Both samples show similar scaling behaviour of the polarization response with ξ for constant Λ, and in each case the polarization azimuth rotation positions of the maximum and null polarization changes appear relatively independent of ξ.

5.3 Summary and conclusion

Chiral grating	Bending angle α	pitch size Λ (μm)	arm length ξ (μm)	Maximum ellipticity η_{max}	Maximum polarization azimuth rotation $\Delta\phi_{max}$
B41	45°	4	1.4	22.8° (ϕ_0=-30°)	23.7° (ϕ_0=-90°)
B42	90°	4	1.4	3.8° (ϕ_0=-20°)	-6° (ϕ_0=-30°)
B43	135°	4	1.4	1.1° (ϕ_0=80°)	1.7° (ϕ_0=0°)
B46	-45°	4	1.4	23.5° (ϕ_0=80°)	-24.4° (ϕ_0=-90°)
B56	-45°	4	1	-14.5° (ϕ_0=30°)	-12.2° (ϕ_0=-70°)
B66	-45°	4	0.8	11.2° (ϕ_0=-70°)	6.1° (ϕ_0=20°)

Table 5.4: Magnitudes of polarization state modulation of (+1,0) order diffracted beams from aluminium planar chiral gratings.

In summary, Table 5.4 summarizes the magnitudes of the polarization changes observed from different aluminium planar chiral structures studied in this chapter.

The effects of planar chirality on the polarization state of beams diffracted by periodically patterned aluminium surface have been investigated. Polarization changes have been shown to correlate to both the sense and the magnitude of the planar chirality of the surface. Furthermore, studies of the scaling of features, dependence on both the characteristic arm length, ξ, of the gammadions patterned into the metallic surfaces, and their bending angles, α, have also been correlated to polarization

phenomenon. The scaling behaviour studied has shown that the magnitude of the observed polarization changes approximately scales with the surface coverage of the chiral gammadions, and that this trend is repeated for several gammadion-based metallic chiral metamaterials with different periodicity and material composition.

The results obtained for aluminium sample are in close agreement with those obtained for the Ti/Au/Ti sample studied previously. The results presented in this chapter show that the polarization behaviour previously seen for Ti/Au/Ti planar chiral metamaterials is not dependent upon any specific feature of the titanium/gold/titanium multilayer arrangement. In fact, another arbitrarily chosen, single metallic layer such as aluminium, patterned with identical planar chiral nanostructures could exhibit very similar optical activities.

Chapter 6

Optical activity of dielectric planar chiral metamaterials

6.1 Introduction

Results in the previous chapter have shown that metallic planar chiral metamaterials with characteristic length-scales of a few microns exhibit a significant polarization response. A strong polarization rotation and elliptization of the polarization state of linearly polarized light have been observed in the first-order diffracted beams reflected from arrays of planar chiral gammadions that were etched into thin metallic films, including a Ti/Au/Ti multilayer structure and a single aluminium thin film. All these chiral structures were fabricated on silicon substrates and their polarization responses were only investigated in the reflection regime.

Optical activity of the metallic planar chiral metamaterials was explained by the presence of induced currents and surface plasmons in the metallic layers [10, 12]. It was postulated that these surface currents and plasmons were driven by the incident electromagnetic field, while the interaction of the surface with these currents and plasmons led to a polarization change for the emitted electromagnetic wave. If these mechanisms are correct, will dielectric metamaterials with the same surface microstructures be expected to exhibit a similar polarization response? If this is the case, what will be the mechanism behind these dielectric planar chiral metamaterials?

In order to answer these questions, a range of dielectric planar chiral metamaterials, including a polymeric chiral sample with silicon substrate and a number of silicon nitride and silicon dioxide chiral samples with silica substrates, were fabricated. Their optical activities are studied in this chapter. The polarization response

of opposite enantiomers is investigated and discussed. The dependence of the polarization response on the chiral geometry and the thickness of the silicon nitride film are also investigated. A possible underlying mechanism to explain the optical activity of planar chiral metamaterials is proposed.

6.2 Polymeric planar chiral metamaterials

The first dielectric planar chiral metamaterials investigated comprised of a 300 nm thick patterned layer of UVIII electron beam resist on a double-polished highly resistive (110 Ω-cm) silicon wafer. The resist layer was patterned by EBL with the same regular square arrays of gammadion-shaped holes as the metallic chiral samples introduced in the previous chapter. The fabrication process consisted of a simple resist spin and bake, followed by the resist exposure and development. An enantiomeric pair of polymeric gammadion arrays (B41, B46), which have the same characteristic parameters as the metallic chiral samples (both the Ti/Au/Ti sample and the Al sample), were studied. Fig. 6.1 includes optical micrographs of arrays of right-handed gammadions (B41) and left-handed gammadions (B46) etched into a 300 nm thick layer of UVIII positive electron beam resist. Both gammadion arrays have a arm length, $\xi = 1.4$ μm, and a pitch size, $\Lambda = 4.0$ μm. In a similar manner as the characterization of the metallic chiral samples, the polarization states of the first-order diffracted beams from these two polymeric chiral square gratings were measured as a function of the input polarization state. Fig. 6.2 shows the changes in the polarization state of the (-1,0) and (+1,0) diffracted beams from B41 and B46 as a function of input polarization state, ϕ_0. It can be clearly seen that both gammadion chiral arrays induced large changes in the polarization states of the first-order diffracted beams in the reflection regime. A maximum modulation of almost 15° in the ellipticity and 10° in the polarization azimuth rotation were obtained. A comparison of B41 to its opposite enantiomer, B46, indicates that the polarization change for opposite enantiomeric samples appears to be opposite in sign for opposite input states (ϕ_0), while the opposite diffraction orders from the same sample yield virtually identical results. This pattern of behaviour is similar to that observed from the metallic chiral samples as described in the previous chapter (see Fig. 5.6).

The results in Fig. 6.2 indicate that dielectric planar chiral metamaterials are also capable of exhibiting optical activity in reflection in a similar form and magnitude to metallic planar chiral metamaterials. As the common factor in both sets of samples was the presence of a semiconducting silicon substrate, it was decided to replace the silicon substrates with fused silica and to repeat the experiments on all-dielectric loss-less planar chiral structures in the transmission regime.

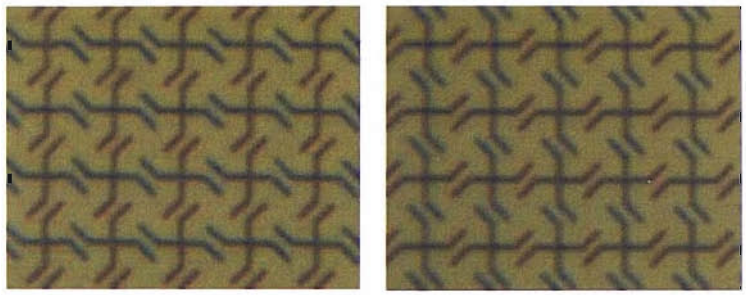

(a) (b)

Figure 6.1: Optical micrographs of arrays of (a) right-handed, and (b) left-handed gammadions etched in a layer of UVIII resist deposited on a silicon substrate.

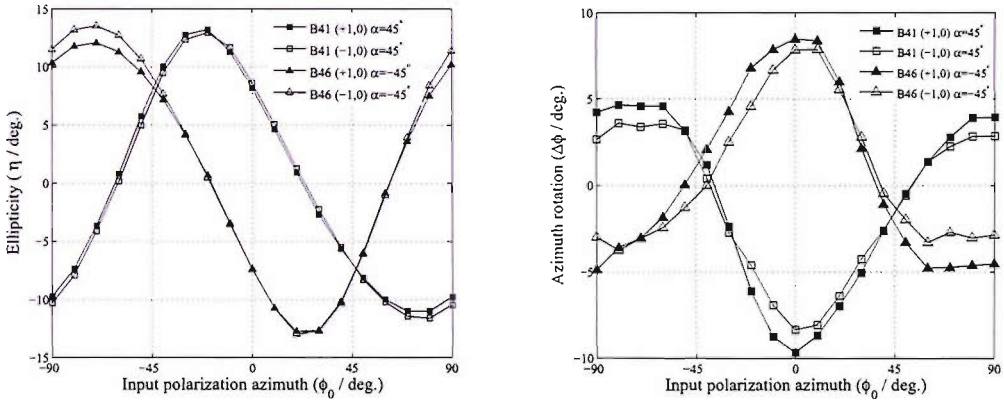

(a) (b)

Figure 6.2: The polarization changes for the first-order diffracted beams reflected from enantiomeric arrays of gammadion-shaped holes etched in a thin layer of polymeric electron beam resist (UVIII) when illuminated with 632 nm linearly polarized light at normal incidence.

6.3 All-dielectric silicon nitride planar chiral metamaterials

6.3.1 Device design and fabrication

All-dielectric planar chiral metamaterial samples were fabricated using a combination of high-resolution EBL and RIE techniques as outlined in Chapter 4. In order to understand the mechanism behind the optical activities of dielectric planar chiral metamaterials, two types of dielectric materials, Si_3N_4 and SiO_2, were used for the fabrication of planar chiral structures. The first set of chiral structures consisted of a Si_3N_4 film deposited on a fused silica substrate. The silica was chosen because it is transparent at 633 nm while the fused structure ensured that the substrates were

not optically active or birefringent (unlike single-crystal quartz). In each case, the Si_3N_4 film was patterned with various chiral and achiral arrays, with the pattern beings etched through the entire Si_3N_4 film.

Wafer No.	Thickness of deposited Si_3N_4 film (nm)	Type of E-beam resist
2	160	negative
3	320	positive
4	320	negative
5	80	positive
6	240	positive

Table 6.1: Design parameters of silicon nitride chiral samples fabricated by EBL.

Wafer No.	SiO_2 Etch depth in the substrate (nm)	Type of E-beam resist
1	170	positive
2	340	positive
3	690	positive
4	820	positive

Table 6.2: Design parameters of silicon dioxide chiral samples fabricated by EBL.

Chiral array number	Bending angle α	Pitch size Λ (μm)	Arm length ξ (μm)
BA41	0	5	1.8
BA42	-45°	5	1.8
BA43	-90°	5	1.8
BA44	90°	5	1.8
BA45	45°	5	1.8
BA46	0	5	1.8

Table 6.3: Characteristic parameters of the dielectric chiral gammadion arrays under investigation.

Four different thicknesses of the Si_3N_4 layer were deposited on the fused silica substrates using two types of electron beam resist (see Table 6.1). The reason for choosing different thicknesses of the material in which the planar chiral structures were fabricated, was to investigate light interactions with matter and their polarization response as a function of film thickness. By choosing opposite types

of electron beam resists, both gammadion-shaped holes (fabricated using positive UVIII electron beam resist) and gammadion-shaped mesas (fabricated using negative UVN30 electron beam resist) were generated. Therefore, the optical properties of two complementary structures could then be compared. Additionally, identical patterns were also etched into wafers of uncoated silica (without the Si_3N_4 film) to a range of depth up to 826 nm (see Table 6.2). The characteristic parameters of a number of chiral gratings investigated in this work are included in Table 6.3. A full list of the design parameters is included in **Appendix A**.

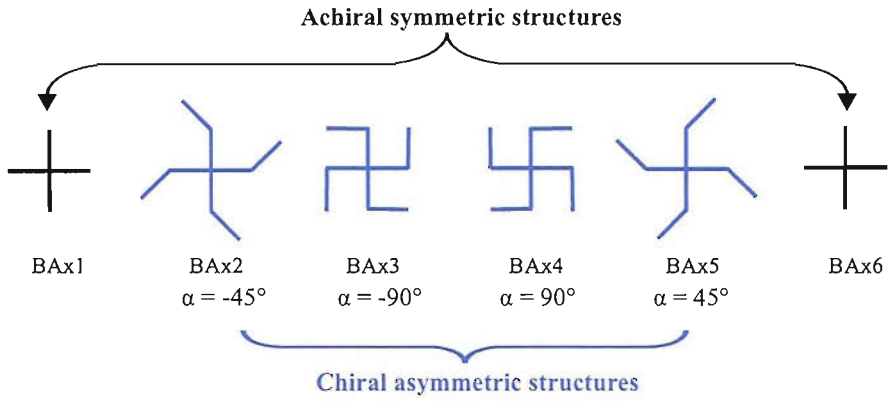

Figure 6.3: Schematic diagram of six microstructural designs fabricated in the dielectric chiral samples.

Fig. 6.3 illustrates the six basic microstructural patterns used to pattern all of the dielectric planar chiral metamaterials. They include four arrays of chiral gammadions and two arrays of achiral crosses. For each gammadion the arm segment length (ξ) is 1.8 μm, and the pitch size (Λ) is set to be 5 μm. In all cases, the designed width of the gammadion arm is 200 nm, although the actual width of the final structures was generally slightly larger due to broadening of the lines during both the lithography and RIE process steps. In addition to the chiral gammadion design, arrays of achiral cross-shaped structures were also included to provide a direct comparison between the polarization response of chiral and achiral structures. As a result, the effects that arise due to the chirality of the patterned surface can be easily identified and distinguished from those effects that may occur due to other asymmetries, such as those inherent in the experimental alignment or those due to fabrication imperfections.

6.3.2 Optical arrangement

The design and implementation of the optical system used to characterize the dielectric chiral samples follows the same principles as the optical system used to

characterize the metallic chiral samples. However, due to the transparent property of both the silica substrate and silicon nitride chiral medium, the polarization response of planar chiral metamaterials is studied in the transmission regime. However, if the samples are aligned so that their patterned Si_3N_4 or SiO_2 surfaces face the incident beam, the first and higher order diffracted beams on transmission will subsequently strike the back surface (the unpatterned interface with the air) of the fused silica substrate at a non-zero angle of incidence. These beams can then undergo additional polarization changes on refraction through this boundary. In order to eliminate this undesired effect, the polarization state measurements in the transmission regime were performed by illuminating the samples at normal incidence from the back surface of the silica substrate first as illustrated in Fig. 6.4. In this way, the incident beam will pass through the silica substrate first and only interact with patterned Si_3N_4 or SiO_2 films as it is transmitted from the sample. This ensures that the measured polarization changes are entirely due to the interaction of the light beam with the chiral patterned Si_3N_4 or SiO_2 layers and are not modified by any subsequent refraction process. All the definitions of the polarization parameters, including ellipticity, η, input polarization azimuth, ϕ_0, and polarization azimuth rotation, $\Delta\phi$, are defined in Table 5.2 in the previous chapter. The polarization state of each transmitted beam is defined by its polarization azimuth (ϕ) and ellipticity (η), with ϕ being measured in an anticlockwise direction from the vertical as viewed by an observer looking directly into the beam.

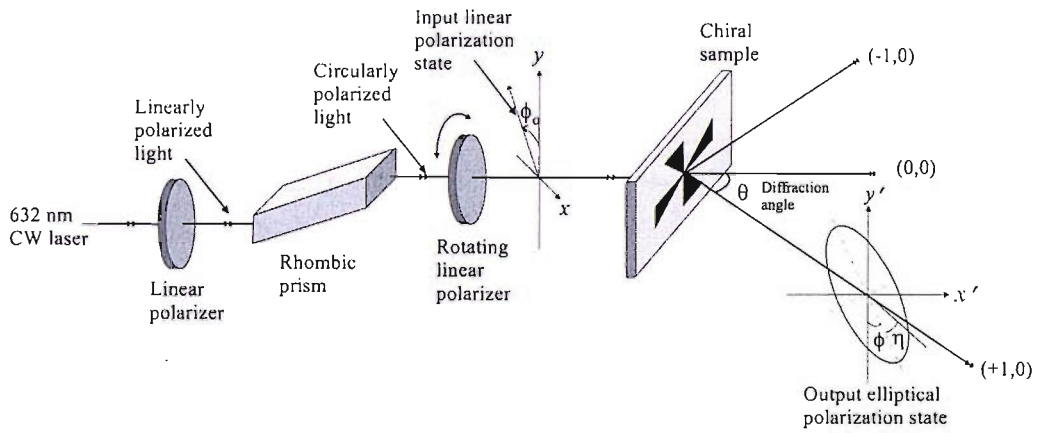

Figure 6.4: Experimental arrangement used to characterize the optical activities of the dielectric planar chiral metamaterials in the transmission regime (Θ, η and ϕ are defined in Table 5.2 in the previous chapter).

6.3.3 Optical activity of loss-less silicon nitride chiral metamaterials

Enantiomeric Symmetry Transformation

The first experiment was performed on wafer 3 in the transmission configuration at normal incidence. The sample consists of different arrays of nanoscale structures that were etched into a 320 nm thick Si_3N_4 layer deposited on a fused silica substrate. An enantiomeric pair of arrays of gammadion-shaped holes (BA42 and BA45) with opposite bending angles ($\alpha = \pm 45°$) but with identical pitch size ($\Lambda = 5.0$ μm), the characteristic arm length ($\xi = 1.8$ μm) and the line width ($w = 200$ nm) were studied first. The polarization response of these enantiomeric structures at different input polarization states, ϕ_0, was investigated and plotted in Fig. 6.5. The figure clearly shows that as the polarization azimuth of the input beam is rotated about the beam direction, the polarization states of both the (+1,0) and the (-1,0) diffraction orders vary from that of the input beam. Additionally, Fig. 6.5 shows that not only strong rotations of the polarization azimuth, but significant elliptization of the output beams is also observed. The magnitude of the change to the output polarization azimuth, $\Delta\phi$, and the induced ellipticity, η, are both strongly dependent on the input polarization azimuth, ϕ_0.

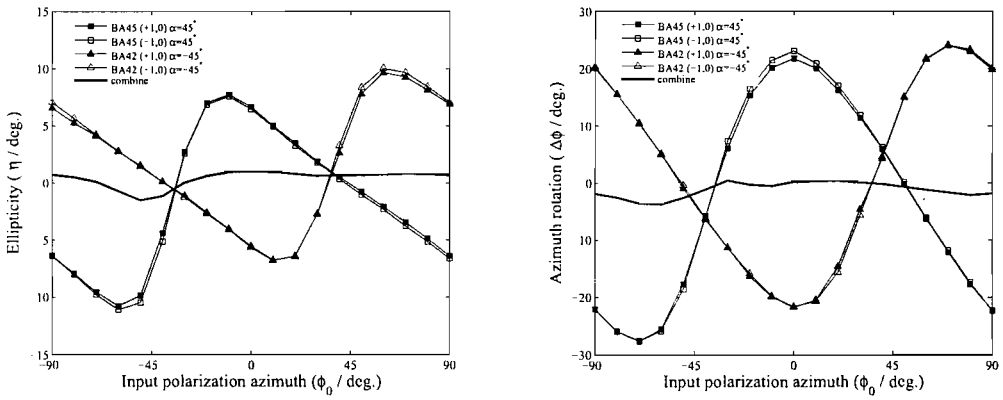

(a) (b)

Figure 6.5: The polarization changes for the first-order diffracted beams transmitted from enantiomeric arrays of gammadion-shaped holes etched in a 320 nm thick Si_3N_4 film when illuminated with 632 nm linearly polarized light at normal incidence. The solid lines represent a plot of Eqn. 6.3 and Eqn. 6.4 respectively for the case (i=1, j=0) (ϕ_0, η and $\Delta\phi$ have the same definitions as shown in Table 5.2 in the previous chapter).

The results depicted in Fig. 6.5 illustrate two clear trends of behaviour. Firstly, the identical diffraction orders from opposite chiral enantiomers appear to produce

different optical responses. Secondly, opposite diffraction orders from the same enantiomer give almost identical responses. This is believed to represent significant evidence of the influence of planar chirality in determining the form of the polarization response of these structures. If the behaviour of the polarization azimuth rotation, $\Delta\phi$, and the induced ellipticity, η, were due to asymmetry in the experimental configuration, then the opposite diffraction orders might be expected to produce different results from the same sample, while opposite enantiomers would elicit the same response for the same diffraction order. However, this is not observed in Fig. 6.5.

The different polarization changes exhibited by opposite enantiomers can be explained by the application of mirror symmetry (parity) to the experimental configuration for one enantiomer to generate a corresponding experimental arrangement for the opposite enantiomeric structure. The theoretical principle underpinning this approach can be found in the expected invariance of Maxwell's equations under parity inversion (P-symmetry), and hence also the invariance of the light-matter interaction under the same transformation. Consequently, if the measured polarization change for a diffraction order (i,j) from a left-handed structure is $(\Delta\phi,\eta)$ when that structure is illuminated with linearly polarized light of azimuthal orientation, ϕ_0, then P-symmetry invariance implies that the opposite diffraction order $(-i,-j)$ from a right-handed structure illuminated with linearly polarized light of the opposite orientation, $-\phi_0$, will exhibit an opposite polarization change $(-\Delta\phi,-\eta)$, as schematically illustrated in Fig. 6.6. A comparison of scenarios (a) and (c) indicates that the polarization response of the opposite diffraction order from the opposite enantiomer is opposite $(-\phi,-\eta)$ for the opposite linearly polarized input polarization state $(-\phi_0,0)$. In terms of the data in Fig. 6.5, this implies that the polarization data for opposite diffraction orders from opposite enantiomers can be interchanged simply by rotating one set of data by 180° about the origin of the graph. This can be expressed mathematically as:

$$\Delta\phi_{i,j}^{(R)}(\phi_0,\beta) = -\Delta\phi_{-i,-j}^{(L)}(-\phi_0,-\beta) \tag{6.1}$$

and

$$\eta_{i,j}^{(R)}(\phi_0,\beta) = -\eta_{-i,-j}^{(L)}(-\phi_0,-\beta) \tag{6.2}$$

where R and L refer to right-handed and left-handed structures respectively; β is the angle of incidence for light impinging on the sample. Parity invariance can then be tested by defining a pair of combined function for the polarization azimuth rotation and the ellipticity as:

$$\Delta\phi_{i,j}^{(S)}(\phi_0,\beta) = \Delta\phi_{i,j}^{(R)}(\phi_0,\beta) + \Delta\phi_{-i,-j}^{(L)}(-\phi_0,\beta) \tag{6.3}$$

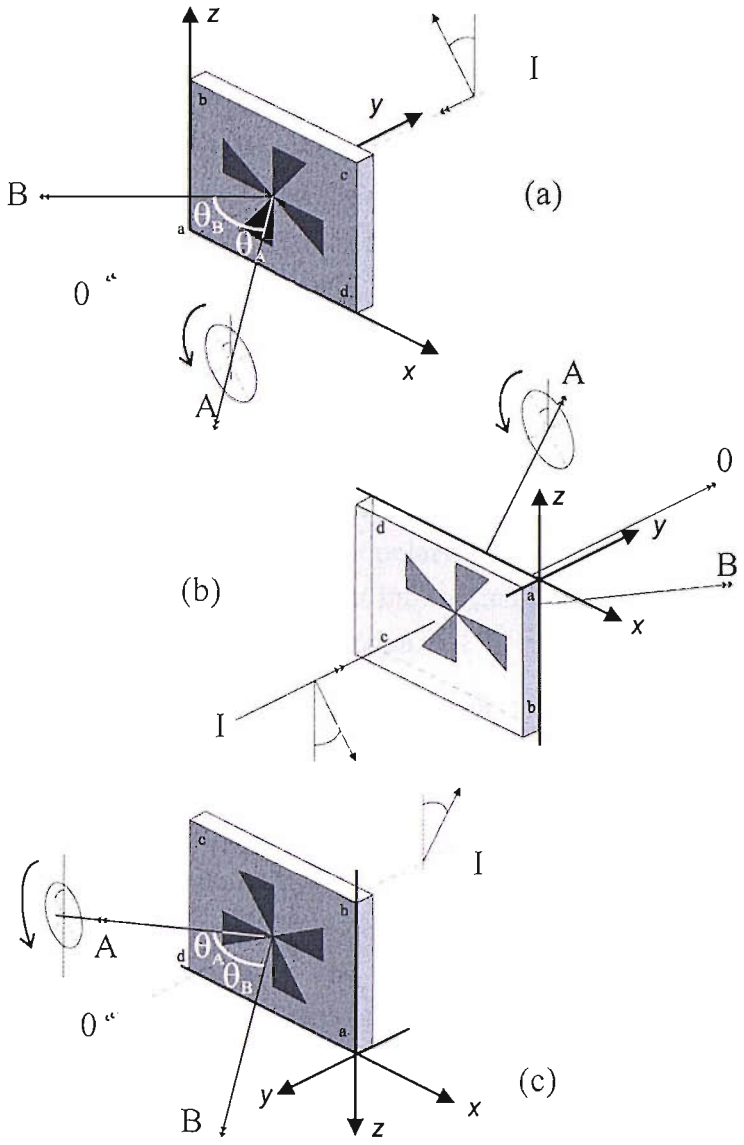

Figure 6.6: The effect of a parity transformation on relating the polarization response of opposite chiral enantiomers. (a) Initial experimental arrangement showing the incident beam (I) and various diffracted beams including the zero-order beam (O). (b) after parity inversion. (c) after a 180° rotation of the observers viewpoint about the x-axis.

and

$$\eta_{i,j}^{(S)}(\phi_0, \beta) = \eta_{i,j}^{(R)}(\phi_0, \beta) + \eta_{-i,-j}^{(L)}(-\phi_0, \beta) \tag{6.4}$$

For example, for the first-order diffracted beam, (+1,0) at normal incidence illumination, Eq. 6.3 and Eq. 6.4 become:

$$\Delta\phi_{1,0}^{(S)}(\phi_0, 0) = \Delta\phi_{1,0}^{(R)}(\phi_0, 0) + \Delta\phi_{-1,0}^{(L)}(-\phi_0, 0) \tag{6.5}$$

and

$$\eta_{1,0}^{(S)}(\phi_0, 0) = \eta_{1,0}^{(R)}(\phi_0, 0) + \eta_{-1,0}^{(L)}(-\phi_0, 0) \tag{6.6}$$

If the light interaction with these planar chiral structures is invariant under parity transformation, it is expected that the polarization effects observed from opposite enantiomers for opposite input values of β and ϕ_0 should cancel. Consequently the symmetric functions $\Delta\phi_{+1,0}^{(S)}(\phi_0, 0)$ and $\eta_{+1,0}^{(S)}(\phi_0, 0)$, defined by Eq. 6.5 and Eq. 6.6, are expected to be zero for all values of ϕ_0. In order to test this hypothesis, the functions are plotted by substituting the corresponding data measured from the enantiomeric gammadion pair (BA42 and BA45), as shown in Fig. 6.5 (solid-line). The resulting excellent degree of cancelation of the polarization changes from opposite chiral structures provides further compelling evidence that the planar chirality is the primary feature responsible for the polarization effects observed. It also confirms the hypothesis that the light-matter interaction for these structures is a linear effect that is invariant under parity inversion.

The second striking property of the data in Fig. 6.5 is the apparent equivalence of opposite diffraction orders from the same enantiomer. At first sight this appears more curious than the behaviour of opposite chiral structures, particularly given that the experimental arrangement in its totality is of mixed symmetry (the sample is asymmetric while the configuration of the opposite diffraction orders is symmetric). However, this result can be explained by applying rotational symmetry operations to both the experimental configuration and the input beam independently as demonstrated in Fig. 6.7. Successive rotations of 180° applies first to the view point of the observer (Fig. 6.7(b)), and then to the input polarization state (Fig. 6.7(c)). This results in an inversion of the sample and a swapping of the polarization states for opposite diffraction orders. If the sample also possesses four-fold rotational symmetry, the sample can then be rotated back by 180° to its original position without perturbing the output states of the diffracted beams (Fig. 6.7(d)). A comparison of the scenarios Fig. 6.7(a) and Fig. 6.7(d) indicates that the experimental arrangement in each case is identical, so that the opposite diffraction orders must also be identical.

Since the chiral gammadion structures possess a four-fold rotational symmetry and the incident beam is normal to the sample, the consequence of the two symmetry rotations, as illustrated in Fig. 6.7, is to leave the input configuration of the system unchanged while swapping over the output diffraction orders. This then implies that the output polarization states must also be unaffected by this combination of symmetry operations, and hence the two diffraction orders must have identical polarization states. This is a useful result as it provides a critical test of non-uniformity for the samples fabrication as well as the experimental arrangement. Any

discrepancy in the polarization output observed in the (-1,0) and (+1,0) diffraction orders must be due to sample imperfections or inaccuracies in the optical alignment of the system. Therefore, with such data it is possible to estimate the (minimum) experimental error inherent in the optical system. From the data in Fig. 6.5, it can be seen that this error is less than 1° for both polarization azimuth rotation angle, $\Delta\phi$, and the induced ellipticity, η.

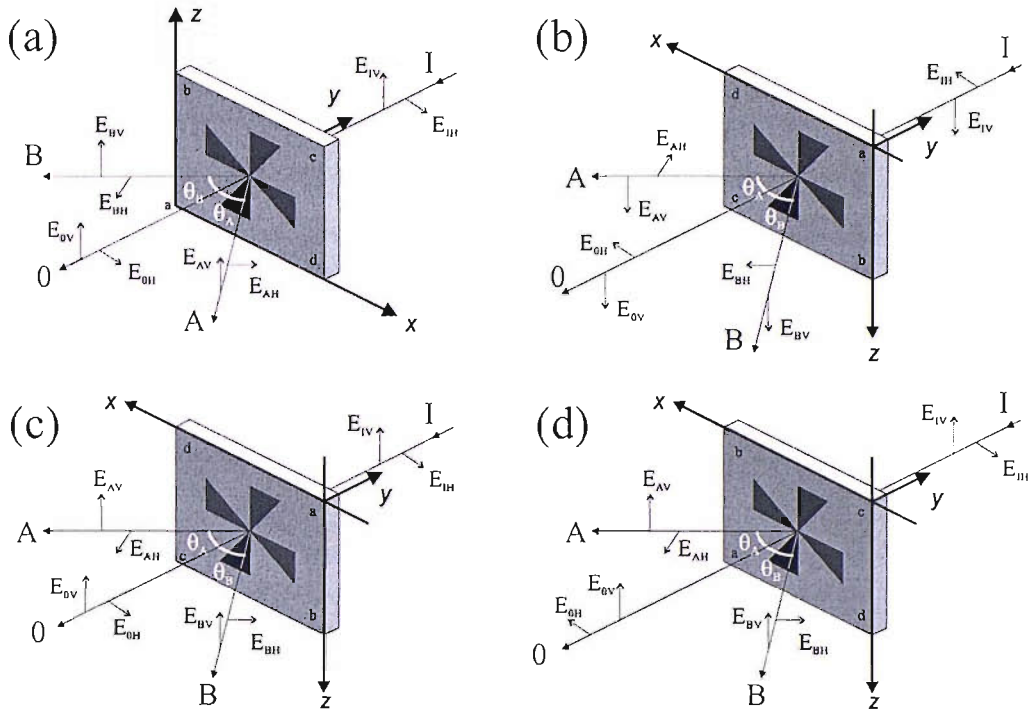

Figure 6.7: The role of rotational symmetry in defining the equivalence of opposite diffraction orders from a sample possessing two-fold rotational symmetry. (a) Initial experimental arrangement showing the incident beam (I) at normal incidence to the sample and two diffracted beams, A and B. (b) After a 180° rotation of the observers viewpoint about an axis normal to the sample. (c) After the input polarization state is rotated by 180° about the beam axis. (d) After the sample is rotated by 180° about the beam axis.

The data in Fig. 6.5 indicate that the polarization response from opposite enantiomers appears to be reversed in accordance with the predictions of parity inversion. Therefore, it is expected that a symmetric structure, such as an array of crosses (+), may produce no polarization response. As a consequence, the polarization response of an array of simple crosses (BA41) on wafer 3 was measured at normal incidence using the same optical arrangement as shown in Fig. 6.4. The measured results are plotted in Fig. 6.8, which shows that the first-order diffracted beams transmitted through the array of achiral cross-shaped holes etched in the Si_3N_4 film show very small degree of polarization rotation and elliptization compared to the polarization changes observed in the chiral gammadions. This significantly smaller polarization

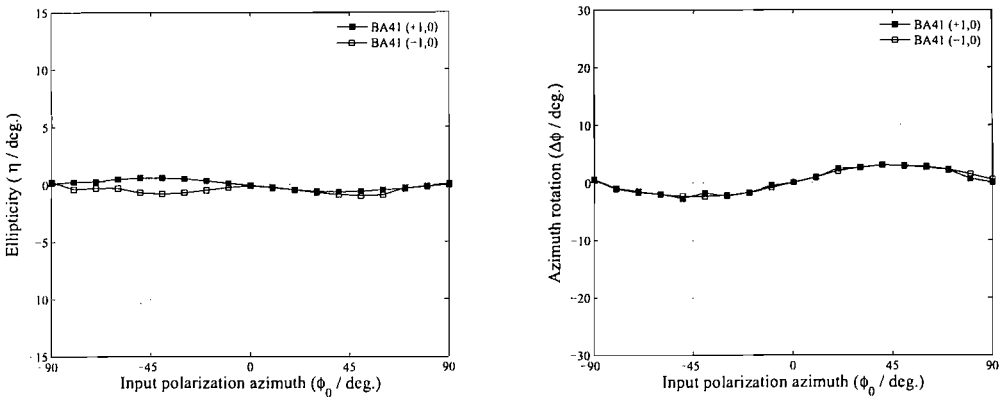

Figure 6.8: The polarization changes for the first-order diffracted beams transmitted through an array of achiral cross-shaped holes etched in a 320 nm thick Si_3N_4 film when illuminated with 632 nm linearly polarized light at normal incidence.

change observed in achiral symmetric crosses is perceived as birefringence in the sample. By comparing the results from arrays of asymmetric chiral gammadions (Fig. 6.5) with those from achiral arrays of symmetric crosses of similar size and periodicity (Fig. 6.8), it can be seen that the polarization changes for each chiral sample are due to a mixture of 2D chirality and perceived birefringence.

Chiral Geometry

In the previous chapter, the optical response of the metallic planar chiral surface (including both the Ti/Au/Ti and the Al chiral samples) was shown to be influenced by the shape of the chiral elements on the surface and by their degree of chirality. It was observed that light rays diffracted from gammadion-shaped holes with bending angles of ±45° exhibited greater changes to their polarization states than light diffracted from similar sized gammadion features with $\alpha = \pm 90°$ and $\alpha = \pm 135°$. In order to investigate if a similar polarization response can be observed from dielectric planar chiral surface, the polarization response of two pairs of enantiomeric chiral gammadion arrays (BA42 and BA45, BA43 and BA44 on wafer 3) with bending angles, $\alpha = \pm 45°$ and $\pm 90°$ respectively, were measured. Fig. 6.9 presents the ellipticity, η, and the polarization azimuth rotation angle, $\Delta\phi$, of the first-order transmitted beams through these gammadion-shaped chiral gratings. It clearly shows that gammadion arrays with bending angles of $\alpha = \pm 45°$ generate significantly larger changes to the polarization state of the (+1,0) diffracted beams than those seen for arrays with $\alpha = \pm 90°$. This suggests that the optical response from these all-dielectric structures exhibits a similar form of dependence on the gam-

madion bending angle, α, as was observed for the metallic planar chiral structures studied in the previous chapter.

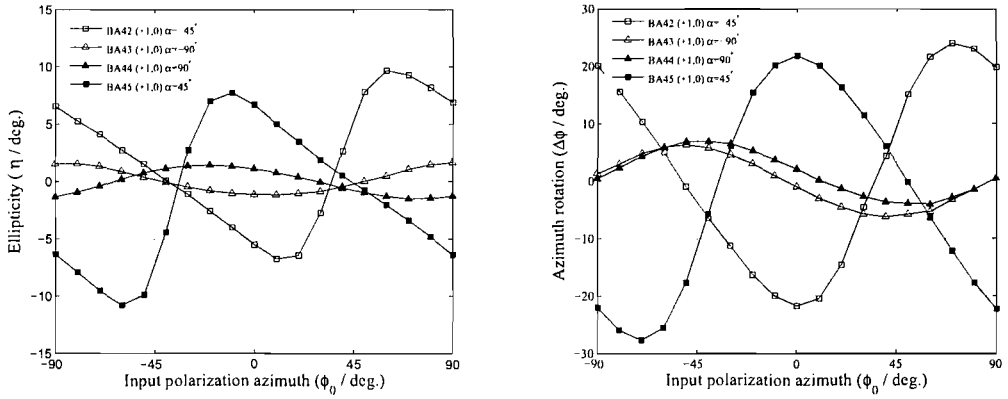

(a) (b)

Figure 6.9: A comparison of the polarization changes for the (+1,0) order diffracted beam transmitted through arrays of gammadion-shaped holes with different bending angles etched in a 320nm thick Si_3N_4 film when illuminated with 632 nm linearly polarized light at normal incidence.

Additionally, it is clear from the data in Fig. 6.9 that changes to the bending angle of the gammadions do more than govern the magnitude of the overall polarization changes. They also significantly modify the conditions under which the polarization changes are maximized. For example, the values of the input polarization azimuth, ϕ_0, at which the greatest change in polarization azimuth is detected for gammadions with $\alpha = +45°$ (BA45) is significantly different from that seen when $\alpha = +90°$ (BA44). This suggests that the dependence of the maximum and minimum polarization changes on the input polarization state, ϕ_0, is strongly influenced by the shape of the individual diffracting elements on the surface of the metamaterial, and hence by the degree of 2D chirality. This provides further evidence that the polarization modulating properties of these metamaterials are mostly due to the presence of 2D chirality.

Complementarity

In this section, the polarization responses of complementary planar chiral structures are studied. Complementary planar chiral structures are structures fabricated from identical materials such that if they were superimposed, they would combine to form a uniform featureless surface. In this instance this means fabricating one structure that consists of an array of gammadion-shaped holes in a Si_3N_4 film (wafer 3), and a second structure that consists of free-standing gammadion-shaped Si_3N_4 mesas

(wafer 4) on a silica substrate. For the comparative purpose, it is essential that the gammadion features of both structures are identical, which means that the gammadion arrays have the same pitch size (Λ), characteristic arm length (ξ), line width (w) and bending angle (α). Similarly, it is equally essential that the Si_3N_4 layers on both substrates are of equal thickness. However, it is very likely that there is some disparity in the final line-width for the two structures due to the different exposure and development conditions of the two resists employed in EBL process used on the two wafers. This disparity is then further exacerbated by the RIE process which is also highly dependent on both the chemical nature of the resist used to mask the substrate and the relative proportions of resist-covered and uncovered areas of the substrate.

Fig. 6.10 shows the polarization response of the first-order diffracted beams transmitted through these complementary chiral structures. It clearly shows that the polarization response of the Si_3N_4 gammadion mesas (wafer 4) is very similar to that of the gammadion-shaped holes (wafer 3). This result is a striking manifestation of the principle of superposition as it applies to the far field (Fraunhofer) diffraction regime. According to the *Babinet's principle* [5], when adding two complementary diffraction screens together, a non-diffracting unpatterned thin film of uniform thickness is generated. Thus, the diffracted field from one patterned Si_3N_4 screen should cancel with that of its complementary relative (with the exception of the zero-order beams which of course do not cancel). However, this cancellation can only happen if equivalent diffraction orders from complementary screens have identical amplitudes and polarizations, but opposite phases. Therefore, the phases generated in the first-order diffracted beam from the complementary planar chiral metamaterials must be the same due to the fact that their polarization response do not cancel, as shown in Fig. 6.10. This implies that the diffraction process for these Si_3N_4 planar chiral structures is linear, and that phase coherence is preserved throughout the process.

Film Thickness

One of the principal attractions of planar chiral metamaterials is their planarity. Not only does this property offer the potential for these structures to be used as optical coatings that can be applied to a large range of existing optical components, it also suggests that such structures can be patterned directly into the existing surfaces of these components without the need for the addition of supplementary thin films that may have other less desirable optical properties. Whether or not this is indeed the case, it suggests that the depth to which the chiral pattern is etched, and the choice of material for the patterned surface, can both strongly influence the strength

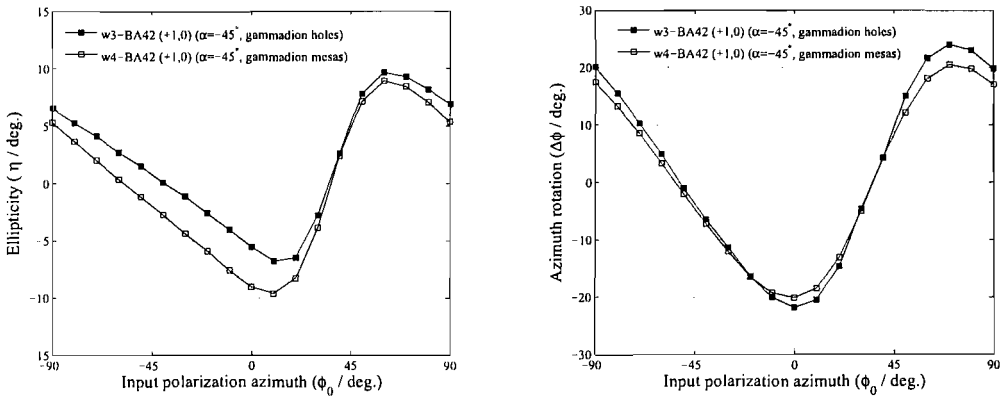

(a) (b)

Figure 6.10: A comparison of the polarization changes for the (+1,0) diffracted beam transmitted through two complementary Si_3N_4 planar chiral structures when illuminated with 632 nm linearly polarized light at normal incidence.

of the resulting polarization effect.

The polarization change due to arrays of gammadion-shaped holes etched into a Si_3N_4 layers of three different thicknesses: 80 nm (wafer 5), 160 nm (wafer 2), and 320 nm (wafer 3), is studied in this section. In each case the etch depth of the gammadion-shaped holes is equal to the thickness of the deposited Si_3N_4 layer, so that the etching depth is deep enough to reveal the underlying silica substrate. The same design of chiral gammadion array (BA42), with a bending angle, α = -45°, a pitch size, Λ = 5.0 μm, and a characteristic arm length, ξ = 1.8 μm, is characterized for each wafer. The results of the polarization changes observed from these three gammadion-shaped arrays with different Si_3N_4 thickness are presented in Fig. 6.11. It clearly shows that for all three thicknesses of Si_3N_4, strong polarization changes in the (+1,0) diffracted beam are observed. The magnitude of the polarization change is clearly dependent on the thickness of the Si_3N_4 film, but on the other hand, it is also apparent that the input polarization azimuth, ϕ_0, where the polarization changes are greatest, remain relatively unchanged as the film thickness is varied. This suggests that the thickness of the Si_3N_4 layer is an important factor in determining the magnitude of the polarization change induced by these chirally patterned films, but plays a significantly smaller role in determining the polarization response.

For comparison, a number of arrays of chiral gammadion-shaped holes etched directly into the fused silica substrate were also fabricated. A range of different etch depths for the chiral patterns etched into the uncoated surface of the fused silica wafers were chosen. These various etch depths include: 170 nm, 340 nm and 690

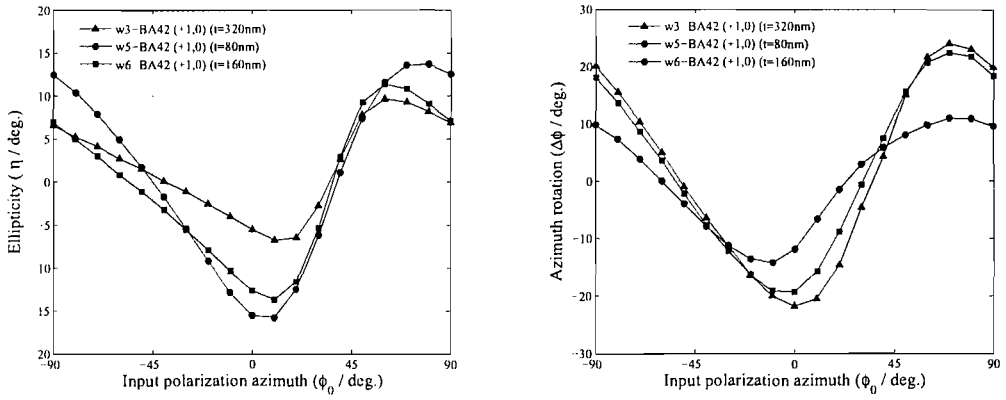

(a) (b)

Figure 6.11: A comparison of the polarization changes for the (+1,0) diffracted beam transmitted through arrays of gammadion-shaped holes with different thicknesses of Si_3N_4 when illuminated with 632 nm linearly polarized light at normal incidence.

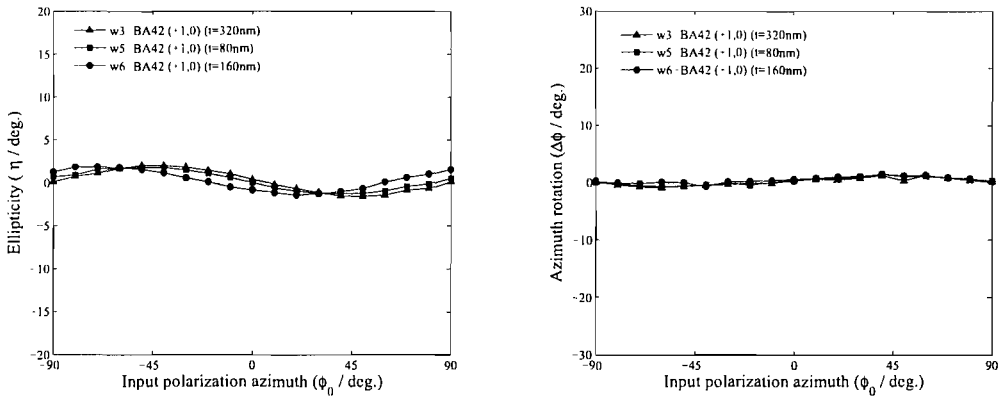

(a) (b)

Figure 6.12: A comparison of the polarization changes for the (+1,0) diffracted beam transmitted through arrays of gammadion-shaped holes etched directly into the silica substrate with different etch depths when illuminated with 632 nm linearly polarized light at normal incidence.

nm. The polarization response of the same chiral gammadion array (BA42) on these chiral samples was characterized individually in the same manner as the characterization of silicon nitride chiral samples. The results are plotted in Fig. 6.12. In contrast to the results shown in Fig. 6.11, none of the first-order diffracted beams from the achiral patterned silica substrates showed any significant change in polarization state with input polarization states when these structures were illuminated at normal incidence. The very small ellipticity and polarization azimuth that are exhibited are caused by the birefringence as seen in the achiral silicon nitride crosses discussed previously in this chapter. These results appear to demonstrate that the

presence of a thin surface film (comparable in thickness to the wavelength of the incident radiation) is critical for the operation of planar chiral metamaterials. As this implies that (a minimum of) two closely spaced interfaces between media of different refractive indices are necessary for these polarization effects to be observed. It suggests that the polarization changes are a consequence of combined multiple interference effects in the thin film in which the planar chiral structures are created and birefringence. The multiple interference, when combined with the chiral patterning of the film, results in different phases and amplitudes for the vertical and horizontal polarization components for the diffracted beams, and hence a change in the ellipticity. This in turn suggests that quantum interference in a Fabry-Perot type of optical cavity may be an essential ingredient of these loss-less all-dielectric structures, with the etched chiral pattern providing the entry point by which light is coupled into, and diffracted out of, the cavity.

6.4 Discussions

6.4.1 Transfer matrix

Based on the above experimental polarization measurements implemented on silicon nitride planar chiral metamaterials, a semi-empirical model was created by Potts. *et al.* [84]. In this model, a transfer matrix, $\mathcal{A}$, is first calculated. In order to calculate the 2×2 transfer matrix for a given propagation channel through planar chiral metamaterials, it is first assumed that the system is linear, and the principle of superposition holds true. The validity of this assumption can be determined by the success, or otherwise, of the resulting transfer matrix in accurately predicting the polarization response for that propagation channel for all other possible input polarization states in addition to those used to derive the component s of the transfer matrix. Therefore, if the predictions of the transfer matrix agree with the experimental data, then the initial assumption is valid. Provided that this is the case, then only three independent polarization measurements are required in order to determine the four elements of the transfer matrix. For simplicity it is preferable to perform those measurements using three separate linearly polarized input states, with each having a different polarization azimuth. The first two chosen polarization states have azimuthal angles of ϕ_0 = 0° and ϕ_0 = -90° as these correspond to the y- and x-directions of the calibrated coordinate system respectively, while the third is chosen to be a linear superposition of the first two (ϕ_0 = -40°). Therefore, the

transfer matrix can be expressed mathematically as [84]:

$$\mathcal{A} = \begin{bmatrix} 1 & -Z_0 Z_2 \\ Z_1 & Z_0 \end{bmatrix} \tag{6.7}$$

in which the characteristic Z-parameter $Z_i = r_i \exp i\delta_i$. r_i and δ_i represent the amplitude and the phase of the three chosen polarization measurements (ϕ_0 = 0°, -90° and -40° respectively). The parameter Z_0 is determined by Z_1, Z_2 and Z_3 together.

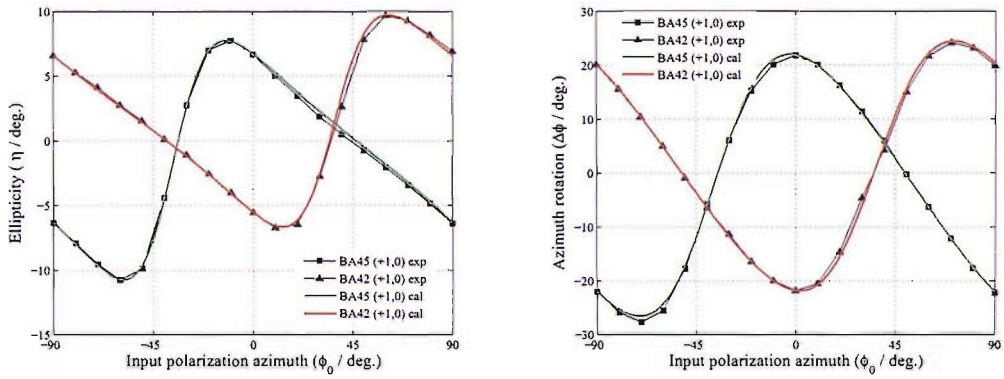

(a) (b)

Figure 6.13: The experimental and theoretical predictions of the polarization changes for the first-order diffracted beams transmitted from enantiomeric arrays of gammadion-shaped holes etched in a 320 nm thick Si_3N_4 film when illuminated with 632 nm linearly polarized light at normal incidence.

In order to test the validity of this semi-empirical model, theoretical data for the polarization response of the Si_3N_4 chiral samples (BA42 and BA45) analysed in above sections is generated. There experimental data points corresponding to input polarization azimuths of ϕ_0 = 0°, ϕ_0 = -40° and ϕ_0 = -90° in Fig. 6.5 were used to fit in the theoretical model. These calculated polarization changes, including ellipticity and polarization azimuth rotation angle are plotted with the experimental results in Fig. 6.13 for the purpose of comparison. The figure clearly shows that the calculated curves agree with the experimental data points to an accuracy of better than 0.5°. This level of agreement between the calculated predictions based on the transfer matrix and the experimental data clearly validates the initial assumptions regarding the postulated linearity of the optical properties of the planar chiral structures and the applicability of the principle of superposition. This also proves the accuracy of the experimental works carried out in this work. Therefore, the transfer matrix provides the chance to predict the polarization response of the planar chiral metamaterial system for all possible input polarization states, and therefore to completely map the parameter space. Further details of the transfer matrix derivation

are provided in **Appendix C**.

6.4.2 The polarization eigenstates

Once the necessary elements of the transfer matrix, $\mathcal{A}$, have been determined, calculation of the polarization eigenstates of the diffraction channel can proceed [84]. Each eigenstate can be defined by a Jones vector $\mathbf{J}_\sigma$ with a characteristic Z-parameter of Z_σ such that the input and output polarization states for the diffraction channel are identical, although the two states will in general have different amplitudes and phases. Thus the eigen equation will be:

$$\mu_{\sigma\sigma}\mathbf{J}_\sigma = \mathcal{A}\mathbf{J}_\sigma \tag{6.8}$$

where $\mu_{\sigma\sigma}$ is the associated eigenvalue that dictates the relative amplitude and phase of the output state. From the matrix equation:

$$\mu_{\sigma\sigma}\begin{bmatrix} 1 \\ Z_\sigma \end{bmatrix} = \begin{bmatrix} 1 & -Z_0Z_2 \\ Z_1 & Z_0 \end{bmatrix}\begin{bmatrix} 1 \\ Z_\sigma \end{bmatrix} \tag{6.9}$$

Z_σ can be determined by eliminating $\mu_{\sigma\sigma}$ from the two simultaneous equations to yield the quadratic form:

$$Z_0Z_2Z_\sigma^2 + (Z_0 - 1)Z_\sigma + Z_1 = 0 \tag{6.10}$$

the solution to which is:

$$Z_\sigma = r_\sigma e^{i\delta_\sigma} = \frac{1 - Z_0 \pm [(1 - Z_0)^2 - 4Z_0Z_1Z_2]^{\frac{1}{2}}}{2Z_0Z_2}. \tag{6.11}$$

From the parameters r_σ and δ_σ the ellipticity (η_σ) and the azimuthal angle (ϕ_σ) of the polarization eigenstate can be determined by the relations:

$$\sin(2\eta_\sigma) = \frac{2r_\sigma \sin(\delta_\sigma)}{r_\sigma^2 + 1} \tag{6.12}$$

and

$$\tan(2\phi_\sigma) = \frac{2r_\sigma \cos(\delta_\sigma)}{r_\sigma^2 - 1} \tag{6.13}$$

Furthermore, one of the clearest and most illustrative methods of determining the orthogonality of two polarization states is by considering their representation as

three-dimensional Stokes vectors $\mathbf{S} = (S_1,S_2,S_3)$ where the three components of the vector are the Stokes parameters for the polarization state (ϕ,η) given by:

$$S_1 = \cos(2\eta)\cos(2\phi) \tag{6.14}$$

and

$$S_2 = -\cos(2\eta)\sin(2\phi) \tag{6.15}$$

and

$$S_3 = \sin(2\eta). \tag{6.16}$$

The two polarization eigenstates for a particular diffraction channel, J_a and J_b, will be orthogonal if the angle (Θ) between their respective Stokes vectors $\mathbf{S}_a$ and $\mathbf{S}_b$ in the three-dimensional Stokes parameter space is 90°. As the Stokes vectors are unit vectors, this angle can be determined by the scalar product of the Stokes vectors:

$$\cos(\Theta) = S_1^{(a)}S_1^{(b)} + S_2^{(a)}S_2^{(b)} + S_3^{(a)}S_3^{(b)} \tag{6.17}$$

The deviation of these two Stokes vectors can then be quantified from total orthogonality by the supplementary angle $\Delta\Theta = 180° - \Theta$.

Based on this theoretical model, the two polarization eigenstates, J_a (ϕ_a,η_a) and J_b (ϕ_a,η_a), for the first-order diffracted beams transmitted through various asymmetric planar chiral structures as well as achiral symmetric simple crosses fabricated in thin films of Si_3N_4 of different thicknesses (as described at the beginning of this chapter) when each structure is illuminated at normal incidence from the substrate side of the sample can be calculated. The calculated polarization eigenstates for each sample are shown in Table 6.4.

From the data in Table 6.4 it can be seen that the symmetric structures (crosses) have symmetric eigenstates, while the asymmetric chiral gammadion structures have asymmetric eigenstates. Additionally, the opposite enantiomers (BA42 and BA45) have opposite eigenstates. Therefore, the polarization changes due to 2D chirality from those due to birefringence can be distinguished by the polarization eigenstates of the system in each case. This provides further evidence to the fact that the polarization changes observed in the arrays of symmetric crosses are due to birefringence and so the eigenstates are symmetric, while the polarization changes for arrays of chiral gammadions are due to 2D chirality and so the eigenstates are asymmetric and opposite for opposite structures. Moreover, comparing to the azimuthal angles (ϕ_a and ϕ_b) of the eigenstates in each chiral gammadion grating with the same geometry (BA42 and BA45), it shows that changes to the thickness of the Si_3N_4 film have a profound effect on the ellipticity of the two eigenstates, η_i, rather than their

Wafer	Chiral grating	Si_3N_4 film thickness (nm)	Bending angle (°)	ϕ_a (°)	η_a (°)	ϕ_b (°)	η_b (°)	non-orthogonality $\Delta\Theta$ (°)
3	BA41(+1,0)	320	–	0	0	90	0	0
3	BA42(-1,0)	320	-45	35.09	-1.12	-50.24	2.59	9.78
3	BA42(+1,0)	320	-45	35.01	-0.43	-50.80	2.60	9.41
3	BA45(-1,0)	320	45	-34.87	0.99	50.26	-1.17	9.74
3	BA45(+1,0)	320	45	-34.92	0.58	49.25	-0.73	11.65
3	BA43(-1,0)	320	-90	85.52	-7.37	-4.87	-6.7	28.15
3	BA43(+1,0)	320	-90	84.13	-5.86	-5.45	-5.46	22.65
3	BA44(-1,0)	320	90	-89.89	9.41	12.12	4.36	36.31
3	BA44(+1,0)	320	90	-91.04	6.53	12.83	4.02	34.71
5	BA42(-1,0)	80	-45	35.42	6.6	-54.01	7.05	27.31
5	BA42(+1,0)	80	-45	35.58	6.49	-53.75	7.34	27.63
5	BA45(-1,0)	80	45	-35.31	-5.15	56.46	-8.69	27.90
5	BA45(+1,0)	80	45	-35.35	-5.59	56.62	-9.11	29.66
6	BA42(+1,0)	240	-45	32.79	3.40	-54.26	-0.38	8.43
6	BA45(+1,0)	240	45	-28.97	-2.11	56.23	0.09	10.42

Table 6.4: Calculated polarization eigenstates for the first-order transmitted beams from achiral symmetric structures and various asymmetric planar chiral structures fabricated in thin films of Si_3N_4 of different thicknesses when each structure is illuminated at normal incidence.

azimuthal angle, ϕ_i. It is these variations in ellipticity that appear to be the main factor in contributing to non-orthogonality in the eigenstates, J_a and J_b, as defined by the parameter $\Delta\Theta$. However, when the geometry of the chiral gammadions is changed (BA43 and BA44), these chiral samples have different eigenstates (both ellipticity and azimuthal angle are changed) compared to BA42 and BA45 for the same wafer.

6.5 Summary of results

Table 6.5 summarizes the magnitudes of the polarization changes observed from different dielectric samples with various planar chiral structures studied in this chapter. The table shows that the optical response of structures is reversed when the sense of chirality of the surface is reversed; this indicates that the polarization response is due to the microscopic chiral patterning of the sample surface. By performing identical experiments on pairs of chiral gammadions with opposite handedness, it has

been shown that the polarization changes reverse in a manner consistent with mirror symmetry (or parity inversion), whereas performing the mirror-reflected experiment on the same chiral sample (i.e. measuring the opposite diffraction orders from the same sample) yields the same polarization changes in each case. This optical activity is qualitatively similar to those of the metallic planar chiral metamaterials, despite the fundamentally different material properties.

Sample	Wafer	Film thickness (nm)	Chiral grating	Bending angle (°)	Maximum ellipticity η_{max}	Maximum polarization azimuth rotation $\Delta\phi_{max}$
UNIII	-	300	B41	-	13.2° (ϕ_0=-20°)	-9.7° (ϕ_0=0°)
			B46	-45	-12.7° (ϕ_0=20°)	8.4° (ϕ_0=10°)
Si_3N_4	3	320	BA41	-	-0.6° (ϕ_0=40°)	3.1° (ϕ_0=40°)
			BA42	-45	9.6° (ϕ_0=60°)	24° (ϕ_0=70°)
			BA43	-90	1.7° (ϕ_0=90°)	6.3° (ϕ_0=-50°)
			BA44	90	-1.5° (ϕ_0=80°)	6.9° (ϕ_0=-50°)
			BA45	45	-10.8° (ϕ_0=-60°)	-27.7° (ϕ_0=-70°)
Si_3N_4	4	320	BA42	-45	-9.6° (ϕ_0=10°)	20.5° (ϕ_0=70°)
			BA45	45	-8.4° (ϕ_0=-60°)	21.3° (ϕ_0=0°)
Si_3N_4	6	240	BA42	-45	-13.7° (ϕ_0=10°)	22.4° (ϕ_0=70°)
			BA45	45	-13.5° (ϕ_0=-60°)	-22.5° (ϕ_0=-70°)
Si_3N_4	2	160	BA42	-45	-8.3° (ϕ_0=10°)	-20.8° (ϕ_0=0°)
			BA45	45	-6.7° (ϕ_0=-60°)	20.8° (ϕ_0=0°)
Si_3N_4	5	80	BA42	-45	-15.7° (ϕ_0=10°)	-14.1° (ϕ_0=-10°)
			BA45	45	-8.4° (ϕ_0=-60°)	21.3° (ϕ_0=0°)

Table 6.5: Maximum magnitudes of polarization state modulation of (+1,0) order diffracted beams from various dielectric planar chiral metamaterials.

6.6 Conclusion

Dielectric planar chiral metamaterials have exhibited significant optical activities although there is clearly no possibility of induced currents or plasmons being part of the underlying mechanism. Strong polarization changes are observed from the first-order diffracted beams from chiral gammadion arrays in both the reflection and the transmission regimes. The optical polarization experiments have shown that changes to the geometry have similar effects on the magnitude and sense of the

polarization change of the dielectric metamaterials as they do for the equivalent metallic counterparts.

Additionally, the polarization response of dielectric planar chiral metamaterials is also shown to be dependent on the thickness of the film in which the planar chiral structures are created. However, no polarization change has been observed in identical chiral structures created directly in uncoated fused silica substrates. These results strongly suggest that the presence of a multiple reflecting surface film (or Fabry-Perot cavity) is a critical component to the optical activity of these structures. Furthermore, complementary structures appear to possess identical optical properties, which suggest that optical response is linear and is governed by the principle of superposition.

By comparing the results from arrays of chiral gammadions with those from achiral arrays of symmetric crosses of a similar size and periodicity, the polarization changes in each chiral gammadion array are seen to be a result of a mixture of 2D chirality and perceived birefringence. The two effects are distinguishable by the polarization eigenstates in each case. By analyzing the polarization change for an individual first-order diffraction beam from any sample allows a transfer matrix to be established that predicts the polarization response of the planar chiral metamaterial system for all possible input polarization states.

Two polarization eigenstates are calculated trough the transfer matrix, which indicates that for achiral structures the polarization eigenstates are linear and orthogonal, while for chiral arrays of gammadions the eigenstates are generally elliptical and non-orthogonal. Furthermore, it is shown that this non-orthogonality is primarily due to the ellipticity of the two eigenstates which is also seen to be dependent on the thickness of the chirally-patterned Si_3N_4 layer, unlike the polarization azimuth of the two eigenstates which depends only on the magnitude of the 2D chirality of the surface. The dependence of the polarization eigenstates on film thickness supports the point that the polarization changes are a consequence of phase-shifts in the Si_3N_4 layer, as a result of that occur multiple reflections and interference effects.

Chapter 7

Intensity modulation by planar chiral metamaterials

7.1 Introduction

A complete description of the state of a quasi-monochromatic wavefield requires the specification of four parameters, one for the intensity of the wave, two for the polarization state (including ellipticity and polarization azimuth angle) and one for the degree of polarization of the wave. In the previous two chapters, the polarization response of light interactions with planar chiral metamaterials at visible wavelengths has been investigated. Significant polarization changes in the higher-order diffracted beams were observed from both metallic and dielectric planar chiral metamaterials. In this chapter, a second key objective of this work, the intensity modulations induced by planar chiral metamaterials are investigated. A new device, which integrates a thin Ti layer patterned with planar chiral structures onto silicon photodiodes, was designed, fabricated and characterized to investigate the optical activity of the total transmitted beams by planar chiral metamaterials and their potential device applications.

7.2 Intensity modulation by planar chiral metamaterials

Following the same methodology used to characterize the polarization states of different planar chiral samples, the intensities of the first-order diffracted beams reflected from or transmitted by planar chiral structures were measured. A characteristic

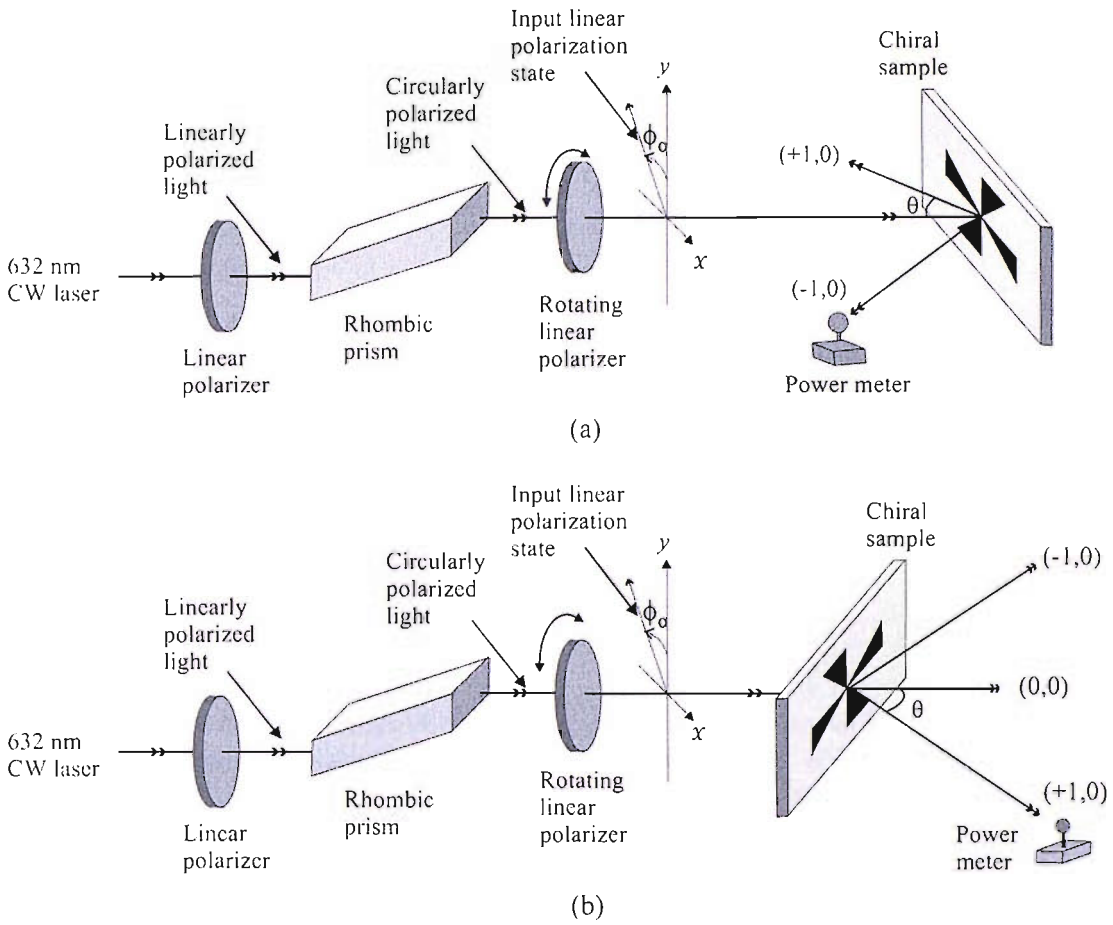

Figure 7.1: Experimental arrangement used to characterize the intensity response of the first-order diffracted beams from planar chiral metamaterials. (a) reflection regime (b) transmission regime

parameter: *Relative Intensity*, R_I, is defined as the ratio of the intensity of the diffracted beam to that of the incident beam, which is expressed mathematically by:

$$R_I = \frac{I_{ij}}{I_I} \tag{7.1}$$

where, I_I represents the intensity of the incident beam and I_{ij} represents the intensity of diffracted beam of diffraction order (i,j), where i denotes the order in the horizontal direction and j represents the diffraction order in the vertical direction. This equation is applicable in both the reflection and the transmission regimes. The intensity response was characterized by the same optical arrangement as that used to characterize the polarization responses but with the polarimeter replaced by a high resolution optical power meter. A schematic diagram of this experimental arrangement, including both the reflection and the transmission regimes, is shown in Fig. 7.1. All the characteristic parameters in Fig. 7.1 are as defined as in Table 5.2 in chapter 5..

7.2.1 Aluminium chiral metamaterials

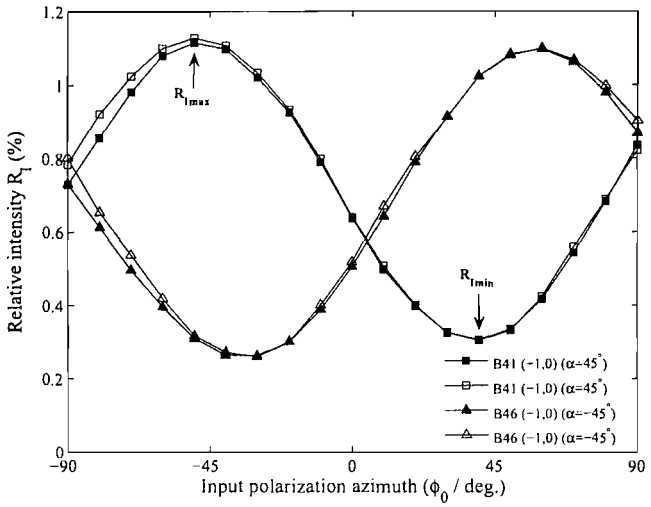

Figure 7.2: Relative intensity of the first-order diffracted beams reflected from enantiomeric arrays of chiral gammadion-shaped holes etched in a thin aluminium film when illuminated with 632 nm linearly polarized light at normal incidence. ϕ_0 represents the input polarization azimuth as defined in Table 5.2 in chapter 5.

First, the optical intensity of the first-order diffracted beams reflected from the enantiomeric pair of aluminium chiral gammadion arrays (B41 and B46) was measured as a function of the input polarization state, ϕ_0 (Fig. 7.2). Fig. 7.2 clearly shows that there is a significant oscillatory behaviour of the relative intensity with input polarization azimuth, ϕ_0, exhibited for each chiral enantiomer. The magnitude of the intensity modulation over the range of input polarization states can be defined qualitatively in two ways, including the contrast between the maximum and minimum value of the relative intensity ($\mathbb{C}$) or the amplification of the intensity modulation ($\mathbb{A}$). These two parameters can be mathematically expressed as:

$$\mathbb{C} = \frac{R_{Imax} - R_{Imin}}{R_{Imax} + R_{Imin}}(\%) \tag{7.2}$$

$$\mathbb{A} = \frac{R_{Imax}}{R_{Imin}} - 1(\%) \tag{7.3}$$

Therefore, regarding the intensity modulation observed in the aluminium chiral sample as shown in Fig. 7.2, the contrast and the amplification of the intensity modulation in the first-order diffracted beams from gammadion array B46 is about 62% and 324% respectively.

7.2.2 Polymeric chiral sample

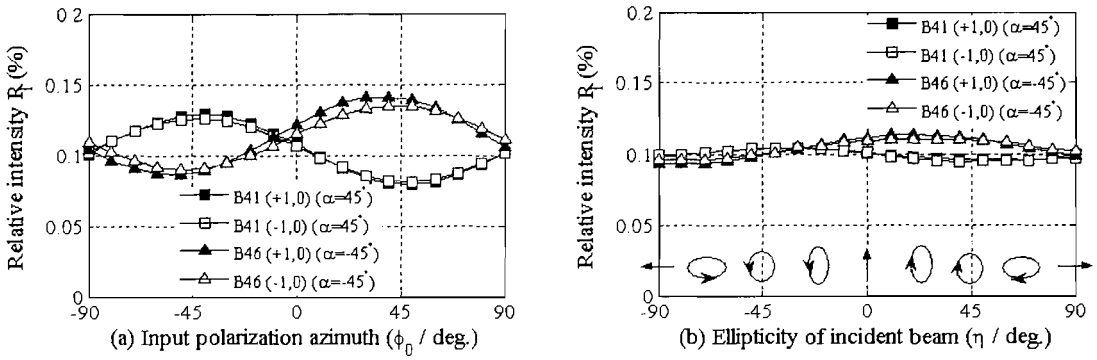

Figure 7.3: Relative intensity of the first-order diffracted beams reflected from enantiomeric arrays of gammadion-shaped holes etched in a thin polymeric UVIII resist when illuminated with 632 nm at normal incidence. (a) linearly polarized light (b) elliptically polarized light

The optical intensity of the first-order diffracted beams reflected from the enantiomeric polymeric chiral gammadion pairs (B41 and B46) were also measured. Fig. 7.3 (a) illustrates the relative intensity of the first-order diffracted beams reflected from these two polymeric chiral gratings. Using the same mathematical model, the contrast and the amplification of the intensity modulation in these diffracted beams is about 24% and 63% respectively. Comparing this intensity response of the polymeric chiral sample to that of the aluminium chiral sample shown in Fig. 7.2, it is clear that similar intensity modulation behaviour occurs. However, the average relative intensity measured from the polymeric chiral sample is much smaller than the one measured from the aluminium chiral sample. This could be due to the significant difference in the thickness of the two films (100nm aluminium and 300nm UVIII polymeric electron beam resist) in which the planar chiral structures are created. This result seems to be consistent with the significant role of the film thickness in determining the polarization response of planar chiral metamaterials as discussed in the previous chapter.

Furthermore, the intensity response of the polymeric planar chiral metamaterials with an elliptically polarized incident beam was also investigated. An extra quarter-wave plate was introduced into the experimental arrangement to generate elliptically polarized incident light with variable ellipticity and polarization azimuth. The fast axis of the quarter-wave plate was aligned vertically to the plane of incidence and was introduced in the system as shown in Fig. 7.4. By rotating this second linear polarizer, the ellipticity of the input beam was changed while leaving the polarization azimuth direction, ϕ_0, unchanged. Fig. 7.3 (b) shows the relative intensity of the first-order diffracted beams reflected from the same enantiomeric

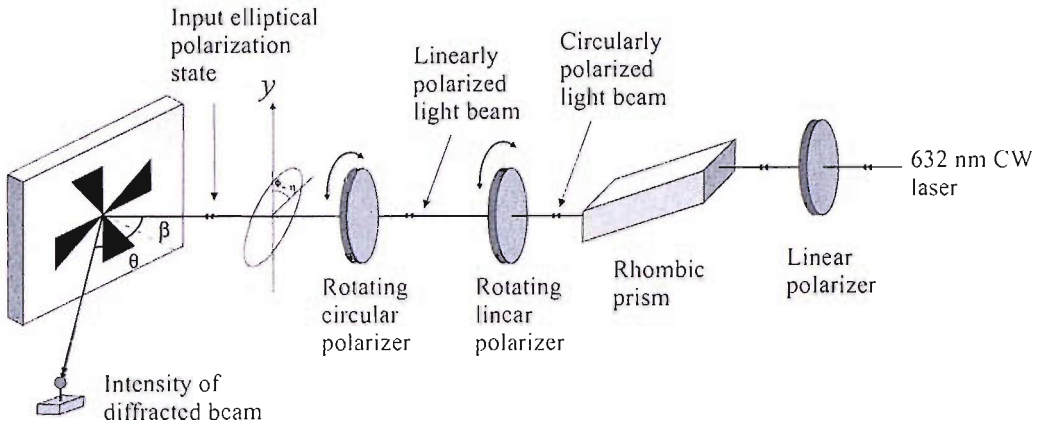

Figure 7.4: Experimental arrangement used to characterize the intensity response of diffracted beams reflected from planar chiral metamaterials with elliptically polarized light.

chiral gammadions (B41 and B46) on the polymeric sample but with elliptically polarized incident light. In contrast to the modulation of the relative intensity over the input polarization azimuth, ϕ_0, exhibited in Fig. 7.3 (a), the changes of the relative intensities of the first-order diffracted beams reflected from the same chiral gratings over different input ellipticity, η, appear to be significantly smaller. The contrast in the intensity modulation from an individual enantiomer is barely 1% and the difference in the relative intensity between opposite chiral designs is significantly less than that observed when the samples were illuminated with a linearly polarized incident beam. These results appear to suggest that the variation in the relative intensity of diffracted beams reflected from planar chiral metamaterials is significantly more sensitive to variations in the polarization azimuth of the incident beam than variations in the ellipticity of the incident beam.

7.2.3 Silicon nitride chiral sample

Following the same characterization procedures as for the analysis of the polarization response of the silicon nitride chiral sample discussed in the previous chapter, the dependence of the intensity response on both the chirality and the thickness of the silicon nitride film was investigated.

First, the same pair of enantiomeric arrays of chiral gammadion-shaped holes with $\pm 45°$ bending angles in a 320 nm thick Si_3N_4 layer (wafer 3 BA42 and BA45) were investigated. Fig. 7.5 illustrates the relative intensity of the first-order diffracted beams transmitted through the chiral gammadion arrays as a function of input polarization azimuth, ϕ_0. Again, significant intensity modulation was exhibited in these chiral gammadion structures in the transmission regime. As an example, the

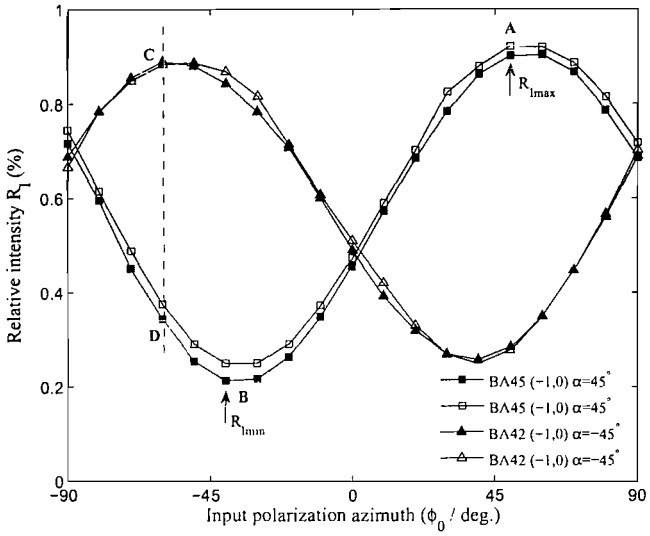

Figure 7.5: Relative intensity of the first-order diffracted beams transmitted through enantiomeric arrays of gammadion-shaped holes etched in a 320 nm thick Si_3N_4 film when illuminated with 632 nm linearly polarized light at normal incidence.

maximum relative intensity (point **A** in Fig. 7.5, $\phi_0 = 50°$) of the right-handed gammadion grating (BA45) is more than four times the minimum (point **B** in Fig. 7.5, ϕ_0 = -40°). Additionally, comparing the intensity response of opposite enantiomers at the same input polarization state, it can be seen that the maximum relative intensity of a left-handed gammadion grating (BA42) at an input polarization state, ϕ_0 = -60° (point **C** in Fig. 7.5) is almost four times the relative intensity of a right-handed gammadion grating (BA45) at the same input polarization state (point **D** in Fig. 7.5).

The intensity response from different planar chiral metamaterials in both the reflection and transmission regimes has been studied. Collectively the results shown in Fig. 7.2, Fig. 7.3 and Fig. 7.5 demonstrate strong intensity anisotropy for all chiral samples. This behaviour is similar to the polarization anisotropy of the optical transitions observed in the planar chiral metamaterials. However, as shown in Fig. 7.2, Fig. 7.3 and Fig. 7.5, the relative intensity from opposite enantiomers is almost identical at input polarization states, $\phi_0 = 0°$ and $\pm$ 90°. Moreover, the relative intensity for right-handed planar chiral metamaterials at ϕ_0 = x° is almost identical to the relative intensity for left-handed planar chiral metamaterials at ϕ_0 = -x° (mirror-image). This again is due to invariance under parity inversion as explained in the previous chapter.

Then, the intensity response of the first-order diffracted beams transmitted through the same arrays of chiral gammadion gratings (BA42 and BA45) but on

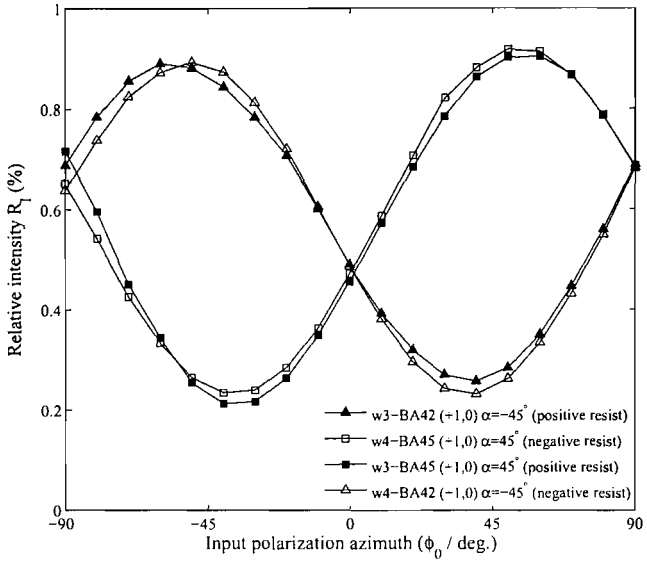

Figure 7.6: Relative intensity of the (+1,0) order diffracted beams transmitted through enantiomeric arrays of chiral gammadion-shaped Si_3N_4 holes (wafer 3) and mesas (wafer 4) when illuminated with 632 nm linearly polarized light at normal incidence.

wafer 4 was also investigated. As described in the previous chapter, the gammadion-shaped silicon nitride chiral mesas on wafer 4 are the complementary designs of the arrays of gammadion-shaped holes on wafer 3. For comparison, Fig. 7.6 plots the relative intensity of the (+1,0) order diffracted beam transmitted through the complementary chiral gammadion designs as a function of input polarization azimuth, ϕ_0. The figure clearly shows that the intensity response of the chiral gammadion mesas is almost identical to that of their complementary structures. This behaviour is also in agreement with the polarization response observed from the complementary structures discussed in the previous chapter.

Finally, the intensity response of the first-order diffracted beam transmitted through arrays of gammadion-shaped holes etched into a Si_3N_4 layer with three different thicknesses was studied. In each case, the same array of right-handed gammadions (BA45) with a bending angle, $\alpha = 45°$, arm length, $\xi = 1.8$ μm, and pitch size, $\Lambda = 5.0$ μm, was investigated. Fig. 7.7 illustrates the relative intensity of the (+1,0) order diffracted beam transmitted through these arrays of chiral gammadions with different thickness as a function of input polarization azimuth, ϕ_0, illuminated with linearly polarized light at normal incidence. Fig. 7.7 shows clearly that with the increasing thickness of the Si_3N_4 layer, the relative intensity, which represents the absolute value of the optical intensity of the diffracted beams, increases significantly regardless of the input polarization state. This demonstrates that the magnitude of

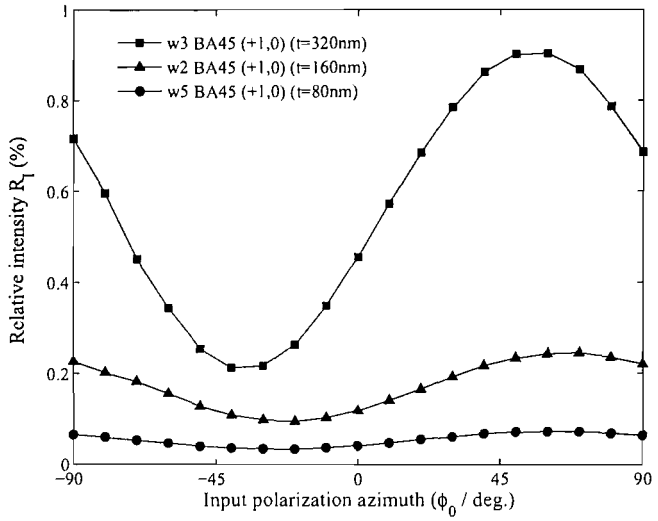

Figure 7.7: Relative intensity of the (+1,0) order diffracted beams transmitted through arrays of right-handed gammadion-shaped holes etched in a Si_3N_4 film with different thicknesses when illuminated with 632 nm linearly polarized light at normal incidence.

the intensity modulation is dependent on the thickness of the material in which the planar chiral structures are generated. On the other hand, Fig. 7.7 also shows that the input polarization azimuth, ϕ_0, where the relative intensity modulation is the greatest or the smallest, appears to remain relatively unchanged as the film thickness is varied. In comparison, similar behaviour in the dependence of the polarization state on the Si_3N_4 film thickness was also observed as introduced in the previous chapter.

In summary, both metallic and dielectric thin films patterned with nanoscale planar chiral structures exhibit strong intensity modulation at different input polarization states when they are illuminated by visible linearly polarized light at normal incidence. Different magnitudes of intensity modulation were observed in different chiral samples and they are summarized in Table 7.1.

7.3 Silicon photodiode with planar chiral gratings

7.3.1 Introduction

The effect of strong polarization anisotropy in optical transitions has a great influence on optoelectronic devices. For example, these ideas are employed in LED's emitting polarized light [85], for polarization-sensitive modulators [86] and switching

Sample	Wafer	Type of resist	Film thick-ness (nm)	Chiral grating	Bending angle (°)	$R_{I max}$ (%)	$R_{I min}$ (%)	$\mathbb{C}$ (%)	$\mathbb{A}$ (%)
Al	-	Positive	100	B41(+1,0)	45	1.12	0.31	56.9	264.5
				B46(+1,0)	-45	1.1	0.26	61.4	318.1
UNIII	-	Positive	300	B41(+1,0)	45	0.13	0.08	24.2	63.7
				B46(+1,0)	-45	0.14	0.09	23.9	62.8
Si_3N_4	3	Positive	320	BA42(+1,0)	-45	0.90	0.26	55.2	246.0
				BA45(+1,0)	45	0.90	0.21	61.8	324.2
Si_3N_4	4	negative	320	BA42(+1,0)	-45	0.92	0.23	59.3	290.8
				BA45(+1,0)	45	0.89	0.23	58.8	285.1
Si_3N_4	6	Positive	240	BA42(+1,0)	-45	0.89	0.23	59.1	288.6
				BA45(+1,0)	45	0.91	0.25	57.5	270.1
Si_3N_4	2	Positive	160	BA42(+1,0)	-45	0.26	0.07	57	268.1
				BA45(+1,0)	45	0.24	0.1	43.9	256.6
Si_3N_4	5	Positive	80	BA42(+1,0)	-45	0.07	0.03	37.0	117.5
				BA45(+1,0)	45	0.07	0.03	36.1	112.9

Table 7.1: Magnitudes of intensity modulation of first-order diffracted beams from various planar chiral metamaterials.

devices [87]. Additionally, Kiesel *et al.* reported intrinsically polarization sensitive semiconductor switches taking advantage of the polarization anisotropy of ordered GaInP [88]. Significant intensity modulation with input polarization state at visible wavelengths has been observed from both metallic and dielectric planar chiral metamaterials. The magnitude of the intensity modulation exhibited a dependence on the chirality, geometry and the film thickness. This intensity response exhibited in planar chiral metamaterials might offer device applications for polarization detectors and modulators. Inspired by this idea, a new device integrating a Ti planar chiral grating on the active area of silicon photodiodes was designed, fabricated and characterized. Furthermore, this device was designed to acquire information on the optical activity of the sum of all of the transmitted beams by planar chiral metamaterials, which was not known.

7.3.2 Device structure

The basic structure of the device is composed of a standard pn^+ silicon photodiode with a planar chiral grating on the active area (absorption region) of the photodi-

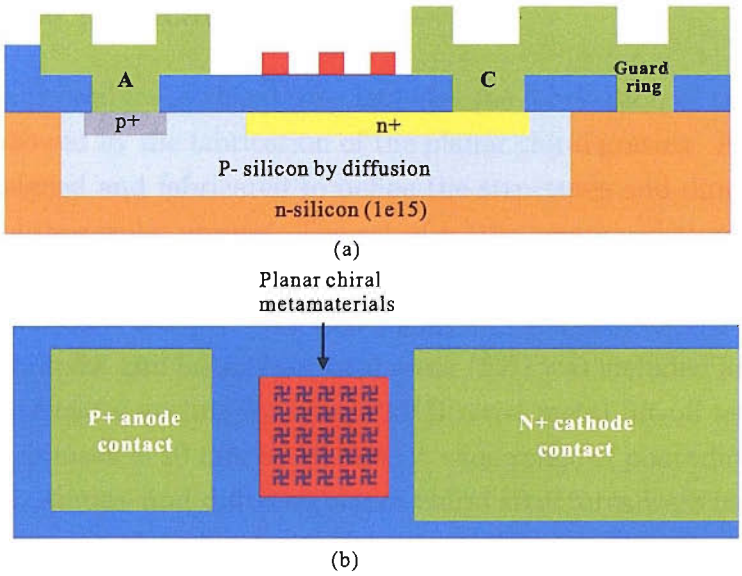

Figure 7.8: Schematic diagram of a pn^+ silicon photodiode with an integration of planar chiral structures.

ode. Fig. 7.8 shows a schematic diagram of the device. A standard n-type silicon substrate was used and a p-type silicon layer (the anode) was formed inside the n-type silicon substrate by ion implantation and thermal diffusion. As a result, a p-n junction was created between the p-doped silicon anode and the n-type silicon substrate. The n^+ silicon (the cathode) was fabricated by ion implantation with a high arsenic doping concentration followed by a rapid thermal annealing (RTA) process. As a consequence, a p-n junction, which provides a depletion region to absorb photons generated by the incident light, was formed between the anode and cathode underneath the surface of the substrate. A standard aluminium alloy with 1% of silicon and titanium was used for ohmic contacts to the highly doped p^+ and n^+ regions. An additional contact was added to make contact to the substrate and was directly contacted to the cathode at the same time. Therefore, when applying a reverse biased voltage across the two terminals of the photodiode, both cathode (n^+ region) and n-substrate were at higher bias compared to the p-anode. In this case, the reverse-biased p-n junction between the anode and the substrate can prevent carriers generated by light from diffusing into the substrate, thereby keeping them in the depletion region. This structure is called *guard-ring* and its purpose is to reduce the electric field strength at the edge of the p implant inside the substrate and prevent breakdown. A thin Ti layer patterned with planar chiral structures on the top of the active area of the photodiode was fabricated by a combination of metal lift-off and EBL techniques.

7.3.3 Device fabrication

The fabrication procedure of this device includes the fabrication of the silicon photodiode first followed by the fabrication of the planar chiral grating. A set of optical masks were designed and fabricated to define the structures and dimensions of the device in photolithography process. The set of masks comprised seven layers: NW, AA, CR, AR, CW, M1, EB, all of which were reticle masks and were designed for 5:1 reduction on a GCA stepper. The first six layers were used for the fabrication of the silicon photodiode, and an extra optical mask (EB) was included for the fabrication of the planar chiral grating by using PMGI resist metal lift-off technique. The dimension of each mask is 10 mm by 10 mm. A wide range of photodiodes with various dimensions, shapes, and different planar chiral structures were included in the masks for the purpose of device characterization. The details of the optical masks are included in **Appendix A**. Prior to the fabrication, a 2D process simulation tool, SILVACO ATHENA, and a physically based 3D device simulator, ATLAS, were used to simulate the pn^+ silicon photodiode in order to design a photodiode with high responsivity, high quantum efficiency and low dark current. Its physical behaviour, such as the carrier doping profile, the energy bandgap and junction depth, were also simulated. The simulation results are provided in **Appendix D**.

Fig. 7.9 illustrates the main fabrication process of the pn^+ silicon photodiode covered by a thin titanium layer with planar chiral structures. The fabrication process started with a standard n-type $< 100 >$, 30 Ω/cm silicon substrate. The wafer was first cleaned using a standard RCA process, followed by a 100 nm thick layer of silicon dioxide grown by wet oxidation (Fig. 7.9 (1)). Then the active area as well as the guard-ring structure were defined by an optical photolithography stage (mask NW) and RIE SiO_2 dry etching process (Fig. 7.9 (2)). The etch depth is equal to the thickness of the deposited SiO_2 layer. Next, a 20 nm thick silicon dioxide layer was deposited all over the wafer before the following ion implantation stage to reduce the damage to the surface induced by the ion implantation process (Fig. 7.9 (3)). Then, boron irons were implanted into the surface of the n-type silicon substrate and were diffused into the substrate by a long thermal annealing process at 1150°C to form the p-doped anode (**A**) (Fig. 7.9 (4)). Different boron doping concentrations ($5\times10^{13}cm^{-2}$, $1\times10^{14}cm^{-2}$ and $2\times10^{15}cm^{-2}$), drive-in energies (40 and 80 KeV), thermal annealing times (4-6 hours) were used on different wafers. By controlling the dopant concentration and thermal annealing parameters, the junction depth, a crucial parameter that determines the performance of the photodiode, was adjusted. The variation of the junction-depth provided different thicknesses of the depletion region, where the photons generated by light were absorbed. The next step was the fabrication of the n^+ cathode by arsenic (n-type) ion-implantation. A 1.1 μm

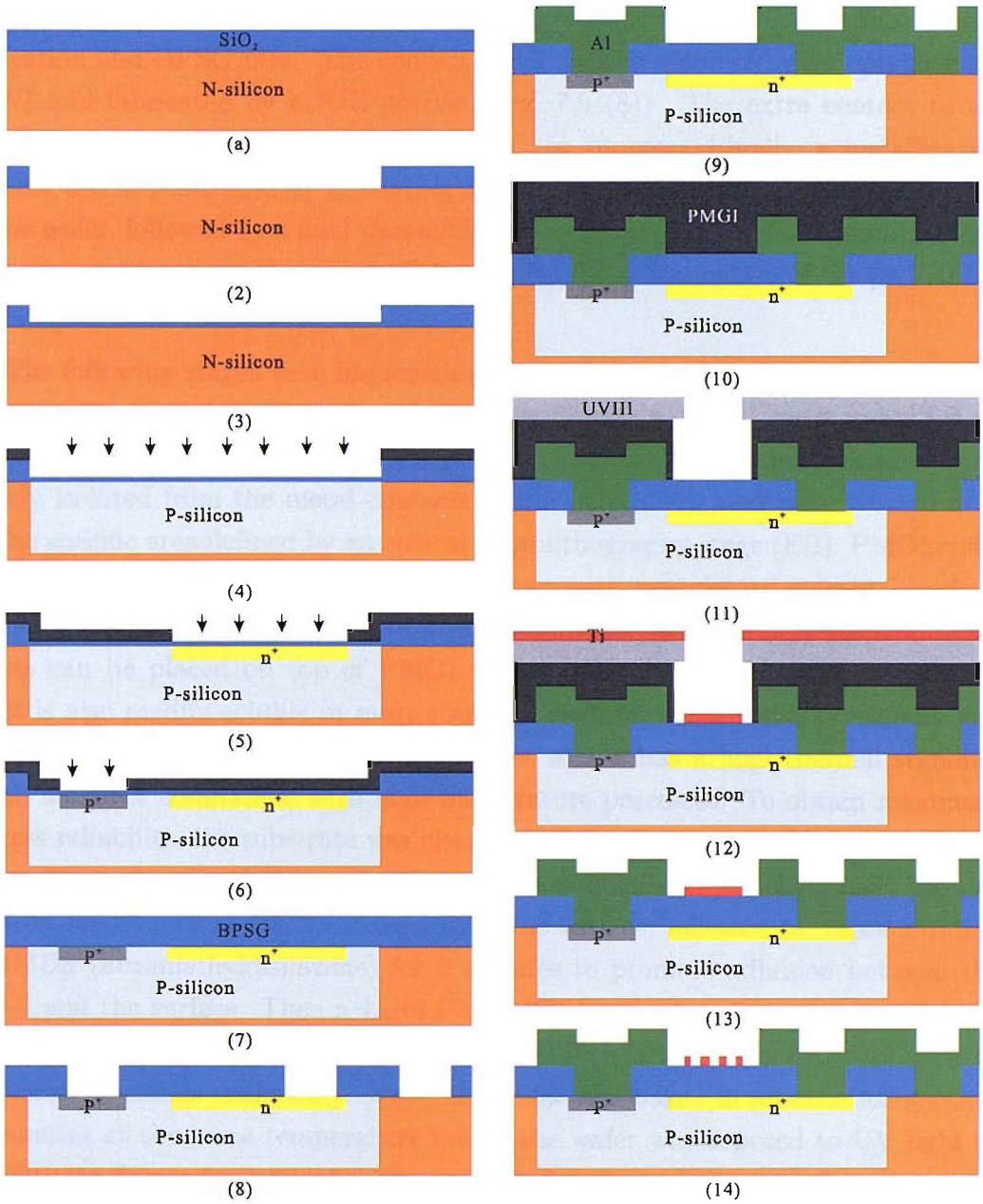

Figure 7.9: Schematic diagram of the fabrication process of a pn^+ silicon photodiode integrated with planar chiral metamaterials.

optical resist was spun upon the surface of the substrate and was exposed with the assistance of an optical mask (CR) to define the cathode (**C**) region in the optical resist (Fig. 7.9 (5)). In the same manner, a highly-doped p^+ anode ohmic contact region was defined using an optical mask (AR) in a standard photolithography step and fabricated by implanting the wafer with BF_2 at a dose of $5\times10^{15}cm^{-2}$ and an energy of 50 KeV (Fig. 7.9 (6)). Afterwards, a multilayer composed of 100 nm of undoped silox and 500 nm of borophosphosilicate glass (BPSG) was deposited onto the surface for device passivation (Fig. 7.9 (7)), followed by a rapid thermal

annealing (RTA) process for approximately 10 seconds at 1100°C to induce dopant activation and BPSG flow. The contact windows were defined by an optical mask (CW) and fabricated by a RIE process (Fig. 7.9 (8)). The extra contact to the substrate was implemented in this stage of the process. Finally, a metallization process was implemented by sputtering a 1000 nm Ti-Al/Si alloy layer onto the top of the wafer, followed by a final photolithography stage (M1) and an aluminium dry etch process to pattern the metal. This completed the fabrication of the pn^+ silicon photodiode (Fig. 7.9 (9)).

The following stages were implemented to position the fabrication of the planar chiral gratings on the active area of the photodiode. A PMGI resist metal lift-off process was used to ensure that the titanium planar chiral structures were completely isolated from the metal contacts of the photodiode and were created only on the specific area defined by an optical photolithography stage (EB). PMGI resist consisting of polydimethylglutarimide polymer with proprietary solvent blends is virtually insoluble in typical electron beam resists solvent. Therefore electron beam resists can be placed on top of PMGI without intermixing. In addition, PMGI resist is also readily soluble in most standard electron beam resist developers and has highly controllable dissolution properties, and it has a high thermal stability, which makes it compatible with high temperature processes. To obtain maximum process reliability, the substrate was cleaned and dried prior to applying the PMGI resist. Then the photolithography process was started with a dehydration bake in an oven for 30 min at 190°C to dehydrate the surface, followed by vapor priming in HMDS (hexamethyldisilazane) for 3 minutes to promote adhesion between the PMGI and the surface. Then a 1 μm PMGI SF11 resist layer was spun on the top of the wafer at a speed of 4000 rpm (Fig. 7.9 (10)); a low ramp rate was used to get better thickness uniformity. Next, the wafer was baked in an oven for another 30 minutes at the same temperature before the wafer was exposed to UV light in an EPROM Eraser for 1 minute. The primary functions of this prebake process are to dry the PMGI film and to fix the development and undercut rate. Once the exposure and development processes have been defined, careful design of the prebake process enables precise control of the undercut and maximizes the process window.

After the prebake stage, the wafer was baked at 190°C for an hour before spinning a second layer of electron beam resist, a 300 nm thick layer of UVIII resist at 2500 rpm. After first priming the surface for 3 minutes, the resist layer was exposed for 60 seconds to define the 2D chiral structures, followed by one minute baking at 140°C. Afterwards, both resists were developed for 2 minutes in MF322 developer. An undercut in the PMGI resist layer was formed (Fig. 7.9 (11)) due to the different development speed between the PMGI resist and the electron beam resist (UVIII).

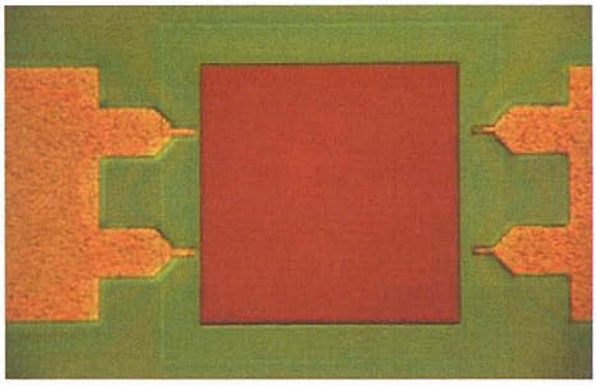

Figure 7.10: Optical micrograph of a silicon photodiode with a thin Ti layer on the top of the active area of the photodiode fabricated by PMGI resist metal lift-off technique.

After exposure and development, the position of chiral gratings was defined in both resist layers. Next, a thin uniform layer of 50 nm Ti was evaporated on the surface of the wafers by electron-gun evaporation (Fig. 7.9 (12)). During this evaporation stage, the substrate was at room temperature. The base pressure was set at 10^{-6} mbar and the pressure rose to 10^{-5} mbar to 10^{-4} mbar during evaporation due to outgassing and the evaporating material. The deposition rate of the aluminium layer was about 250 nm per minute. Due to the high thermal stability of PMGI, it is compatible with both high temperature sputtered or evaporated metal and dielectric deposition processes. After the metal deposition, the PMGI resist was dissolved in the NMP (n-methylpyrrolidine) solvent in a covered dish on a "Wobbler" for about 4 hours. The wafers were then carefully transferred to a clean dish of NMP leaving all detached metal behind and any loose clinging metal was washed away by squirting with NMP. Afterwards, the wafer was washed in a clean dish of Super Q with a spray gun to remove any remaining pieces of loose metal, followed by another 10 minutes rinse in a Super Q water tank. As a result, a thin Ti layer was deposited upon only the active area of the silicon photodiodes (Fig. 7.9 (13)). Finally, the Ti layer was patterned with different nanoscale structures using the same EBL process as introduced in Chapter 4 (Fig. 7.9 (14)).

Fig. 7.10 shows an optical micrograph of a fabricated pn^+ silicon photodiode with a unpatterned Ti layer on the active area after the metal lift-off process. The figures shows clearly that the design of the extra optical mask (EB) provided good alignment between the thin Ti layer and the active area of the photodiode. Fig. 7.11 includes two optical micrographs of the fabricated pn^+ silicon photodiode with arrays of chiral gammadion-shaped holes etched into the thin Ti layer evaporated on top of the active area. Well defined chiral patterns, clearly specified contact windows and good alignment between the optical and electron beam lithography processes

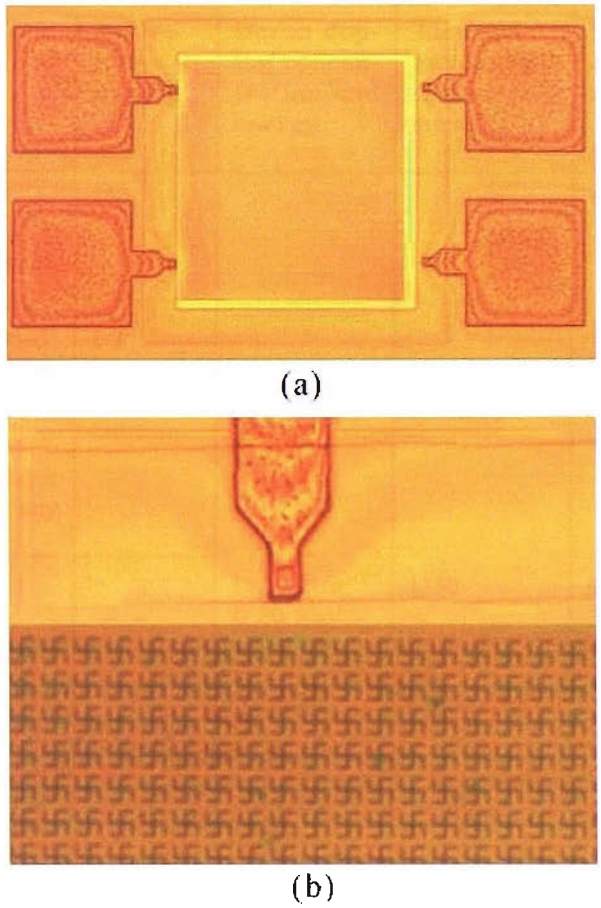

Figure 7.11: Optical micrographs of a silicon photodiode with a thin Ti layer patterned with chiral structures, on the active area of the photodiode.

are clearly seen in the figures. The complete process list for this device is included in **Appendix B**.

7.3.4 Device characterization

Several devices (DC1A, DC1E, DC1F, DC3A, DC3C and DC3E) each with different Ti nanostructured patterns were characterized by investigating their photoresponse (I-V measurement) with both unpolarized light and linearly polarized light. The details of the specifications of these devices are summarized in Table 7.2.

I-V characterization with un-polarized light

First, the photoresponse of a single pn^+ silicon photodiode (DC1F) with a uniform unpatterned thin Ti layer was illuminated by an unpolarized white light source with three adjustable optical intensities. A HP4155A semiconductor parameter analyzer

Device number	Ti pattern	Active area (mm^2)	Boron doping concentration and energy	Thermal annealing temperature (°C)	Thermal annealing time	Arsenic doping concentration and energy
DC1A	Right-handed chiral gammadion	1.2	$1\times10^{14}cm^{-2}$ @ 80 KeV	1150	6 hours	$5\times10^{15}cm^{-2}$ @ 80KeV
DC1E	Left-handed chiral gammadion					
DC1F	Uniform Ti layer without any pattern					
DC3A	Right-handed chiral gammadion	0.3				
DC3C	Achiral simple cross					
DC3E	Left-handed chiral gammadion					

Table 7.2: The characteristic parameters of the pn^+ silicon photodiodes under investigation.

was used to characterize the photoresponse of the device. The instrument contains four stimulus and measurement units (SMU1-SMU4) which can be configured to source current and measure voltage or to source voltage and measure current. Regarding the characterization of the fabricated pn^+ silicon photodiode, two units (SMU1 and SMU2) were used and were configured as the voltage applied across the pn junction (V) and the photocurrent (I_p) respectively. The instrument was connected to a probe station. Two metallic probes were adjusted and positioned with the assistance of a high magnification microscope to form a good contact to the aluminium pads, which were connected to the two terminals (cathode and anode) of the silicon photodiode respectively. As a result, the photodiode was biased according to the configuration of the HP4155A semiconductor parameter analyzer and the photocurrent signal was monitored at the same time.

Fig. 7.12 shows the photocurrent, I_p, of the silicon photodiode (DC1F) as a function of biased voltage, V_{pn} applied to the p-n junction. The multiple curves represent the photoresponse of the same device but illuminated with three level of

optical intensities of the white light source, ($P_1 < P_2 < P_3$) respectively, and in a dark environment ($P = 0$). The figure shows clearly that the photocurrent generated in the depletion region of the photodiode increases significantly with increasing incident beam intensity. This result agrees with the simple physics of the photodiode.

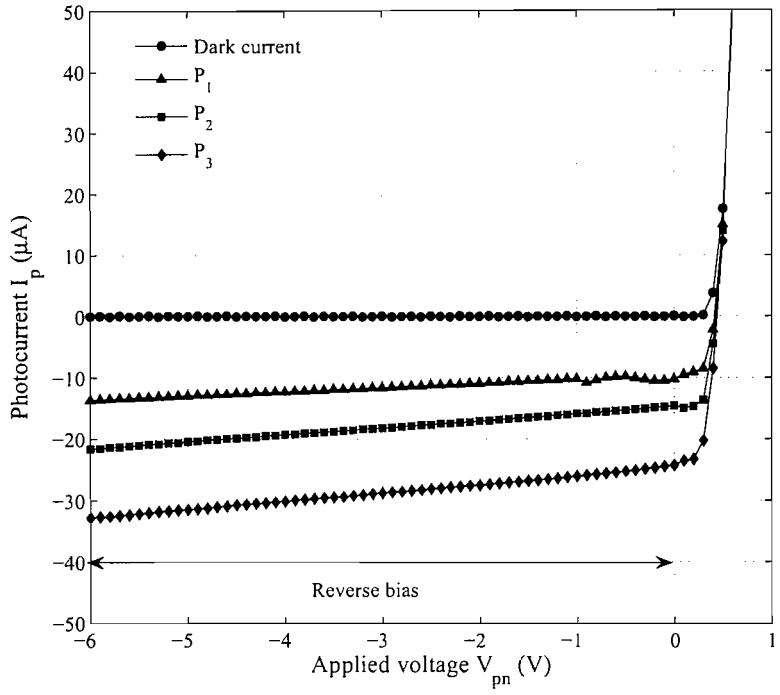

Figure 7.12: Photoresponse of a pn^+ silicon photodiode coated with an unpatterned thin Ti film illuminated by unpolarized light at different intensities at normal incidence.

Next, the photoresponse of three photodiodes (DC3A, DC3E and DC3C) were characterized using the same unpolarized white light source with a constant intensity (P_1) at normal incidence. These three devices have identical silicon photodiodes but are covered by Ti layers with arrays of right-handed gammadions, left-handed gammadions and achiral crosses respectively. Fig. 7.13 includes the photoresponse of these three devices with the same range of bias voltage, V_{pn}. It clearly shows that there is no significant difference in the generated photocurrent observed from the three devices when they are biased with a same voltage (the oscillations are due to the power supply to the light source). Therefore, it seems that these planar nanoscale chiral structures display no global response to unpolarized light and the planar chiral structures responded to the unpolarized incident beam in the same manner as the achiral planar structures.

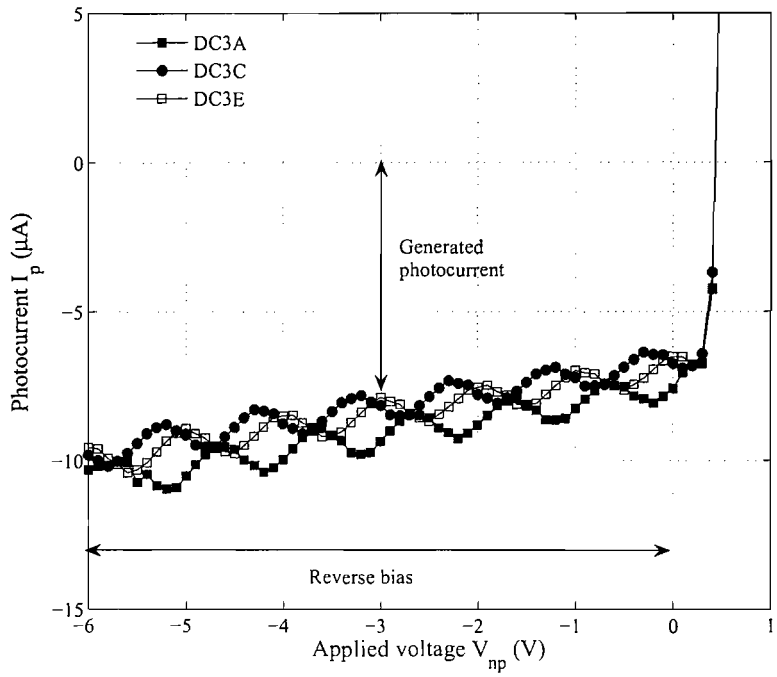

Figure 7.13: Photoresponse of three silicon photodiodes coated with a thin Ti layer patterned with arrays of chiral right-handed gammadions (DC3A), chiral left-handed gammadions (DC3E), and achiral crosses (DC3C), illuminated by unpolarized light at normal incidence.

I-V characterization with linearly polarized light

The same three photodiodes (DC3A, DC3C and DC3E) were then characterized with linearly polarized light. The characterization system includes two parts: an optical system to generate linearly polarized light with a specific input polarization state and an electrical characterization system to measure the photoresponse of the device. The optical arrangement previously used to characterize the polarization response and the intensity response of diffracted beams was used. The HP4155A semiconductor parameter analyzer was integrated with the optical system to measure the photoresponse of the device under the illumination of the linearly polarized light generated by the optical system. Several 10 mm by 10 mm silicon chips, containing a number of devices with a range of dimensions and specifications, were packaged in standard dual in-line (DIL) sockets with 24 pins. Each of the two terminals of the photodiodes was bonded to individual pin. The socket with the packaged chip was mounted on a standard SRBP stripboard, which provided direct connection between the device and the HP4155A semiconductor parameter analyzer as well as a DC voltage source to provide a voltage bias to the photodiode. Fig. 7.14 shows a photograph of a custom designed circuit board, which integrates the packaged

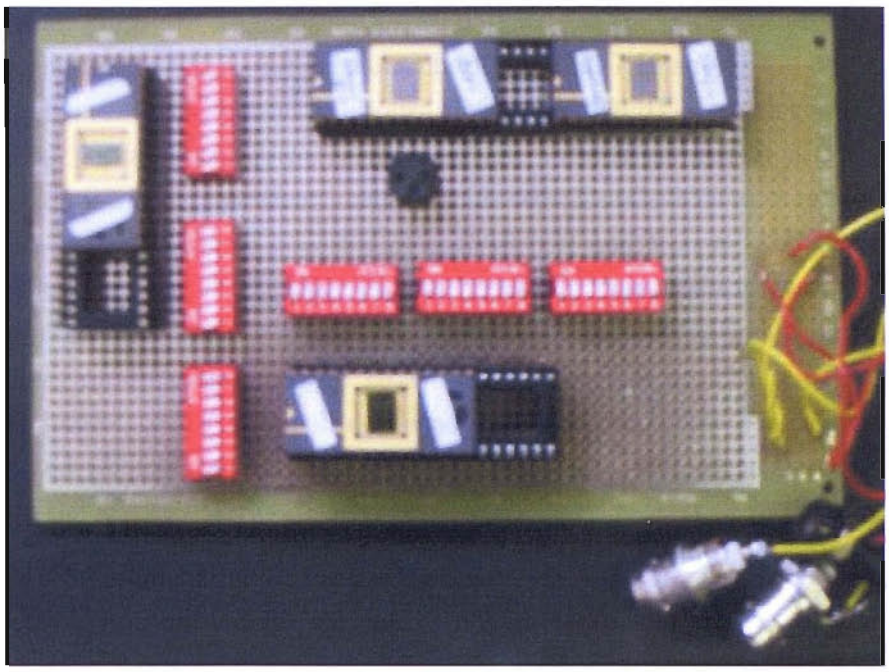

Figure 7.14: Photograph of the fabricated pn^+ silicon photodiodes packaged in standard DIL sockets mounted on a SRBP stripboard.

devices in DIL sockets, dip switches and output units, which are compatible with the HP4155A semiconductor parameter analyzer. A schematic diagram of the combined electrical and optical system, used to characterize the pn^+ silicon photodiode with Ti planar chiral structures, is shown in Fig. 7.15.

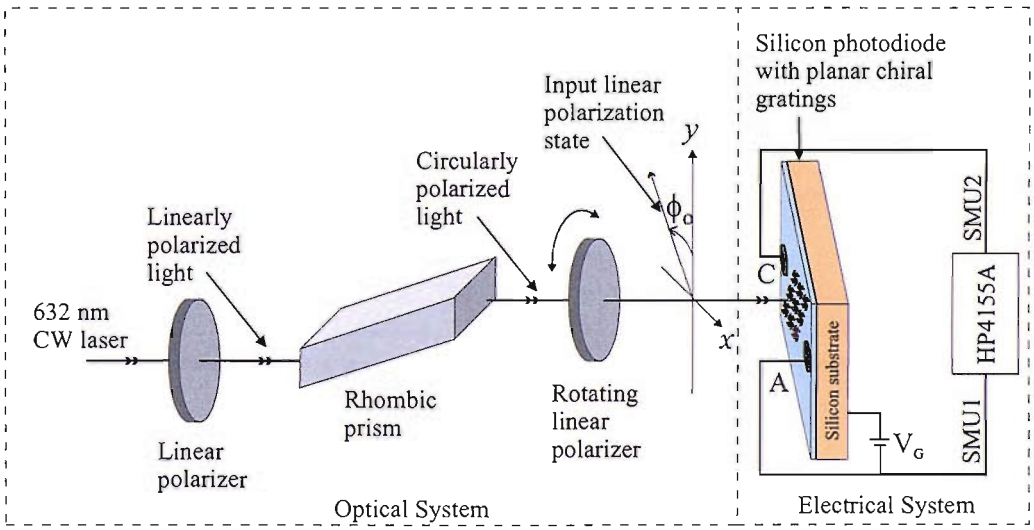

Figure 7.15: Experimental arrangement used to characterize the photoresponse of silicon photodiode covered with Ti planar chiral gratings, illuminated with 632 nm linearly polarized light at normal incidence.

The devices were characterized with the same range of input polarization states

(ϕ_0 was varied from -90° to +90° with a step of 10°) as the polarization state characterizations implemented in the previous chapters. Fig. 7.16 shows the dependence of the photoresponse of the two photodiodes (DC1A and DC1E), which consist of opposite Ti chiral gammadion arrays (right- and left-handed gammadions respectively), on the input polarization state at normal incidence. The devices were reversed biased at two different voltages, V_pn = -2V (Fig. 7.16 (a)) and V_pn = -1V (Fig. 7.16 (b)) respectively. From Fig. 7.16, two types of behaviour can be seen clearly. First, the photocurrent of both devices modulates with the input polarization state (maximum magnitude of modulation is about 10%). Second, comparing the photoresponse of DC1A to that of DC1E when illuminated with the same linearly polarized light, the generated photocurrent is different. Since the only difference between the two devices are the microstructures with opposite chirality patterned in the thin Ti film, it can be inferred that the chirality of the surface on the photodiode is a factor to the different photoresponse observed in the devices. If this is the case, the photoresponse of the photodiodes is due to the sum of all the beams transmitted by the planar chiral structure, as such, the zero order beam will dominate the signal. If considering that the zero-order beam might in itself represent more than 90% of the total transmitted intensity, then it implies that the photocurrent modulation due to the sum of all of the higher-order diffracted beams by the planar chiral structures on the photodiodes is very significant. Consequently, these results show some potential device applications for planar chiral metamaterials as polarization sensitive photodetectors, but more detailed studies are required at this stage.

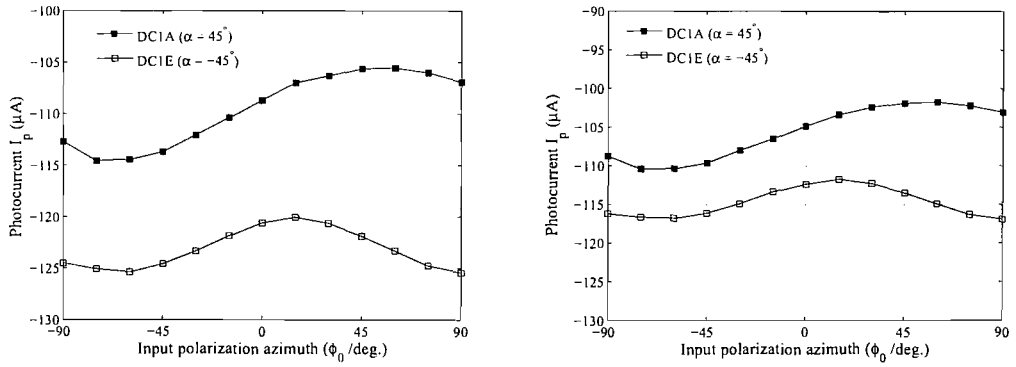

Figure 7.16: The dependence of the photoresponse of two silicon photodiodes coated with Ti planar chiral gratings with opposite chirality on the input polarization state. (a) V_{pn} = -2V, and (b) V_{pn} = -1V

7.4 Conclusion

Both metallic and dielectric thin films patterned with nanoscale planar chiral structures have exhibited strong intensity modulation with input polarization state when illuminated by visible linearly polarized light at normal incidence. The opposing enantiomeric chiral structures exhibit large variations in intensity between orthogonal linear polarization states. The exception, however, is the case of horizontal and vertical states (ϕ_0 = -90°, 0°, +90°), where the mirror anti-symmetry of two enantiomeric structures results in the same anti-symmetry of their intensity response. This is in contrast to their polarization response as discussed in the previous chapters. Additionally, the intensity modulation of planar chiral metamaterials has exhibited a dependence on the chirality and the thickness of the thin film in which the structures are created. This property shows a significant similarity comparing to the polarization response of the planar chiral metamaterials discussed in the previous chapters. These results provided further circumstantial evidence for the role of constructive interference in mediating the optical activities of the novel planar chiral metamaterials structures.

In an initial study of planar chiral metamaterials integrated onto pn^+ silicon photodiodes, it has been demonstrated that the polarization state of linearly polarized incident light modulates the photoresponse of the photodiode. Although the sum of all beams transmitted by the planar chiral grating are detected (including the zero order) significant modulations are observed. These results show some potential device applications for planar chiral metamaterials.

Chapter 8

Non-reciprocal diffraction from planar chiral metamaterials

8.1 Introduction

Polarization elements are often classified as reciprocal or nonreciprocal depending on whether their effect on the polarization state of the transmitted light is the same or different for light propagating in the forward and reverse direction. The application of reciprocity principles in optics has a long history that goes back to Stokes, Lorentz, Helmholtz and others. Reciprocal response underlies the behaviour of optical components such as polarizers, waveplates and beam splitters.

As discussed in the previous chapters, significant polarization state changes have been observed in both metallic and dielectric planar chiral metamaterials, and the direction of the polarization change is reversed if both the chirality of the surface and the input polarization state are reversed. This suggests that for beams traveling in the reverse direction, the polarization changes manifested by these structures will be opposite, therefore the system will behave non-reciprocally. The intrinsic 2D chirality means that, for a given diffraction path, reversal of the sample by a rotation of 180° about any axis in the plane of the thin film patterned with chiral structures results in a reversal of the sense of chirality of the patterned film as seen by the incident beam. Therefore light transmitted through these planar chiral structures should be subject to opposite polarization changes induced in opposite directions. As reviewed in Chapter 2, such non-reciprocal properties of 2D chiral metamaterials have been predicted theoretically for a number of idealized physical structures subject to various preliminary assumptions and approximations [8, 13, 65].

If non-reciprocal properties can be demonstrated experimentally for real planar

chiral structures, it would represent a major change in understanding the symmetry of light interactions with planar chiral metamaterials, and it could lead to the development of an entirely new range of optical devices, based on optical rectifiers and isolators. In order to test non-reciprocal properties on planar chiral metamaterials, several experiments were conducted on both the aluminium and silicon nitride samples studied in the previous chapters.

8.2 Fundamental principles of symmetry and reciprocity in optics

8.2.1 Fundamental principles of symmetry

Three conservation laws have been defined with respect to symmetries and invariance principles associated with inversion or reversal of space, time, and charge. Space inversion yields a mirror-image world where the handedness of particles and processes are reversed; the conserved quantity corresponding to this symmetry is called *space parity*, or simply *parity*, **P**. Similarly, the symmetries leading to invariance with respect to time reversal and charge conjugation (changing particles into their respective antiparticles) result in conservation of *time parity*, **T**, and *charge parity*, **C**. Although these three conservation laws do not hold individually for all possible quantum mechanical processes, the combination of all three is thought to be an absolute conservation law, known as the *CPT theorem* [41]. This states that if a given process occurs, then a corresponding process must also be possible in which particles are replaced by their antiparticles, the handedness of each particle is reversed, and the process proceeds in the opposite direction in time.

Parity

Parity (spatial reflection symmetry) is an intrinsic symmetry property of subatomic particles, which is characterized by the behaviour of the wave function of such particles under reflection through the origin of spatial coordinates [41]. In physics, a parity transformation (also called parity inversion) is the simultaneous flip in the sign of all spatial coordinates, which can be expressed as:

$$P : (x, y, z) \longrightarrow (-x, -y, -z) \tag{8.1}$$

thus, the parity transformation changes a right-handed coordinate system into a left-handed system and vice versa.

Time reversal

Time-invariance in optics presumes that a system works the same way for light propagation in either direction, as illustrated in Fig. 8.1. These two configurations are related to one another by time-reversal, and both can be realized in practice. The symmetry operation of time reversal reverses the motions of all the physical entities in the system. A physical process is said to be time reversed invariant, or to have reversality, if the equations that describe the process are unchanged when the time coordinate, t, is replaced by -t [41]. The time-reversed version of an optics experiment has time-reversed, phase-conjugated versions of all of the lightwaves in the original experiment, and can be realized if the propagation medium is lossless and is itself time-symmetric. For example, reflection and refraction at a dielectric interface is a time-reversible phenomenon [89]. It requires time-reversed reflected and refracted waves to be brought together with the correct phase relationship to generate the time-reversed version of the incident wave.

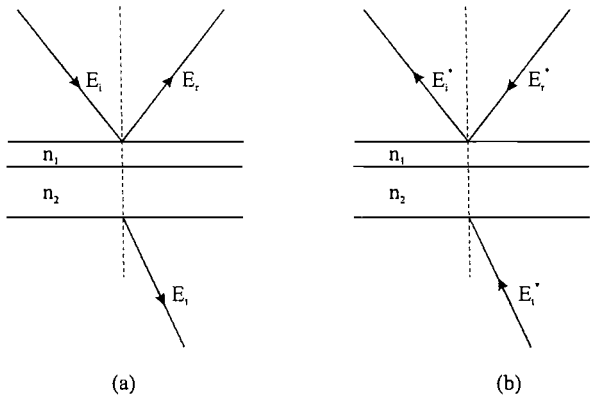

Figure 8.1: Schematic diagram of time reversal configuration (a) division of amplitude at a beam splitter (b) time-reverse process (beam combining).

8.2.2 Reciprocity in optics

Reciprocity relates input and output waves in pairs irrespective of the presence or absence of other waves. Like other forms of symmetry, reciprocity can be used to simplify the analysis of light propagation. The reciprocity principle (or reciprocity law) is a theorem on the connection between the electromagnetic fields $\mathbf{E}_1$, $\mathbf{H}_1$ and $\mathbf{E}_2$, $\mathbf{H}_2$ which are induced by electrical sources, I_1 and I_2, with the same frequency ω. One of the most important reciprocity theorems is *Lorentz's reciprocity theorem.* Considering monochromatic electromagnetic fields in an isotropic and time indepen-

dent medium, the electromagnetic fields of two sources satisfy the relation [90]:

$$\int_S (\mathbf{E}_1 \times \mathbf{H}_2) - (\mathbf{E}_2 \times \mathbf{H}_1) dS = 0 \tag{8.2}$$

where $\mathbf{E}_1$,$\mathbf{H}_1$ and $\mathbf{E}_2$,$\mathbf{H}_2$ are the electric and magnetic fields created by waves propagating in opposite directions. Eqn. 8.2 constitutes *Lorentz's reciprocity theorem* and it forms the basis of interesting reciprocity relations in scattering theory [91]. However, according to the magneto-optic Faraday effect, when a magnetic field is applied normal to the layer, its refractive index is different for opposite direction of propagation [89]. This is a failure of reciprocity.

8.3 Reciprocity and reversibility tests of planar chiral metamaterials

8.3.1 Reciprocity

First, the polarization properties of a pair of enantiomeric Si_3N_4 chiral gammadion arrays, illuminated from opposite directions, are investigated as a function of the input polarization azimuth, ϕ_0. The two opposite directions are defined as: the forward direction with the laser incident on the silica substrate first; and the reverse direction with the laser incident on the patterned Si_3N_4 layer first. The configurations of these two processes are schematically illustrated in Fig. 8.2. The purpose of this experiment is to test the assertion of Kuwata-Gonokami *et al.* [66] that the polarization changes exhibited by planar chiral layers are due to the presence of residual 3D chirality rather than 2D chirality. According to this configuration, the polarization response of diffracted beams transmitted through chiral gammadion gratings, W3 BA42 and BA45 on the silicon nitride sample, is characterized in the reverse direction in this section. These results are compared to those from the forward directions as discussed in Chapter 6.

The polarization changes of the (+1,0) diffracted beam from the enantiomeric pair of gammadion arrays with arm length $\xi = 1.8$ μm, pitch size $\Lambda = 5.0$ μm, and bending angles $\alpha = 45°$ (wafer 3 BA45), $\alpha = -45°$ (wafer 3 BA42), were investigated. Each sample was illuminated with linearly polarized light at normal incidence from both forward and reverse directions. This leads to the polarization changes that are parity inverted when the structure is illuminated from opposite directions. The measurement results are shown in Fig. 8.3, which clearly shows that the polarization changes, including both ellipticity and polarization azimuth rotation, of the (+1,0)

diffracted beam from left-handed gammadion (BA42) in the reverse direction is almost identical to that of its enantiomeric structure (BA45) in the forward direction. This is evidence that the polarization changes manifested by these chirally patterned Si_3N_4 films are due to 2D chirality, which contradicts to the reports from Kuwata-Gonokami *et al.* [66].

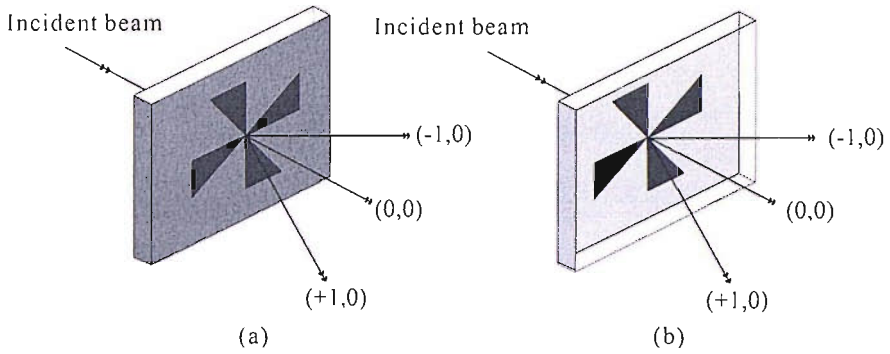

Figure 8.2: Configurations of the polarization state measurement of transmitted beams through Si_3N_4 planar chiral gammadion arrays. (a) forward direction (b) reverse direction.

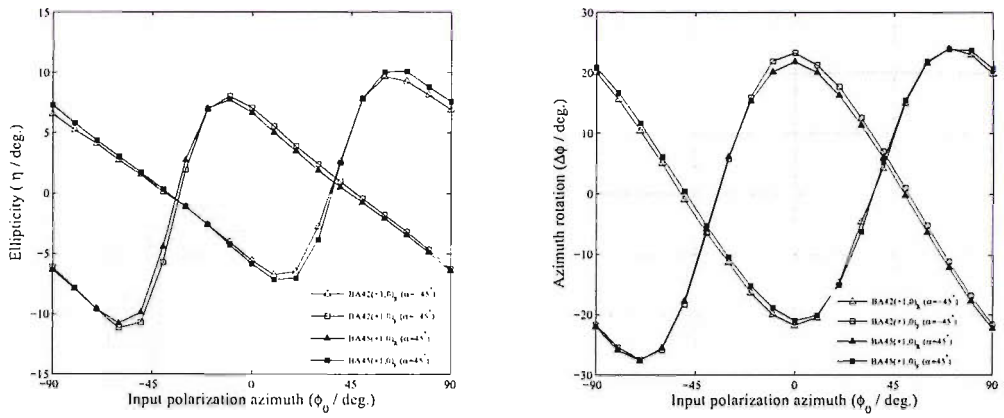

Figure 8.3: A comparison of the polarization changes for the (+1,0) order diffracted beam transmitted through enantiomeric arrays of gammadion-shaped holes etched in a 320 nm thick Si_3N_4 film when illuminated from opposite direction with 632 nm linearly polarized light at normal incidence.

It is now important to determine if these polarization changes are reciprocal. It should be noted that the concept of reciprocity can be defined in a number of different ways, as introduced previously. Suppose the initial input state is defined

by a Jones vector, $\mathbf{J}(\phi,\eta)$, such that:

$$\mathbf{J}(\phi,\eta) = \begin{bmatrix} p \\ q \end{bmatrix} \tag{8.3}$$

where

$$p = \cos(\phi)\cos(\eta) + i\sin(\phi)\sin(\eta) \tag{8.4}$$

and

$$q = -\sin(\phi)\cos(\eta) + i\cos(\phi)\sin(\eta). \tag{8.5}$$

The process for forward propagation through an optical system can be represented as:

$$\mathcal{A}\mathbf{J}(\phi_0,\eta_0) = \mu_a\mathbf{J}(\phi_1,\eta_1) \tag{8.6}$$

while that for the reverse direction will be:

$$\mathcal{B}\mathbf{J}(\phi_3,\eta_3) = \mu_b\mathbf{J}(\phi_2,\eta_2) \tag{8.7}$$

The matrices $\mathcal{A}$ and $\mathcal{B}$ represent the transfer matrices for the respective forward and reverse processes. In general these matrices are not unitary, which is why the complex scaling functions, μ_a and μ_b, are included. It should be noted that μ_a and μ_b are functions of the input polarization state in each case, whereas the matrices $\mathcal{A}$ and $\mathcal{B}$ are not. As the Jones vectors are unit vectors, the parameters μ_a and μ_b therefore define the dependence of the output intensity on the input polarization state, a dependence which was discussed in the previous chapter.

A reciprocal system can therefore be defined as one where, if $\mathbf{J}(\phi_3,\eta_3) = \mathbf{J}(\phi_0,\eta_0)$, then $\mathbf{J}(\phi_2,\eta_2) = \mathbf{J}(\phi_1,\eta_1)$. If this is the case then $\mathcal{B} = \mathcal{A}$, and the system will behave the same when viewed from either side. According to the polarization changes shown in Fig. 8.3, it is clear that these dielectric planar chiral structures do not behave in this way, as reversing the sample does not yield the same polarization change for a fixed diffraction path. The only exception to this is the zero-order diffracted beam which consistently fails to exhibit any polarization change. In this sense, these results are consistent with those of Kuwata-Gonokami *et al.* [66] whose experiments on non-diffracting samples are analogous to the experiments on the zero-order diffracted beam conducted in this work.

The experiment described above clearly shows that the polarization state of the transmitted light from dielectric planar chiral gratings is different for light propagating in each direction. However, while higher order diffracted beams such as the (+1,0) beam appear to produce non-reciprocal polarization effects, it has been found that in all experiments implemented so far the zero order beam consistently

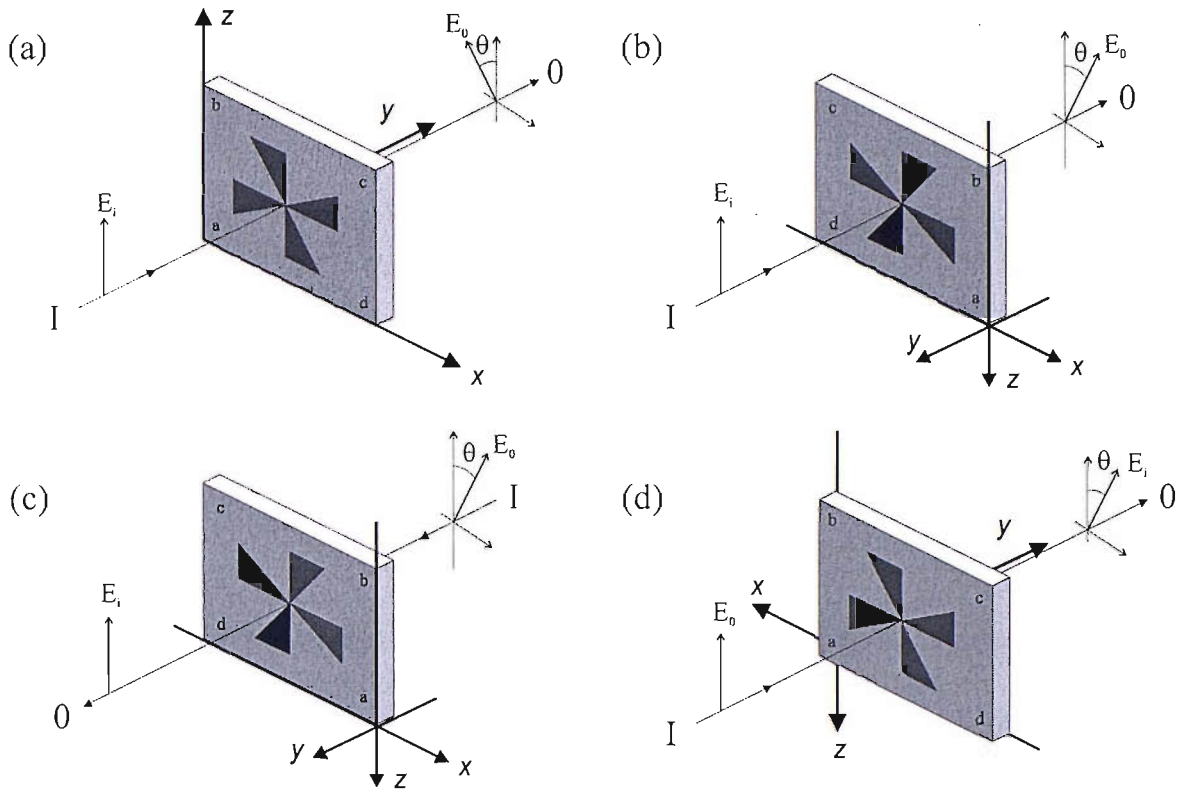

Figure 8.4: The effects of parity inversion (P-symmetry) and time reversality (T-symmetry) on the polarization state of the zero order beam at normal incidence. (a) Initial experimental arrangement showing the incident beam (I) at normal incidence to the sample and the transmitted zero-order beam (0). (b) Parity inverted form of the experimental arrangement in (a). (c) Time-reversed form of the experimental arrangement in (b). (d) After the sample is rotated by θ about the beam axis.

fails to exhibit any polarization rotation, either in the metallic chiral sample in the reflection regime, or in the dielectric chiral sample in the transmission regime. The reason for this can perhaps be understood by considering the effect of parity and time-reversal symmetry transformations on an experimental configuration where the only output beam is the undiffracted zero-order beam, as illustrated in Fig. 8.4. The effect of successive parity and time-reversal transformations is to leave the beam incident on the same side of the planar chiral metamaterial. However, the input is now rotated with respect to the initial input (Fig. 8.4 (a)) and the polarization change of the output beam is in the opposite direction. If the planar chiral metamaterials have four-fold rotational symmetry, the sample can be rotated so that the input in Fig. 8.4 (c) is in the same direction relative to the sample as in Fig. 8.4 (a), without altering the output polarization change relative to the input. The result is an input configuration (Fig. 8.4 (d)), that is the same as the initial experimental configuration as shown in Fig. 8.4 (a) but produces the opposite polarization change. This

paradox can only be resolved if the the polarization change of the zero-order beam is zero. Hence the zero-order beam must be reciprocal. This reasoning relies on the unique symmetry of the zero-order beam and so is not applicable to higher order beams.

8.3.2 Reversality

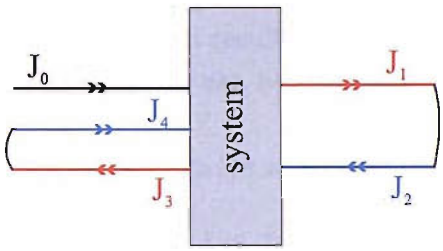

Figure 8.5: Schematic diagram of the configuration of a reversible system.

The second form of reciprocity to be considered is reversality. 3D chirality, 2D chirality and birefringence effect can be distinguished by the behaviour of these different systems under different forms of reversibility [92]. A reversible process can be defined schematically as shown in Fig. 8.5. In this case, the input beam, defined by state J_0 is first converted to an output state J_1 by the system. J_1 is then reversed to state J_2 and is passed back to the system to create state J_3. The reversibility of the system is therefore qualified by comparing state J_3 with the original input state J_0. However, because these states travel in different directions, a second reversal process which is identical to the first reverse process ($J_1 \rightarrow J_2$) is used to generate a final state J_4. Therefore, the reversibility of the system is then tested by comparing state J_4 and state J_0. If $J_4 = J_0$, then the system is reversible.

As shown in Fig. 8.5, there are four different types of reversibility processes. The first reverse process involves inputting the output beam of the forward process along the reverse beam path, and testing to see if the initial state of the forward process is recovered. This process is designated as the *I-process* and can be represented as:

$$\mathcal{B}\mathbf{J}_I(\phi_1, \eta_1) = \mu_b \mathbf{J}(\phi_3, \eta_3). \tag{8.8}$$

The system is reversible if $\mathbf{J}(\phi_3,\eta_3) = \mathbf{J}(\phi_0,\eta_0)$.

The second reverse process is time-reversibility, or T-symmetry. When applying T-symmetry to the planar chiral structures, the input state will have the same ellipticity as the output of the forward process but the opposite polarization azimuth,

thus the T-process can be represented as:

$$\mathcal{B}\mathbf{J}_T(-\phi_1, \eta_1) = \mu_b \mathbf{J}(\phi_3, \eta_3) \tag{8.9}$$

with the input beam $\mathbf{J}(-\phi_1,\eta_1)$ again being directed along the reverse beam path to the forward process. In this case reversible reciprocity requires $\mathbf{J}(\phi_3,\eta_3) = \mathbf{J}(-\phi_0,\eta_0)$.

A third reversal process can be envisaged by placing a mirror in the path of the output beam of the forward process and reflecting it back along its original path. This reverse process (the P-process) will result in an input where both polarization azimuth and ellipticity are reversed can can be represented as:

$$\mathcal{B}\mathbf{J}_P(-\phi_1, -\eta_1) = \mu_b \mathbf{J}(\phi_3, \eta_3) \tag{8.10}$$

In this case reversibility requires $\mathbf{J}(\phi_3,\eta_3) = \mathbf{J}(-\phi_0,-\eta_0)$.

The final possibility for a reversed process is a combination of the P-process and the T-process. This process (the PT-process) can be represented as:

$$\mathcal{B}\mathbf{J}_{PT}(\phi_1, -\eta_1) = \mu_b \mathbf{J}(\phi_2, \eta_2) \tag{8.11}$$

and the system will be reversible if $\mathbf{J}(\phi_2,\eta_2) = \mathbf{J}(\phi_0,-\eta_0)$.

As introduced above, 3D chirality, 2D chirality and birefringence effect can therefore be distinguished by the behaviour of these four reversible processes, I, T, P, PT. As introduced in Chapter 6, the polarization response for a given propagation channel through planar chiral metamaterials can be represented mathematically by the 2×2 transfer matrix, $\mathcal{A}$ [84]. Therefore, through an analysis of the properties of the transfer matrix for different processes, it shows that a 3D chiral system is reversible under both P and T processes, while a 2D chiral system is reversible under I and PT processes. A linear birefringent system, on the other hand, is reversible under both T and PT processes [92]. In this section, the reversibility of both aluminium and silicon nitride planar chiral metamaterials are analyzed for each of the these four processes in order to determine if their optical properties are a product of 3D or 2D chirality or birefringence effect.

It has been shown that the planar chiral structures patterned in either a thin aluminium film or a Si_3N_4 layer changed the linearly polarized incident beam to an elliptically polarized diffracted beam, characterized by ellipticity, η, and polarization azimuth rotation angle, $\Delta\phi$. This is defined as the *forward process* (F-process). In the opposite states, the I-, P-, T- and PT-processes are then performed using each of the states $\mathbf{J}(\phi_1,\eta_1)$, $\mathbf{J}(-\phi_1,-\eta_1)$, $\mathbf{J}(-\phi_1,\eta_1)$, and $\mathbf{J}(\phi_1,-\eta_1)$ respectively as inputs.

Based on these configurations, the aluminium sample was first tested in the reflection regime. The forward process was performed by illuminating the patterned surface at normal incidence ($\beta = 0$) with a linearly polarized incident beam. In this configuration the polarization state of the (+1,0) order diffracted beam reflected from the patterned surface was measured. The reverse processes were implemented individually by illuminating the patterned surface with elliptically polarized light, which had the polarization states based on the (+1,0) order diffracted beam in the forward process as described in Eqn. 8.8, Eqn. 8.9, Eqn. 8.10 and Eqn. 8.11 respectively. Each input was incident on the patterned aluminium surface at an angle of incidence β = -9°, which equals the refraction angle of the (+1,0) order diffracted beam reflected from the aluminium chiral grating (BA41) in the forward process, as described in Chapter 5. The schematic experimental configurations of the time reversality of the aluminium chiral sample in the reflection regime is shown in Fig. 8.6.

Similarly, the reversality of the dielectric Si_3N_4 chiral sample in the transmission regime was also investigated. The forward process was performed by illuminating the chiral sample at normal incidence with a linearly polarized beam passing through the fused silica substrate first before diffracting from the Si_3N_4 gammadion array (W4 BA42) on the opposite surface. In the reverse process, the polarization state of the (+1,0) order diffracted beam transmitted through the same chiral array at an angle of incidence, β = 7°, was measured as a function of the input polarization azimuth angle, ϕ_0. The experimental configurations are schematically illustrated in Fig. 8.7.

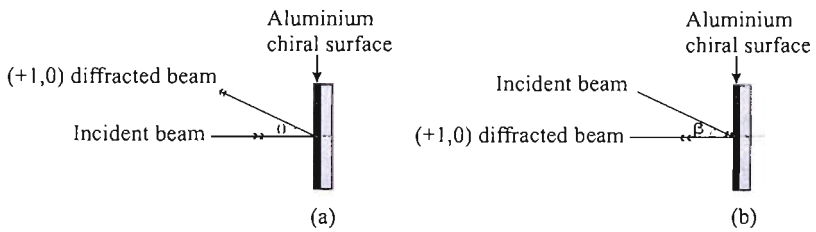

Figure 8.6: Schematic diagram of the experimental configurations to characterize the time-reversibility property of the aluminium chiral sample in the reflection regime. (a) time-forward process (b) time-reverse process.

In order to create the elliptically polarized incident beams for the reverse inputs $\mathbf{J}(\phi_1,\eta_1)$, $\mathbf{J}(-\phi_1,\eta_1)$, $\mathbf{J}(\phi_1,-\eta_1)$ and $\mathbf{J}(-\phi_1,-\eta_1)$ for each output generated by the forward process in Eqn. 8.6, another quarter wave-plate was added to the optical system. A schematic diagram of the optical arrangement used to create elliptically polarized light with a specific polarization state is shown in Fig. 8.8. During the measurement process, the rotating linear polarizer was first adjusted to create linearly polarized

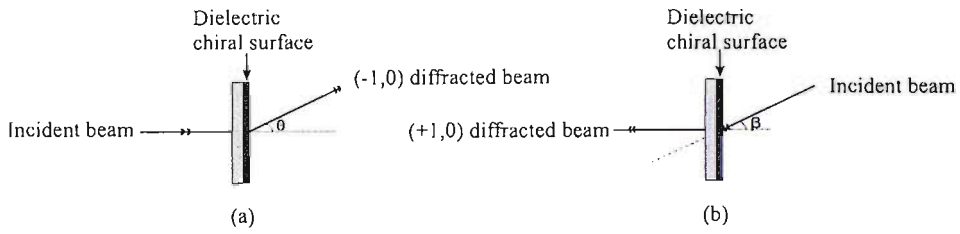

Figure 8.7: Schematic diagram of the experimental configurations to characterize the time-reversibility property of the silicon nitride chiral sample in the transmission regime. (a) time-forward process (b) time-reverse process.

light, with $\mathbf{J}(\phi_1,0)$ (for the I- and PT-processes) or $\mathbf{J}(-\phi_1,0)$ (for P- and T-processes), before introducing the quarter waveplate into the system. The quarter waveplate was then rotated until the beam coming out of the quarter waveplate became exactly the same linearly polarized light as was produced before the quarter wave-plate was introduced into the system. In this configuration, the fast and slow axes of the quarter waveplate are parallel and perpendicular to the electric field direction from the second linear polarizer. Next, the reverse inputs were created by keeping the configuration of the quarter wave-plate, and rotating the linearly polarizer until the required elliptical polarized reversed beam was produced, with $\mathbf{J}(\phi_1,\eta_1)$ for the I-process, $\mathbf{J}(-\phi_1,-\eta_1)$ for the P-process, $\mathbf{J}(\phi_1,-\eta_1)$ for the PT-process, or $\mathbf{J}(-\phi_1,\eta_1)$ (for the T-process). While adjusting the quarter waveplate, the polarization azimuth angle, ϕ, of the reversed beam was kept stable. Therefore, by using a combination of a linear polarizer and a quarter wave-plate, elliptically polarized light with the desired polarization azimuth angle and ellipticity was created.

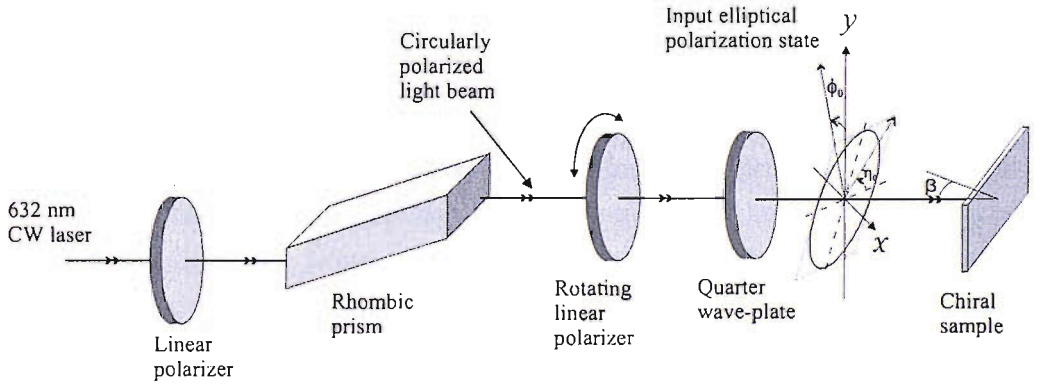

Figure 8.8: Experimental arrangement used to characterize the time-reversibility property of planar chiral metamaterials.

Fig. 8.9 shows the polarization states, including both ellipticity and polarization azimuth rotation, of the (+1,0) order diffracted beam reflected from an array of right-handed aluminium gammadions in the F-, T-, I-, P-, and PT-processes. For comparison, Fig. 8.10 plots the polarization states of the (+1,0) order diffracted

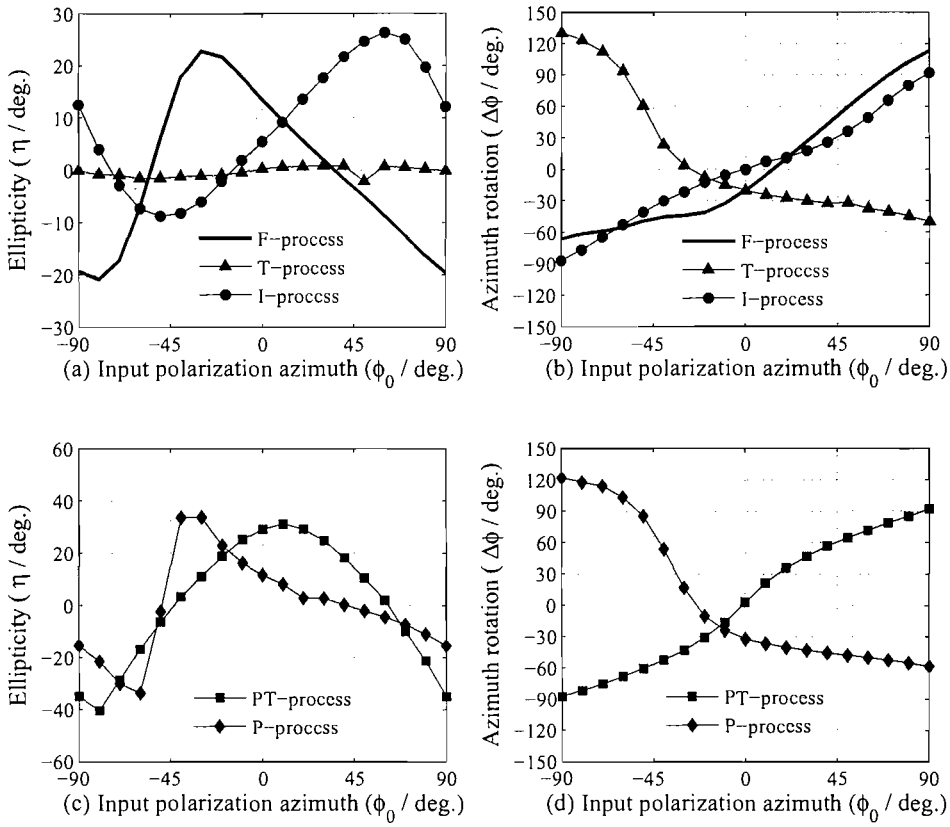

Figure 8.9: The polarization response for the (+1,0) order diffracted beam reflected from right-handed aluminium gammadion array in F-, I-, T-, P- and PT-process.

beam transmitted through an array of left-handed silicon nitride gammadions for the same processes. All of the data sets are plotted against the polarization azimuth angle of the linearly polarized incident for the F-process, ϕ_0. The data in both Fig. 8.9 and Fig. 8.10 provides clear evidence that the diffraction process for an individual diffracted beam from planar chiral metamaterials is in general non-reciprocal in both the reflection and the transmission regimes, as none of the I-, T-, P- or PT-processes fully recovered the relevant initial input state. If any of these processes were to satisfy the reciprocity requirements outlined above, the final ellipticity should be zero and the final polarization azimuth rotation angle should equal to $+\phi_0$ for the I- and PT-processes or $-\phi_0$ for the T- and P-processes. However, from Fig. 8.9 and Fig. 8.10 it can be seen that only the T-process resulted in an almost total cancelation of the ellipticity generated by the forward process, however, the output polarization azimuth rotation angle deviated significantly from the required linear dependence on ϕ_0. For the I-, P- and PT-processes, neither the azimuth nor

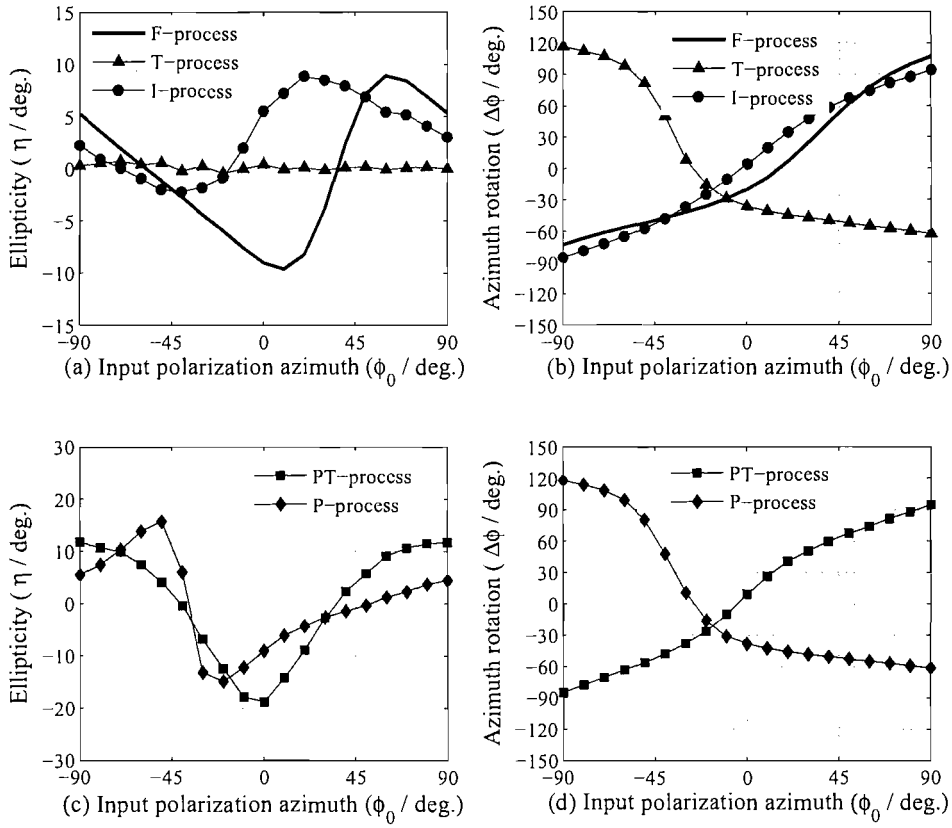

Figure 8.10: The polarization response for the (+1,0) order diffracted beam transmitted through left-handed Si_3N_4 gammadion array in I-, T-, P- and PT-process and (-1,0) order diffracted beam in F-process.

the ellipticity fully reversed to that generated by the forward process.

8.3.3 Conclusion

The light interactions with planar chiral metamaterials have been tested experimentally to be asymmetric for both forward and reverse diffraction paths. The forward and reverse light propagation processes through aluminium or dielectric planar chiral gratings can be related by spatial symmetry transformations. Through the polarization state measurements at specific configurations, the polarization changes for the first-order diffracted beams from planar chiral structures exhibit non-reciprocal and non-reversible properties, regardless of the chirality of the surface and the materials in which the planar chiral structures are created. These planar chiral structures are non-reversible under all the four processes (I, T, P, PT). This lack of reversibility is believed to be due in part to the birefringence and quantum interference effect

in the diffraction process. This agrees with the small polarization response seen in the planar chiral metamaterials created in the silica substrate discussed in Chapter 6. However, the reciprocity results clearly show there is a 2D chiral behaviour in the system. As a consequence, it can be deduced that the polarization response of these planar chiral structure arise from the combination of 2D chirality and birefringence. This provides further evidence to the mechanism behind the polarization response of these nanoscale planar chiral metamaterials as described in Chapter 6. These non-reciprocal effects are intriguing, however while non-reciprocity can only be observed for diffracted beams it is difficult to envisage useful applications. In order to replace the Faraday isolator for instance, non-diffractive systems preferably operating at normal incidence would be needed.

Chapter 9

3D dielectric multilayer stack with planar chiral waveguide

In this chapter a new device design comprised of a highly reflective dielectric multilayer stack in the middle of two planar chiral gratings is presented. The purpose of proposing this device is to test the symmetry of the planar chiral structures. Unfortunately although the devices described in this chapter were successfully fabricated, they were destroyed (by a serious fire) before any optical characterization could be performed. This chapter is being included as it provides design and fabrication information and insight that will be of assistance to a researcher wishing to continue the work.

9.1 Device design

As discussed in the previous chapters, the polarization state of light diffracted from planar chiral metamaterials is found to be manipulated in a manner that depends on the sense and magnitude of the chirality. However, such polarization effects have only been observed in the higher-order diffracted beams. When light is incident normal to a sample with 2D chirality, no significant polarization rotation or elliptization has been observed in the zero-order diffracted beam. However, since opposite diffraction orders have shown the same sense and magnitude of polarization rotation, they are unlikely to cancel with each other when recombined. This symmetry in the rotation of opposite diffraction orders suggests that a similar rotation should be present in the zero-order diffracted beam, but it is not. There are two possible reasons for this: either the zero-order beam is the subject of a fundamental symmetry that prevents it from experiencing any polarization change, or any change that does exist is being swamped by the intensity of light in the beam that has not interacted with the chiral

patterns.

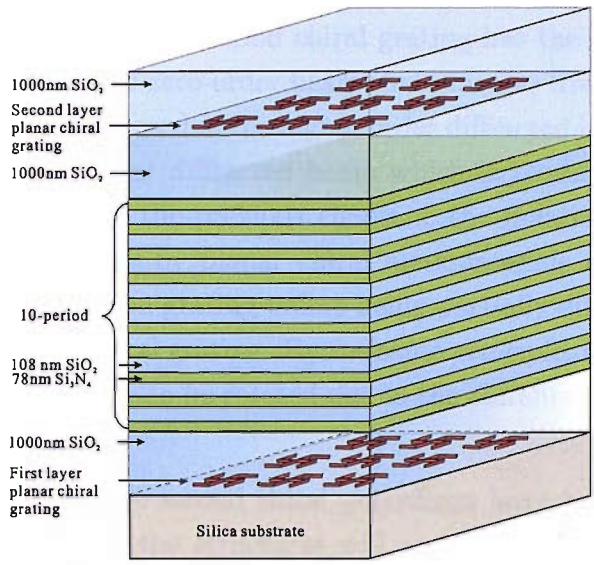

Figure 9.1: Schematic diagram of the structure of a high reflective dielectric multilayer stack integrated with two planar chiral gratings on both sides of the stack.

To test these two hypotheses the following device is proposed. Instead of a single chiral grating, two chiral gratings are deployed in series. The structure of this device is schematically illustrated in Fig. 9.1. The first chiral grating will diffract the light while the second will be used to recombine proportions of each diffracted beam from the first grating into a new set of diffracted beams. There is also a dielectric multilayer stack situated midway between the two planar chiral gratings. The dielectric multilayer stack is composed of ten periods of alternating layers of Si_3N_4 (with a refractive index of 2.05) and SiO_2 (with a refractive index of 1.46) films, where the thickness of each dielectric layer is calculated according to:

$$t = \frac{\lambda}{4} = \frac{\lambda_0}{4n_i} \tag{9.1}$$

where λ is the wavelength of the incident beam, and n_i is the refractive index of the dielectric material. Therefore, the thicknesses of the Si_3N_4 and SiO_2 layers, illuminated by a visible red light (λ=632 nm), are 78 nm and 108 nm respectively.

The purpose of this dielectric multilayer is to block the zero-order beam diffracted from the first chiral grating at a wavelength of 632 nm. As a consequence, it will reflect any light that passes through the first chiral grating that is not diffracted. Thus, it can be assumed that all the light in the remaining beams that emerge from the combination of the first diffraction grating and the dielectric multilayer will have interacted with the first chiral grating. Therefore, the higher order diffracted beams

from the first grating with a certain diffraction angle can pass through the dielectric multilayer and then be partially re-diffracted back into a single beam by the second diffraction grating, as long as the second chiral grating has the same period as the first one. As a result, the final zero-order beam that emerges from the second chiral grating must be entirely composed of the higher order diffracted beams from the first grating, but not the zero-order diffracted beam which is blocked by the dielectric multilayer. As introduced in the previous chapters, the polarization states of the higher order diffracted beams by planar chiral metamaterials are expected to be rotated by the first gammadion grating before being partially diffracted back into a single beam by the second chiral grating. By the same principle, all beams diffracted by the second grating should also be rotated due to the chirality of the second chiral grating.

It should be noted that the second chiral polysilicon layer has the opposite chirality to the first, therefore, the structures will appear to be reciprocal. It will however still appear asymmetric to any incident light ray, and therefore chiral. In this case, the chirality will be in three-dimensional rather than two-dimensional. Thus by reversing the chirality of the second polysilicon layer, a transition from 2D to 3D chirality can be achieved, and hence a comparison of the optical properties of each structure will indicate the relative contributions of 2D and 3D chirality in the optical response of these chiral metamaterials. If the single diffracted beam by the second chiral grating exhibits no polarization change compared to the input to the first chiral grating, it can only be due to an exact cancelation of the polarization rotations of different diffracted beams by the first chiral grating. As opposite diffraction orders do not cancel, this can only be interpreted as evidence of a fundamental symmetry for light interactions with the planar chiral materials. However, if the final zero-order beam is found to be rotated, then it would be evidence for the non-reciprocity of the planar chiral system.

9.2 3D dielectric multilayer mirror

9.2.1 Introduction

Dielectric mirrors composed of multilayer of high and low refractive index materials are very important optical device components. Such a stack is a simpler and more efficient way to control the light propagation than 3D photonic bandgap structures [93]. If the transition between two media is continuous, which means if the dielectric constant (or the refractive index) changes from that of one medium to that of the other over a distance of a wavelength or more, there will be very little

reflection and the interface effectively vanishes [5]. In contrast, a transition from one medium to the other over a distance of a quarter of a wavelength or less behaves like a discontinuous change [5]. The periodic spatial modulation opens up a forbidden gap in the electromagnetic dispersion relation irrespective of its propagation direction [94]. The prohibition of wave propagation in the forbidden gap makes these periodic dielectric structures ideal reflective mirrors. As a result, anti-reflection coatings, band-pass interference filters, dichroic mirrors and polarizing beam splitters are among the most common multilayer devices in use today [95].

9.2.2 Principles of reflection and refraction at the boundaries of multilayer thin films

For N periods of multilayer structure, the transmittance goes to zero rapidly at the band edges. Within the bandgap the reflectance tends to unity exponentially with N. Therefore only a small number of the multilayer periods are needed to give high reflectance [96]. This is because light which is reflected within the high-index layers (for example, Si_3N_4 layers) will not be phase shifted on reflection, while those beams reflected within the low-index layers (such as SiO_2 layers) will suffer a phase change of π. Therefore the various components of the incident light produced by reflection will reappear at the front surface in phase and recombine constructively. Thus the effective reflectance of the assembly can be made very high by increasing the number of layers [97].

Consider a linearly polarized wave as shown in Fig. E.1, impinging on a thin dielectric film with a thickness of d. Each wave $\mathbf{E}_{iI}$, $\mathbf{E}_{rI}$ and $\mathbf{E}_{tI}$ at boundary **I**; and $\mathbf{E}_{iII}$, $\mathbf{E}_{rII}$ and $\mathbf{E}_{tII}$ at boundary **II**, represents the resultant of all possible waves traveling in that direction at that point in the medium. According to the boundary conditions derived from Maxwell's equations, both the electric field ($\overrightarrow{\mathbf{E}}$) and the magnetic field ($\overrightarrow{\mathbf{H}}$) should be continuous across the boundaries. Therefore, the total electric and magnetic fields at boundary **I** and boundary **II** are related by the equation:

$$\begin{bmatrix} \mathbf{E}_i + \mathbf{E}_r \\ \mathbf{H}_i + \mathbf{H}_r \end{bmatrix} = M_1 \begin{bmatrix} \mathbf{E}_t \\ \mathbf{H}_t \end{bmatrix} \tag{9.2}$$

In which M_1, the *characteristic matrix*, relates the fields at the two adjacent boundaries. The characteristic matrix of a uniform, isotropic dielectric layer is:

$$M_1 = \begin{bmatrix} \cos(k_1 h) & i\frac{sin(k_1 h)}{\Upsilon_1} \\ i\Upsilon_1 \sin(k_1 h) & \cos(k_1 h) \end{bmatrix} \tag{9.3}$$

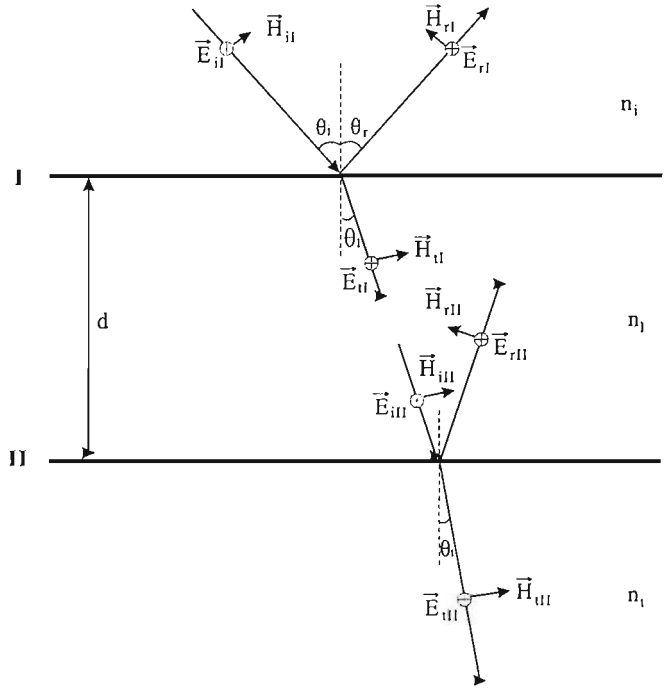

Figure 9.2: Schematic diagram illustrating the different electric field (**E**) and magnetic field (**H**) vectors at the boundaries of a dielectric layer of thickness d.

where

$$h = n_1 d \cos\theta_1 \tag{9.4}$$

When $\overrightarrow{\mathbf{E}}$ is perpendicular to the plane of incidence (TE mode), Υ_1 is given by:

$$\Upsilon_1 = \sqrt{\frac{\varepsilon_0}{\mu_0}} n_1 \cos\theta_1 \tag{9.5}$$

When $\overrightarrow{\mathbf{E}}$ is parallel to the plane of incidence (TM mode), Υ_1 is given by:

$$\Upsilon_1 = \sqrt{\frac{\varepsilon_0}{\mu_0}} \frac{n_1}{\cos\theta_1} \tag{9.6}$$

By extending the transmission and reflection scheme of a single dielectric layer to a multilayer dielectric stack, the characteristic matrix of a dielectric multilayer stack is:

$$M = M_1 M_2 M_3 \ldots M_n = \begin{bmatrix} m_{11} & m_{12} \\ m_{21} & m_{22} \end{bmatrix} \tag{9.7}$$

This characteristic matrix of the entire system connects the complex amplitudes of the electric and magnetic fields at the top and bottom surfaces of the stack for a particular polarization state. As a result, the amplitude reflection and transmission

coefficients r and t of a stack are given by:

$$r = \frac{\Upsilon_i m_{11} + \Upsilon_i \Upsilon_t m_{12} - m_{21} - \Upsilon_t m_{22}}{\Upsilon_i m_{11} + \Upsilon_i \Upsilon_t m_{12} + m_{21} + \Upsilon_t m_{22}} \tag{9.8}$$

$$t = \frac{2\Upsilon_i}{\Upsilon_i m_{11} + \Upsilon_i \Upsilon_t m_{12} + m_{21} + \Upsilon_t m_{22}} \tag{9.9}$$

This mathematical treatment to obtain the solution of the wave equations for a light wave propagating in a planar structures is known as the *transfer matrix method* (TMM). A detailed description of the derivation of the above solutions is included in **Appendix E.**

9.2.3 Simulation of 3D dielectric multilayer stack

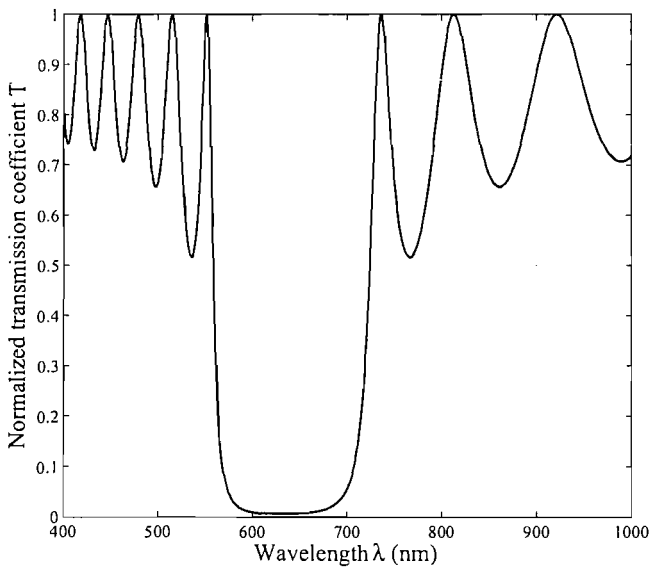

Figure 9.3: Simulated normalized transmission spectrum of normal incidence propagation in a periodic alternating Si_3N_4 and SiO_2 multilayer stack.

The transmission coefficient of a dielectric multilayer stack with alternating Si_3N_4 and SiO_2 layers was simulated in order to optimize its reflective behaviour at different angles of incidence and various optical wavelengths. While simulating this device, it was assumed that the arrangement of dielectric material was invariant with respect to continuous translation in the two orthogonal directions. A computer programming file was designed in MATLAB based on the TMM to calculate the reflection and transmission coefficients of the dielectric multilayer stack. By defining several variables, including the number of layers in the stack, N; both the high and low refractive indices of the alternating layer, n_h and n_l; the thickness of

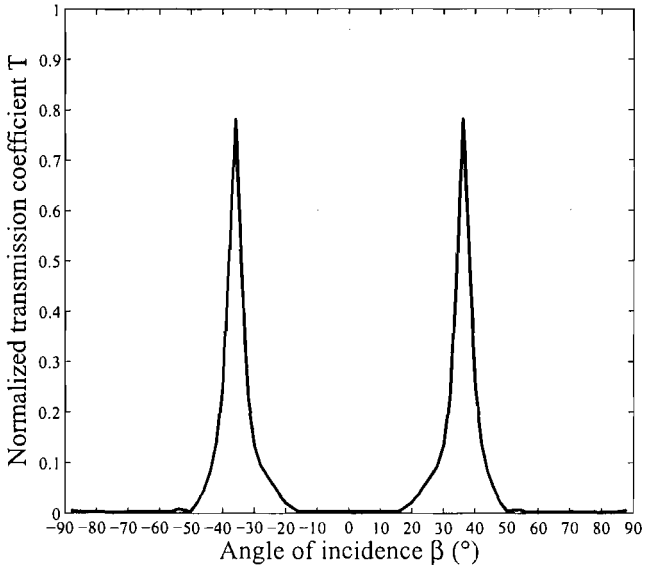

Figure 9.4: Simulated normalized transmission coefficient propagation in a periodic alternating Si_3N_4 and SiO_2 multilayer stack as a function of angle of incidence.

each layer, t_h and t_l; the angle of incidence, β; as well as the range of spectrum under investigation; the normalized reflection coefficient, R, and transmission coefficient, T, were calculated over a specified wavelength range. As a result, the dependence of light interactions with the dielectric multilayer structure on the wavelength of the incident beam was obtained. Fig. 9.3 shows the simulation results of the normalized transmission coefficient (T) through a ten-period Si_3N_4/SiO_2 dielectric multilayer stack as a function of wavelength (λ) at normal incidence. It clearly shows that this dielectric multilayer structure acts as a filter to prevent any incident beam being transmitting within a wavelength range between approximately 580 nm and 710 nm. Fig. 9.4 shows the simulation results of the normalized transmission coefficient (T) through the same Si_3N_4/SiO_2 multilayer stack as a function of angle of incidence, β, at a visible wavelength (λ = 633 nm). From Fig. 9.4, it can be seen that the when the angle of incidence is in a range of about 18° to 50° and -50° to -18°, the transmission coefficient is not zero and different portion of the incident beam is transmitted through the dielectric multilayer. However no light transmits through at normal incidence, indicating that the zero-order transmitted beam will be blocked by the designed dielectric multilayer stack at normal incidence. Due to the fact that the maximum transmission is obtained when the angle of incidence is approximately ±36°, the first chiral grating should be designed in order that the diffraction angle of the first-order diffracted beam is equal to ±36° to guarantee the first-order diffracted beams can transmit through the first chiral grating at a wavelength of 632 nm. In

summary, according to the simulation results, by designing both the chiral gratings and the dielectric multilayer appropriately, this device can highly reflect the zero-order beam diffracted from the first chiral grating while transmit the higher-order diffracted beams.

9.2.4 Fabrication of 3D dielectric multilayer stack

The Si_3N_4 and SiO_2 dielectric multilayer stack was fabricated by the use of PECVD. PECVD is a fast and popular method to deposit layers reliably in the microelectronics and optoelectronic industry, where the requirements are often very high regarding structural homogeneity of the deposited layers, but less stringent with respect to thickness tolerances. As described above, the required thicknesses of Si_3N_4 and SiO_2 layers are a quarter of the wavelength of visible red light of 632 nm, which leads to thicknesses of 78 nm and 108 nm respectively. The layer thickness must be accurate to a few nanometers throughout the whole deposition process. Additionally, the surface roughness and the total thickness variation across the whole substrate must be minimized to obtain homogeneous spectral properties at all locations on the wafer.

A standard 4-inch crystalline silicon wafer and a 4-inch, 0.75 mm thick fused silica substrate were used to fabricated the dielectric multilayer stack. The silicon wafer was processed to calibrate the PECVD process and the silica wafer was chosen for the purpose of optical characterizations. An Oxford Plasmalab System 90 (OPT90) machine was used to deposit the PECVD layers. The gases used to deposit Si_3N_4 and SiO_2 films include silane (SiH_4), nitrogen oxide (N_2O) and ammonia (NH_3). The process conditions of depositing Si_3N_4 and SiO_2 are listed in Table 9.1.

Film	Pressure		Gases (sccm)				Power (W)		Temp (°C)
-	Base (T)	Run (mT)	SiH_4	NH_3	N_2O	CH_4	FOR	REF	-
Si_3N_4	4.5e-6	502	779	51	-	-	9	0	302
SiO_2	2.1e-6	1006	158	-	712	-	19	0	301

Table 9.1: PECVD process conditions for depositing Si_3N_4 and SiO_2 thin films.

The process began with 10 to 15 minutes of plasma cleaning in the process chamber using CH_4 and O_2 gas mixture with a flow rate of 40 standard cubic centimeter minute (sccm). Then the process chamber was heated up to the deposition temperature, 300°C. In order to provide a constant environment during depositions, the process chamber was conditioned before the substrates were introduced by precoating the inside of the chamber with the material to be deposited on the substrates.

As the mirror deposition involved alternating the materials, the chamber was conditioned with the second material before depositing the first one on the wafer. For the purpose of characterization, single layers of Si_3N_4 and SiO_2 were first deposited on two test silicon substrates individually before the multilayer stack deposition. The thicknesses of the deposited single layers of Si_3N_4 and SiO_2 were measured using a Nanometrics Nanospec AFT 4150 ellipsometer, assuming the standard values for the refractive indices of the investigated materials ($n = 1.46$ for silicon dioxide and $n = 2.05$ for silicon nitride at a wavelength of 632 nm). This thickness measurement, therefore, provided information on the deposition rate of the two dielectric materials. These calibrated deposition rates were used afterwards in the multilayer stack deposition. Next, the substrate was loaded into the loading compartment (load-lock) of the machine. After the load-lock was evacuated, the plate which supported the substrate was transferred into the processing chamber and its temperature was brought up to the deposition temperature (300°C). The thermal inertia of the plate was large and the heat was transferred to the substrates by contact and radiation in high-vacuum conditions. When the pressure in the processing chamber reached the specified deposition level, the deposition started. Before the deposition of the multilayer stack, a 1000nm SiO_2 thick layer was grown to create a buffer layer for the growth of the multilayer stack. Then the deposition process of ten-period of alternating Si_3N_4 and SiO_2 layers began. Finally, another 1000nm thick SiO_2 layer was deposited on the top of the dielectric multilayer stack to create a symmetrical profile.

Steps	Fabrication process
1	Plasma clean
2	Substrat heating
3	Si_3N_4 condition running
4	SiO_2 cycle
5	Si_3N_4 cycle
6	First SiO_2 layer deposition
7	Si_3N_4 + SiO_2 multilayer stack deposition
8	Top SiO_2 deposition
9	Vent pump load

Table 9.2: Fabrication process of periodic Si_3N_4 and SiO_2 dielectric multilayer stack by PECVD.

The main fabrication processes of the dielectric multilayer stack with alternating Si_3N_4 and SiO_2 layers are listed in Table 9.2. This multi-step deposition recipe was designed using a computer controlled software, which was integrated into the PECVD system to obtain an accurate deposition profile of a repeating multi-period stack. The deposition environment, including gases flow rate, temperature and pressure, were all monitored and controlled automatically by this system. The

surface roughness of the deposited layers were assessed with an Alpha Step 200 surface profilometer, and was found to be approximately $\lambda_{visible}/100$. This good surface roughness confirmed the suitability of the fabricated dielectric multilayer stack for its optical applications in the visible range of the spectrum. Fig. 9.5 shows a SEM image of a cross-sectional view of the fabricated Si_3N_4/SiO_2 multilayer stack. The image shows each single layer to be well defined with good thickness uniformity. Fig. 9.6 is a SEM image with high magnification illustrating the cross section of two alternating Si_3N_4 and SiO_2 layers deposited on a silicon wafer. The bottom layer (layer 1) is Si_3N_4 with a thickness of about 79 nm, and the top layer (layer 2) is SiO_2 with a thickness of about 106 nm. These thicknesses are very close to the required thicknesses, which provides additional evidence of the accuracy of the film thickness control throughout the PECVD deposition process.

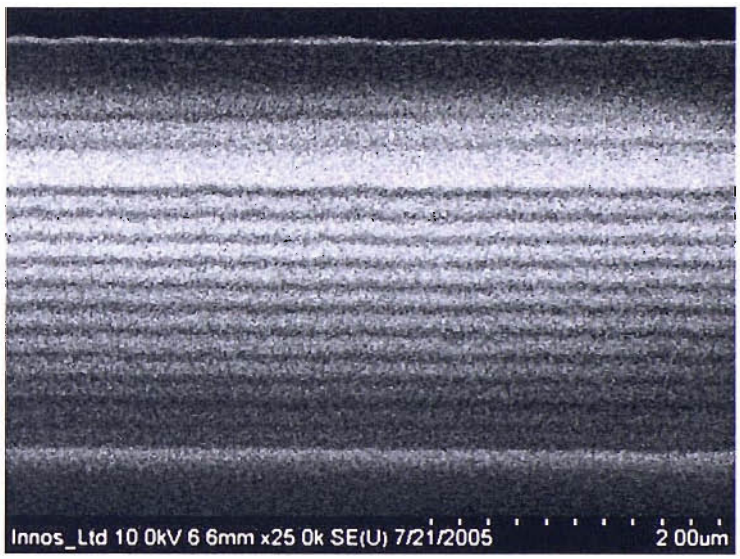

Figure 9.5: SEM image of the cross section of a multilayer stack with ten-period of alternating Si_3N_4 and SiO_2 uniform layers deposited by PECVD.

9.2.5 Transmission measurement

After the dielectric multilayer mirror was fabricated by PECVD, its optical properties were investigated. The transmission spectrum of this dielectric multilayer stack was measured using a custom designed optical system. A schematic diagram of the experimental arrangement of this system is shown in Fig. 9.7. The light source used was a white light super continuum source, which was polarized using a Glan Thompson polarizer. The polarizer was mounted in a 360° rotation stage to change the polarization state of the light source. The incident beam was coupled into the sample via a $\times 40$ microscope objective, which was mounted on a high precision

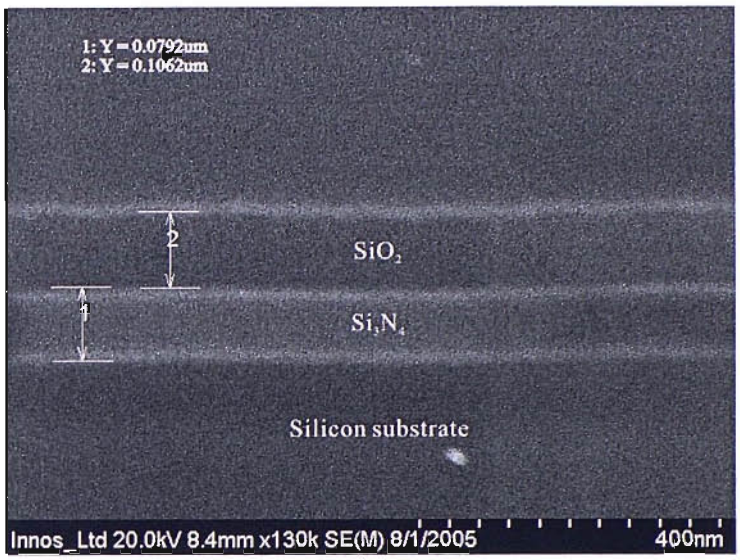

Figure 9.6: SEM image of single Si_3N_4 and SiO_2 layers deposited on a silicon substrate by PECVD.

3-axis flexure stage. The sample was mounted on a high precision 5-axis flexure stage to allow the position of the sample to be adjusted in three dimensions. The transmitted beam through the sample was then collected by a telecom optical fibre with a 125 μm diameter and 8 μm core diameter, which was mounted on another high precision 3-axis flexure stage using a V-groove fibre holder. A camera with a $\times 10$ zoom lens was used to increase the accuracy of the alignment of the input coupling and of the collection fibre.

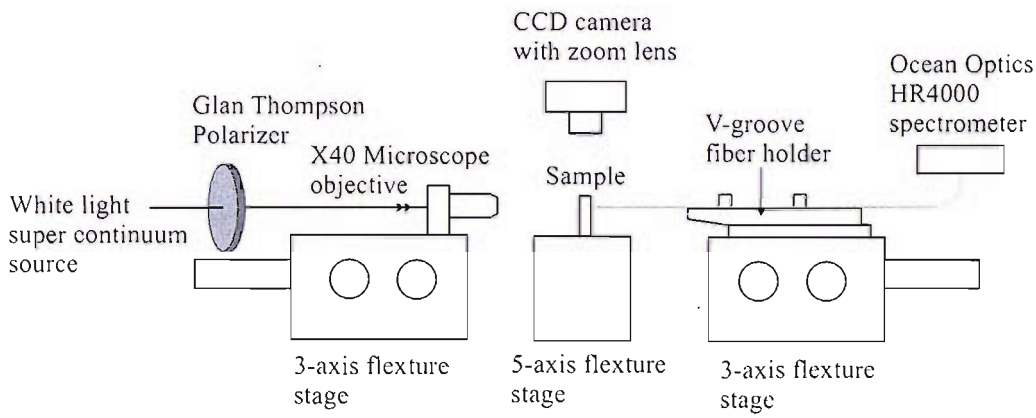

Figure 9.7: Schematic diagram of the experimental arrangement used to measure the transmission spectrum of the dielectric multilayer stack.

By using this optical system, the normalized transmission spectrum of the dielectric multilayer stack at normal incidence was measured as a function of the optical wavelength. The results are shown in Fig. 9.8, and the simulated normalized transmission spectrum is plotted in the same figure, which clearly shows that the

measurement matches the simulations very well. The fabricated dielectric multilayer stack reflects almost all of the incident light at visible red light wavelength (632 nm), as predicted by theoretical calculation. The excellent agreement between the experimental results and the simulated results also provided further evidence of the successful fabrication of the device.

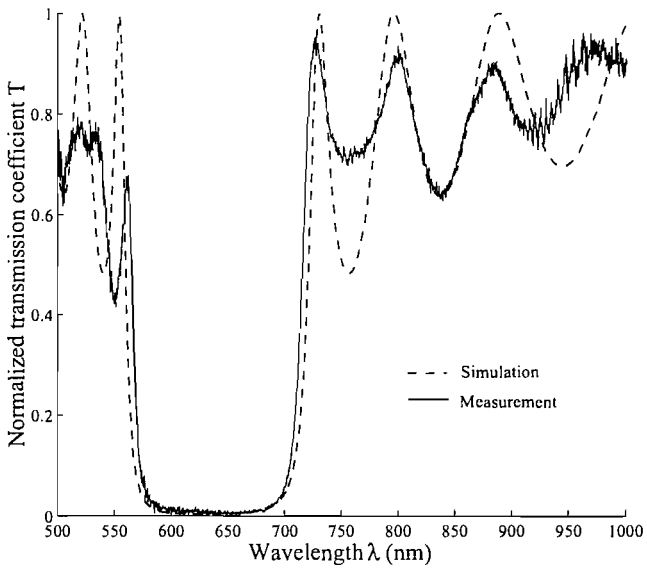

Figure 9.8: A comparison of simulation data and experimental measurements for normalized transmission spectrum of normal incidence through the periodic Si_3N_4/SiO_2 multilayer stack.

9.3 Fabrication of 3D dielectric multilayer mirror with planar chiral waveguide

Following the successful fabrication of the dielectric multilayer stack, a 3D device that combines this dielectric multilayer stack and two planar chiral gratings was fabricated. The starting materials were 1 mm thick, 100 mm diameter, double optically polished fused silica wafers. The use of double-polished wafers was essential to perform subsequent optical transmission experiments on the planar chiral structures in the visible, infra-red and microwave regimes.

First, the wafers were cleaned in fuming nitric acid for 10 minutes. Before depositing the first polysilicon layer upon the silica substrate, a photolithography stage was performed to create a set of global optical alignment marks (ALN) defined by etching 2 μm holes into the silica substrate using OPT80 in a mixture of CHF_3

and Ar. These alignment marks were used to align the first EBL process. Next, a 100 nm uniform polysilicon layer was deposited by low temperature chemical vapour deposition (LPCVD) on one side of the ultrasonically cleaned silica substrates at a temperature of around 610°C. Then a 400 nm thick layer of UVN30 electron beam resist was spun on the top of the thin polysilicon layer. The resist was then exposed with a high density of chiral gammadion patterns by EBL as described in chapter 4. After the resist development stage, the polysilicon layer was etched in a mixture of HBr, Cl_2 and O_2 gases to form millions of isolated gammadion-shaped mesas on the silica substrate. Fig. 9.9 includes two SEM images of chiral gammadion-shaped mesas etched into a thin polysilicon film deposited on a fused silica substrate. Next, a 1000 nm thick SiO_2 layer was deposited on the top of these nanoscale chiral structures by PECVD to provide a flat and smooth surface before the dielectric multilayer stack deposition process. Then the dielectric multilayer stack composed of periodic alternating Si_3N_4/SiO_2 layers was fabricated by PECVD followed by a 892 nm SiO_2 buffer layer.

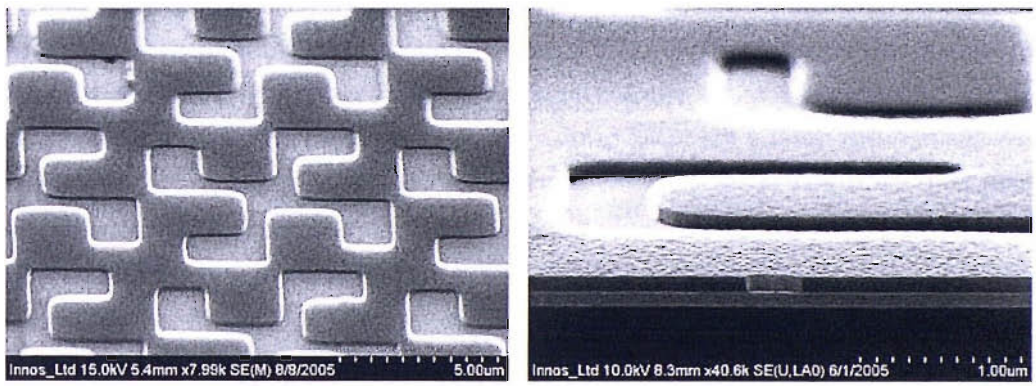

(a) (b)

Figure 9.9: SEM images of gammadion-shaped planar chiral mesas fabricated in a thin polysilicon film deposited on a fused silica substrate. (a) plane view (b) cross-sectional view.

The next step was the fabrication of the second chiral gammadion layer on the top of the dielectric multilayer stack. The second planar chiral grating was required to form a symmetrical profile compared to the first chiral grating underneath the dielectric multilayer stack. Therefore, an accurate alignment between the two planar chiral gratings became a very important issue. For this device, it is very important that the planar chiral elements on the second chiral grating have the same characteristic parameters as those on the first grating. Equally important, the two layers of chiral gammadion gratings need to be aligned accurately so that the axes of the two arrays coincide and the arrays themselves overlap as closely as possible. Unfortunately the thick dielectric multilayer stack makes it very difficult for the EBL

process to 'image' the global alignment marks on the first patterned polysilicon layer and therefore to align to them directly. To solve this problem a second optical photolithography stage was applied before the fabrication of the second planar chiral grating. This optical layer was aligned to the global alignment marks first, followed wet etching in 7:1 buffered HF solvent to etch deep holes through the thick multilayer dielectric stack. Considering the thickness of the dielectric multilayer stack plus the two thick silicon dioxide capping layers on either side of the stack, the total etch depth is about 4 μm. A thick layer of optical resist S1812 (2.2 μm) was spun on the sample surface to prevent the etch solvent from attacking any structures underneath the resist. An Alpha Step 200 surface profilometer was used to calibrate the etch rates of Si_3N_4 and SiO_2 deposited by PECVD, which was about 250 nm/min. As a result, this wet etch process took about 15 to 16 minutes to etch deep trenches through almost 4 μm thick dielectric multilayer stack down to the silica substrate. The long wet etch time also required a thick layer of optical resist to protect the sample surface. By etching trenches through the dielectric stack, the global alignment marks were able to be seen clearly when applying the second EBL stage. This allowed accurate alignment between the two EBL stages. The second polysilicon chiral gratings were processed under the same conditions as the first one, thereby creating a symmetrical profile. At the end, a final 1000 nm silicon dioxide cap layer was deposited on the top of the second chiral grating to form a symmetrical profile to silica substrate and to planarize the surface. The chiral patterns defined on the two polysilicon layers were varied on different chips. The design details are listed in **Appendix A**.

In summary, the fabrication process of the highly reflective dielectric multilayer mirror with planar chiral metamaterial waveguide is schematically shown in Fig. 9.10. A complete fabrication process list is provided in **Appendix B**.

9.4 Summary

A new multilayered device, designed to investigate the symmetry properties of planar chiral metamaterials was successfully fabricated. PECVD technique was applied to the fabrication of thin silicon nitride and silicon dioxide alternating multilayer stack. The normalized transmission spectrum of the fabricated dielectric multilayer stack was characterized by a custom designed optical system. The intermediate optical measurements showed the highly reflective nature of the dielectric multilayer stack in good agreement with the simulated results. Although these devices looked very promising they were lost before any results could be obtained. Suggestions for the future optical characterizations of such devices are provided in the next chapter.

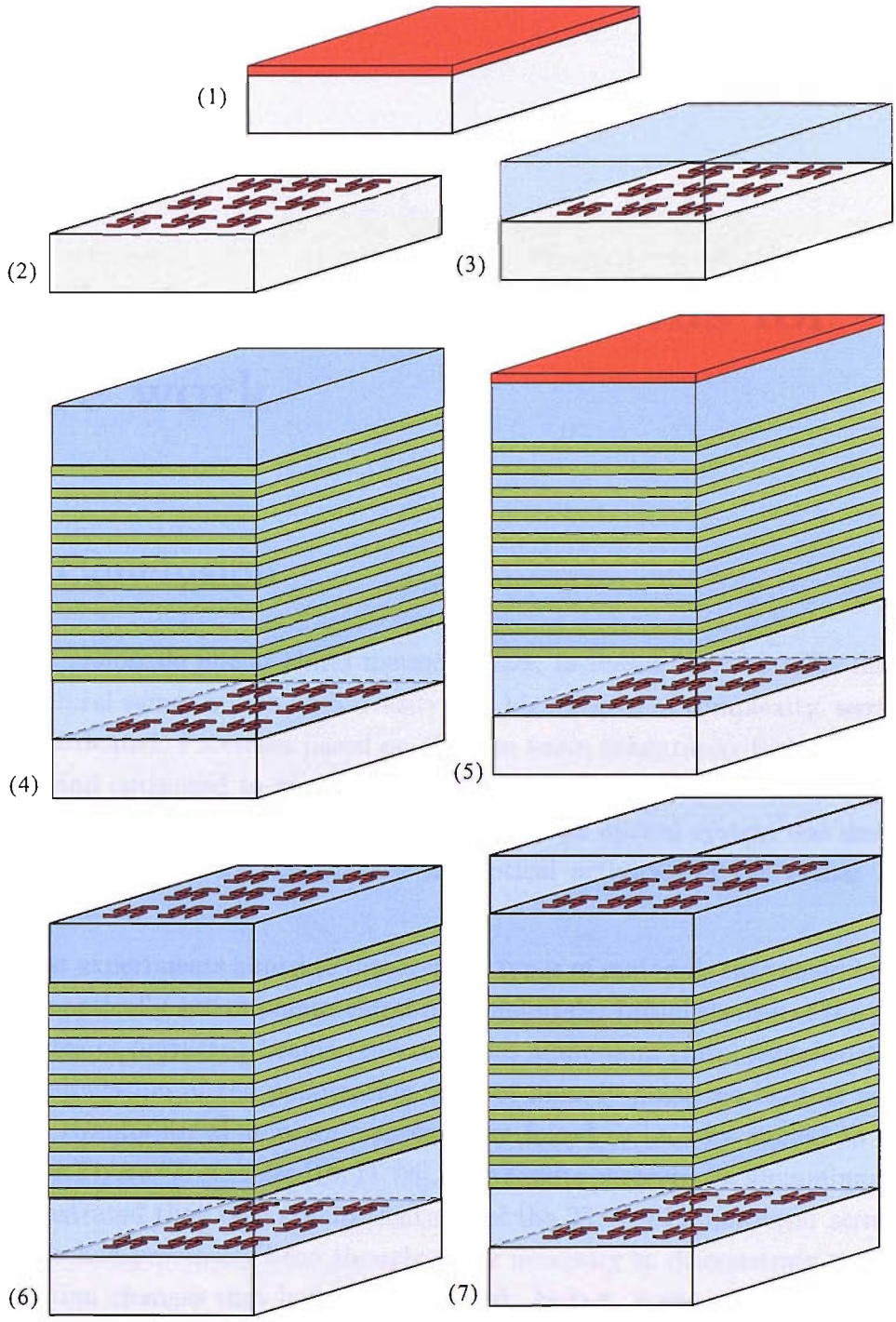

Figure 9.10: Fabrication process of a dielectric multilayer stack with planar chiral waveguide. (1) Polysilicon deposition (2) First chiral grating patterning by EBL (3) SiO_2 PECVD (4) Si_3N_4 and SiO_2 multilayer deposition by PECVD (5) Second polysilicon layer deposition (6) Second chiral grating patterning by EBL (7) Top SiO_2 layer deposition.

Chapter 10

Conclusion and suggestions for future work

10.1 Conclusion

A range of nanoscale planar chiral metamaterials, including both metallic and all-dielectric chiral samples with high density and high degree of complexity, were successfully fabricated. Processes based on electron beam lithography technology were developed and optimized to produce a broad range of metamaterials with very particular specifications. Additionally, a multi-functional optical system was designed and implemented to fully characterize the optical activities of the planar chiral metamaterials.

The first experiments aimed to discover the types of materials that could be used to produce optically active planar chiral metamaterials. Initial studies of the polarization states of diffracted beams reflected from aluminium chiral samples showed strong manipulation of the polarization state of linearly polarized light at normal incidence. Results for aluminium samples were found to be very similar to those reported for Ti/Au/Ti samples [10, 11, 58]. The results observed for aluminium samples demonstrated that very specific features of the Ti/Au/Ti multilayer structure were not, as had previously been thought, fully necessary to demonstrate the types of polarization changes that had been observed. In fact, a single layer of an arbitrarily selected metallic layer could yield very similar results. These results suggest that the fundamental mechanisms that drive the polarization behaviour of planar chiral metamaterials are less to do with the nature of the metal and are much more strongly dependent on the chirality index of the designs.

To further explore material issues a second generation of planar chiral metamate-

rials were produced using only dielectric materials. These new class of planar chiral metamaterials fabricated using only "loss-less" dielectric layers were also found to exhibit strong optical activity in reflection and in transmission. The complete absence of any metallic features showed that induced currents or plasmons were not required as part of the fundamental mechanism that produced polarization activity in planar chiral metamaterials as had been previously thought.

The polarization behaviours observed for these new dielectric planar chiral metamaterials have been found to be rather similar to those of the metallic planar chiral metamaterials, despite the very different properties of the materials used; polarization experiments carried out on the dielectric planar chiral samples have shown that changes to design features such as the bending angle (and thereby chirality index) have a pronounced effect on the magnitude and sense of the polarization response of the planar chiral metamaterials. Once again the planar geometry is seen to be a very important parameter in determining the optical activity of the planar chiral metamaterials. Additionally, the polarization response of the dielectric planar chiral metamaterials was shown to be dependent on the thickness of the film in which the planar chiral structures were created. However, no polarization change was observed in the planar chiral metamaterials created directly in uncoated fused silica substrate.

By analyzing the polarization data from various Si_3N_4 chiral samples, it was demonstrated that the light-matter interactions with these planar chiral structures was a linear optical effect and was governed by the principle of superposition. It was found that the degree of orthogonality of the pair of polarization eigenstates (ellipticity and azimuth rotation angle) appeared to depend considerably on the thickness of the Si_3N_4 film. This was mainly due to changes in the ellipticity of the respective eigenstates as the film thickness was varied. This suggested that the polarization changes were, in part, a consequence of multiple interference effects in the Si_3N_4 film. This interference, when combined with the planar chiral structures in the film, resulted in differing phases and amplitudes for the vertical and horizontal polarization components for most of the diffracted beams, and hence induced changes in ellipticity. This is now believed to be the most promising direction for further studies looking to understand the underlying mechanisms that produce polarization response of planar chiral metamaterials.

The optical intensity response of the first-order diffracted beams from planar chiral metamaterials was also studied. Significant intensity modulation with input polarization state was observed when samples were illuminated by linearly polarized light at normal incidence. This intensity modulation also exhibited a dependence on the chirality and geometry of the planar chiral structures as well as the thickness of the active layers.

Polarization sensitive photodetectors have been produced by fabricating planar chiral metamaterials on the surface of a pn^+ silicon photodiode. When illuminated with linearly polarized light, intensity modulation was observed as a function of the input polarization state. Left-handed and right-handed chiral photodiodes were shown to produce different photocurrent when illuminated by the same linearly polarized light. Although further work is required to study these effects, it seems that the planar chiral metamaterials can cause a significant polarization-dependent modulation of the photocurrent. Given that the zero-order beam is as much as 90% of the sum of transmitted light and exhibits no polarization response, it seems that all of the higher-order diffracted beams are significantly affected and certain polarizations might be mostly reflected and others mostly transmitted [8, 56].

The reciprocal properties of planar chiral metamaterials have been investigated in detail, several experiments have shown that the polarization changes for the first-order diffracted beams are generally non-reciprocal, with equivalent diffracted beams producing different polarization changes when the sample was illuminated from the forward and reverse directions. The light interactions with planar chiral metamaterials were demonstrated experimentally to be asymmetric for both the forward and the reverse diffraction paths, related by spatial symmetry transformations. This non-reversible property was proved to be independent on the chirality of the surface and the materials in which the planar chiral structures were created.

This work has done much to progress the understanding of planar chiral metamaterials and has provided an opportunity for much scientific discussion, however obtaining a detailed fundamental understanding of the mechanisms involved still remains a challenge. In the mean time, the strong polarization and intensity anisotropy of the optical transitions exhibited in planar chiral metamaterials make them particularly promising components for use in integrable solid-state polarization sensitive devices. Additionally, the global significance of the polarization modulation results obtained from planar chiral metamaterials is that they allude to the possibility of creating non-reciprocal optical structures from materials that are inherently non-magnetic. Therefore, planar chiral metamaterials offer a unique opportunity for the detection, control and modulation of the polarization state of light in a very compact planar layer integrated in nanoscale photonic devices. These could include polarization sensitive detectors, polarimeters, beam splitters, or polarization sensitive spectral filters. To date chiral metamaterials have been developed to provide scientific insight, now work is required to optimize structures for specific applications, fortunately the availability of well developed micro- and nano-fabrication technologies make structural variation a relatively easy task, however, there is a large parameter space to explore and without a full fundamental understanding this

could be a time consuming process.

Although there is a high possibility that useful applications can be developed, there remains a number of problematic issues that may prevent any significant applications being realized. Of these difficulties the most fundamental one is the fact that the zero-order beam has failed to show any polarization changes either in the reflection or the transmission regimes. Although significant polarization responses and intensity modulations are observed in the first-order diffracted beams from the planar chiral metamaterials, the optical intensities are much less than the optical intensities of the zero-order beam. This will seriously limit the applications of planar chiral structures as efficiencies and accuracies of detection systems will be reduced to around 10% at best.

So far all of the planar chiral metamaterials investigated are fabricated with chiral features at around the wavelengths scale and this causes beams to be diffracted. If it were possible to reduce the dimensions of these planar chiral structures to sub-wavelength scale, there would be no diffraction and applications could be more readily anticipated. However, it is far from clear that sub-wavelength planar chiral elements would interact sufficiently to provide any optical activity.

At the outset of this project there was some confidence that non-diffractive, normal incidence, non-reciprocal optical devices could be created from planar chiral metamaterials, at this point it seems a more distance possibility and at best it is likely that any useful non-reciprocal devices would be more complicated than simple single layers, in this work a complex non-reciprocal device has been suggested, this new device would work at normal incidence, and if

properly tuned would transmit a single beam, however, losses of this device would be very large. In the short term, the most likely application of optical planar chiral metamaterials will be in polarization sensitive detection and polarimetry where integrable, solid-state systems can be envisaged that could replace expensive Stokes' filter based systems.

10.2 Suggestions for future work

Two parts of this project were curtailed by a very serious fire that occurred in Southampton in October 2005. It is clear that further work on the polarization sensitive photodiodes could yield some very interesting results with very direct applications. The dielectric multilayer stack with planar chiral structures described in chapter 9 should be re-fabricated, this type of device would allow some very simple and very exciting non-reciprocity and symmetry tests to be performed.

Beyond work that was planned in detail but not carried out, there are a great many experiments that could yield interesting results in the future...

All the planar chiral metamaterials fabricated so far contained planar chiral elements that are larger than the optical wavelengths of the incident beam. It would be interesting to explore the optical activity of planar chiral metamaterials fabricated on a sub-wavelength scale. By doing this, diffraction will be removed and characterization will be easier and applications will be much more tangible. Evidence available suggests that sub-wavelength structures might demonstrate strong optical activity [61, 66]. Exploration of optical activity of sub-wavelength planar chiral metamaterials can be proceeded in two ways, either by using existing structures at longer wavelengths (existing light sources and polarimetry system are not applicable anymore) or by fabricating new planar chiral metamaterials with much smaller (and much more challenging) feature size. In fact, two new wafers with silicon nitride planar chiral structures of a characteristic size of 50 to 100 nm have recently been fabricated. A wide range of nanostructures, such as chiral gammadions, L-shapes, H-shapes, I-shapes and simple crosses are included in the design that currently awaits characterization.

A large number of experiments could be readily carried out using the equipment and the chiral samples already discussed. Studies of the polarization response of planar chiral metamaterials with angle of incidence, the optical activities of higher-order (m>1) diffracted beams and of the polarization responses at different wavelengths have not yet been completed, and yet each might offer greater insight into fundamental mechanisms and might indicate new application routes.

Most of this work has focussed on the chiral gammadion structures, and yet a large number of alternative chiral elemental and structural patterns can be conceived. Triskella (three-legged gammadions) and six-legged gammadions would be interesting "elemental" systems that are not birefringent at normal incidence. Arrays of such elements could be arranged in patterns of different symmetry or they could be randomly arranged or randomly orientated. Patterns based on quasi-crystalline schemes, tiling schemes and fractals can also be realized. By designing metamaterials with these varied forms of symmetry arrangements it should be possible to adjust the angular, directional and responses of metamaterials. Patterns including fractals and different feature sizes would also broaden spectral responses. A great many options of these various chiral structures may bring new applications.

The semi-empirical mathematical model [84] established to calculate the associated polarization eigenstates could be extended to multi-wavelengths system based on the future experiments. The Stokes parameter can be determined by the related polarization eigenstates, which allows to predict many of the polarization dependent

properties of planar chiral metamaterials. It is believed that such a system can be used to facilitate the manufacture of a new range of polarization measurement devices that do not require the inclusion of multiple waveplates in the future. Such devices will have many competitive advantages, including reduced cost, increased reliability and ease of use.

Appendix A

Mask Layout Details

In this appendix, details of the mask layout for individual planar chiral sample, the silicon photodiode with planar chiral structures, and the dielectric multilayer stack with planar chiral waveguide are given. The masks include electron beam masks and standard optical masks. All the masks were first designed in Tanner EDA L-Edit CAD layer design tool (version 11.0) [98]. The basic unit is a cell and a cell can include another cell as an instance. The highest level cell, called 'topcell', shows the distribution of the different design across the wafer. It includes the cells for all different designs. All these description on each mask is easy to follow on a computer with the corresponding L-edit file, opening the cells according to the description. Only a few schematic diagrams of the mask layout are given. The designs can be viewed efficiently from the computer screen, where zooming in and out is easily possible.

A.1 Dielectric planar chiral metamaterials (KB47W)

Mask KB47W is designed to fabricate the loss-less dielectric planar chiral metamaterials, including the silicon nitride chiral samples and the silicon dioxide chiral samples. A capture of the 'topcell' of the mask KB47W is shown in Fig. A.1. There are 16 chips distributed on the mask and they are arranged in a simple square matrix. The different designs on each chip are schematically illustrated in Fig. A.2. Table A.1 lists the names of all the chiral gratings and characteristic dimensions of different designs.

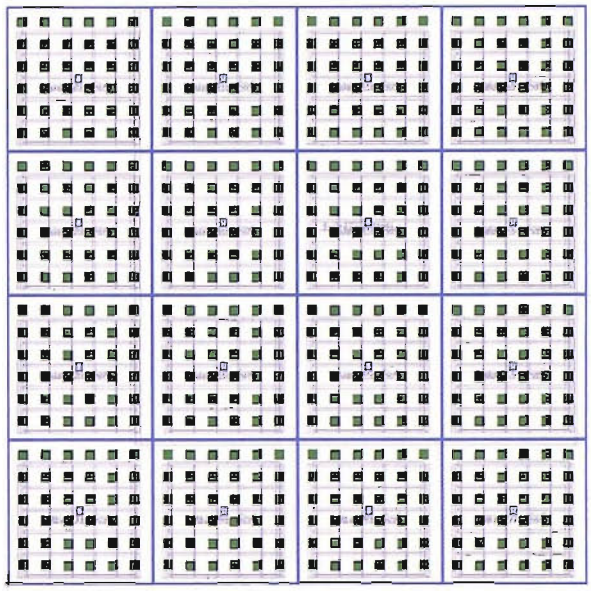

Figure A.1: Layout (topcell) of mask KB47W used to fabricate the dielectric planar chiral metamaterials.

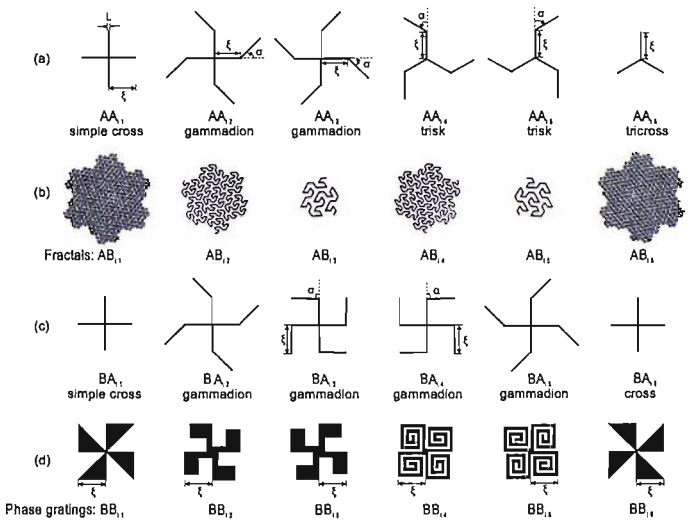

Figure A.2: Schematic diagram of the different microstructures distributed on mask KB47W (a) Chip AA (b) Chip AB (c) Chip BA (d) Chip BB.

KB47W Grating	Design	Horizontal pitch size $\Lambda_h(\mu m)$	Vertical pitch size $\Lambda_v(\mu m)$	Arm length ξ(nm)	Bending angle $\alpha(^\circ)$	Line Width L(nm)
AA11	Cross	8	12.5	1.4	0	200
AA21	Cross	8	12.5	1.8	0	200
AA31	Cross	8	12.5	2.2	0	200
AA41	Cross	8	16	1.4	0	200
AA51	Cross	8	16	1.8	0	200
AA61	Cross	8	16	2.2	0	200
AA12	Gammadion	8	12.5	1.4	-45	200
AA22	Gammadion	8	12.5	1.8	-45	200
AA32	Gammadion	8	12.5	2.2	-45	200
AA42	Gammadion	8	16	1.4	-45	200
AA52	Gammadion	8	16	1.8	-45	200
AA62	Gammadion	8	16	2.2	-45	200
AA13	Gammadion	8	12.5	1.4	45	200
AA23	Gammadion	8	12.5	1.8	45	200
AA33	Gammadion	8	12.5	2.2	45	200
AA43	Gammadion	8	16	1.4	45	200
AA53	Gammadion	8	16	1.8	45	200
AA63	Gammadion	8	16	2.2	45	200
AA14	Trisk	8	8	1.2	-60	200
AA24	Trisk	8	8	1.6	-60	200
AA34	Trisk	8	8	2	-60	200
AA44	Trisk	8	14	1.2	-60	200
AA54	Trisk	8	14	1.6	-60	200
AA64	Trisk	8	14	2	-60	200
AA15	Trisk	8	8	1.2	60	200
AA25	Trisk	8	8	1.6	60	200
AA35	Trisk	8	8	2	60	200
AA45	Trisk	8	14	1.2	60	200
AA55	Trisk	8	14	1.6	60	200
AA65	Trisk	8	14	2	60	200
AA16	Tricross	8	8	2.4	0	200
AA26	Tricross	8	8	1.6	0	200
AA36	Tricross	8	8	2	0	200
AA46	Tricross	8	14	2.4	0	200
AA56	Tricross	8	14	1.6	0	200
AA66	Tricross	8	14	2	0	200

KB47W Grating	Design	Horizontal pitch size $\Lambda_h(\mu m)$	Vertical pitch size $\Lambda_v(\mu m)$	Arm length ξ(nm)	Bending angle $\alpha(^\circ)$	Line Width L(nm)
BA11	Cross	8	8	3	0	200
BA21	Cross	8	8	2.6	0	200
BA31	Cross	8	8	2.2	0	200
BA41	Cross	8	8	1.8	0	200
BA51	Cross	8	8	1.4	0	200
BA61	Cross	8	8	1	0	200
BA12	Gammadion	8	8	3	-45	200
BA22	Gammadion	8	8	2.6	-45	200
BA32	Gammadion	8	8	2.2	-45	200
BA42	Gammadion	8	8	1.8	-45	200
BA52	Gammadion	8	8	1.4	-45	200
BA62	Gammadion	8	8	1	-45	200
BA13	Gammadion	8	8	3	-90	200
BA23	Gammadion	8	8	2.6	-90	200
BA33	Gammadion	8	8	2.2	-90	200
BA43	Gammadion	8	8	1.8	-90	200
BA53	Gammadion	8	8	1.4	-90	200
BA63	Gammadion	8	8	1	-90	200
BA14	Trisk	8	8	3	90	200
BA24	Trisk	8	8	2.6	90	200
BA34	Trisk	8	8	2.2	90	200
BA44	Trisk	8	8	1.8	90	200
BA54	Trisk	8	8	1.4	90	200
BA64	Trisk	8	8	1	90	200
BA15	Trisk	8	8	3	45	200
BA25	Trisk	8	8	2.6	45	200
BA35	Trisk	8	8	2.2	45	200
BA45	Trisk	8	8	1.8	45	200
BA55	Trisk	8	8	1.4	45	200
BA65	Trisk	8	8	1	45	200
BA16	Tricross	8	8	3	0	200
BA26	Tricross	8	8	2.6	0	200
BA36	Tricross	8	8	2.2	0	200
BA46	Tricross	8	8	1.8	0	200
BA56	Tricross	8	8	1.4	0	200
BA66	Tricross	8	8	1	0	200
BB11-BB16	Phase-grating	5	5	–	–	–
BB21-BB26	Phase-grating	10	10	–	–	–
BB31-BB36	Phase-grating	20	20	–	–	–
BB41-BB46	Phase-grating	25	25	–	–	–
BB51-BB56	Phase-grating	40	40	–	–	–
BB61-BB66	Phase-grating	50	50	–	–	–

Table A.1: Characteristic parameters of different designs on mask KB47W used for the fabrication of dielectric planar chiral samples.

A.2 Silicon photodiode with planar chiral metamaterials (KB09R)

KB09R is composed of seven layers: NW, AA, CR, AR, CW, M1, EB. The main function of each optical layer is summarized in Table A.2. The reticle mask set is designed for 5:1 reduction on a GCA stepper and each layer is required to be accurately aligned to each other during the fabrication process. The alignment sequence of the different layers is presented in Fig. A.3. The chip-site of the mask set is shown in Fig. A.4. Fig. A.5 schematically illustrates the layout of an individual device. A wide range of photodiodes with various dimensions, shapes, and different planar chiral structures are included in the mask. The characteristic dimensions of different devices are listed in Table A.3, Table A.4 and Table A.5 respectively.

Layer	Function
NW	N-well structure in the substrate
AA	Active area
CR	n^+ Cathode implantation
AR	p^+ Anode implantation
CW	Contact windows
M1	Metal contacts
EB	Metallic layer deposition for EBL

Table A.2: Function of the individual layer in mask KB09R used for the fabrication of pn^+ silicon photodiode integrated with planar chiral gratings.

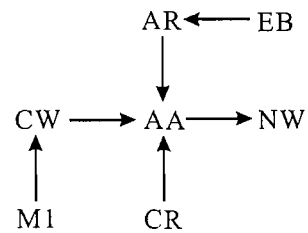

Figure A.3: Mask KB09R alignment sequence during the fabrication of silicon photodiode coated with planar chiral structures.

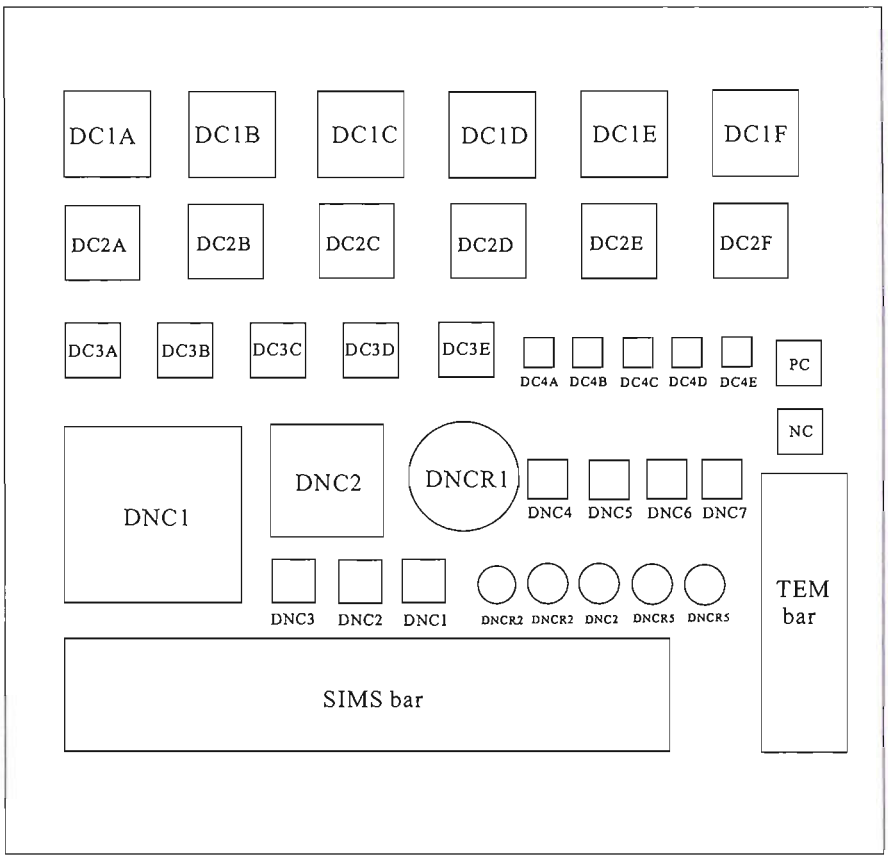

Figure A.4: One chip-site of mask KB09R.

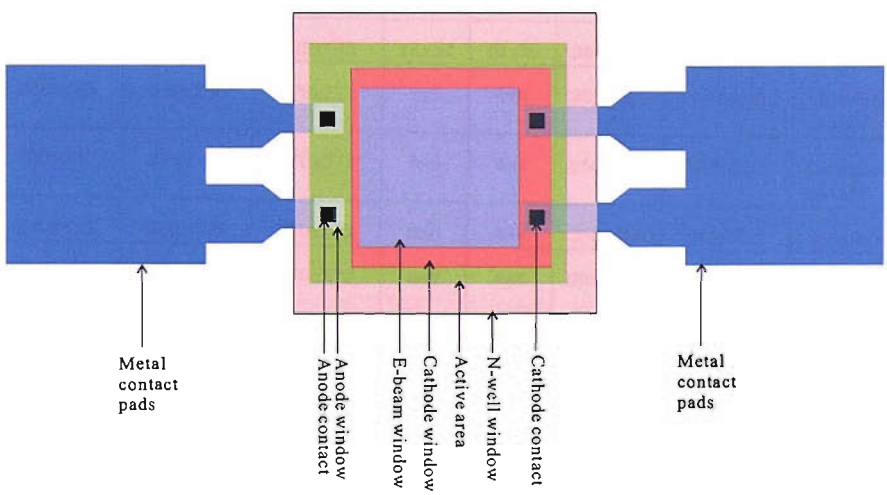

Figure A.5: Layout of an individual pn^+ silicon photodiode coated with a planar chiral grating.

Devices with chiral gratings (Unit: μm)								
Device	NW	AA	CR	AR	CW	M1	EB	Chiral design
DC-1A	1160x1160	1080x1096	1040x1048	14x14	10x10	250x250	1000x1000	Gammadion α=90°
DC-1B	1160x1160	1080x1096	1040x1048	14x14	10x10	250x250	1000x1000	Gammadion α=45°
DC-1C	1160x1160	1080x1096	1040x1048	14x14	10x10	250x250	1000x1000	Simple cross
DC-1D	1160x1160	1080x1096	1040x1048	14x14	10x10	250x250	1000x1000	Gammadion α=-45°
DC-1E	1160x1160	1080x1096	1040x1048	14x14	10x10	250x250	1000x1000	Gammadion α=-90°
DC-1F	1160x1160	1080x1096	1040x1048	14x14	10x10	250x250	1000x1000	No pattern
DC-2A	960x960	880x890	840x840	14x14	10x10	250x250	800x800	Gammadion α=90°
DC-2B	960x960	880x890	840x840	14x14	10x10	250x250	800x800	Gammadion α=45°
DC-2C	960x960	880x890	840x840	14x14	10x10	250x250	800x800	Simple cross
DC-2D	960x960	880x890	840x840	14x14	10x10	250x250	800x800	Gammadion α=-45°
DC-2E	960x960	880x890	840x840	14x14	10x10	250x250	800x800	Gammadion α=-90°
DC-2F	960x960	880x890	840x840	14x14	10x10	250x250	800x800	No pattern
DC-3A	640x640	540x572	520x533	14x14	10x10	250x250	500x500	Gammadion α=90°
DC-3B	640x640	540x572	520x533	14x14	10x10	250x250	500x500	Gammadion α=45°
DC-3C	640	540x572	520x533	14x14	10x10	250x250	500x500	Simple cross
DC-3D	640x640	540x572	520x533	14x14	10x10	250x250	500x500	Gammadion α=-45°
DC-3E	640x640	540x572	520x533	14x14	10x10	250x250	500x500	Gammadion α=-90°
DC-3F	640x640	540x572	520x533	14x14	10x10	250x250	500x500	No pattern
DC-4A	330x330	280x296	270x272	8x8	4x4	250x250	250x250	Gammadion α=90°
DC-4B	330x330	280x296	270x272	8x8	4x4	250x250	250x250	Gammadion α=45°
DC-4C	330x330	280x296	270x272	8x8	4x4	250x250	250x250	Simple cross
DC-4D	330x330	280x296	270x272	8x8	4x4	250x250	250x250	Gammadion α=-45°
DC-4E	330x330	280x296	270x272	8x8	4x4	250x250	250x250	Gammadion α=-90°
DC-4F	330x330	280x296	270x272	8x8	4x4	250x250	250x250	No pattern

Table A.3: Characteristic parameters of silicon photodiodes covered by a thin Ti film patterned with various microstructures.

Devices without chiral gratings (rectangular devices) (Unit: μm)						
Device	NW	AA	CR	AR	CW	M1
	μm	μm	μm	μm	μm	μm
DNC1	2080x2080	2040x2040	2000x2000	14x14	10x10	250x250
DNC2	1100x1100	1040x1040	1000x1000	14x14	10x10	250x250
DNC3	580x580	540x540	500x500	14x14	10x10	250x250
DNC4	300x300	280x280	250x250	8x8	4x4	250x250
DNC5	140x140	120x120	100x100	8x8	4x4	250x250
DNC6	70x85	60x75	50x50	8x8	4x4	250x250
DNC7	45x60	35x50	25x25	8x8	4x4	250x250

Table A.4: Characteristic parameters of rectangular silicon photodiodes without chiral gratings.

Devices without chiral gratings (circular devices) (Unit: μm)						
Device	NW	AA	CR	AR	CW	M1
	μm	μm	μm	μm	μm	μm
DNCR1	Ø550	Ø520	Ø500	8x8	4x4	250x250
DNCR2	Ø280	Ø270	Ø250	8x8	4x4	250x250
DNCR3	Ø160	Ø145	Ø125	8x8	4x4	250x250
DNCR4	Ø80	Ø70	Ø50	8x8	4x4	250x250

Table A.5: Characteristic parameters of circular silicon photodiodes without chiral gratings.

A.3 Dielectric multilayer stack with planar chiral waveguide (KB57W)

Mask KB57W is designed to fabricate the high reflective dielectric multilayer mirror with planar chiral waveguide. A capture of the 'topcell' of the mask is shown in Fig. A.6. The different designs on the two planar chiral gratings on either side of the dielectric multilayer stack are schematically illustrated in Fig. A.7 and Fig. A.8 respectively. Details of the characteristic dimensions of the different designs on the two planar chiral gratings are given in Table A.6 and Table A.7 respectively.

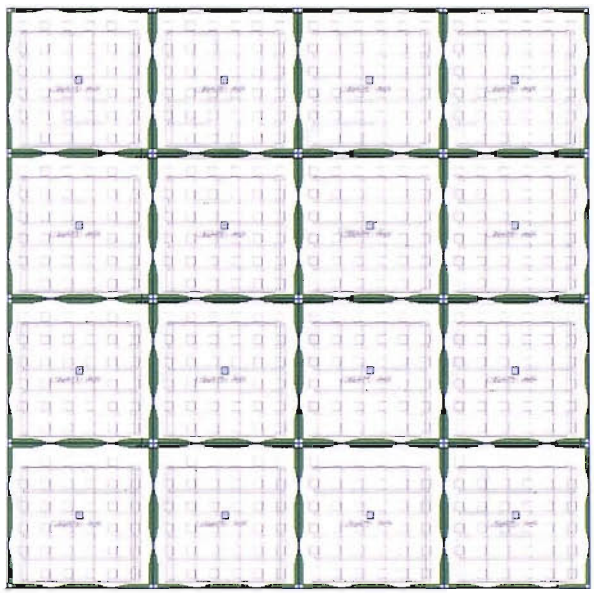

Figure A.6: Layout (topcell) of mask KB57W used to fabricate the dielectric multilayer stack with planar chiral waveguide.

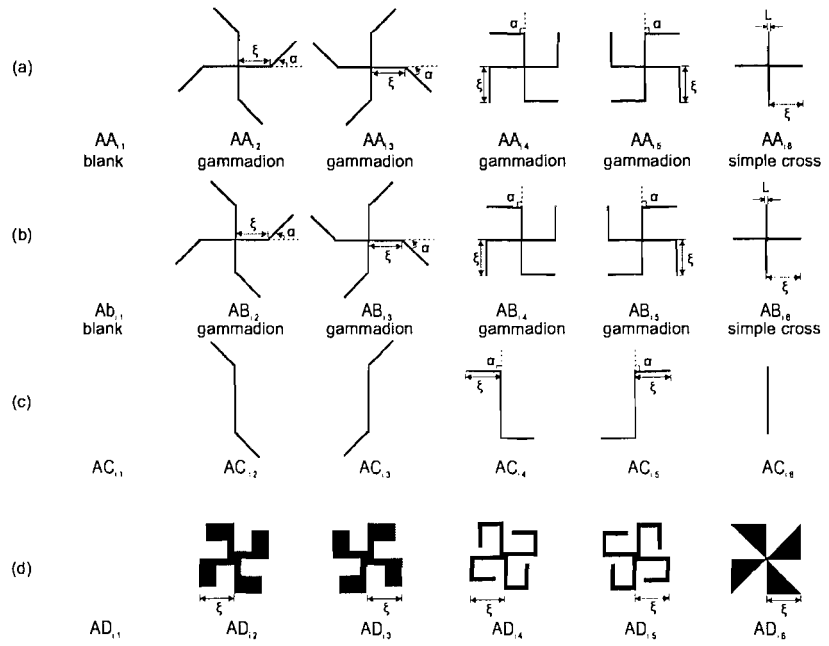

Figure A.7: Schematic diagram of the different designs on the first polysilicon grating underneath the dielectric multilayer stack distributed on mask KB57W. (a) Chip AA (b) Chip AB (c) Chip AC (d) Chip AD.

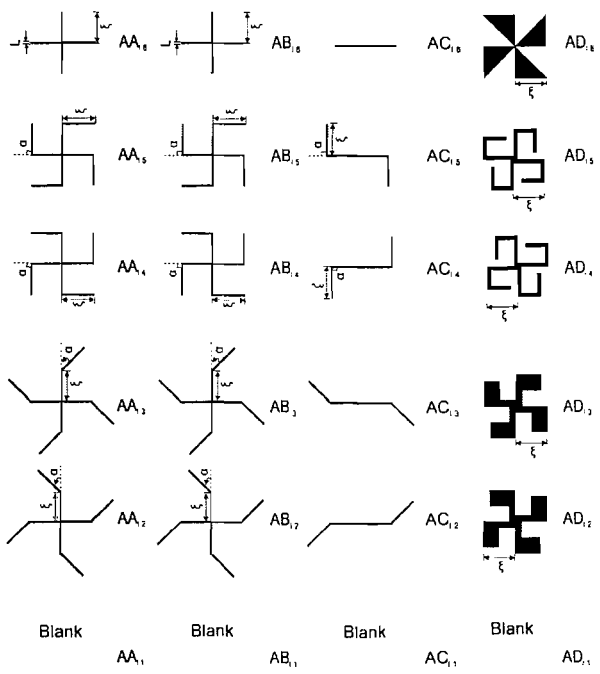

Figure A.8: Schematic diagram of the different designs on the second polysilicon grating above the dielectric multilayer stack distributed on mask KB57W. (a) Chip AA (b) Chip AB (c) Chip AC (d) Chip AD.

KB57W Grating	Design	Horizontal pitch size $\Lambda_h(\mu m)$	Vertical pitch size $\Lambda_v(\mu m)$	Arm length $\xi(nm)$	Bending angle $\alpha(°)$	Line Width $L(nm)$
AA11-AA61	No pattern	-	-	-	-	-
AA12-AA62	Gammadion	8	8	2.2	-45	400
AA13-AA63	Gammadion	8	8	2.2	45	400
AA14-AA64	Gammadion	8	8	2.2	-90	400
AA15-AA65	Gammadion	8	8	2.2	90	400
AA16-AA66	Cross	8	8	2.2	0	400
AB11-AB61	No pattern	-	-	-	-	-
AB12-AB62	Gammadion	10	10	2.2	-45	400
AB13-AB63	Gammadion	10	10	2.2	45	400
AB14-AB64	Gammadion	10	10	2.2	-90	400
AB15-AB65	Gammadion	10	10	2.2	90	400
AB16-AB66	Cross	10	10	2.2	0	400
AC11-AC61	No pattern	-	-	-	-	-
AC12-AC62	Half gammadion	8	8	2.2	-45	400
AC13-AC63	Half gammadion	8	8	2.2	45	400
AC14-AC64	Half gammadion	8	8	2.2	-90	400
AC15-AC65	Half gammadion	8	8	2.2	90	400
AC16-AC66	Vertical line	8	8	2.2	0	400
AD11-AD61	No pattern	-	-	-	-	-
AD12-AD62	Phase grating	8	8	-	-	100-200
AD13-AD63	Phase grating	8	8	-	-	100-200
AD14-AD64	Phase grating	8	8	-	-	100
AD15-AD65	Phase grating	8	8	-	-	100
AD16-AD66	Phase grating	8	8	-	-	-

Table A.6: Characteristic parameters of different designs on the first polysilicon grating underneath the dielectric multilayer stack distributed on mask KB57W.

KB57W Grating	Design	Horizontal pitch size $\Lambda_h(\mu m)$	Vertical pitch size $\Lambda_v(\mu m)$	Arm length $\xi(nm)$	Bending angle $\alpha(°)$	Line Width $L(nm)$
AA11-AA16	No pattern	-	-	-	-	-
AA21-AA26	Gammadion	8	8	2.2	-45	400
AA31-AA36	Gammadion	8	8	2.2	45	400
AA41-AA46	Gammadion	8	8	2.2	-90	400
AA51-AA56	Gammadion	8	8	2.2	90	400
AA61-AA66	Cross	8	8	2.2	0	400
AB11-AB16	No pattern	-	-	-	-	-
AB21-AB26	Gammadion	10	10	2.2	-45	400
AB31-AB36	Gammadion	10	10	2.2	45	400
AB41-AB46	Gammadion	10	10	2.2	-90	400
AB51-AB56	Gammadion	10	10	2.2	90	400
AB61-AB66	Cross	10	10	2.2	0	400
AC11-AC16	No pattern	-	-	-	-	-
AC21-AC26	Half gammadion	8	8	2.2	-45	400
AC31-AC36	Half gammadion	8	8	2.2	45	400
AC41-AC46	Half gammadion	8	8	2.2	-90	400
AC51-AC56	Half gammadion	8	8	2.2	90	400
AC61-AC66	Horizontal line	8	8	2.2	0	400
AD11-AD16	No pattern	-	-	-	-	-
AD21-AD26	Phase grating	8	8	-	-	100-200
AD31-AD36	Phase grating	8	8	-	-	100-200
AD41-AD46	Phase grating	8	8	-	-	100
AD51-AD56	Phase grating	8	8	-	-	100
AD61-AD66	Phase grating	8	8	-	-	-

Table A.7: Characteristic parameters of different designs on the second polysilicon grating above the dielectric multilayer stack distributed on mask KB57W.

A.4 Planar chiral metamaterials with subwavelength scale (KB03W)

Mask KC03W is designed to fabricate the subwavelength scale silicon nitride chiral samples. A capture of the 'topcell' of the mask is shown in Fig. A.9. There are four chips distributed in a square matrix on the mask. On chip AA and BA, each square grating is 1 by 1 mm; and on chip AB and BB, the dimension of the square grating is reduced to 0.5 by 0.5 mm. The different designs are schematically illustrated in Fig. A.10. Details of the characteristic dimensions of the different designs are given in Table A.8.

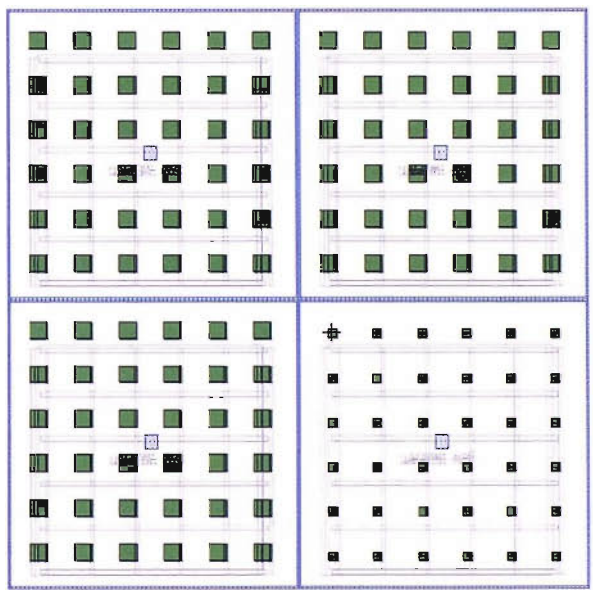

Figure A.9: Layout (topcell) of mask KB03W used to fabricate the silicon nitride planar chiral metamaterials with subwavelength scale.

KB03W	pitch size $\Lambda(\mu m)$	Arm length ξ(nm)	Line Width L(nm)
M_{i1}	0.5	0.15	50
M_{i2}	0.63	0.2	50
M_{i3}	1	0.3	50
M_{i4}	2	7	50
M_{i5}	3	1	50
M_{i6}	4	1.4	50

Table A.8: Characteristic parameters of different designs on mask KC03W used for the fabrication of silicon nitride planar chiral structures with subwavelength scale.

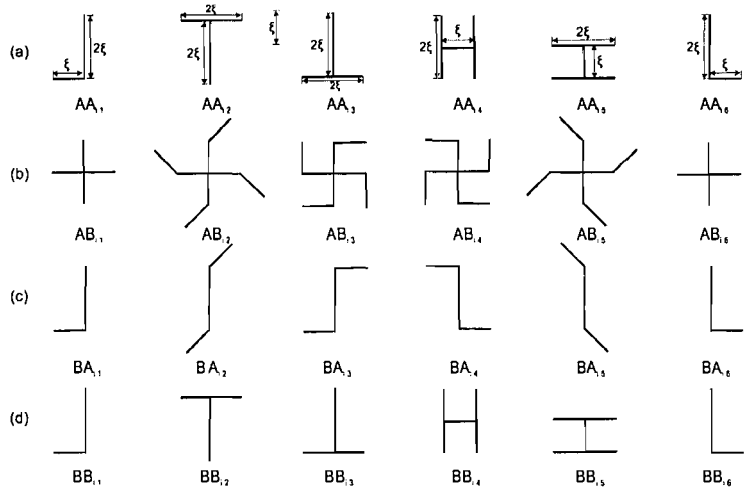

Figure A.10: Schematic diagram of the different microstructure designs distributed on mask KC03W (a) Chip AA (b) Chip AB (c) Chip BA (d) Chip BB.

Appendix B

LMS process listings

B.1 Ti/Au/Ti planar chiral metamaterials (K2385)

Step	ID	Description
1	P-EM	E-BEAM Mask/Retical Writing
2	G-S12	Title page: 4" n-type double polished,<100>, 110Ω/cm
3	G-1P	Lithography notes
4	G-1	Notebook page
5	W-C2	Fuming nitric acid clean, 2nd pot only, Wafer ♯1,2
6	ME-0	15nm Ti + 80nm Au E-beam evaporated films, COULD BE gold CONTAMINATED, Wafer ♯3,4
7	ME-0	20nm Ti+100nm Au+20nm Ti E-beam evaporated films, COULD BE gold CONTAMINATED, Wafer ♯1
8	P-E0X	E-BEAM lithography: 400nm UVIII resist; KB66w, topcell3,layer MC+Cambridge source, D/F (for wafers with GOLD)
9	P-RHBX	Hardbake for Ion beam milling (for wafers with GOLD)
10	B-0	Ion beam mill: mill 80nm Au + 15nm Ti BEST EFFORT NO OVERETCH
11	P-RSX	Resist strip (for wafers with GOLD), Wafer ♯2
12	P-E0X	E-BEAM lithography: 400nm UVIII resist; KB66w, topcell4,layer MC+Cambridge source, D/F (for wafers with GOLD)
13	P-RHBX	Hardbake for Ion beam milling (for wafers with GOLD)
14	B-0	Ion beam mill:mill 80nm Au + 15nm Ti. BEST EFFORT NO OVERETCH
15	P-RSX	Resist strip (for wafers with GOLD), Wafer ♯3
16	P-E0X	E-BEAM lithography: 400nm UVIII resist; KB66w, topcell4,layer MC+Cambridge source, D/F (for wafers with GOLD)
17	P-RHBX	Hardbake for Ion beam milling (for wafers with GOLD)
18	B-0	Ion beam mill:mill 20nm Au + 100nm Ti + 20nm Au. BEST EFFORT NO OVERETCH
19	P-RSX	Resist strip (for wafers with GOLD), Wafer ♯4
20	P-E0X	E-BEAM lithography: 400nm UVIII resist; KB66w, topcell5,layer MC+Cambridge source, D/F (for wafers with GOLD)
21	P-RHBX	Hardbake for Ion beam milling (for wafers with GOLD)
22	B-0	Ion beam mill:mill 80nm Au + 15nm Ti. BEST EFFORT NO OVERETCH
23	P-RSX	Resist strip (for wafers with GOLD)

Table B.1: LMS-file for the fabrication batch of Ti/Au/Ti planar chiral metamaterials.

B.2 Silicon dioxide planar chiral metamaterials (K2775s)

Step	ID	Description
1	P-EM	E-BEAM Mask/Retical Writing
2	G-S12	Title page: 4 wafers, MATERIAL: UV fused silica, 1mm thick double polished
3	G-1P	Lithography notes
4	G-1	Notebook page
5	W-C2	Fuming nitric acid clean, 2nd pot only, Wafer ♯1
6	P-E0	E-BEAM lithography: 400nm UVIII resist; KB47w, topcell=topcell26,layer MC+MF, D/F
7	P-RHBD	Hardbake for dry etch: 110oC oven bake for 60 min
8	D-O1F	Etch SiO2. Anisot. D/F EBMF/OPTICAL resist, OPT80+CHF3+Ar. Etch depth=172nm
9	X-0	General inspection stage
10	P-RS	Resist strip
11	X-0	General inspection stage, Wafer ♯2
12	P-E0	E-BEAM lithography: 400nm UVIII resist; KB47w, topcell=topcell27,layer MC+MF, D/F
13	P-RHBD	Hardbake for dry etch: 110oC oven bake for 60 min
14	D-O1F	Etch SiO2. Anisot. D/F EBMF/OPTICAL resist, OPT80+CHF3+Ar. Etch depth=343nm
15	X-0	General inspection stage
16	P-RS	Resist strip
17	X-0	General inspection stage, Wafer ♯3
18	P-E0	E-BEAM lithography: 400nm UVIII resist; KB47w, topcell=topcell28,layer MC+MF, D/F
19	P-RHBD	Hardbake for dry etch: 110oC oven bake for 60 min
20	D-O1F	Etch SiO2. Anisot. D/F EBMF/OPTICAL resist, OPT80+CHF3+Ar. Etch depth=690nm
21	X-0	General inspection stage
22	P-RS	Resist strip
23	X-0	General inspection stage, Wafer ♯4
24	P-E0	E-BEAM lithography: 400nm UVIII resist; KB47w, topcell=topcell29,layer MC+MF, D/F
25	P-RHBD	Hardbake for dry etch: 110oC oven bake for 60 min
26	D-O1F	Etch SiO2. Anisot. D/F EBMF/OPTICAL resist, OPT80+CHF3+Ar. Etch depth=826nm
27	X-0	General inspection stage
28	P-RS	Resist strip
29	X-0	General inspection stage

Table B.2: LMS-file for the fabrication batch of silicon dioxide planar chiral metamaterials.

B.3 Silicon nitride planar chiral metamaterials (K2783s)

Step	ID	Description
1	P-EM	E-BEAM Mask/Retical Writing
2	G-S12	Title page: 6 wafers, MATERIAL: UV fused silica, 1mm thick double polished
3	G-1P	Lithography notes
4	G-1	Notebook page
5	W-C2	Fuming nitric acid clean, 2nd pot only, Wafer ♯1,2
6	LD-N0	PECVD NITRIDE deposition; 160nm±20nm, Wafer ♯3,4
7	LD-N0	PECVD NITRIDE deposition; 320nm±20nm, Wafer ♯5
8	LD-N0	PECVD NITRIDE deposition; 80nm±20nm, Wafer ♯6
9	LD-N0	PECVD NITRIDE deposition; 240nm±20nm, Wafer ♯1
10	P-E0	E-BEAM lithography: 400nm UVIII resist; KB47w, topcell=topcell20,layer MC+MF, D/F
11	P-RHBD	Hardbake for dry etch: 110oC oven bake for 60 min
12	D-N1F	Etch Si3N4. Anisot. D/F EBMF/OPTICAL resist, OPT80+CHF3+Ar. Etch depth=160nm
13	X-0	General inspection stage
14	P-RS	Resist strip
15	X-0	General inspection stage, Wafer ♯2
16	P-E0	E-BEAM lithography: 400nm UVN30 resist; KB47w, topcell=topcell21,layer MC+MF, L/F
17	P-RHBD	Hardbake for dry etch: 110oC oven bake for 60 min
18	D-N1E	Etch Si3N4. Anisot. L/F EBMF/OPTICAL resist, OPT80+CHF3+Ar. Etch depth=160nm
19	X-0	General inspection stage
20	P-RS	Resist strip
21	P-E0	E-BEAM lithography: 400nm UVIII resist; KB47w, topcell=topcell22,layer MC+MF, D/F
22	P-RHBD	Hardbake for dry etch: 110oC oven bake for 60 min
23	D-N1F	Etch Si3N4. Anisot. D/F EBMF/OPTICAL resist, OPT80+CHF3+Ar. Etch depth=320nm
24	X-0	General inspection stage
25	P-RS	Resist strip
26	X-0	General inspection stage, Wafer ♯4
27	P-E0	E-BEAM lithography: 400nm UVN30 resist; KB47w, topcell=topcell23,layer MC+MF, L/F
28	P-RHBD	Hardbake for dry etch: 110oC oven bake for 60 min
29	D-N1E	Etch Si3N4. Anisot. L/F EBMF/OPTICAL resist, OPT80+CHF3+Ar. Etch depth=320nm
30	X-0	General inspection stage
31	P-RS	Resist strip
32	X-0	General inspection stage, Wafer ♯5
33	P-E0	E-BEAM lithography: 400nm UVIII resist; KB47w, topcell=topcell24,layer MC+MF, D/F
34	P-RHBD	Hardbake for dry etch: 110oC oven bake for 60 min
35	D-N1F	Etch Si3N4. Anisot. D/F EBMF/OPTICAL resist, OPT80+CHF3+Ar. Etch depth=80nm
36	X-0	General inspection stage
37	P-RS	Resist strip
38	X-0	General inspection stage, Wafer ♯6
39	P-E0	E-BEAM lithography: 400nm UVIII resist; KB47w, topcell=topcell22,layer MC+MF, D/F
40	P-RHBD	Hardbake for dry etch: 110oC oven bake for 60 min
41	D-N1F	Etch Si3N4. Anisot. D/F EBMF/OPTICAL resist, OPT80+CHF3+Ar. Etch depth=80nm
42	X-0	General inspection stage
43	P-RS	Resist strip
44	X-0	General inspection stage

Table B.3: LMS-file for the fabrication batch of silicon nitride planar chiral metamaterials.

B.4 Silicon photodiode integrated with planar chiral structures (K2644s)

Step	ID	Description
1	P-EM	E-BEAM Mask/Retical Writing
2	G-S12	Title page: 18 wafers, MATERIAL: 12 n-type silicon wafer, 30 Ohm.cm, <100>, ♯1-12, 6 p-type silicon wafer, 30Ohm.cm, ¡100¿, ♯13-18
3	G-1P	Lithography notes
4	G-1	Notebook page
5	W-C1	RCA clean
6	F4-W0010	Wet oxidation 100nm±10nm, 1000°C, 10'O2, x'wetO_2, 30'N_2
7	P-GS1	Stepper Photolith: reticle KB09R (NW), D/F, nom. 1.1 μm resist STANDARD
8	G-2	See Engineer for instructions
9	P-RHBD	Hardbake for dry etch
10	D-O1F	Etch SiO_2. Anisot. D/F EBMF/OPTICAL resist,OPT80+CHF3+Ar.
11	P-RS	Resist strip
12	W-C2	Fuming nitric acid clean, 2nd pot only
13	W-C1	RCA clean
14	F5-9002P	Pad oxidation: 900°C, 20nm±5nm, O2+HCl
		Active area implantation and diffusion
15	P-GS1	Stepper Photolith: reticle KB09R (AA), D/F, nom. 1.1 μm resist STANDARD
16	G-2	See Engineer for instructions
17	P-RHB1	Hardbake for implant
18	IB-4035	Implant Boron:5E13B + 40KeV (BICMOS base implant through oxide), Wafer♯1-4
19	IB-8041	Implant Boron:1E14B + 80KeV (Implant uniform checks), Wafer♯5-8
20	IB-4052	Implant Boron:2E15B + 40KeV (I2L extrinsic base implant), Wafer♯9-12
21	IB-8022	Implant Boron:1.8E12P + 80KeV (CMOS N-Well), Wafer♯13-18
22	P-RS	Resist strip
23	W-C1	RCA clean
		Dopant drive-in
24	F10-00	Furnace 10: Load in O2, 1100°C, 10'dryO2, 30'N_2, 4hrs, Wafer♯1,5,9,12
25	F10-00	Furnace 10: Load in O2, 1150°C, 10'dryO2, 30'N_2, 5hrs, Wafer♯2,4,6,10,13-15
26	F10-00	Furnace 10: Load in O2, 1150°C, 10'dryO2, 30'N_2, 6hrs, Wafer♯3,7,8,11,16-18
27	P-GS1	Stepper Photolith: reticle KB09R (NW), D/F, nom. 1.1 μm resist STANDARD
28	G-2	See Engineer for instructions
29	WH-7E1	Wet etch oxide, 7:1 BHF 25°C. To hydrophobic Si + 20secs.
30	P-RS	Resist strip
31	W-C2	Fuming nitric acid clean, 2nd pot only
32	W-C1	RCA clean
33	F5-9002P	Pad oxidation: 900°C, 20nm±5nm, O2+HCl
		Depletion junction implantation
34	P-GS1	Stepper Photolith: reticle KB09R (CR), D/F, nom. 1.1 μm resist STANDARD
35	G-2	See Engineer for instructions
36	P-RHB1	Hardbake for implant
37	IA-4061	Implant Arsenic: 1E16 As + 40 KeV (CMOS S D), Wafer♯1,2,5,6,9,10
38	IA-8055	Implant Arsenic: 5E15 As + 80 KeV (C/NMOS S D), Wafer♯3,4,7,8,11,12
39	IA-5055	Implant BF2+: 5E15 BF2 + 50 KeV (CMOS P-ch S D), Wafer♯13,14,16
40	IA-7055	Implant BF2+: 5E15 BF2 + 70 KeV (CMOS P-ch SD through gate ox.), Wafer♯15,17,18
41	P-RS	Resist strip
42	W-C2	Fuming nitric acid clean, 2nd pot only
		Ohmic bulk contact in diffusion layer implantation

43	P-GS1	Stepper Photolith: reticle KB09R (AR), D/F, nom. 1.1 μm resist STANDARD
44	G-2	See Engineer for instructions
45	P-RHB1	Hardbake for implant
46	IBF-5055	Implant BF2: 5E15 BF2 + 50KeV (CMOS P-ch S D) Wafer♯1-12
47	IA-4055	Implant Arsenic: 5E15 As + 40KeV (CMOS S D), Wafer♯13-18
48	P-RS	Resist strip
49	W-C1	RCA clean
		Dielectric passivation layer
50	LS-BO1	BPSG:Deposit 100nm updoped Silox + 500nm BPSG (4%P/10%B approx)
51	W-C1	RCA clean
52	RA-1	RTA implant activation, BPSG flow: 10secs 1100°C (Std.CMOS S D)
53	W-C2	Fuming nitric acid clean, 2nd pot only
54	P-GS1	Stepper Photolith: reticle KB09R (CW), D/F, nom. 1.1 μm resist STANDARD
55	G-2	See Engineer for instructions
56	P-RHBD	Hardbake for dry etch
57	D-O1F	Etch SiO_2. Anisot. D/F EBMF/OPTICAL resist,OPT80+CHF3+Ar.
58	P-RS	Resist strip
59	W-C2	Fuming nitric acid clean, 2nd pot only
		Metallization for contacts
60	WH-2D2	Dip etch, 20:1 BHF 25degC, 30secs
61	MS-TA10	Sputter 1000nm Ti-Al/Si 1% in TRIKON SIGMA, RESIST PROHIBITED
62	P-GS1	Stepper Photolith: reticle KB09R (M1), L/F, nom. 2.2 μm resist (For Si etch>1μm or metal)
63	G-2	See Engineer for instructions
64	P-RHBD	Hardbake for dry etch
65	D-MAT1	Etch Al, Al/Si and/or Ti. For OPTICAL resist SRS SSIC CI2+SiCl4+Ar
66	P-RS	Resist strip
67	W-C2	Fuming nitric acid clean, 2nd pot only
68	F9-H42	Alloy/Anneal: 30mins H2/N2 420degC, 5'N2, 30'H2/N2, 5'N2
69	X-0	General inspection stage
		Metamaterial chiral structures fabrication (wafer ♯2,3,8,13,18
70	P-0	Blank sheet for non standard process, Resist spin: 1000nm PMGI
71	P-GL1	PMGI lift-off process: Photolith KB09R (EB), D/F
72	P-GL3	PMGI lift-off Hardbake + Descum
73	ME-0	E-gun evaporation: 50nm uniform Ti layer deposition
74	P-GL5	Lift-off metal (PMGI resist)
75	G-2	See Engineer for instructions about EBL
		Wafer ♯2,3,8,18
76	P-E0	E-BEAM lithography: KB09RW, layer Metal2, D/F, 300nm UVIII resist; (need to be aligned with optical mask EP!), BEST EFFORT FOR E-BEAM
77	X-0	General inspection stage: E-beam patterns
78	P-RHBX	Hardbake (for wafers with gold) (with E-beam resist on!) 90oC 30min
79	D-D60X	Descum: 30 secs. Au CONTAM SRS GOLD ASHER
80	D-0	Dry etch: Wafers with GOLD ORANGE BOX, PT RIE80 Slave, Back end Quartz Cover plate! CF4, 50sccm, 100mT, 200W. Etch time needs to be calibrated!
81	D-MT3X	Etch Ti. Isot. Au CONTAM, PT RIE80 Slave, SF6
82	X-l1	Inspect 1 wafer for residue after dry etch
83	P-RS	Resist strip
84	W-C2	Fuming nitric acid clean, 2nd pot only

Table B.4: LMS-file for the fabrication batch of silicon photodiode integrated with planar chiral structures.

B.5 Highly reflective dielectric multilayer mirror with planar chiral waveguide (K2843s)

Step	ID	Description
1	P-EM	E-BEAM Mask/Retical Writing
2	G-S12	Title page: 8 wafers, MATERIAL: 2 p-type 15ohm.cm <100> silicon wafers ♯1-2; 6 UV fused silica double-side polished quartz (1mm thick) ♯3-8
3	G-1P	Lithography notes
4	G-1	Notebook page
5	W-C2	Fuming nitric acid clean, 2nd pot only Silica wafers ONLY! (Global E-beam alignment mask fabrication)
6	P-G1	Photolith mask KB57W, layer ALN, D/F, 1.1μm resist, STANDAND
7	P-RHBD	Hardbake for dry etch
8	D-O1F	Etch SiO2. Anisot. D/F EBMF/OPTICAL resist OPT80+ CHF3 +Ar Etch 2μm holes down into the silica substrate for alignment mask.
9	P-RS	Resist strip
10	W-C2	Fuming nitric acid clean, 2nd pot only
11	F4-W1050	Wet oxidation 100nm+-10nm, 1000degC, 10'O2, x'wetO2, 30'N2, wafer ♯1-2 silicon wafers will be used to check polysilicon etching process!
12	F15-P9	LPCVD Polysilicon deposition Deposit uniform 100 nm polysilicon film on all wafers Silicon test Wafers ♯1,2
13	P-E0	E-BEAM lithography: 400nm UVN30 resist; KB57mW,layer MC1+MC, L/F
14	G-2	See engineer for instructions (about polySi etching process)
15	P-RHBE	Hardbake for dry etch (with E-beam resist on)
16	D-O	Dry etch: STS ICP PolySi dry etch (HBr + O2 process)
17	W-E1	EKC 265 Post ICP silicon etch passivation removal
18	P-RS	Resist strip in Technics Asher
19	W-C2	Fuming nitric acid clean, 2nd pot only
20	X-0	Cleave wafer and SEM to calibrate PolySi etch process Wafer ♯3 (test silica wafer)
21	P-E0	E-BEAM lithography: 400nm UVN30 resist; KB57mW,layer MC1+MC, L/F
22	X-0	General inspection stage (E-beam development of the chiral design)
23	G-2	See engineer for instructions (about polySi etching process)
24	P-RHBE	Hardbake for dry etch (with E-beam resist on)
25	D-O	Dry etch: STS ICP PolySi dry etch (HBr + O2 process)
26	W-E1	EKC 265 Post ICP silicon etch passivation removal
27	P-RS	Resist strip in Technics Asher
28	W-C2	Fuming nitric acid clean, 2nd pot only
29	X-0	General inspection stage
30	P-RF	Frontspin resist
31	P-RHBD	Hardbake for dry etch
32	D-NOS	Back strip: Si3N4, SiO2/PolySi OPT80+ CHF4 +O2 strip all the PolySi at the back of the silica wafer!
33	P-RS	Resist strip
34	W-C2	Fuming nitric acid clean, 2nd pot only
35	X-0	General inspection stage (check if any PolySi left on the back and any resist left on the frontier on the features? Wafer ♯4-8
36	P-E0	E-BEAM lithography: 400nm UVN30 resist; KB57mW,layer MC1+MC, L/F
37	X-0	General inspection stage (E-beam development of the chiral design)
38	G-2	See engineer for instructions (about polySi etching process)
39	P-RHBE	Hardbake for dry etch (with E-beam resist on)
40	D-O	Dry etch: STS ICP PolySi dry etch (HBr + O2 process)
41	W-E1	EKC 265 Post ICP silicon etch passivation removal
42	P-RS	Resist strip in Technics Asher
43	W-C2	Fuming nitric acid clean, 2nd pot only
44	X-0	General inspection stage
45	P-RF	Frontspin resist
46	P-RHBD	Hardbake for dry etch
47	D-NOS	Back strip: Si3N4, SiO2/PolySi OPT80+ CHF4 +O2

Step	ID	Description
		strip all the PolySi at the back of the silica wafer!
48	P-RS	Resist strip
49	W-C2	Fuming nitric acid clean, 2nd pot only
50	X-0	General inspection stage (check if any PolySi left on the back and any resist left on the frontier on the features? Dielectric stack
51	G-2	See engineer for instructions (Refer to Luca's mirror work) Need to calibrate the deposition rate with silicon wafer! Silicon test wafer ♯2
52	LD-0	General PECVD deposition test on the silicon wafer; 1000nm PEO + 10 times (78nm PEN + 108nm PEO)+892nm PEO
53	X-SEM	Cleave and SEM wafer to calibrate Silica wafers ♯3-8
54	LD-0	General PECVD deposition test on the silicon wafer; 1000nm PEO + 10 times (78nm PEN + 108nm PEO)+892nm PEO; wafers ♯3,4
55	LD-0	General PECVD deposition test on the silicon wafer; 1000nm PEO + 11 times (78nm PEN + 108nm PEO)+892nm PEO; wafers ♯5,6
56	LD-0	General PECVD deposition test on the silicon wafer; 1000nm PEO + 12 times (78nm PEN + 108nm PEO)+892nm PEO; wafers ♯7,8
57	G-2	See engineer for instructions (about the alignment of two E-beam stages)
58	P-G1	Photolith mask KB57W, layer MM, D/F, 1.1μm resist, STANDAND
59	P-RHBW	Hardbake for wet etch Silicon test wafer ♯2 for wet etching test
60	G-3	Special instructions: cleave wafer ♯2 into half, use half to test wet etch first!)
61	WH-0	Wet etch in 7:1 BHF through whole dielectric stack!time and etching rate needs to be calibrated! Attention:Make sure the resist WILL NOT PEEL OFF with long time wet etching! 1st HALF
61	WH-0	Wet etch in 7:1 BHF through whole dielectric stack!time and etching rate needs to be calibrated! Attention:Make sure the resist WILL NOT PEEL OFF with long time wet etching! 2nd HALF
63	X-0	General inspection stage Silica wafer ♯3-8
64	WH-0	Wet etch in 7:1 BHF through whole dielectric stack! time and etching rate depends on wafer ♯2
65	X-0	General inspection stage
66	P-RS	Resist strip
67	W-C2	Fuming nitric acid clean, 2nd pot only Second layer chiral grating fabrication, wafer ♯3-8
68	F15-P9	LPCVD Polysilicon deposition, 2nd uniform PolySi, 100nm Wafer ♯3 (test silica wafer)
69	P-E0	E-BEAM lithography: 400nm UVN30 resist; KB57mW,layer MC1+MC, L/F
70	X-0	General inspection stage (E-beam development of the chiral design)
71	G-2	See engineer for instructions (about polySi etching process)
72	P-RHBE	Hardbake for dry etch (with E-beam resist on)
73	D-O	Dry etch: STS ICP PolySi dry etch (HBr + O2 process)
74	W-E1	EKC 265 Post ICP silicon etch passivation removal
75	P-RS	Resist strip in Technics Asher
76	W-C2	Fuming nitric acid clean, 2nd pot only
77	X-0	General inspection stage Wafer ♯4-8)
78	P-E0	E-BEAM lithography: 400nm UVN30 resist; KB57mW,layer MC1+MC, L/F
79	X-0	General inspection stage (E-beam development of the chiral design)
80	G-2	See engineer for instructions (about polySi etching process)
81	P-RHBE	Hardbake for dry etch (with E-beam resist on)
82	D-O	Dry etch: STS ICP PolySi dry etch (HBr + O2 process)
83	W-E1	EKC 265 Post ICP silicon etch passivation removal
84	P-RS	Resist strip in Technics Asher
85	W-C2	Fuming nitric acid clean, 2nd pot only
86	X-0	General inspection stage Top symmetrical SiO2 layer deposition ♯3-8
87	W-C2	Fuming nitric acid clean, 2nd pot only
88	LD-O0	PECVD OXIDE deposition, 200nm
86	X-0	General inspection stage: Optical measurement and characterization

Table B.5: LMS-file for the fabrication of dielectric multilayer stack with planar chiral waveguide.

B.6 Dielectric planar chiral metamaterials with subwavelength scale (K3035s)

Step	ID	Description
1	P-EM	E-BEAM Mask/Retical Writing
2	G-S12	Title page: 2 wafers, MATERIAL: UV fused silica, 1mm thick double polished
3	G-1P	Lithography notes
4	G-1	Notebook page
5	W-C2	Fuming nitric acid clean, 2nd pot only
6	W-C1	RCA clean
7	LD-N0	PECVD NITRIDE deposition; 150nm Wafer ♯1
8	LD-N0	PECVD NITRIDE deposition; 320nm Wafer ♯2
9	P-E0	E-BEAM lithography: 400nm ZEP520 resist, KC03w, layer MC+MF, D/F
10	P-RHBD	Hardbake for dry etch: 110oC oven bake for 60 min
11	D-N1F	Etch Si3N4. Anisot. D/F EBMF/OPTICAL resist,OPT80+CHF3+Ar, Etch depth:150nm Wafer ♯1,320nm Wafer ♯2
12	X-0	General inspection stage
13	P-RS	Resist strip
14	W-C2	Fuming nitric acid clean, 2nd pot only
15	X-0	General inspection stage
16	S-S	Sawing:sawing the wafer to chips along the script line
17	X-0	General inspection stage:Device characterization
18	G-C	Completion of listing/section

Table B.6: LMS-file for the fabrication batch of silicon dioxide planar chiral metamaterials with subwavelength scale.

Appendix C

Polarization eigenstates calculation using transfer matrix

In order to calculate the 2×2 transfer matrix, $\mathcal{A}$, for a given propagation channel through planar chiral metamaterials, it is first assumed that the system is linear, and the principle of superposition holds true. Provided that is the case, then only three independent polarization measurements are required to determine the four elements of the transfer matrix. For simplicity it is preferable to perform those measurements using three separate linearly polarized input states, with each having a different polarization azimuth. The first two chosen polarization states have azimuthal angles of $\phi_0 = 0°$ and $\phi_0 = -90°$ as these correspond to the y- and x-directions of the calibrated coordinate system respectively, while the third is chosen to be a linear superposition of the first two. As any generalized elliptically polarized input state for the system can be described by the two-component vector:

$$\mathbf{x} = \begin{bmatrix} \mathbf{E}_y \cos(\Omega) \\ \\ \mathbf{E}_x \cos(\Omega + \delta) \end{bmatrix} \tag{C.1}$$

where $\Omega = \omega t$ - k·r, by determining the output polarization response for each component separately and applying the principle of superposition, it should be possible to construct the transfer matrix for the system.

The first measurement is performed with an input state that is vertically polarized (i.e. $\phi_0 = 0°$), with the electric field in the y-direction and perpendicular to the plane of incidence. The input and output states of the system can then each be defined by the two-component vectors $\mathbf{x}_1$ and $\mathbf{y}_1$ respectively, where the two components of each vector represent the electric fields in the y- and x-directions

respectively. Thus, for the case $\phi_0 = 0°$ the input vector is:

$$\mathbf{x}_1 = \begin{bmatrix} 1 \\ \\ 0 \end{bmatrix} \mathbf{E}_0 \cos(\Omega) = \frac{\mathbf{E}_0}{2} \begin{bmatrix} 1 \\ \\ 0 \end{bmatrix} e^{i\Omega} + \frac{\mathbf{E}_0}{2} \begin{bmatrix} 1 \\ \\ 0 \end{bmatrix} e^{-i\Omega}. \tag{C.2}$$

Assuming that the output beam experiences a change to its polarization state in comparison to the input of $\Delta\phi_1$ (azimuth rotation in the anticlockwise direction) and η_1 (induced ellipticity), the output state can then be described by the vector, $\mathbf{y}_1$ as follows:

$$\mathbf{y}_1 = \mathbf{E}_1 \begin{bmatrix} \cos(\Omega) \\ \\ r_1 \cos(\Omega + \delta_1) \end{bmatrix} \tag{C.3}$$

In general, the x-component of the electric field is now no longer zero, and will also be out of phase with the y-component if the output state exhibits any ellipticity. By combining r_1 and δ_1 into a single term, $Z_1 = r_1 \exp(i\delta_1)$, we can rewrite Eq. C.3 as:

$$\mathbf{y}_1 = \frac{\mathbf{E}_1}{2} \begin{bmatrix} 1 \\ \\ Z_1 \end{bmatrix} e^{i\Omega} + \frac{\mathbf{E}_1}{2} \begin{bmatrix} 1 \\ \\ Z_1^* \end{bmatrix} e^{-i\Omega}. \tag{C.4}$$

The terms r_1 and δ_1 can then be related to $\Delta\phi_1$ and η_1 by the general equations:

$$r_i^2 = \frac{\tan^2(\Delta\phi_i) + \tan^2(\eta_i)}{1 + \tan^2(\Delta\phi_i)\tan^2(\eta_i)} \tag{C.5}$$

and

$$\tan(\delta_i) = \frac{\tan(\eta_i)[1 + \tan^2(\Delta\phi_i)]}{\tan(\Delta\phi_i)[\tan^2(\eta_i) - 1]} \tag{C.6}$$

where $i = 1$.

If repeating the above process for an input state that is linearly polarized in the x-direction (i.e. horizontally polarized in the plane of incidence with ϕ_0 = -90°), and with the same intensity as in vertically polarized case (but different phase δ), the input state can be represented by a second two-component vector, $\mathbf{x}_2$, where:

$$\mathbf{x}_2 = \frac{\mathbf{E}_0}{2} \begin{bmatrix} 0 \\ \\ 1 \end{bmatrix} e^{i(\Omega+\delta)} + \frac{\mathbf{E}_0}{2} \begin{bmatrix} 0 \\ \\ 1 \end{bmatrix} e^{-i(\Omega+\delta)} \tag{C.7}$$

and the resulting polarization changes given by $\Delta\phi_2$ and η_2 allow us to define the

output vector, $\mathbf{y}_2$, as follows:

$$\mathbf{y}_2 = \frac{\mathbf{E}_2}{2}\begin{bmatrix} -Z_2 \\ 1 \end{bmatrix} e^{i(\Omega+\delta+\delta_0)} + \frac{\mathbf{E}_2}{2}\begin{bmatrix} -Z_2^* \\ 1 \end{bmatrix} e^{-i(\Omega+\delta+\delta_0)}. \tag{C.8}$$

Although it is assumed in the above analysis that the y-component of the input vector $\mathbf{x}_1$ and the x-component of the input vector $\mathbf{x}_2$ are out of phase by δ, same assumption can not be made about the relative phases of the y-component of the output vector $\mathbf{y}_1$ and the x-component of $\mathbf{y}_2$. Therefore an extra phase term δ_0 is required in the above equation. Additionally, the amplitude terms $\mathbf{E}_x$ and $\mathbf{E}_y$ are also unlikely to be equal and must therefore be related by another free scaling parameter r_0 such that $\mathbf{E}_2 = r_0\mathbf{E}_1$. Therefore, $\mathbf{y}_2$ can be rewritten as:

$$\mathbf{y}_2 = \frac{\mathbf{E}_1}{2}\begin{bmatrix} -Z_2 \\ 1 \end{bmatrix} Z_0 e^{i(\Omega+\delta)} + \frac{\mathbf{E}_1}{2}\begin{bmatrix} -Z_2^* \\ 1 \end{bmatrix} Z_0^* e^{-i(\Omega+\delta)}. \tag{C.9}$$

where the modulous (r_2) and argument (δ_2) of Z_2 are related to $\Delta\phi_2$ and η_2 via Eq. C.5 and Eq.C.6 (with $i = 2$) in a similar manner to r_1, δ_1, $\Delta\phi_1$ and η_1.

Because any generalized elliptical input state can be expressed as a linear superposition of Eq. C.2 and Eq. C.7, the generalized output state will be the same linear superposition of Eq. C.4 and Eq. C.9 thus:

$$\mathbf{y} = \frac{\mathbf{E}_1}{2\mathbf{E}_0}\begin{bmatrix} \mathbf{E}_y - Z_2 Z_0 \mathbf{E}_x e^{i\delta} \\ Z_1\mathbf{E}_y + Z_0\mathbf{E}_x e^{i\delta} \end{bmatrix} e^{i\Omega}$$

$$+\frac{\mathbf{E}_1}{2\mathbf{E}_0}\begin{bmatrix} \mathbf{E}_y - Z_2^* Z_0^* \mathbf{E}_x e^{-i\delta} \\ Z_1^*\mathbf{E}_y + Z_0^*\mathbf{E}_x e^{-i\delta} \end{bmatrix} e^{-i\Omega}. \tag{C.10}$$

Eq. C.10 can be rewritten in terms of the transfer matrix, $\mathcal{A}$, and Jones vectors for the input ($\mathbf{J}_x$) and output ($\mathbf{J}_y$) states as follows:

$$\mathbf{y} = \frac{1}{2}(\mu_{xy}\mathbf{J}_y + \mu_{xy}^*\mathbf{J}_y^*) = \frac{\mathbf{E}_1}{2\mathbf{E}_0}(\mathcal{A}\mathbf{J}_x + \mathcal{A}^*\mathbf{J}_x^*) \tag{C.11}$$

where

$$\mathcal{A} = \begin{bmatrix} 1 & -Z_0 Z_2 \\ Z_1 & Z_0 \end{bmatrix} \tag{C.12}$$

and the input Jones vector is

$$\mathbf{J}_x = \begin{bmatrix} \mathbf{E}_y \\ \mathbf{E}_x e^{i\delta} \end{bmatrix} e^{i\Omega} = \begin{bmatrix} 1 \\ Z_x \end{bmatrix} \mathbf{E}_y e^{i\Omega}. \tag{C.13}$$

The output Jones vector ($\mathbf{J}_y$) can then be similarly defined as:

$$\mathbf{J}_y = \begin{bmatrix} 1 \\ Z_y \end{bmatrix} \mathbf{E}_y e^{i\Omega}. \tag{C.14}$$

provided that the complex parameter μ_{xy} is appropriately defined as follows:

$$\mu_{xy} = \frac{\mathbf{E}_1}{\mathbf{E}_0}(1 - Z_0 Z_2 Z_x) \tag{C.15}$$

The double subscript on the parameter μ_{xy} is used to indicate that, while it is a parameter that is associated with the output state, its magnitude depends explicitly on the input polarization state, Z_x. This dependence on the input state can result in large variations in the relative intensity of the output beam for different input polarization states.

It can be seen that Eq. C.10 contains a pair of terms on each side of the equality sign that are mutual complex conjugates. It is therefore sufficient to consider only one term of each pair in our algebraic analysis:

$$\mu_{xy}\mathbf{J}_y = \mathcal{A}\mathbf{J}_x \tag{C.16}$$

and take the real part of $\mathbf{J}_y$ to generate the final result for $\mathbf{y}$. The input and output Jones vectors are then each characterized uniquely by their individual Z-parameters (Z_x and Z_y respectively) that are in turn related to the polarization azimuth, ϕ, and the ellipticity, η, via Eq. C.5 and Eq. C.6 if $\Delta\phi$ is replaced by ϕ in those equations.

As Z_1 and Z_2 have already been determined experimentally, the only remaining unknown is Z_0. This can be calculated by performing a third polarization measurement with a linearly polarized input that is a linear superposition of $\mathbf{x}_1$ and $\mathbf{x}_2$. If the input has a polarization azimuth of ϕ_3, and the resulting polarization azimuth

rotation and ellipticity of the output are $\Delta\phi_3$ and η_3 respectively, we can generate a Z-parameter, $Z_3 = r_3\exp(i\delta_3)$ for the output state $\mathbf{y}_3$, again using Eq. C.5 and Eq. C.6. The parameter Z_0 can then be determined as follows:

$$Z_0 = \frac{Z_1 + Z_1 Z_3 \tan\phi_3 + \tan\phi_3 - Z_3}{Z_3\tan^2\phi_3 + Z_2 Z_3 \tan\phi_3 + \tan\phi_3 - Z_2\tan^2\phi_3}. \tag{C.17}$$

Because only three experimental data points are needed from the polarization response to calculate the three independent elements of the transfer matrix, $\mathcal{A}$, for a particular diffraction channel from a given PCM sample, the fidelity of $\mathcal{A}$ will be strongly dependent on the accuracy of those three measurements. This accuracy can, of course, be improved by choosing additional combinations of data points to calculate the matrix elements, and then taking an average over the different results. However, due to the consistency achieved in the relative accuracy of the measurement data, it is found that generally such a procedure is unnecessary. By using the data points corresponding to input polarization azimuths of $\phi_0 = 0°$, $\phi_0 = -40°$ and $\phi_0 = -90°$, it is able to generate theoretical data sets that agreed with the remaining experimental data to an accuracy of better than 0.5°. This degree of agreement between the predictions of the transfer matrix and the remainder of the experimental data is within the measurement accuracy of these data.

Appendix D

Simulation of pn^+ silicon photodiode

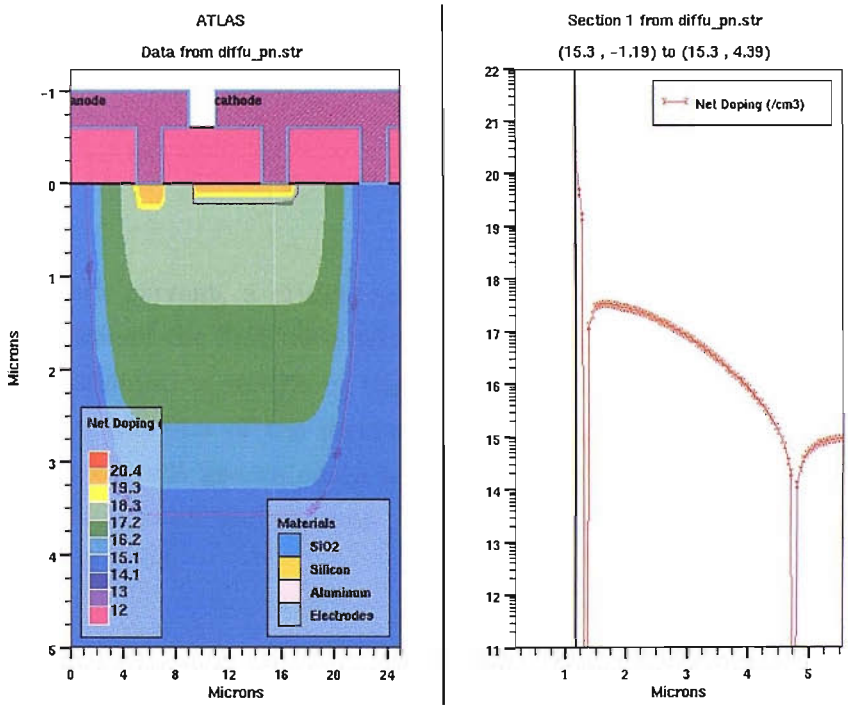

Figure D.1: The cross-sectional structure and the carriers doping profile of the designed pn^+ silicon photodiode from 2D ATHENA process simulation.

In order to design a photodiode with high responsivity, high quantum efficiency and low dark current, the pn^+ silicon photodiode was simulated by two simulation tools, including SILVACO ATHENA (a 2D process simulation tool), and ATLAS (a physically based 3D device simulator). By running the process simulation, a 2D device structure was created and its physical behaviours, such as carriers doping profile, energy bandgap and junction depth, were simulated. These parameters are

associated with device performance directly. As an example, Fig. D.1 shows the simulation result of the cross-sectional structure of the designed pn^+ silicon photodiode and its net doping profile from ATHENA simulation. From the doping profile, it could be seen that a shallow pn-junction was formed between n^+-cathode and p-anode at about 0.7 μm underneath the substrate surface. ATLAS device simulation tool was used to simulate the electronic and optical responses of the silicon photodiode, including the quantum efficiency, dark current, spectrum sensitivity, frequency response and transient response. These responses were simulated by using a LUMINOUS package of the ATLAS framework, which calculated the optical intensity profiles within the semiconductor device, and converted these profiles into photogeneration rates in the device simulators. This unique coupling of tools allowed the simulation of electronic responses to an optical signal for a broad range of optical detectors. The structure file, which defines the structure of photodiode used in ATLAS, came directly from the ATHENA process simulation. When running ATLAS, the structure file was passed through the interface of these two simulation tools. A single optical source was described by defining different extraction commands and the illumination characteristics of the silicon photodiode were therefore calculated and plotted.

Dark current

Finding the dark current, a critical parameter which limits the operation of the photodiode, is one of the first tasks when characterizing a photo-detector. Fig. D.2 (a) shows the simulation results of the dark current generated in the pn^+ silicon photodiode as a function of the reverse biased voltage. It shows clearly that the maximum dark current generated in the photodiode is up to 0.6 pA under a 2V reverse bias. This small dark current implies that the sensitivity of the designed photo-detector is good.

Frequency response

Except for all the above DC simulations, an AC simulation analyzed the response of the device to small signals optical source. The simulated frequency response of the pn^+ silicon photodiode was shown in Fig. D.2 (b) by ramping the frequency within a wide range. From the figure, it shows clearly that the designed pn^+ silicon photodiode has a cut-off frequency of about 1GHz.

Spectral response

The spectral response of the photodetector was simulated by extracting both cathode current and available photo current as a function of the wavelength of the incident light. The various wavelength, λ, was defined by a LAMBDA parameter in LUMINOUS package. The spectral response of the pn^+ silicon photodiode was extracted for discrete source wavelengths from 100 nm to 900 nm as illustrated in Fig. D.2 (c). These simulation results demonstrate that the designed pn^+ silicon photodiode exhibits a good quantum efficiency within a visible wavelength range from about 400 to 800 nm.

Transient Response

Last, it is desirable to examine the time domain response of the photodetector to understand the response speed of the photodetector. The extracted available photo current and cathode current were plotted as a function of the transient time, as illustrated in Fig. D.2 (d). By comparing the cathode current with the available photo current as a function of time, it shows that the cathode current lags behind the available photo-current by a fraction of a nanosecond. This simulation result provides strong evidence of the fast response speed of the designed pn^+ silicon photodiode.

Quantum efficiency

The quantum efficiency of the photodetector was calculated by taking the ratio of the terminal current to the source or available photo-currents. It represents the detection efficiency of the photodetector. All the currents, including the terminal current, the source photo current and the available photo current, were all extracted from the LUMINOUS package. The source photo current is the equivalent current that the photodetector would produce if the source beam energy were collected with unity quantum efficiency, and the available photo current represents the portion of the source photo current that is actually absorbed in the material regions. As a consequence, the quantum efficiency of the $p\text{-}n^+$ silicon photodiode was calculated and plotted in Fig. D.2 (e). From the figure, it can be seen that the quantum efficiency of this pn^+ silicon photodiode is up to 95% and relatively independent of the incident light intensity.

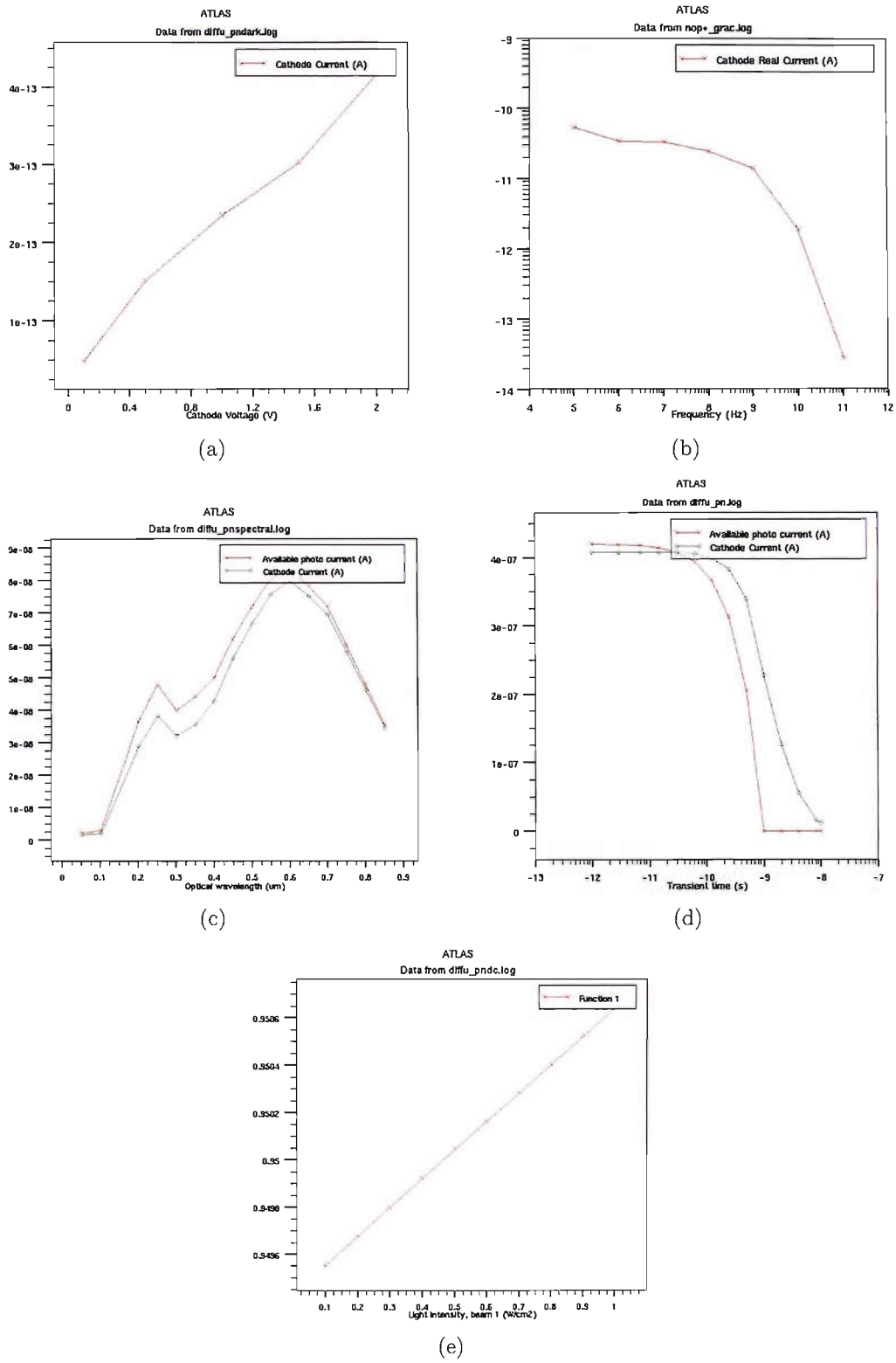

Figure D.2: (a) Simulated dark current of the pn^+ photodiode under reverse bias. (b) AC simulation results showing that the device has a cut-off frequency of about 1GHz. (c) The spectral response of the designed pn^+ silicon photodiode. (d) Simulated transient response of the pn^+ photodiode with the cathode current lags the available photo current by a fraction of a nanosecond. (e) Simulated quantum efficiency of the pn^+ silicon photodiode as a function of incident light intensity.

Appendix E

Transfer matrix method (TMM) for light wave propagating in single and multilayer films

The transfer matrix method to obtain the solution of the wave-equation for light propagating in single and multilayer planar structures is described here.

Considering a linearly polarized wave with an electric filed $\overrightarrow{E}$ perpendicular to the plane-of incidence as shown in Fig. E.1, impinges on a thin dielectric film with a thickness of d, which is a fraction of a wavelength. Each wave $\mathbf{E}_{iI}$, $\mathbf{E}_{rI}$ and $\mathbf{E}_{tI}$ at boundary I; $\mathbf{E}_{iII}$, $\mathbf{E}_{rII}$ and $\mathbf{E}_{tII}$ at boundary II, represents the resultant of all possible waves traveling in that direction at that point in the medium. The boundary conditions require that the tangential components of both the electric ($\overrightarrow{\mathbf{E}}$) and magnetic ($\overrightarrow{\mathbf{H}}$= $\overrightarrow{\mathbf{B}}/\mu$) fields be continuous across the boundaries. At boundary I:

$$\mathbf{E}_I = \mathbf{E}_{iI} + \mathbf{E}_{rI} = \mathbf{E}_{tI} + \mathbf{E}'_{rII} \tag{E.1}$$

Due to the fact that ($\overrightarrow{\mathbf{E}}$) and ($\overrightarrow{\mathbf{H}}$) in nonmagnetic media are related through the refractive index and the unit propagation vector:

$$\overrightarrow{\mathbf{H}} = \sqrt{\frac{\varepsilon_0}{\mu_0}} n\hat{k} \times \overrightarrow{\mathbf{E}} \tag{E.2}$$

therefore

$$\mathbf{H}_I = \sqrt{\frac{\varepsilon_0}{\mu_0}} (\mathbf{E}_{iI} - \mathbf{E}_{rI}) n_i \cos\theta_{iI}$$

and

$$\mathbf{H}_I = \sqrt{\frac{\varepsilon_0}{\mu_0}} (\mathbf{E}_{tI} - \mathbf{E}'_{rII}) n_1 \cos\theta_{iII} \tag{E.3}$$

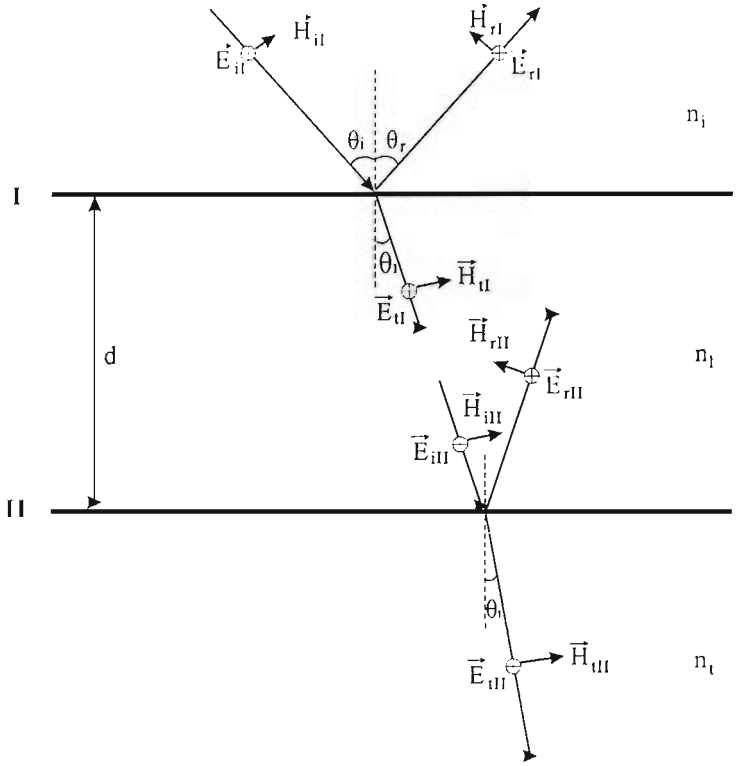

Figure E.1: Schematic diagram of electric field (**E**) and magnetic field (**H**) distribution at the boundaries of a dielectric layer a fraction of a wavelength thick.

At boundary **II**

$$\mathbf{E}_{II} = \mathbf{E}_{iII} + \mathbf{E}_{rII} = \mathbf{E}_{tII} \tag{E.4}$$

and

$$\mathbf{H}_{II} = \sqrt{\frac{\varepsilon_0}{\mu_0}}(\mathbf{E}_{iII} - \mathbf{E}_{rII})n_1 \cos\theta_{iII}$$

$$\mathbf{H}_{II} = \sqrt{\frac{\varepsilon_0}{\mu_0}}\mathbf{E}_{tII}n_s \cos\theta_{tII} \tag{E.5}$$

A wave that traverses the film once undergoes a shift in-phase of:

$$\Lambda = 2k_0 n_1 d \cos\theta_{iII} \tag{E.6}$$

which is denoted by k_0h, so that

$$\mathbf{E}_{iII} = \mathbf{E}_{tI}e^{-ik_0h} \tag{E.7}$$

and

$$\mathbf{E}_{rII} = \mathbf{E}'_{rII}e^{ik_0h} \tag{E.8}$$

Eqn. E.4 and Eqn. E.5 can now be written as:

$$\mathbf{E}_{II} = \mathbf{E}_{tI} e^{-ik_0 h} + \mathbf{E}'_{rII} e^{ik_0 h} \tag{E.9}$$

and

$$\mathbf{H}_{II} = (\mathbf{E}_{tI} e^{-ik_0 h} - \mathbf{E}'_{rII} e^{ik_0 h}) \sqrt{\frac{\varepsilon_0}{\mu_0}} n_1 \cos\theta_{iII} \tag{E.10}$$

Eqn. E.9 and Eqn. E.10 can be solved for E_{tI} and E'_{rII}, which when substituted into Eqn. E.1 and Eqn. E.3 yield:

$$\mathbf{E}_I = \mathbf{E}_{II} \cos k_0 h + \mathbf{H}_{II} (i \sin k_0 h)/\Upsilon_1 \tag{E.11}$$

and

$$\mathbf{H}_I = \mathbf{E}_{II} \Upsilon_1 i \sin k_0 h + \mathbf{H}_{II} \cos k_0 h \tag{E.12}$$

where

$$\Upsilon_1 = \sqrt{\frac{\varepsilon_0}{\mu_0}} n_1 \cos\theta_{iII} \tag{E.13}$$

When $\vec{E}$ is parallel to the plane-of-incidence, however:

$$\Upsilon_1 = \sqrt{\frac{\varepsilon_0}{\mu_0}} n_1 / \cos\theta_{iII} \tag{E.14}$$

In matrix notation, the above linear relations take the form:

$$\begin{bmatrix} \mathbf{E}_I \\ \mathbf{H}_I \end{bmatrix} = \begin{bmatrix} \cos k_0 h & (i \sin k_0 h)/\Upsilon_1 \\ \Upsilon_1 i \sin k_0 h & \cos k_0 h \end{bmatrix} \begin{bmatrix} \mathbf{E}_{II} \\ \mathbf{H}_{II} \end{bmatrix} \tag{E.15}$$

or

$$\begin{bmatrix} \mathbf{E}_I \\ \mathbf{H}_I \end{bmatrix} = M_1 \begin{bmatrix} \mathbf{E}_{II} \\ \mathbf{H}_{II} \end{bmatrix} \tag{E.16}$$

M_1 is referred as *characteristic matrix* and it relates the fields at the two adjacent boundaries. It can be extended to multilayer films, each of which has a particular value of refractive index, n, and thickness, h. Then the first and the last boundaries are related by:

$$\begin{bmatrix} \mathbf{E}_I \\ \mathbf{H}_I \end{bmatrix} = M_1 M_2 M_3 \ldots M_n \begin{bmatrix} \mathbf{E}_{n+1} \\ \mathbf{H}_{n+1} \end{bmatrix} \tag{E.17}$$

The characteristic matrix of the entire system can be expressed as:

$$M = M_1 M_2 M_3 \ldots M_n = \begin{bmatrix} m_{11} & m_{12} \\ m_{21} & m_{22} \end{bmatrix} \tag{E.18}$$

this characteristic matrix of the entire system connects the complex amplitudes of the electric and magnetic fields at the top and bottom surfaces of the stack for a particular polarization state of light.

In order to derive expressions for the amplitude coefficients of reflection and transmission using the above scheme, Eqn. E.17 can be reformed in terms of the boundary conditions (Eqn. E.1, Eqn. E.3 and Eqn. E.5) and setting:

$$\Upsilon_i = \sqrt{\frac{\varepsilon_0}{\mu_0}} n_i \cos\theta_{iI}$$

$$\Upsilon_t = \sqrt{\frac{\varepsilon_0}{\mu_0}} n_t \cos\theta_{tII}$$

Therefore

$$\begin{bmatrix} (\mathbf{E}_{iI} + \mathbf{E}_{rI}) \\ (\mathbf{E}_{iI} - \mathbf{E}_{rI})\Upsilon_i \end{bmatrix} = M_1 \begin{bmatrix} \mathbf{E}_{tII} \\ \mathbf{E}_{tII}\Upsilon_t \end{bmatrix} \tag{E.19}$$

The amplitude coefficients of reflection and transmission can be obtained by:

$$r = \frac{\mathbf{E}_{rI}}{\mathbf{E}_{iI}}$$

$$t = \frac{\mathbf{E}_{tII}}{\mathbf{E}_{iI}}$$

Expanding Eqn. E.19 and substitute Eqn. E.20 and Eqn. E.20:

$$1 + r = m_{11}t + m_{12}\Upsilon_t t$$

$$(1 - r)\Upsilon_i = m_{21}t + m_{22}\Upsilon_t t$$

As a result, the amplitude reflection and transmission coefficients r and t of a stack are given by:

$$r = \frac{\Upsilon_i m_{11} + \Upsilon_i\Upsilon_t m_{12} - m_{21} - \Upsilon_t m_{22}}{\Upsilon_i m_{11} + \Upsilon_i\Upsilon_t m_{12} + m_{21} + \Upsilon_t m_{22}} \tag{E.20}$$

$$t = \frac{2\Upsilon_i}{\Upsilon_i m_{11} + \Upsilon_i\Upsilon_t m_{12} + m_{21} + \Upsilon_t m_{22}} \tag{E.21}$$

Consequently, either r or t for any configuration of planar structures can be calculated by the above equations.

Appendix F

Publications

F.1 Publications

1. W. Zhang, A. Potts, and D. M. Bagnall, 'Giant optical activity in dielectric planar metamaterials with 2D chirality', *Journal of Optics A: Pure and Applied Optics*, **8**, pp.878-890, 2006.

2. W. Zhang, A. Potts, D. M. Bagnall, and B. R. Davidson, 'High resolution electron beam lithography for the fabrication of high density dielectric metamaterials', *Thin Solid Films*, To be published, August 2006.

3. W. Zhang, A.Potts, D. M. Bagnall and B. R. Davidson, 'Large area all-dielectric planar chiral meta-materials by electron beam lithography', *Journal of Vacuum Science and Technology B*, , **24**, pp.1455, 2006.

4. W. Zhang, A. Potts, A. Papakostas and D. M. Bagnall, 'Intensity modulation and polarization rotation of visible light by dielectric planar chiral metamaterials', *Applied Physics Letters* **86** (23), pp. 231905, 2005

5. A. M. Waite, N. S. Lloyd, K. Osman, W. Zhang, T. Ernst, H. Achard, Y. Wang, S. Deleonibus, P. L. F. Hemment, D. M. Bagnall, A. G. R. Evans and P. Ashburn, 'Elevated Source/Drains for 50nm MOSFETs using HCl-Free Selective Epitaxy', *Solid State Electronics* **49**, pp. 529-534, 2005

6. A. Papakostas, A. Potts, W. Zhang, D. M. Bagnall and N. I. Zheludev, 'Planar

chiral meta-materials', *Proceedings of the 5th International Conference on Materials for Microelectronics and Nanoengineering*, Institute of Materials IOM, Southampton, UK pp. 87-90, 2005

7. W. Zhang, N. S. Lloyd, K. Osman, L. M. Bonar, J. S. Hamel and D. M. Bagnall, 'Selective epitaxial growth using dichlorosilane and silane by low pressure chemical vapor deposition', *Microelectronics Engineering* **73-74**, pp. 514-518, 2004

8. W. Zhang, A. Papakostas, A. Potts, D. M. Bagnall and N. I. Zheludev, 'Planar chiral metamaterials and their application to optoelectronics devices', *Proceedings of Nano and Giga Challenges in Microelectronics*, Cracow, Poland, 2004

F.2 Conferences and Talks

1. "Dielectric planar chiral metamaterials", *The Rank Prize Funds, Mini-Symposium on metamaterials in nature and technology*, UK, Aug 2006.

2. "Polarization state and intensity modulation of dielectric planar chiral metamaterials", *Photonics North 2006*, Quebec, Canada, June 2006.

3. "High resolution electron beam lithography for the fabrication of high density optical metamaterials", *Conference on Micro and Nano Engineering 2005*, Vienna, Austria, Sept 2005.

4. "Planar chiral metamaterials", *The 5th International Conference on Materials for Microelectronics and Nanoengineering*, Institute of Materials IOM, Southampton, UK, Sep 2005.

5. "Planar chiral metamaterials and their application to optoelectronics devices", *Nano and Giga Challenges in Microelectronics, Symposium and Summer School Research and Development Opportunities*, Cracow, Poland, Sep 2004.

6. "Selective Epitaxial Growth Using Dichlorosilane and Silane by Low Pressure Chemical Vapour Deposition", *Conference on Micro and Nano Engineering 2003*, Cambridge UK, Sep 2003.

references

[1] T. F. Krauss and R. M. DeLaRue. Photonic crystals in the optical regime-past, present and future. *Progress in Quantum Electronics*, 23:51, 1999.

[2] J. Lekner. Omnidirectional reflection by multilayer dielectric mirrors. *Journal of Optics A: Pure and Applied Optics*, 2:349, 2000.

[3] K. Robbie and M.J. Brett. A chiral sculptured thin films. *Nature*, 384:616, 1996.

[4] L. D. Barron. On the definition of chirality. *Chemistry - A European Journal*, 2(6):743, 1996.

[5] E. Hecht. *Optics*. Addison-Wesley, 4th edition, 2002.

[6] J. Wilson and J. Hawkes. *Optoelectronics an Introduction*. Prentice Hall, 3rd edition, 1998.

[7] L. Hecht and L. D. Barron. Rayleigh and raman optical activity from chiral surfaces and interfaces. *Journal of Molecular Structure*, 348:217, 1995.

[8] L. R. Arnaut and L. E. Davis. Dispersion characteristics of planar chiral structures. *Proceedings of the international conference on electromagnetics in advanced applications*, page 381, 1995.

[9] A. Potts, A. Papakostas, N. I. Zheludev, H. J. Coles, R. Greef, and D. M. Bagnall. Optical properties of planar chiral metamaterials. *Materials Research Society Symposium Proceedings*, 722:293, 2002.

[10] A. Papakostas, A. Potts, D. M. Bagnall, S. L. Prosvirnin, H. J. Coles, and N. I. Zheludev. Optical manifestations of planar chirality. *Physical Review Letters*, 90:107404, 2003.

[11] A. Potts, A. Papakostas, N. I. Zheludev, H. J. Coles, R. Greef, and D. M. Bagnall. Planar chiral meta-materials for photonic devices. *Journal of Material Science: Materials in Electronics*, 14(5/7):393, May 2003.

[12] A. Potts, D. M. Bagnall, and N. I. Zheludev. A new model of geometric chirality for two-dimensional continuous media and planar meta-materials. *Journal of Optics A: Pure and Applied Optics*, 6:193, 2004.

[13] Y. Svirko, N. Zheludev, and M. Osipov. Layered chiral metallic microstructures with inductive coupling. *Applied Physics Letters*, 78(4):498, 2001.

[14] A. S. Schwanecke, A. Krasavin, D. M. Bagnall, A. Potts, A. V. Zayats, and N. I. Zheludev. Broken time reversal of light interaction with planar chiral nanostructures. *Physical Review Letters*, 91(24):247404, 2003.

[15] W. J. Padilla, D. N. Basov, and D. R. Smith. Negative refractive index metamaterials. *Materials today*, 9(7-8):28, 2006.

[16] J. B. Pendry, A. J. Holden, D. J. Robbins, and W. J. Stewart. Magnetism from conductors and enhanced nonlinear phenomena. *IEEE Transactions on Microwave Theory and Techniques*, 47(11):2075, 1999.

[17] R. A. Shelby, D. R. Smith, S. C. Nemat-Nasser, and S. Schultz. Microwave transmission through a two-dimensional, isotropic, left-handed metamaterial. *Applied Physics Letters*, 78(4):489, 2001.

[18] S. O'Brien, D. McPeake, S. A. Ramakrishna, and J. B. Pendry. Near-infrared photonic band gaps and nonlinear effects in negative magnetic metamaterials. *Physical Review B*, 69:241101, 2004.

[19] A. N. Grigorenko, A. K. Geim, H. F. Gleeson, Y. Zhang, A. A. Firsov, I. Y. Khrushchev, and J. Petrovic. Nanofabricated media with negative permeability at visible frequencies. *Nature*, 438(17):335, 2005.

[20] V. G. Veselago. The electrodynamics of substances with simultaneously negative values of μ and ε. *Soviet Physics Uspekhi*, 10(4):509, 1968.

[21] J. B. Pendry, A. J. Holden, W. J. Stewart, and I. Youngs. Extremely low frequency plasmons in metallic mesostructures. *Physical Review Letters*, 76(25):4773, 1996.

[22] R. M. Walser, A. P. Valanju, and P. M. Valanju. Comment on "extremely low frequency plasmons in metallic mesostructures". *Physical Review Letters*, 87(11):119701, 2001.

[23] D. R. Smith, W. J. Padilla, D. C. Vier, S. C. Nemat-Nasser, and S. Schultz. Composite medium with simultaneously negative permeability and permittivity. *Physical Review Letters*, 84(18):4184, 2000.

[24] C. G. Parazzoli, R. B. Greegor, K. Li, B. E. C. Koltenbah, and M. Tanielian. Experimental verification and simulation of negative index of refraction using snell's law. *Physical Review Letters*, 90:107401, 2003.

[25] M. C. K. Wiltshire, J. B. Pendry, I. R. Young, D. J. Larkman, D. J. Gilderdale, and J. V. Hajnal. Microstructured magnetic materials for RF flux guides in magnetic resonance imaging. *Science*, 291:849, 2001.

[26] T. J. Yen. Terahertz magnetic response from artificial materials. *Science*, 303:1494, 2004.

[27] S. Linden, C. Enkrich, M. Wegener, J. Zhou, T. Koschny, and C. M. Soukoulis. Magnetic response of metamaterials at 100 terahertz. *Science*, 306:1351, 2004.

[28] C. Enkrich, M. Wegener, S. Linden, S. Burger, L. Zschiedrich, F. Schmidt, J. F. Zhou, Th. Koschny, and C. M. Soukoulis. Magnetic metamaterials at telecommunication and visible frequencies. *Physical Review Letters*, 95:203901, 2005.

[29] A. Boardman, N. King, Y. Rapoport, and L. Velasco. Gyrotropic impact upon negatively refracting surfaces. *New Journal of Physics*, 7:191, 2005.

[30] K. Aydin, K. Guven, and E. Ozbay. Two-dimensional left-handed metamaterial with a negative refractive index. *Journal of Physics: Conference Series*, 36:6, 2006.

[31] E. Cubukcu, K. Aydin, E. Ozbay, S. Foteinopoulou, and C. M. Soukoulis. Electromagnetic waves: Negative refraction by photonic crystals. *Nature*, 423:604, 2003.

[32] P. V. Parimi, W. T. Lu, P. Vodo, and S. Sridhar. Photonic crystals: Imaging by flat lens using negative refraction. *Nature*, 426:404, 2003.

[33] M. Ahmadlou, M. Kamarei, and M. H. Sheikhi. Negative refraction and focusing analysis in a left-handed material slab and realization with a 3d photonic crystal structure. *Journal of Optics A: Pure and Applied Optics*, 8:199, 2006.

[34] D. R. Smith and N. Kroll. Negative refractive index in left-handed materials. *Physical Review Letter*, 85(14):2933, 2000.

[35] R. W. Ziolkowski and E. Heyman. Wave propagation in media having negative permittivity and permeability. *Physical Review E*, 64(5):056625, 2001.

[36] F. J. Rachford, D. L. Smith, P. F. Loschialpo, and D. W. Forester. Calculations and measurements of wire and/or split-ring negative index media. *Physical Review E*, 66:036613, 2002.

[37] W. L. Barnes, A. Dereux, and T. W. Ebbesen. Surface plasmon subwavelength optics. *Nature*, 424:824, 2003.

[38] J. Elliott, I. Smolyaninov, N. I. Zheludev, and A. V. Zayats. Polarization control of optical transmission of a periodic array of elliptical nanoholes in a metal film. *Optics Letters*, 29(12):1414, 2004.

[39] P. L. Guennec. Two-dimensional theory of chirality. i. absolute chirality. *Journal of Mathematical Physics*, 41(9):5594, 2000.

[40] L. D. Barron. Chemistry: Chirality, magnetism and light. *Nature*, 405:895, 2000.

[41] L. Barron. *Molucular Light Scattering and Optical Activity.* Cambridge Univeristy Press, 2nd edition, 2004.

[42] B. I. Halperin, J. March-Russell, and F. Wilczek. Consequences of time-reversal-symmetry violation in models of high-tc superconductors. *Physical Review B*, 40(13):8726, 1989.

[43] J. V. Selinger, Z.G. Wang, R. F. Bruinsma, and C. M. Knobler. Chiral symmetry breaking in langmuir monolayers and smectic films. *Physical Review Letters*, 70(8-22):1139, 1993.

[44] J. M. Hicks, T. P. Mallow, and J. D. Byers. Consequences of chirality in second-order non-linear spectroscopy at surfaces. *Faraday Discussions*, 99:341, 1994.

[45] J. Maclennan and M. Seul. Novel stripe textures in nonchiral hexatic liquid-crystal films. *Physical Review Letters*, 69(14-15):2082, 1992.

[46] J. Pang and N. A. Clark. Observation of a chiral-symmetry-breaking twist-bend instability in achiral freely suspended liquid-crystal films. *Physical Review Letters*, 73(17):2332, 1994.

[47] D. K. Schwartza, J. R. Garciaa, X. Qiua, J. V. Selingerb, and C. M. Knoblera. Tilt stripe textures in langmuir monolayers of fatty acids. *Physica A: Statistical and Theoretical Physics*, 204(1-4):606, 1994.

[48] X. Qiu, J. Ruiz-Garcia, K. J. Stine, C. M. Knobler, and J. V. Selinger. Direct observation of domain structure in condensed monolayer phases. *Physical Review Letters*, 67(6):703, 1991.

[49] F. Charra and J. Cousty. Surface-induced chirality in a self-assembled monolayer of discotic liquid crystal. *Physical Review Letters*, 80(8):1682, 1998.

[50] G. A. Attard. Electrochemical studies of enantioselectivity at chiral metal surfaces. *Journal of Physical Chemistry B*, 105(16):3158, 2001.

[51] D. S. Sholl, A. Asthagiri, and T. D. Power. Naturally chiral metal surfaces as enantiospecific adsorbents. *Journal of Physical Chemistry B*, 105(21):4771, 2001.

[52] H. Zabrodsky and D. Avnir. Continuous symmetry measures. *Journal of the American Chemical Society*, 117:462, 1995.

[53] N. Weinberg and K. Mislow. Distance functions as generatiors of chirality measures. *Journal of Mathematical Chemistry*, 14:427, 1993.

[54] M. A. Osipov, B. T. Pickup, M. Fehervari, and D. A. Dunmur. Chirality measure and chiral order parameter for a two-dimensional system. *Molecular Physics*, 94(2):283, 1998.

[55] L. Hecht and L. D. Barron. Rayleigh and raman optical activity from chiral surfaces. *Chemical Physics Letters*, 225(4-6):525, 1994.

[56] L. R. Arnaut. Chirality in multi-dimensional space with application to electromagnetic characterisation of multi-dimensional chiral and semi-chiral media. *Journal of electromagnetic waves and applications*, 11:1459, 1997.

[57] P. V. Drachev, W. D. Bragg, V. A. Podolskiy, V. P. Safonov, W. T. Kim, Z. C. Ying, R. L. Armstrong, and V. M. Shalaev. Large local optical activity in fractal aggregates of nanoparticles. *Journal of the Optical Society of America B*, 18(12):1896, 2001.

[58] A. Potts, A. Papakostas, D. M. Bagnall, and N. I. Zhuludev. Planar chiral meta-materials for optical applications. *Microelectronic engineering*, 73-74:367, 2004.

[59] B. K. Canfield, S. Kujala, K. Jefimovs, T. Vallius, J. Turunen, and M. Kauranen. Polarization effects in the linear and nonlinear optical responses of gold nanoparticle arrays. *Journal of Optics A: Pure and Applied Optics*, 7(2):110, 2005.

[60] T. W. Ebbesen, H. J. Lezec, H. F. Ghaemi, T. Thio, and P. A. Wolff. Extraordinary optical transmission through sub-wavelength hole arrays. *Nature*, 391:667, 1998.

[61] T. Vallius, K. Jefimovs, J. Turunen, P. Vahimaa, and Y. Svirko. Optical activity in subwavelength-period arrays of chiral metallic particles. *Applied Physics Letters*, 83(2):234–236, 2003.

[62] D. Bedeaux, M. A. Osipov, and J. Vlieger. Reflection of light at structured chiral interfaces. *Journal of the Optical Society of America A*, 21(12):2431, 2004.

[63] S. L. Prosvirnin. Transformation of polarization when waves are reflected by a microstrip array made of complex-shaped elements. *Journal of Communications Technology and Electronics*, 44(6):635, 1999.

[64] M. B. Sobnack, W. C. Tan, N. P. Wanstall, T. W. Preist, and J. R. Sambles. Stationary surface plasmons on a zero-order metal grating. *Physical Review Letters*, 80(25):5667, 1998.

[65] S. L. Prosvirnin and N. I. Zheludev. Polarization effects in the diffraction of light by planar chiral structure. *Physical Review E*, 7:037603, 2005.

[66] M. Kuwata-Gonokami, N. Saito, Y. Ino, M. Kauranen, K. Jefimovs, T. Vallius, J. Turunen, and Y. Svirko. Giant optical activity in quasi-two-dimensional planar nanostructures. *Physical Review Letters*, 95:227401, 2005.

[67] D. W. Dearholt and W. R. McSpadden. *Electromagnetic Wave Propagation.* McGraw-Hill, 1973.

[68] E. Collett. *Polarized Light Fundamentals and Applications.* Marcel Dekker Inc., 1993.

[69] F. L. Pedrotti, L. S. Pedrotti, and L. M. Pedrotti. *Introduction to Optics.* Prentice Hall, 2000.

[70] Serge Huard. *Polarization of Light.* John Wiley and Sons, Inc., 1997.

[71] M. Born and E. Wolf. *Principles of Optics (7th edition).* Cambridge University Press, 2005.

[72] J. D. Kraus and D. A. Fleisch. *Electromagnetics with Applications.* WCB McGraw-Hill, fifth edition, 1999.

[73] D. R. Smith, P.M. Rye, J. J. Mock, D. C. Vier, and A. F. Starr. Enhanced diffraction from a grating on the surface of a negative-index metamaterial. *Physical Review Letters*, 93(13):137405, 2004.

[74] S. A. Maier, M. L. Brongersma, P. G. Kik, S. Meltzer, A. A. G. Requicha, and H. A. Atwater. Plasmonics - a route to nanoscale optical devices. *Advanced Materials*, 13(19):1501, 2001.

[75] O. Painter, R. K. Lee, A. Scherer, A. Yariv, J. D. O'Brien, P. D. Dapkus, and I. Kim. Two-dimensional photonic band-gap defect mode laser. *Science*, 284:1819, 1999.

[76] J. Valenta, R. Juhasz, and J. Linnros. Photoluminescence spectroscopy of single silicon quantum dots. *Applied Physics Letters*, 80(6):1070, 2002.

[77] S. M. Sze. *Semiconductor Devices Physics and Technology.* John Wiley and Sons, Inc., 2nd edition, 2001.

[78] S. M. Sze. *VLSI Technology Second Edition.* McGraw-Hill, 1998.

[79] A. Kowalik, K. Góra, Z. Jaroszewicz, and A. Kolodziejczyk. Multi-step electron beam technology for the fabrication of high performance diffractive optical elements. *Microelectronic engineering*, 77(3-4):347, 2005.

[80] V. Jaubert, P. Lucas, L. Mollard, S. Tedesco, B. Dalzotto, and S. Landis. Characterization of charging effect on 8-inch wafer during e-beam lithography exposure. *Microelectronic engineering*, 67-68:149–156, 2003.

[81] R. Steingruber, M. Ferstla, and W. Pilzb. Micro-optical elements fabricated by electron-beam lithography and dry etching technique using top conductive coatings. *Microelectronic engineering*, 57-58:285, 2001.

[82] J. Hirumi, T. Hayashimoto, T. Kawabata, K. Hosono, E. Hoshino, and J. Kai. Deflection error due to charge-up effect of reticle substrate. *Photomask and X-Ray Mask Technology V*, 3412:307, 1998.

[83] A. Potts, A. Papakostas, W. Zhang, D. M. Bagnall, and N. I. Zheludev. The roles of size effects and symmetry transformations in defining the electromeganetic response from planar chiral surfaces. unpublished, 2006.

[84] A. Potts, W. Zhang, and D. M. Bagnall. The effect of 2d chirality and film thickness on the polarization eigenstates of dielectric planar chiral metamaterials. unpublished, 2006.

[85] E. Greger, K. H. Gulden, P. Riel, H. P. Schweizer, M. Moser, G. Schmiedel, P. Kiesel, and G. H. Döhler. Polarization effect in light emitting diodes with ordered GaInP active layers. *Applied physics letters*, 68(17):2383, 1996.

[86] G. Schmiedel, P. Kiesel, G. H. Döhler, E. Greger, K. H. Gulden, H. P. Schweizer, and M. Moser. Electroabsorption in ordered and disordered GaInP. *Journal of Applied Physics*, 81(2):1008, 1997.

[87] E. Greger, P. Riel, M. Moser, T. Kippenberg, P. Kiesel, and G. H. Döhler. Polarization threshold switches based on ordered GaInP. *Applied physics letters*, 71(22):3245, 1997.

[88] P. Kiesel, J. Spieler, T. Kippenberg, M. Muller, and G. H. Dohler. Polarization-sensitive opto-electronic devices based on spontaneous self-ordering in semiconductor alloys. *Materials Science and Engineering B*, 88(2-3):307, 2002.

[89] R. J. Potton. Reciprocity in optics. *Institute of Physics publishing*, 67:714, 2004.

[90] J. Kong. *Electromagnetic Wave Theory*. John Wiley and Sons, Inc., New York, 1986.

[91] M. Nieto-Vesperinas. *Scattering and Diffraction in Physical Optics*. John Wiley and Sons, Inc., 1991.

[92] A. Potts, A. Papakostas, W. Zhang, D. M. Bagnall, and N. I. Zheludev. Non-reciprocal diffraction from dielectric planar metamaterials with 2d chirality. unpublished, 2006.

[93] D. Labilloy, H. Benisty, C. Weisbuch, C. J. M. Smith, T. F. Krauss, R. Houdré, and U. Oesterle. Finely resolved transmission spectra and band structure of two-dimensional photonic crystals using emission from InAs quantum dots. *Physics Review B*, 59(3):1649, 1999.

[94] E. Yablonovitch. Inhibited spontaneous emission in solid-state physics and electronics. *Physical review letters*, 58(20):2059, 1987.

[95] A. Thetford. The basic theory of multilayers. *Optics and Laser Technology*, 3(3):131, 1971.

[96] J. Lekner. Light in periodically stratified media. *Journal of the Optical Society of America A*, 11(11):2892, 1994.

[97] D. Bhattacharyya, N. K. Sahoo, S. Thakur, and N. C. Das. Spectroscopic ellipsometry of multilayer dielectric coatings. *Vacuum*, 60(4):419, 2001.

[98] *Tanner EDA*. 2650 East Foothill Boulevard Pasadena, CA 91107, USA, l-edit proversion 11.0 edition.